A Mesoscopic Simulation Method for Electrolyte Solutions

Dissertation zur Erlangung des Grades
“Doktor der Naturwissenschaften”
am Fachbereich 08 (Institut für Physik) der

Johannes Gutenberg-
Universität Mainz

JG|U

Stefan Medina Hernando

geboren in Alsfeld

Mainz, Juli 2013

First Reader:

Second Reader:

Date of oral examn: 27-Nov-2013
D77 - Dissertation der Johannes-Gutenberg Universität Mainz

Zusammenfassung

Diese Dissertation beschäftigt sich mit der Entwicklung einer neuartigen Simulationsmethode zur Untersuchung von Makromolekülen in Elektrolytlösungen mit dem Ziel einer Effizienzsteigerung gegenüber üblichen, auf Molekulardynamik basierenden, Simulationsmethoden. Die zu untersuchenden Makromoleküle sind in Lösung umgeben von Salzionen, wodurch ein komplexes Zusammenspiel von elektrostatischen und hydrodynamischen Wechselwirkungen die Gleichgewichts- und Nichtgleichgewichtseigenschaften der Lösung bestimmt. Hierbei fordern die Beschreibung des Lösungsmittels als auch der gelösten Salzionen den Großteil der Rechenzeit. Daher ist eine effiziente Modellierung beider Komponenten essentiell für die Leistungsfähigkeit einer Simulationsmethode. Im hier beschriebenen Ansatz wählen wir eine vergröberte Darstellung des Lösungsmittels und behandeln die Ionen in dynamischer Molekularfeldnäherung, womit wir effektiv die elektrokinetischen Gleichungen für die Dynamik lösen. Somit kombinieren wir Partikel- und Feldbeschreibungen zu einer Hybridmethode. Der Algorithmus wird umfangreich auf Genauigkeit und Schnelligkeit getestet und geeignete Einstellungsparameter bestimmt. Daraufhin folgen zwei Anwendungen. Zuerst widmen wir uns der Untersuchung von geladenen Polymerlösungen (Polyelektrolyte) unter Scherung zur Bestimmung der viskoelatischen Eigenschaften. Dabei werden auch rechnerisch aufwendige semiverdünnte Lösungen betrachtet. Danach untersuchen wir den elektro-osmotischen Fluss auf superhydrophoben Oberflächen, wobei ein detaillierter Vergleich mit theoretischen Vorhersagen durchgeführt wird. Hierbei bestätigt sich, dass eine Optimierung der Oberflächenstruktur die Flussgeschwindigkeit deutlich erhöhen kann, was hinsichtlich mikrofluidischer Anwendungen von großer Bedeutung ist.

Abstract

This thesis deals with the development of a novel simulation technique for macromolecules in electrolyte solutions, with the aim of a performance improvement over current molecular-dynamics based simulation methods. In solutions containing charged macromolecules and salt ions, it is the complex interplay of electrotatic interactions and hydrodynamics that determines the equlibrium and non-equilibrium behavior. However, the treatment of the solvent and dissolved ions makes up the major part of the computational effort. Thus an efficient modeling of both components is essential for the performance of a method. With the novel method we approach the solvent in a coarse-grained fashion and replace the explicit-ion description by a dynamic mean-field treatment. Hence we combine particle- and field-based descriptions in a hybrid method and thereby effectively solve the electrokinetic equations. The developed algorithm is tested extensively in terms of accuracy and performance, and suitable parameter sets are determined. As a first applicaton we study charged polymer solutions (polyelectrolytes) in shear flow with focus on their viscoeleastic properties. Here we also include semidilute solutions, which are computationally demanding. Secondly we study the electro-osmotic flow on superhydrophobic surfaces, where we perform a detailed comparison to theoretical predictions.

CONTENTS

INTRODUCTION

Computer simulations of matter can be divided into several categories separated according to the length and time scales, ranging from quantum mechanical calculations of electronic structures up to cosmological simulations of entire galaxies. This study will focus on the mesoscale of physics, which is found between the macroscopic scale, which we deal with in every day life, and the atomistic scale, where quantum physical effects start to set in. Thus it spans length scales of nanometers and micrometers, and accordingly, time scales of nanoseconds up to microseconds, as illustrated in Figure 0.1. The description of matter on the mesoscale is rather ambiguous, as both continuum and particle descriptions are useful, depending on the circumstances. However, the particle description is usually rather coarse. Thus it is a microscopic macromolecular approach, i.e. the role of smallest building blocks is not played by atoms, but by molecules. Strictly speaking this description is also phenomenological, because some parameters have to be introduced and determined empirically [1]. Nevertheless it allows to explain phenomena from the macromolecular point of view without the need to know all the microscopic details.

From a microscopic, bottom-up perspective, we are interested in the behavior of electrolyte solutions, which contain salt ions and solvent particles. Often macromolecules are additionally dissolved in the solution, which are in the focus of the scientific investigations. A typical example would be the study of DNA-molecule dynamics in salt solution. The complex conglomerate of molecules is dominated by long-ranged interactions, namely the electrostatics and the hydrodynamics. The former are related to the electric charges carried by ions, and the latter are related to forces transmitted by the motion of solvent. From a macroscopic, top-down perspective, it is the electrokinetic equations that describe the dynamics of such solutions, leaving out all the particle-details and describing the constituents as continuous concentration fields.

By combining the two perspectives, we are able to build a hybrid simulation scheme, where both particle and continuous descriptions come into play. More precisely, we re-

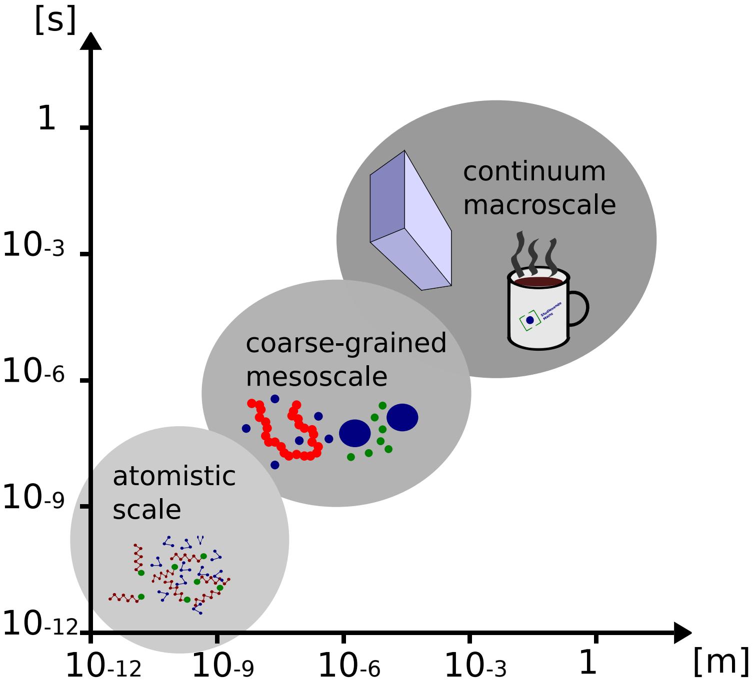

Figure 0.1: Illustration of the mesoscale, bounded by atomistic and continuum descriptions of matter.

place the explicit ions in the electrolyte solution by a dynamic mean-field description of the ion concentration field. Thereby the computational cost for the electrostatics is largely reduced as all pair-interaction contributions between ions vanish. The drawback is that this approach also neglects any ion-correlation effects. Though, when considering high salt concentrations, the importance of pair correlations is largely reduced due to screening effects. Thus the concept of a mean-field description of ions is particularly applicable to high salt concentrations, which can be found, for instance, under physiological conditions. Meanwhile the description of the solvent molecules, as well as of dissolved macromolecules, is left in the particle frame.

Such a hybrid approach to the description of electrolyte solutions is very promising in terms of computational efficiency. Even with the nowadays ever-growing computational capabilities, we are still in need of more efficient methods for simulations of soft materials, such as biological matter, solutions of polyelectrolytes or colloidal suspensions. The development of efficient simulation methods is thus an ongoing challenge. In the recent past several methods have been developed to solve electrokinetic problems. A recent overview has been published in [2]. In addition, we mention a non-complete list [3, 4, 5, 6, 7, 8, 9, 10], which we will cover at a later point in this study. Many of the presented simulation methods have their own drawbacks as they make strong approximations to the interactions. Therefore, depending on the purpose and aim of the study, the right simulation method will have to be chosen. A few methods also solve the electrokinetic equations on the mesoscale [11, 12]. However, both methods are based on a lattice approach.

As an alternative, in this study we will develop an off-lattice particle-based method to solve the electrokinetic equations, called in the following the **condiff** algorithm [1]. As we will see, the particle description has certain advantages regarding the implementability of boundaries and macromolecules. Therefore the condiff method is not only readily applicable to the study of electrolyte solutions, especially in flow situations, but also to problems that are motivated by molecular biophysics or biotechnology, as biomolecules are often dissolved in physiological solutions in a geometrical confinement, both in vivo (cells) and in vitro (i.e. bioanalytical devices) [13, 14, 15].

Outline

This thesis is structured as follows: In the first chapter we will present the theoretical background required for the development of the algorithm and its applications. The second chapter describes the successive construction of the condiff algorithm and discusses its characteristics. The third chapter is devoted to tests and comparisons, both with regards to accuracy and performance. It concludes with a short summary and outlook for further implementations. Further details to chapter three are remarked in the appendix. The first application of the algorithm is presented in chapter four, where we study polyelectrolyte solutions under shear. Chapter five presents the second application, which is the electro-osmotic flow on superhydrophobic surfaces. Finally, the main results of this study will be discussed in the conclusion.

Unit System and Important Quantities/Abbreviations

Throughout this study we will stick to the simulation unit system, sometimes also called Lennard-Jones units. The length scale is set through the parameter σ, which can be viewed as the typical particle diameter. Generally, we set $\sigma = 1$. As is customary, the particle mass $m = 1$ is set to unity as well, i.e. particle velocities and momenta are equal. The energy scale is set through $\varepsilon = 1$, which sets the interaction strength for excluded-volume interactions, i.e. is related to the "softness" of particles. The time scales follows accordingly with $\tau = \sqrt{m/\varepsilon}$.

In this unit system the simulation results are scale independent. A mapping to real units can be obtained by choosing a model system to be represented. For the length scale this is usually done through the Bjerrum length, which is unity throughout this study, too. For instance, the Bjerrum length for water at room temperate ($T = 300K$) is $l_B \approx 0.7nm$, which then states that particle diameters are of size $\sigma = l_B = 0.7nm$.

While all quantities and abbreviations throughout this study are explained where they are defined or used for the first time, in the following we want to list the most frequently occurring ones:

---

[1] The name originates from the convection-diffusion equation that has to be solved.

Symbol	Name	Meaning
Δt	time step	discrete measure chosen to integrate the equations of motion
σ	length scale of the WCA repulsion	underlying length scale, monomer diameter
ε	energy scale or dielectricity	depending on context, energy scale of WCA repulsion, or dielectric constant of medium (here $\varepsilon = 1/(4\pi)$)
$k_B T = 1$	thermal energy	all energies measured in units of $k_B T$
l_B	Bjerrum length	length scale for electrostatics
κ	inverse Debye length	thickness of electric double-layer, range of screening
η	shear viscosity	
γ_{DPD}	friction coefficient in DPD interactions	
γ_L	friction coefficient of tunable-slip boundary interactions	determines the slip length
b	slip length	measure for slippage of surface
z_B	position of the hydrodynamic boundary	"felt" position of the boundary
cao	charge assignment order	order (# grid points used) of the assignment scheme
D	diffusivity	
N_q	pseudo-charge fraction	amount of pseudo-ions representing one unit charge (not to be confused with z_c)
z_c	valency of ions	defines the charge unit
$L_x \times L_y \times L_z$	dimensions of simulation box	measured in σ, either centered to $[-L/2, L/2]$ or $[0, L]$
PB	Poisson-Boltzmann	approximated theory for electrostatics
EOF	electro-osmotic flow	flow due to local net charges close to a charged boundary, induced by an external electric field
DPD	Dissipative Particle Dynamics	
counts		in profile plots: height of histogram bin

Specific for Chapter 4

Symbol	Name	Meaning
c, ρ	concentrations, densities	mostly number densities
R_e	end-to-end distance	measure for polymer conformation
R_g	radius of gyration	...
R_h	hydrodynamic radius	...
G_{ij}	gyration tensor	...
b	bond length	average distance between connected monomers
τ	pressure/stress tensor	
$\dot{\gamma}$	shear-rate	

Chapter 1

Theoretical Background

1.1 The Electrokinetic Equations

It might seem obvious that an atomistic approach to physics is not applicable to large scale systems of the size of centimeters to meters, where one would deal with an amount of particles in the order of magnitude of Avogadro's constant

$$N_A = 6.022\ 10^{23} \quad . \tag{1.1}$$

But even for systems on the micron and nanoscale the amount of particles is still too large to allow for a detailed atomistic approach. However, classical physics offers the approach of continuum mechanics, where particles are no longer the degrees of freedom. Instead one deals with continuous density fields. The corresponding equations of motion, can be extracted from the underlying symmetries which result in conservation laws for certain quantities. In this study we focus on the description of an electrolyte solution, i.e. a charge-neutral solvent that has some charged species dissolved into it to form a complex solution. This solution will be the basis for all further systems, where other large molecules that do not follow a continuum description can be dissolved in the solution as well.

In order to describe an electrolyte solution in a continuum frame, one needs to account for three fundamental physical laws, namely the conservation of momentum, the conservation of mass and/or charge as well as the conservation of energy. The electrokinetic equations are the manifestation of these fundamental laws, where the degrees of freedom are the local density fields of solvent $\rho_s(\boldsymbol{x}, t)$ and any charged species c, $\rho_c(\boldsymbol{x}, t)$, the local velocity field $\boldsymbol{v}(\boldsymbol{x}, t)$, and the electrostatic potential $\Phi(\boldsymbol{x}, t)$.

In this mean-field description all cross-correlations between particles and thermal fluctuations are neglected. This is the sacrifice we make by introducing the field description, which, however, enables the study of large scale systems, where both these effects vanish. On the other hand the continuum approach is not just limited to the macroscale, but can in principle be taken down to the microscale and even to the nanoscale, where the particle-shape of matter starts to become important. We start out by discussing each part of the electrokinetic equations separately.

1.1.1 The Navier-Stokes Equation

The conservation of momentum leads to a description of the velocity or momentum field inside the system, mostly dominated by the solvent as it usually is the main part in terms of mass. The governing equation is called the Navier-Stokes equation and originates in the description of the local momentum field $\boldsymbol{p}(\boldsymbol{x}, t)$, which obeys a continuity equation

$$\frac{\partial}{\partial t} p_i + \frac{\partial}{\partial x_j}(p_i v_j) = 0 \tag{1.2}$$

with $i, j = x, y, z$ and the Einstein summation rule used for j, and $\boldsymbol{v}$ the local velocity field. The combination $p_i v_j$ can be seen as the momentum current of orientation i in direction j. We will make the assumption of a Newtonian fluid, i.e. a fluid with a proportionality between stress and shear

$$\tau \propto \frac{\partial v}{\partial x} \tag{1.3}$$

to make up our electrolyte solution. By accounting for all momentum changes the local mass-density field ρ can experience, one ends up with the full Navier-Stokes equation for a Newtonian fluid

$$\rho \left[\partial_t \boldsymbol{v} + \boldsymbol{v} \boldsymbol{\nabla} \cdot \boldsymbol{v}\right] = \eta \boldsymbol{\nabla}^2 \boldsymbol{v} + \zeta \boldsymbol{\nabla}(\boldsymbol{\nabla} \cdot \boldsymbol{v}) - \boldsymbol{\nabla} p - k_B T \sum_c z_c \rho_c \boldsymbol{\nabla} \hat{\Phi} \quad , \tag{1.4}$$

which in principle is just a force balance equation with several contributions. In the case of an electrolyte solution, the total density is built up by the solvent and the ionic species

$$\rho = \rho_s + \sum_c \rho_c \quad . \tag{1.5}$$

The left hand side of Eq. 1.4 can also be reshaped

$$\rho \left[\partial_t \boldsymbol{v} + \boldsymbol{v} \boldsymbol{\nabla} \cdot \boldsymbol{v}\right] = \partial_t(\rho \boldsymbol{v}) + \boldsymbol{\nabla} \cdot [\rho \boldsymbol{v} \boldsymbol{v}] \tag{1.6}$$

through the continuity equation for the total mass density

$$\partial_t \rho + \boldsymbol{\nabla} \cdot (\rho \boldsymbol{v}) = 0 \quad . \tag{1.7}$$

With regards to Eq. 1.4, the first and second term on the right hand side are due to the viscous forces in the liquid, where η is the shear viscosity and ζ the bulk viscosity [16]. The second part vanishes in the assumption of an incompressible fluid. The gradient of the pressure p leads to flow from high pressure to low pressure regions. In principle p could have a tensorial form. For a Newtonian fluid, however, we assume isotropy and thus the pressure is only scalar. For an ideal gas it is simply given by the relation

$$p = k_B T \rho \quad , \tag{1.8}$$

with k_B Boltzmann's constant and the temperature T. The third contribution contains the reduced electrostatic potential $\hat{\Phi} = [e/k_B T]\Phi$ with the elementary charge e in the appropriate unit system and the Bjerrum length l_B, which is the distance at which the electrostatic interactions become comparable to the thermal energy, and thus is a measure for the relative strength of the electrostatics

$$l_B = \frac{e^2}{4\pi\varepsilon k_B T} \quad . \tag{1.9}$$

Only the charged ion species contribute to the last term, weighted with their valency z_c. Thus this term describes the convection of the fluid due to electrostatic forces onto its charged components.

For the case of an incompressible fluid, i.e.

$$\frac{D}{Dt}\rho = 0 \Rightarrow \boldsymbol{\nabla} \cdot \boldsymbol{v} = 0 \quad , \tag{1.10}$$

and sufficiently low Reynolds numbers, i.e. laminar flow, the Navier-Stokes equation reduces to the Stokes equation

$$0 = \eta \boldsymbol{\nabla}^2 \boldsymbol{v} - \boldsymbol{\nabla} p + \boldsymbol{F} \quad , \tag{1.11}$$

where $\boldsymbol{F}$ stands representative for any kind of driving force of external nature or, as in this case, of internal nature due to electrostatic interactions. The assumption of incompressibility is reasonable for liquids such as water, while the assumption of laminar flow holds for most situations on the mesoscale. In section 1.1.4 we will discuss the Reynolds number, which quantifies whether the assumption of laminar flow is correct.

1.1.2 The Convection-Diffusion Equation

The laws of mass and charge conservation lead to a description of mass/charge transport, where there are basically two governing processes involved, namely convection and diffusion. If there are different ionic species c, each of them is related to a conserved quantity, which is the integral of the density, i.e. the total charge of this species Q_c

$$Q_c = \int dV z_c \rho_c(\boldsymbol{r}) \quad . \tag{1.12}$$

Here z_c is the valency of the ions which can differ from unity. As conservation also must hold locally, there is a continuity equation for the corresponding current $\boldsymbol{j}_c$

$$\partial_t \rho_c + \boldsymbol{\nabla} \cdot \boldsymbol{j}_c = 0 \quad . \tag{1.13}$$

The current now is composed of three parts, which have to do with the local influence on the density

$$\boldsymbol{j}_c = \rho_c \boldsymbol{v} - D_c \boldsymbol{\nabla} \rho_c - z_c D_c \rho_c \boldsymbol{\nabla} \hat{\Phi} \quad . \tag{1.14}$$

Inserting 1.14 into 1.13, one arrives at the convection-diffusion equation for charged species

$$\partial_t \rho_c = -\boldsymbol{\nabla} \cdot \left[\rho_c \boldsymbol{v} - D_c \boldsymbol{\nabla} \rho_c - z_c D_c \rho_c \boldsymbol{\nabla} \hat{\Phi} \right] \quad . \tag{1.15}$$

In this context it is also called the Nernst-Planck equation. The first term on the rhs. is the motion due to the local flow of solvent. This is called convection, or sometimes also advection, depending on the context. The second term arises from the fact that dissolved ions undergo Brownian motion due to the random collisions with solvent molecules. From a macroscopic view the term also corresponds to Fick's law of diffusion, where D_c is the diffusivity and the negative gradient ensures that the net transport is from regions of higher concentration to ones of lower concentration. D_c is also directly related to the mobility of ions in the particle-frame through the Einstein relation

$$\mu_c = \frac{D_c}{k_B T} \quad . \tag{1.16}$$

The third term describes a migration of ions due to the electrostatic interactions between the charged species, hence the valency z_c and the electrostatic potential $\hat{\Phi}$ in the reduced form. Similarly to the diffusive term, D_c appears in the electrostatic contribution, as the particles try to escape from regions of high electric field. Thus in total, the model depends only on one kinetic parameter. Once the fluid reaches equilibrium, i.e. $\partial_t \rho_c = 0$ and $\boldsymbol{v} = 0$, the ionic species remain in a Boltzmann distribution

$$\rho_c \sim e^{-z_c \hat{\Phi}} \quad . \tag{1.17}$$

If the relaxation of ρ_c is infinitely fast on the considered time scale, then this holds true even in non-equilibrium situations in the so-called adiabatic limit. The relative flow-field strength with respect to temperature and diffusivity determines which of the two mechanisms, convection or diffusion, dominates the movement. Here the Péclet number comes into play, which is also described in section 1.1.4.

1.1.3 The Poisson Equation

As we are dealing with classical matter in a limited velocity range much smaller then the speed of light $v \ll c$, all electromagnetic interactions reduce to electrostatics, so that a description by the full Maxwell equations becomes obsolete. For electrostatics, the Poisson Equation is the basic equation that relates the electrostatic potential to the distribution of charge in space

$$\boldsymbol{\nabla}^2 \hat{\Phi} = -4\pi l_B \left(\sum_c z_c \rho_c + \sigma \right) \quad . \tag{1.18}$$

Here, σ represents the charge of additional objects such as boundaries or macromolecules. On top of that, an external potential could be applied as well, which simply adds up in a linear fashion. Combined with the equilibrium version of the convection-diffusion equation (Eq. 1.17), one obtains the Poisson-Boltzmann equation described in chapter 1.2. Here and in the remainder of this study, we assume a homogeneous background with a constant dielectricity ε, which in our unit system is set to be

$$\varepsilon = \frac{1}{4\pi} \quad . \tag{1.19}$$

As our simulations mostly refer to aqueous solutions, it is worth mentioning that the dielectric constant in water is rather high $\varepsilon \approx 80$, which becomes crucial when dealing with interfaces, where image charge effects occur.

1.1.4 Hydrodynamic Numbers

In principle there is a rich variety of different hydrodynamic behavior, which can be categorized into several regimes by a set of dimensionless numbers. Here we want to briefly discuss the most important ones in the context of this study.

Reynolds Number Re

The Reynolds number Re describes the ratio between inertial forces and viscous forces on a characteristic length scale L

$$\mathrm{Re} = \frac{\rho L v}{\eta} \quad . \tag{1.20}$$

Here v is the average velocity in the fluid. With the Reynolds number one can distinguish between turbulent and laminar flow. For our purposes, almost all flow phenomena can be viewed as laminar, i.e. $\mathrm{Re} \ll 1$. This reduces the complexity of the Navier-Stokes equation.

Schmidt Number Sc

The Schmidt number Sc defines the ratio of momentum diffusivity and mass diffusivity

$$\mathrm{Sc} = \frac{\eta}{\rho D} \quad , \tag{1.21}$$

where often one uses the kinematic viscosity $\nu = \eta/\rho$. Thus the Schmidt number gives information about how fast the flow reaction is spread compared to the average particle movement. The Schmidt number for gases is much lower than for liquids. Physical values range from 1 for gases, i.e. momentum and particles themselves are transported with the same speed, to 1,000-10,000 for liquids, where transport of momentum is happening much faster than that of mass. An illustrative example would be a sea wave, where the average water molecule does not move much while the momentum transport is visible through the wave pattern.

Péclet Number Pe

The Péclet number is the product of Re and Sc

$$\mathrm{Pe} = \mathrm{Re}\,\mathrm{Sc} = \frac{VL}{D} \tag{1.22}$$

and states the relative importance of convection to diffusion for mass transport. Pe can be used to quantify shear flow, where the shear velocity is competing with diffusive motion. Thus the low Péclet-number regime, $\mathrm{Pe} < 1$, is dominated by Brownian motion/ diffusion, while the regime $\mathrm{Pe} > 1$ is dominated by hydrodynamic interactions/ convection.

Knudsen Number Kn

Another hydrodynamic number is the Knudsen number

$$\mathrm{Kn} = \frac{\lambda}{L} \quad , \tag{1.23}$$

which gives information about the relative mean free path λ of a fluid particle on the typical length scale L before collision, i.e. it tells something about whether continuum models or particle models can be used to describe the fluid. Thus it also gives information about the applicability of the Navier-Stokes equation to describe a solvent, where $\mathrm{Kn} \ll 1$.

Mach Number Ma

Furthermore there is the Mach number,

$$\mathrm{Ma} = \frac{v}{c_s} \tag{1.24}$$

which relates the typical velocity to the speed of sound of the fluid, i.e. stating how fast particles move according to the disturbance that they produce.

1.2 Poisson-Boltzmann Theory

A very common approximation made to the electrokinetic equations leads to a combination of the convection-diffusion equation and the Poisson equation in a single relation for the ion distribution. If we consider the system to be in total equilibrium, the following must hold true

$$\partial_t \rho_c = 0 \tag{1.25}$$

$$\boldsymbol{j}_c = 0 \tag{1.26}$$

$$\boldsymbol{v} = 0 \ . \tag{1.27}$$

The last condition may not be totally necessary, if we assume an adiabatic behavior of the ions. As mentioned earlier, this would mean that the ion species have a separated time scale from the solvent and the overall velocity $\boldsymbol{v}$, so that they relax in principle infinitely fast to their equilibrium distribution. With these assumptions the convection-diffusion equation (1.15) reduces to two terms and we write it together with the Poisson equation

$$\begin{aligned} 0 &= \boldsymbol{\nabla}\rho_c + z_c\rho_c\boldsymbol{\nabla}\hat{\Phi} && (1.28) \\ \boldsymbol{\nabla}^2\hat{\Phi} &= -4\pi l_B\left(\sum_c z_c\rho_c + \sigma\right) \quad . && (1.29) \end{aligned}$$

Eq. 1.28 can be integrated to obtain the equilibrium ion distribution

$$\rho_c(\boldsymbol{x}) = \rho_{0c}e^{-z_c\hat{\Phi}(\boldsymbol{x})} \quad , \tag{1.30}$$

and can then be inserted into Eq. 1.29 to obtain the Poisson-Boltzmann (PB) equation

$$\boldsymbol{\nabla}^2\hat{\Phi}(\boldsymbol{x}) = -4\pi l_B\left(\sum_c z_c\rho_{0c}\exp(-z_c\hat{\Phi}(\boldsymbol{x}) + \sigma\right) \quad . \tag{1.31}$$

Its name originates from the fact that Eq. 1.30 is a Boltzmann distribution (note that k_BT is hidden in the definition of $\hat{\Phi}$). ρ_{0c} is the constant concentration of ion species c in the limit of zero potential, which is mostly taken to be in infinite distance.

The PB theory is a commonly used approximation in biophysical calculations, such as for protein structures as well as in self-consistent field theory approaches to polymer systems and similar problems. While it appears reasonable to use this approach for equilibrium situations, it can also be applied to non-equilibrium situations, e.g. driven systems, as long as the essential assumption holds true that the ions relax infinitely fast to their equilibrium distribution, whenever being disturbed. One such application is the electro-osmotic flow in simple geometries such as a slit channel, as described in section 3.2. Here the convective transport of the ions is not affecting the equilibrium distributions. However, in more complex geometries the assumption may not hold, as the convective transport can lead to nontrivial effects [17]. For such cases, where the Poisson-Boltzmann theory breaks down, a more sophisticated approach, called the Poisson-Nernst-Planck (PNP) model, is available [18, 19], where the divergence of the full current density in the convection-diffusion equation is taken into account.

1.2.1 Debye-Hückel Approximation

The PB equation is a non-linear equation and is only solvable analytically for simple cases, e.g. counterions only, and simple geometries such as under a cylinder or plane symmetry. Most other cases have to be studied with numerical methods. However, the equation may be linearized by expanding the exponential term and leaving out terms of quadratic and higher order in the potential Φ, resulting in

$$\boldsymbol{\nabla}^2\Phi - \kappa^2\Phi = 0 \quad , \tag{1.32}$$

the Debye-Hückel approximation [20] with κ being the inverse Debye screening length

$$\begin{aligned} \kappa^2 &= 4\pi l_B \sum_c (z_c)^2 \rho_c \qquad (1.33) \\ \lambda_D &= \kappa^{-1} \quad . \qquad (1.34) \end{aligned}$$

The idea behind the screening length λ_D is that the interaction of a distant charge with a local charge may be screened out by some neighboring charges. The screening length then gives a length scale for which the exponential screening effect reaches $1/e$, which originates from the exponential form of the potential, for instance around a single test charge in the origin

$$\Phi(r) = \Phi_0 \frac{\exp(-\kappa r)}{r} \quad . \tag{1.35}$$

As Eq. 1.33 indicates, the screening effect increases with the electrolyte concentration. Also the valency of the ions is of large importance, as it enters quadratically. While the Debye-Hückel theory is only valid in a limited regime of low concentrations, the intrinsic idea of local screening is more generally valid and thus the Debye-Hückel approach can be carried over to higher concentrations by replacing λ_D with an effective surface screening length, e.g. calculated from the local ion distributions close to a charged surface [21]. The Debye-Hückel theory is a widely used approximation as the linear character makes it analytically easy to handle. Also, due to the exponential decay of the resulting Yukawa-like potential, one can introduce a local cutoff for the interaction range, which makes the potential easily implementable into particle-based numerical simulations like Brownian dynamics, Monte-Carlo or molecular dynamics.

1.2.2 The Picture of the Double Layer

When a solute is brought into the solution, it usually obtains a surface charge σ, as counterions get dissolved into the solution. This holds true for surfaces as well as colloidal particles or polyelectrolytes. Larger objects such as the former two will then be surrounded by a layer of the oppositely charged counterions as they are attracted, while ions of the same charge (coions) are repelled. Thus the ions distribute themselves in a layering structure, called the electric double layer [22]. This double layer contains a net amount of counterions that neutralizes the surface charge of the macro object. The end of the double layer is more or less defined through the Debye length λ_D, from where on the screening takes over. Figure 1.1 illustrates the layering adjacent to a charged boundary and a large spherical object such as a colloidal particle.

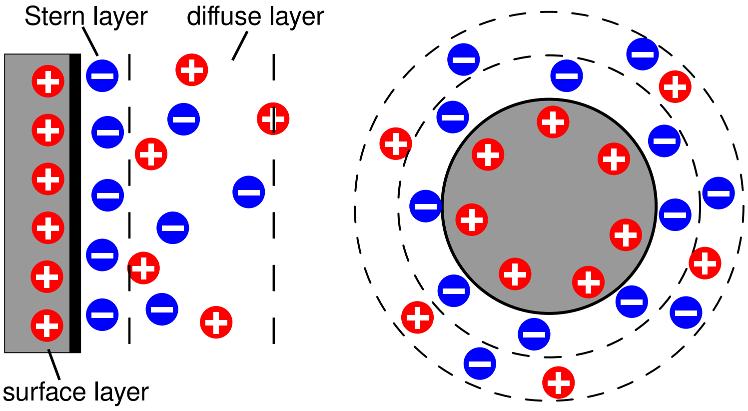

Figure 1.1: Illustration of the electric double layer and its separation into surface, Stern and Gouy-Chapman (diffuse) layer for a charged surface and a charged spherical object.

In the case of a strongly charged double layer, one can separate the solution part into two layers itself. The first layer of counterions which is directly adjacent to the boundary is then also called the Stern layer. These counterions are relatively firmly bound to the surface through the electrostatic attraction. Therefore they even stick to it in the case of shear flow. Further apart from the surface, thermal fluctuations result in a rather diffuse layering of ions than a clear separation. This area is called the Gouy-Chapman diffuse layer.

It is important to note that inside the double layer there is no charge neutrality, which is the origin for effects such as the electro-osmotic flow, where an external electric field can locally cause a net motion of fluid, which can then propagate further into the bulk fluid.

1.2.3 The Screening Effect

While the electrostatic interaction in principle has a long-range character due to its $1/r$ dependence, the screening effect of charges by neighboring charges can be quite large. This especially holds true for high salt concentrations. For instance one finds that under physiological conditions, i.e. salt concentrations of $\sim 0.1M$[1], the screening length is around $1nm$, which is comparable to the size of short polymers and a fair bit smaller than colloidal particles. Thus especially in biologically related problems, one often deals with strong screening effects.

One major effect of screening is that it reduces the cross-correlations of individual ions. For the case of monovalent ions they may even be disregarded, which is the underlying assumption of the method described in this work. However, it is important to note that for multivalent ions this is usually not the case (see [23, 24] and references therein). Thus the method is limited to monovalent charges only.

---

[1] An example for physiological conditions with a monovalent salt: NaCl 0.9%, 154mmol/l or $\rho = 0.03$ in simulation units if $l_B = 1$.

1.3 Molecular Dynamics Simulations

Since its development in the late 1950s [25], molecular dynamics (MD) has been a very successful approach to computer simulations of soft condensed matter and is now a widely used tool [26, 27], similarly popular as Monte Carlo methods [28]. The idea behind MD is to solve Newton's equations of motion for every single particle in the system by discretizing time into time steps Δt and calculating the necessary interparticle forces at each time step to obtain the velocities and positions. The main characteristic of MD is that it is a deterministic approach. Somewhat competing with Monte-Carlo simulations and Brownian dynamics, it has the benefit that it generates trajectories with a physical meaning such that the actual dynamics of the system can be studied. Monte-Carlo does not allow this and Brownian dynamics works in the overdamped limit, i.e. neglecting all inertia terms in the equations of motion and instead introducing diffusive behavior.

1.3.1 Integration Schemes

The simplest form of an algorithm to solve Newton's equations of motion is the Euler method, which is of first order but does not meet the required accuracy. The most commonly used algorithms are of second-order and belong to the Verlet or Leap-Frog type. Both are algebraically equal, however, have a slightly different structure [29]. An improvement over the Verlet scheme is the velocity Verlet scheme, where calculated velocities and positions are no longer shifted by half a time step $\Delta t/2$. In line with the velocity Verlet algorithm, in this work we will use a modified Leap-Frog scheme, where both velocities and coordinates are obtained at the same time [29].

$$\text{1. Step:} \qquad \boldsymbol{v}(t+\tfrac{1}{2}\Delta t) = \boldsymbol{v}(t) + \tfrac{1}{2}\Delta t\boldsymbol{a}(t)$$

...calculate forces...

$$\begin{aligned} \text{2. Step:} \qquad \boldsymbol{v}(t+\Delta t) &= \boldsymbol{v}(t+\tfrac{1}{2}\Delta t) + \tfrac{1}{2}\Delta t\boldsymbol{a}(t+\Delta t) \\ \boldsymbol{r}(t+\Delta t) &= \boldsymbol{r}(t) + \Delta t\boldsymbol{v}(t+\Delta t) \end{aligned}$$

1.3.2 MD at Constant Temperature

The classical MD works in the microcanonical (N,V,E) ensemble, i.e. the energy is a conserved quantity. While MD is being used for classical atomistic simulations, it is also the basis for more coarse-grained approaches to the simulation of matter, where larger molecules play the role of particles. Also, on these length scales thermal fluctuations start to play a role. Their origin will be described later on. Thirdly, situations of experimental interest are rather not to be found in the microcanonical ensemble, but in the canonical (N,V,T) ensemble, where a constant temperature is established by the coupling to a heat bath. In principle this heat bath is just the exterior of the system under study[2]. The

---

[2] Note that in coarse-grained models the thermostat also stands for the possibility of heat transfer to the fast, neglected degrees of freedom.

thermostat function can be introduced into the MD algorithm, which, however, destroys the trajectory interpretation mentioned earlier due to the random fluctuations it involves. In chapter 2.2 we will discuss the dissipative particle dynamics as our method of choice, which includes the thermostat character and thus shifts the simulation to the (N,V,T) ensemble.

1.3.3 ESPResSo

The simulation software package ESPResSo (Extensible Simulation Package for Research on Soft matter)[3] is a versatile tool for simulations of mesoscopic systems such as colloidal suspensions or polymer solutions. Since its release [30] many new features have been included and the package is still growing. In the context of this study ESPResSo has been used not only as a comparison tool, but also as the performance reference. The electrostatics part of the condiff algorithm is based mainly on the P3M algorithm as it is implemented in ESPResSo.

1.4 Coarse-grained Models

Simulation methods such as dissipative particle dynamics and lattice-Boltzmann, both to be described in chapter 2.1, belong to the so-called bottom-up approaches, where one starts with the microscopic picture of matter consisting of particles, i.e. atoms and molecules, and then tries to simplify the model as much as possible while conserving the important features. This concept is called coarse-graining and has been widely used in the study of soft matter and fluid mechanics.

We consider the case of a macromolecule, i.e. a molecule that consists of a large amount of particles (atoms). The corresponding length and time scales for the single particles are typically much smaller than the scales important for the dynamics of the entire macromolecule, i.e. their singular motion is much faster and results in much smaller effects on its neighbors than the combined effect on the whole molecule. But it is essentially this combined effect that matters for the dynamics of the macromolecule. Thus by reducing the description to the corresponding length and time scale, one omits out the unnecessary and computationally demanding single-particle details. Prominent examples, where this holds true are large polymers such as DNA, colloidal particles and sometimes also proteins. Therefore coarse-grained models have been developed to replace the unnecessary parts of the molecules. Many times these are simple bead-string models as in the case of polymers. It is a first step to a computationally more efficient scheme of representation.

Similar to the idea behind coarse-grained macromolecules, the solvent itself falls victim to such a thinking as well. Already from a computational point of view it makes sense to reduce the solvent to an efficient model. Usually the situation is such that it involves orders of magnitude more solvent particles than the particles of actual interest.

---

[3] http://espressomd.org/

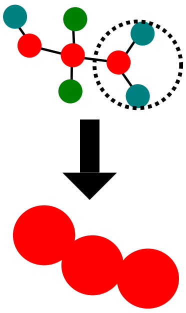

Figure 1.2: Illustration of the concept of coarse graining, modeling a larger molecule as a chain of connected beads.

In chapter 2.1 we will deal with coarse-grained approaches to modeling a solvent in more detail.

Coming back to the idea of separated time scales for the single particles, larger objects and the very large objects such as colloidal particles, coarse-grained models in way can be viewed as "telescoping down" the time scale differences, such that all time scales close ranks to make the longest ones feasible to reach in the computation. Later on, one can map the results back to the proper time and length scales, to compare with experiments, however, requiring more than one mapping norm due to the original time scale difference.

As successful and popular as coarse-grained models are in the scientific community, they, however, most often come with a drawback. Due to the simplified approach, there are certain quantities of the original model that cannot be recovered with the coarse-grained one. Thus, when developing a new model one has to account for the important properties of the underlying system and check for consistency. One has a responsibility to ensure that non-reproducible properties have no impact on the studied phenomena.

1.5 Polymer and Polyelectrolyte Theory

In the last chapter we introduced the concept of coarse-graining to macromolecules. Many such macromolecules are in fact polymers, which are of wide interest due to many applications in industry and pharmaceutics, their appearance in nature and their multifaceted and interesting physical behavior. A polymer is a large molecule built up by a series of identical blocks that are called monomers. These monomers usually consist of carbohydrate groups. The symmetric structure of a polymer is also the foundation of the theoretical description. The length of the polymer in terms of monomers is also called the degree of polymerization. While in principle many polymers can form branches, in this study we will focus on linear polymers.

The behavior of polymers can be quite nontrivial and all sorts of properties can be achieved by the combination of different polymers in mixtures. The interest in polymer science is ubiquitous and research areas encompass prominent fields such as polymer melts and glasses, block copolymers, polymer brushes and polymer coating of surfaces and colloidal particles, and so on.

If we now take a coarse-grained view on the polymer, a monomer is just a bead and the whole polymer thus becomes a chain of beads, connected by some potential spring. This bead-spring model is one of the most commonly used description of polymers and polyelectrolytes in coarse-grained simulations.

1.5.1 Ideal Chains

We start out with a simple ideal chain model, where all monomers are freely jointed to a chain with a fixed bond length b and no interactions. Another interpretation is that the chain is built up of so-called Kuhn segments of size b. The end-to-end vector, a measure for the conformation of the polymer, can be calculated by

$$\boldsymbol{R}_e = \boldsymbol{r}_N - \boldsymbol{r}_1 = \sum_{i=1}^{N-1} \boldsymbol{b}_i \quad , \tag{1.36}$$

for a polymer chain of N monomers. An important feature of this model is that different bond vectors are uncorrelated

$$\langle \boldsymbol{b}_i \cdot \boldsymbol{b}_j \rangle = 0 \qquad , i \neq j \quad . \tag{1.37}$$

One might ask for the scaling of the end-to-end vector with the degree of polymerization, which can be expressed as

$$R_e = \sqrt{< R_e^2 >} = b(N-1)^{1/2} \quad . \tag{1.38}$$

Thus the end-to-end distance scales with N to the power 1/2, which means that the polymer is an object of fractal dimension 2. Here this model shows its direct relation to Brownian motion, as it essentially represents a random walk in space. The same scaling relation holds also for other models, as long as the assumption of uncorrelated bond vectors is valid. Another quantity to measure the polymer conformation is the radius of gyration

$$R_g^2 = \frac{1}{N} \sum_{i=1}^{N} (\boldsymbol{r}_i - \boldsymbol{r}_{cm})^2 \tag{1.39}$$

with $\boldsymbol{r}_{cm} = 1/N \sum_{i=1}^{N} \boldsymbol{r}_i$ the center of mass. R_g in principle shows the same scaling as the end-to-end distance R_e. It is related to the description of the inertia in analytical mechanics. Experimentally, the R_g of a polymer can be measured by static light scattering.

Up to now the ideal chain model did not mention how the chain segments are connected with each other. A more detailed description is the already mentioned bead-spring model, also called Rouse model. Here the chain is built up of identical beads connected by springs following a harmonic potential.

1.5.2 Real Chains

In ideal chains the segments are able to penetrate each other. Thus for real chains there must be a mechanism to avoid interpenetration. Essentially, when parts of a polymer come too close, they will repel each other. This is called the excluded volume effect and serves to give every bead a certain size. The primary result is that the polymer chain starts to swell. Thus new scaling relations come into play

$$R_e^2 \sim (N-1)^{2\nu} \tag{1.40}$$

$$R_g^2 \sim (N-1)^{2\nu} \quad , \tag{1.41}$$

where ν is the scaling exponent. The calculation of ν is possible in the framework of renormalization group theory and leads to $\nu = 0.588$ [31]. The original result obtained by Flory with a much simpler approach, $\nu = 3/5$, differs only slightly from that [32].

Solvent Conditions

Polymers can usually be found in solution. But so far we have neglected any solvent effects on the polymer, which equals the assumption of a good solvent, i.e. the beads like to be surrounded by solvent. But depending on the solvent conditions, the polymer can actually behave as if no excluded-volume effects are present, which is called the Θ-condition. Bad solvent conditions can even lead to a collapse of polymer chains to a globule structure. Other conformations observed under bad solvent conditions include so-called pearl-necklace structures of charged polymers. They result from the optimization of both the electrostatic repulsion between charged monomers and the short-ranged attraction of monomers due to the poor solvent condition [33, 34].

1.5.3 Semi-flexible Models

The model of real chains as described above results in a fully flexible polymer, where the bond vectors in principle are still uncorrelated. In nature, however, there are some polymers that do not show this flexibility but are rather stiff. A prominent example is double-stranded DNA, which is much stiffer than its single-stranded counterpart. An additional interaction taking into account the bond angles has to be included to model such polymers. The bond vectors thus are no longer uncorrelated. In the framework of the ideal chain, the freely-jointed segment model is usually replaced by the worm-like chain to describe the not-fully flexible polymer. For very long polymers on the other hand, one might simply try rescaling to larger segments of the chain, such that the new bond vectors are of uncorrelated nature. As a result a semi-flexible polymer has Kuhn segments that are accordingly larger and thus incorporate various monomers. A useful definition in this context is the persistence length of the polymer, which is set to be half the Kuhn length.

1.5.4 Dynamics of Single Polymer Chains

Before stating the chain dynamics as a whole, we start out with the movement of a single bead in solution. The diffusive motion of a single bead in time t is given by

$$\langle[\boldsymbol{r}(t) - \boldsymbol{r}(0)]\rangle = 6D_0t \tag{1.42}$$

with the single particle diffusion constant D_0. The average is taken over several random walks. D_0 is related through the Einstein relation

$$D_0 = \frac{k_BT}{\zeta_0} \tag{1.43}$$

with the friction coefficient ζ_0, which can be identified through the Stokes law for the friction of a spherical object. There are two possibilities for the friction, namely either a sticky boundary, $\zeta_0 = 6\pi\eta a$ or a full-slip boundary, $\zeta_0 = 4\pi\eta a$. Here a is the bead radius and η the solvent viscosity.

Chain Diffusion

The dynamics of a whole chain is a little more complicated than that. In principle it can be divided into two regimes.

The first one is the Rouse regime. In this model all long range interactions between beads are either neglected or screened. Thus the friction of the polymer chain is just the summed up friction of all single monomers. This results in a $1/N$ scaling for the chain diffusion coefficient

$$D_{\mathrm{Rouse}}(N) = \frac{k_BT}{\zeta_0 N} \quad . \tag{1.44}$$

The second one is called the Zimm regime, which implies that hydrodynamic interactions are not negligible. In principle, hydrodynamic interactions can be screened in certain situations, such as for dense polymer concentrations. But in dilute solutions they certainly play an important role. In this model the polymer moves as a whole, approximated by a sphere of radius R_h, the hydrodynamic radius

$$R_h = \left[\frac{1}{N^2}\sum_{i\neq j}\frac{1}{r_{ij}}\right]^{-1} \quad , \tag{1.45}$$

with $r_{ij} = |\boldsymbol{r}_i - \boldsymbol{r}_j|$. Similar to R_e and R_g it also fulfills a scaling relation

$$R_h(N) \approx bN^{\nu} \quad . \tag{1.46}$$

The hydrodynamic radius can experimentally be determined by dynamic light scattering. Like for the single bead diffusion, one again can use the Stokes law and set R_h as the sphere radius leading to a diffusion coefficient

$$D_{\text{Zimm}}(N) \approx \frac{k_B T}{6\pi\eta b N^{\nu}} \quad . \tag{1.47}$$

1.5.5 Polyelectrolytes

Polyelectrolytes are polymer molecules with ionizable groups. In aqueous solutions these groups can release counterions, depending on the pH of the solution, which results in a net charge of the molecule. Therefore polyelectrolytes are also referred to as charged polymers. Common polyelectrolytes include DNA, RNA, polystyrene sulfonate, and polyacrylic acid. The long-ranged electrostatic interactions between monomers lead to a large deviation from the usual polymer behavior [35]. The most obvious change resulting from the charges is that due to the electrostatic repulsion the molecule takes much more extended conformations. Likewise, the electrostatic interactions with beads of other chains result in different properties of polyelectrolyte solutions.

Polyelectrolyte bead-spring models need an additional parameter, which sets the amount of charged and uncharged beads in the chain by defining the distance of a charged bead to the next one. In this study we will only focus on chains, where every bead is charged identically. As the simplest possible model, it might also be seen as a more coarse-grained representation of any model with higher distance between charged monomers in the chain.

We start out with a single polyelectrolyte chain without any counterions. In comparison to the neutral counterpart, the charge on the monomers leads to a swelling of the chain due to additional repulsion. Hence the Flory exponent of $\nu = 0.588$ for the scaling is no longer valid. In fact the scaling relation without any screening by counterions is simply

$$R_{e/g/h} \sim N \quad . \tag{1.48}$$

Effect of Counterions

The counterions play an important role in the behavior of polyelectrolytes. Their main function is to screen the electrostatic repulsion between different beads, which can reduce the swelling effect. Depending on their behavior, we can distinguish between condensed counterions and free counterions [36, 37, 38, 39]. We speak of condensation for those counterions that stick closely to the polyelectrolyte chain, and are only dragged away for high shear forces or flow rates, similar to the definition of the Stern layer (see chapter 1.2.2). The reason why counterions condensate is that they minimize the free energy by balancing out entropy and the electrostatic interactions. A criterion for the condensation is given by the Manning parameter $\zeta_M = l_B/b$ with Bjerrum length l_B and b the distance between two charged monomers in a polymer. for $\zeta_M < 1$ the system is entropy dominated, for $\zeta_M > 1$ it is energy dominated. While in the first case the counterions try to maximize entropy by being free, in the latter case they try to make the interactions favorable, resulting in condensation. Counterion condensation has also been studied within the Poisson-Boltzmann theory [40, 41, 23]. In simulations a counterion is usually considered as condensed, if it is found within a certain distance to any bead of the chain [42, 43]. Depending on the relative strength of electrostatic interactions, the counterions can lead to a variety of conformations, from a total collapse of the chain to an almost perfectly swollen state.

Whether the Rouse regime or the Zimm regime is applicable to the polyelectrolytes, depends on the interplay of electrostatic and hydrodynamic interactions. While it is certainly computationally more favorable to neglect hydrodynamic interactions in simulations, people have also argued that for polyelectrolytes the Rouse model is applicable for dilute solutions (and semidilute as well) as the electrostatic interactions somewhat resemble the main effects of hydrodynamic interactions [44]. In this study, however, we include both interactions as the developed method is specifically designed for the interplay of electrostatics and hydrodynamics, improving the simulation performance in particular for high (poly)electrolyte concentrations.

1.5.6 Polymer and Polyelectrolyte Solutions

So far we have focused on single polymer or polyelectrolyte chains in solution and the intra-chain effects. While this can be considered the infinitely dilute limit, most applications require a look into more concentrated systems, where in fact the inter-chain effects can play an important role. Polymer solutions can in principle be divided into regimes of different concentrations. In the dilute regime the single polymers mostly act undisturbed by their neighboring chains. Increasing the polymer concentration further, one reaches the overlap concentration $c^\star$, which can be defined through the radius of gyration [45, 46]

$$c^\star = \frac{1}{\frac{4}{3}\pi R_g^3} \quad , \tag{1.49}$$

which states that every polymer only has a volume of the size of a sphere with radius R_g available for itself. A similar definition can include the end-to-end distance instead. From this point on, the inter-chain interactions start to become similar in strength to the intra-chain interactions, leading to a different behavior of the solution. The corresponding concentration regime is called semidilute.

When going even further, one reaches the concentrated regime, where fluctuations begin to decrease and mean-field theoretical descriptions become applicable [46]. An even further increase of polymer concentration finally leads to polymer melts. All mentioned regimes are, however, not sharply separated from each other. More accurately there is a transition from one regime to another by increasing the concentration. An important difference between neutral and charged polymers is that due to the extensional conformations of the latter the crossover to the semidilute regime is reached at much lower concentrations [47]. If we consider a strongly charged chain in a salt-free solution, we can estimate that the chains will be fully stretched, i.e. $R_e \approx bN$ with the segment length b. Inserting this information leads to a scaling of $c^\star$ with the chain length N of

$$c^\star \approx b^{-3} N^{-2} \quad . \tag{1.50}$$

For uncharged polymers the stretching is not as pronounced, such that the end-to-end distance scales weaker and the overlap density results in

$$c^\star_{\mathrm{neutral}} \propto b^{-3} N^{-1/2} \quad , \tag{1.51}$$

which is much weaker than the scaling for charged chains. Therefore the semidilute regime is reached much earlier for polyelectrolytes than for neutral polymers when increasing the density. The N^{-2} scaling is also verified experimentally over a broad range of chain lengths [48]. Reversely, the crossover to the entangled or concentrated regime appears 3-4 decades over $c^\star$ for polyelectrolytes and only one decade over $c^\star$ for neutral polymers. Thus the semidilute regime for polyelectrolytes is much wider. This puts even more emphasis on the importance of understanding semidilute polyelectrolyte solutions.

Semidilute Solutions

Inside a semidilute polyelectrolyte solution, the correlation length ξ can be used to separate the length scales. Illustratively, ξ plays the role of the average mesh size the polymers built up. It also defines the length scale on which the screening of electrostatic interaction starts [49] and can be estimated by

$$\xi \propto c^{-1/2} \quad . \tag{1.52}$$

Outside the correlation-length volume, the chain appears Gaussian with ξ playing the role of an effective persistence length due to the screening. The osmotic pressure in the solution is dominated by the counterions, where it decreases with concentration for dilute solutions, and increases again for semidilute solutions.

Dynamics

A general observation is that an increase in polyelectrolyte concentration leads to an increase of the viscosity of the solution in the form

$$\eta \propto \sqrt{c} \tag{1.53}$$

which is called the empirical Fuoss law. This relation is valid over a surprisingly wide range of c [49]. Neutral polymers show a much different behavior, where the viscosity shows a linear dependence in the dilute regime and a dependence

$$\eta \propto c^{1.3}_{\mathrm{neutral}} \tag{1.54}$$

in the semidilute regime [50]. The strong deviation of charged polymers from this behavior can be explained by the coupling of electrostatic interactions with conformational behavior. In addition the stress relaxation time for polyelectrolytes decreases with concentration, i.e. the chains relax faster to their equilibrium conformation for higher concentrations.

Addition of Salt

The salt concentration in the solution largely determines the screening of electrostatic interactions. In a simple model, the Debye length can be seen as the distance from which on the electrostatics decay exponentially and thus are screened. For smaller distances, however, the full electrostatics apply. For the intra-chain interactions the screening leads to a decrease of the swelling, as the persistence length becomes smaller and thus the polymer conformation changes accordingly. In the high salt limit the behavior of polyelectrolytes resembles more and more that of neutral chains.

Salt can also have larger impacts, as multivalent ions lead to a strong condensation effect and thus can lead to a collapse of the polyelectrolyte chain. For semidilute solutions multivalent ions can act as crosslinks to form a polymer network and thus can introduce gelation effects [49]. These are effects that cannot be studied with mean-field descriptions such as used in this study, as multivalent ions go hand in hand with cross-correlations.

1.5.7 Other Quantities

The behavior of polymers and polyelectrolytes can also be characterized by some other quantities, which we mention briefly below. For instance we can calculate the spherically averaged form factor of a single chain in the fashion

$$S(k) = \frac{1}{N} \sum_{i,j=1}^{N} \frac{\sin(kr_{ij})}{kr_{ij}} \quad , \tag{1.55}$$

which can then be averaged over all chains and configurations. The gyration tensor G is of certain interest whenever dealing with non-isotropic geometries. The component a, b of the tensor can be calculated in the following fashion

$$G_{ab} = \frac{1}{N} \sum_{i}^{N} (r_a^{(i)} - r_a^{(cm)})(r_b^{(i)} - r_b^{(cm)}) \quad , \tag{1.56}$$

where $\boldsymbol{r}^{(cm)}$ is again the center-of-mass of the polymer chain. G is a useful tool to resolve the extension of polymers in certain directions and their correlations. The longest relaxation time τ_0 of a polymer chain gives insight about the intrinsic time scale the polymer motion appears on and is necessary to determine correlations of data series as well as comparing to the overall time scale. It can be determined, for instance, by calculating the end-to-end distance autocorrelation function

$$\langle R_e(t) R_e(t + \Delta t) \rangle \quad , \tag{1.57}$$

which usually follows an exponential decay trend with a characteristic $1/e$ decay time τ_0. The longest relaxation time directly enters the Weissenberg number Wi to quantify shear flow for polymers (see section 1.6.2).

1.5.8 Simulation of Bead-Spring Chains

The bead-spring model for polymers requires a choice of interactions for its representation. The excluded volume effect can be modeled by a Weeks Chandler Anderson (WCA) potential [51]

$$V_{WCA}(r_{ij}) = 4\varepsilon\left[\left(\frac{\sigma}{r_{ij}}\right)^{12} - \left(\frac{\sigma}{r_{ij}}\right)^{6} + 0.25\right] \tag{1.58}$$

with r_{ij} the interparticle distance. The WCA potential is just a purely repulsive version of a Lennard-Jones potential that is shifted and truncated in the minimum such that both the potential and the force are continuous at the cutoff. This leads to a bead diameter of about 1σ. The effect of a poor solvent can be modeled by shifting back to a Lennard-Jones potential with attractive part, such that the beads start to agglomerate.

The bonding of beads is usually modeled by either of the two following interactions. A harmonic spring has a potential of the form

$$V_{\text{harm}}(r_{ij}) = -\frac{1}{2}K(r_{ij} - r_0)^2 \tag{1.59}$$

with two parameters. K is the spring constant which determines the stiffness of the bond and r_0 is the equilibrium distance. When used in combination with the WCA repulsion, r_0 can be omitted as there will be another equilibrium distance set up by the interplay of the harmonic attraction and the WCA repulsion.

The second choice is the FENE (finite extensible nonlinear elastic) bond

$$V_{\text{FENE}}(r_{ij}) = -\frac{1}{2}K(\Delta r_{\text{max}})^2 \log\left[1 - \left(\frac{r - r_0}{\Delta r_{\text{max}}}\right)\right] \tag{1.60}$$

with three parameters. Again K stands for the bond strength and r_0 plays the role of the equilibrium distance. Additionally the parameter Δr_{max} leads to a divergence of the potential at $r_0 - \Delta r_{\text{max}}$ and $r_0 + \Delta r_{\text{max}}$ such that the contraction and extension can only be finite. In this sense the FENE bond has a certain advantage over the harmonic bond, which in principle can be stretched infinitely. Such a behavior would be highly unphysical. However, when Taylor expanded around r_0, it becomes apparent that the FENE potential resembles the harmonic potential in close vicinity of r_0. Thus for most applications both bonds are suitable, as long as the parameters are chosen appropriately. Furthermore the combination of bond parameters and WCA repulsion has to prohibit chain crossing, i.e. the beads must be bonded closely enough.

1.6 Rheology

In section 1.1.1 we discussed the Navier-Stokes equation for a Newtonian fluid with constant shear viscosity η. This is an appropriate assumption for the underlying solvent, which for instance could be water or any other simple liquid. However, when dealing with a complex solution of different species, so-called non-Newtonian behavior occurs.

In this context the term non-Newtonian means that the stress tensor is not a linear function of the strain tensor [22]. Rheology is the study of these kinds of behaviors which are about deformation and flow of matter. Typical examples from daily life for materials that show such a non-Newtonian behavior are tar, putty, honey or ketchup, while in science people may be interested in liquid crystals, polymer solutions, protein solutions or colloidal suspensions. The deviation from typical Newtonian behavior has its origin in the microscopic structure of such materials. A distortion on the micro structure can lead to a macroscopic effect on the fluid, when such distortions come with a long relaxation time. Polymer solutions in particular a very different from particle suspensions, as the polymer structure permits elastic recoil effects, where i.e. a polymer can stretch and contract again. At higher polymer concentrations entanglement sets in such that polymers start to react as a collective network. In a way polymeric systems combine the elasticity of a solid with the fluidity of a liquid in a viscoelastic behavior [1].

1.6.1 Studying Rheology

A simple approach to study the rheology of a fluid can be to enforce Couette flow. A linear velocity profile leads to a constant shear rate $\dot{\gamma}$, such that

$$v_x = \dot{\gamma} z \qquad v_y = 0 \qquad v_z = 0 \quad , \tag{1.61}$$

with an arbitrary choice of the coordinate system. Due to the symmetric geometry only the four components τ_{xx},τ_{yy},τ_{zz} and $\tau_{xz} = \tau_{zx}$ of the stress tensor remain. The latter is called the shear stress and the former are usually combined to the first and second normal stress coefficients as $(\tau_{xx} - \tau_{zz})$ and $(\tau_{yy} - \tau_{zz})$. The relation between the shear stress and shear rate can be written

$$\tau_{zx} = \eta(\dot{\gamma})\dot{\gamma} \tag{1.62}$$

similar to the Newtonian version, but with a shear-rate dependent viscosity. The most common behaviors of viscosity with shear rate can be divided in four categories sketched in Figure 1.3. First there is the well-known Newtonian behavior with a constant viscosity. Then there exist two behaviors called shear-thinning and shear-thickening. Here the viscosity either decreases or increases with shear rate. The last category is the so-called Bingham plastic with an infinite viscosity up to an abrupt reaction at a yield stress τ_0 leading to a finite viscosity. Such behavior can be observed in colloids, e.g. paints

$$\begin{aligned} \eta &= a\tau_0/\dot{\gamma} && ,\tau_{zx} > \tau_0 \\ \eta &= \infty && ,\tau_{zx} < \tau_0 \quad . \end{aligned} \tag{1.63}$$

Most polymer solutions show a shear-thinning behavior. Shear-thickening behavior can be observed in some ranges for polymer solutions and concentrated particle suspensions [52].

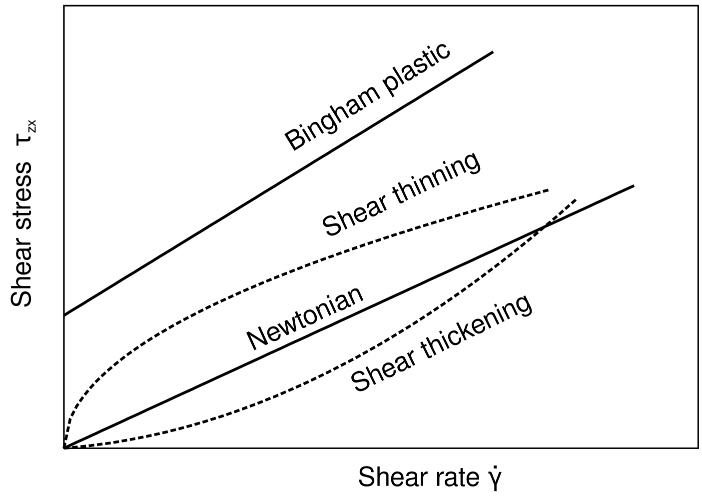

Figure 1.3: Illustration of the four categories of viscosity behavior.

An important effect of non-uniform shear flows such as Poiseuille flow is the migration of particles from regions of high shear to low shear. This disturbs the homogeneous concentration profile and complicates the evaluation. Other reasons for inhomogeneous concentrations may be wall effects. In polymer solutions the uniform concentration profile is usually maintained, but for suspensions it is not.

1.6.2 Polymers in Shear Flow

The behavior of polymers in shear flow is also dependent on their environment, namely the solvent condition. In a good solvent, where the interactions between the monomers and solvent particles is stronger than the monomer-monomer interaction or solvent-solvent interaction, polymers are stretched and uncoiled. This conformation can lead to a very different behavior than under poor solvent conditions, where polymers are more coiled. Thus when comparing different polymer solutions under shear, the shear rate alone is not sufficient, but another parameter is used that includes information of the polymers' configuration. One choice can be the Péclet number, in this context written as

$$Pe = \frac{\eta_s \dot{\gamma} R_F^3}{k_B T} \quad . \tag{1.64}$$

Here η_s is the solvent viscosity and R_F is the Flory radius [22]. Another way could be to define the Péclet number as

$$Pe = \frac{\xi \dot{\gamma} \sigma^2}{k_B T} \quad , \tag{1.65}$$

which the friction coefficient ξ and the typical length scale σ [53]. Another choice for presenting viscometric data is in terms of the Weissenberg number Wi, which is defined as

$$\mathrm{Wi} = \tau_0 \dot{\gamma} \quad , \tag{1.66}$$

with τ_0 the longest relaxation time of the polymer. All conformational quantities including τ_0 are dependent on the polymer concentration. So one has to be careful when comparing viscometric data of different concentrations. Of particular interest is the polymers' contribution to the overall viscosity of the solution, which is called the intrinsic viscosity $[\eta]$. It is defined through the limit of zero polymer concentration c

$$[\eta] = \lim_{c \to 0} \frac{\eta - \eta_s}{c \eta_s} \tag{1.67}$$

and thus has the units of an inverse density. The intrinsic viscosity may be viewed as the first-order coefficient of an expansion in concentration or volume fraction ϕ [54]. For suspensions of spherical particles of radius R_F, the Einstein relation states an intrinsic viscosity of 2.5

$$\eta = \eta_s (1 + 2.5\phi) \quad , \tag{1.68}$$

The relation may be applied to very dilute solutions of polymers where R_F is to be taken as the hydrodynamic radius. With decreasing shear rate the dependence on the shear rate diminishes and η approaches the zero-shear-rate viscosity η^0 in the limit $\dot{\gamma} \to 0$. At very high shear rates (Péclet numbers, Weissenberg numbers) the viscosity might again become independent of the shear rate and approach η^∞ [55].

Chapter 2

The Algorithm

Starting from the electrokinetic equations (1.4, 1.15, 1.18)

$$\rho\left[\partial_t \boldsymbol{v} + \boldsymbol{v}\boldsymbol{\nabla}\cdot\boldsymbol{v}\right] = \eta\boldsymbol{\nabla}^2\boldsymbol{v} + \zeta\boldsymbol{\nabla}(\boldsymbol{\nabla}\cdot\boldsymbol{v}) - \boldsymbol{\nabla}p - k_BT\sum_c z_c\rho_c\boldsymbol{\nabla}\hat{\Phi} \tag{2.1}$$

$$\partial_t\rho_c = -\boldsymbol{\nabla}\cdot\left[\rho_c\boldsymbol{v} - D_c\boldsymbol{\nabla}\rho_c - z_cD_c\rho_c\boldsymbol{\nabla}\hat{\Phi}\right] \tag{2.2}$$

$$\boldsymbol{\nabla}^2\hat{\Phi} = -4\pi l_B\left(\sum_c z_c\rho_c + \sigma\right) \tag{2.3}$$

we now want to derive a solution scheme for efficient simulations of (poly)electrolyte solutions. We will tackle each equation separately, as there already are various approaches to be found in the literature for each of them. Each choice for a solver has to be taken considering the other two equations, such that we end up with a well-fitted combination. In this chapter we start out with the description of dissipative particle dynamics as the Navier-Stokes solver to incorporate hydrodynamics. Then we pick a mesh- and Fourier-transform-based Poisson solver for the electrostatics. Finally, we deal with the convection-diffusion equation and the representation of the electrolytes, where we choose a pseudo-particle approach in the framework of a stochastic process. Furthermore we discuss the coupling of the three individual solvers to a complete algorithm.

2.1 Towards a Navier-Stokes Solver

Hydrodynamic interactions play an important role in the dynamics of fluids and solutions on the mesocale. While the Navier-Stokes equation as a continuum theory of a density field $\rho(\boldsymbol{r}, t)$ is originally a macroscopic approach, it has been observed that it is fairly accurate down to remarkably small length scales, such that only a small amount of solvent molecules can already recover Navier-Stokes behavior. For simple atomistic fluids the range appears to be $\sim 3nm$ [56]. Stable hydrodynamic behavior has been found experimentally and in simulations for scales down to $\sim 1nm$ (see [57] and references therein). Thus the model directly becomes applicable to the study of colloidal particles as well as large polymers in solution. However, the direct solution of the Navier-Stokes equation is not an easy task and for several decades people have developed and improved algorithms to solve the equation in a fast and accurate manner. The reason for the complexity is that one deals with a system of coupled non-linear partial differential equations.

Focusing on mesoscale simulations, there are many applications that require an efficient Navier-Stokes solver, as other interactions, except long-range interactions such as electrostatics or dipolar interactions, are usually much faster to compute. This makes the hydrodynamics the bottleneck of these calculations. Some prominent examples of hydrodynamic simulations include problems in colloidal suspensions, blood flow in capillaries, in-vivo rheology, i.e. flow in cells, and also DNA separation in micro-channels, which has a huge importance for medical applications. Most times one deals with conditions that include low Reynolds numbers, i.e. laminar flow and thus the Stokes equation instead of the full Navier-Stokes equation is applicable. Also thermal fluctuations have a huge importance on the mesoscale, as solutes are still way larger than the solvent molecules but in a regime where the effects of collision with the solvent are necessary to be considered.

2.1.1 An Overview of Hydrodynamic Models

Methods for hydrodynamics can in principle be divided into two categories, which are distinguished by the approach to the solvent. The first idea is to have an explicit solvent, where the hydrodynamic interactions between solutes are carried through by the solvent medium. The other approach is to have an implicit solvent, where the interactions between solutes are calculated directly. Thus it is important to have an overview over hydrodynamic effects on solutes. First we consider a single solute A. The solvent can manipulate the motion of A by flow, i.e. convective transport, where the solvent basically drags the solute along. But it can also lead to rotational motion depending on the solute's shape. Interactions between different solutes occur when solute A conducts a motion which induces a motion of solute B. This interaction between different solutes can be modeled with a mobility matrix in the Stokes equation. The result, which is known as the Oseen tensor, has a $1/r$ dependence. Hence hydrodynamic interactions have a long-range character similar to electrostatic interactions and can generally not be neglected even for long distances. However, for very concentrated solutions the screening effect takes over, so there are situations where it is legitimate to neglect hydrodynamic interactions. This assumption is made frequently for simulations of dense polymer solutions, where the Zimm dynamics is replaced by Rouse dynamics. For polyelectrolytes other arguments [44] allow the negligence of hydrodynamics even for dilute solutions.

A popular implicit-solvent approach to the simulation of solutes such as colloidal particles is the Brownian dynamics method with an implementation of the Rotne-Prager tensor [58] for the hydrodynamic interactions. Brownian dynamics relies on the fact

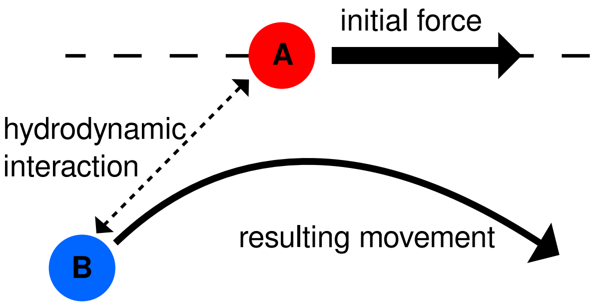

Figure 2.1: Illustration of hydrodynamic interactions between two solutes. The force on solute A results in a nontrivial motion of solute B.

that the motion of solutes is governed by an overdamped Langevin equation, where the inertia term cancels out. Similar to the long-ranged electrostatics, Ewald splitting techniques and fast multipole techniques can be used to improve the performance of the hydrodynamic tensor calculations. The approach turns out to be fast for small systems but scales badly with increased number of solutes. Stokesian dynamics [59] is a similar approach that is capable of including also the near-field effects, such as the lubrication forces between closely approaching solutes. Also, further improvements were made to include inertia effects.

On the side of explicit-solvent methods we want to briefly mention two approaches before going into detail about the dissipative particle dynamics, which is the method of choice in this work. The first one is the multiparticle collision dynamics (MPCD), also called stochastic rotation dynamics (SRD). It is a particle-based approach that originates from the Boltzmann equation for the transport of gases [60, 61, 62]. The solvent particles' motion is separated into a collision step and a streaming step. Collision of particles is modeled by dividing the simulation box into cells and rotating all velocities of the particles inside a cell by a certain angle, which results in a Maxwellian velocity distribution and the behavior of an ideal gas. After the collision the particles are freely streaming with their new velocities until the next collision step. A further development includes fluctuation effects to the velocities, which provides a thermostatic behavior and thus enables non-equilibrium simulations. The coupling to solutes is rather simple and is achieved by including them into the collision steps.

Another approach based on the Boltzmann equation is the Lattice Boltzmann (LB) method, where the equation is solved on a lattice. By means of a Chapman-Enskog expansion the Navier-Stokes equation in the incompressible limit is recovered [63, 64]. As a lattice method, LB has certain drawbacks regarding Galilean invariance and the implementation of curved boundaries. The coupling of solutes to the solvent density sitting in the lattice nodes is either achieved by defining them as hard, spacious objects [65, 66] or by solving a Langevin equation to couple the forces between the solute as a point particle and the solvent [67, 68].

Before proceeding, it may be worthwhile to note that besides the so-called bottom-up approaches to hydrodynamics on the mesoscale, there are also top down approaches. An example would be the smooth particle hydrodynamics (SPH) [69, 70]. This method starts out with the continuum Navier-Stokes equation and a representation of the density in a Lagrangian fashion by particles as integration sites. An interpolation scheme is used to transfer between the particles and the continuum. Further one can introduce thermal fluctuations to those particles, which leads to the method of smoothed dissipative particle dynamics (SDPD) [71].

2.2 Dissipative Particle Dynamics

The Dissipative Particle Dynamics (DPD) is a coarse-grained model for a fluid that has been developed in the early 1990s by Hoogerbrugge and Koelman [72, 73], in a way as a combination of particle simulations and cellular-gas automata. Before, people often used a bead model for solvent molecules with a Lennard-Jones repulsive interaction. Due to the stiffness of the potential, time steps in that approach are limited to small values, as otherwise particle overlap would cause infinities in the force calculations and the computation would break down. The basic idea behind DPD was to use soft potentials instead. Hence it is possible to reach much larger time scales with the simulation, as the integration time step can be chosen much larger. In 1995 Español and Warren [74] constructed the theoretical framework for DPD. From there on till today people have developed improved numerical algorithms for the DPD method. Also there have been several extensions, e.g. to constant energy, constant pressure, implementation of boundaries [75], hybrid schemes, or the Lowe-Andersen thermostat [76] which is based on DPD.

The DPD equations of motion are constructed with three forces between pairs of particles

$$\boldsymbol{F}_{\mathrm{DPD},i} = \sum_{i \neq j} \boldsymbol{F}_{C,ij} + \boldsymbol{F}_{D,ij} + \boldsymbol{F}_{R,ij} \quad , \tag{2.4}$$

which are the conservative force, the dissipative force and the random force. The main ingredients are the latter two. The dissipative force is necessary to reduce excess energy from the system

$$\boldsymbol{F}_{D,ij} = -\gamma_{\mathrm{DPD}} \omega_D(r_{ij}) \left(\hat{r}_{ij} \cdot \boldsymbol{v}_{ij}\right) \hat{r}_{ij} \quad . \tag{2.5}$$

The friction parameter γ_{DPD} sets the strength of the dissipation, while the dissipation itself is taken to be in interparticle direction. The force is symmetric and maintains Galilean invariance, as only the velocity difference between particles j and i matters. A typical choice for the friction also taken throughout this study is $\gamma_{\mathrm{DPD}} = 5$.

The weighting function ω_D brings in the distance dependence. The negative sign assures the dissipative character. As a counterpart to balance the dissipation, a random force is necessary

$$\boldsymbol{F}_{R,ij} = \sigma \omega_R(r_{ij}) \zeta_{ij} \hat{r}_{ij} \quad . \tag{2.6}$$

Here the amplitude is set by σ and a weighting function ω_R is used for the spatial dependence. $\zeta_{ij} = \zeta_{ji}$ is a symmetric, Gaussian random variable with the first and second moments

$$\begin{aligned} \langle \zeta_{ij}(t) \rangle &= 0 \qquad (2.7) \\ \langle \zeta_{ij}(t) \zeta_{kl}(t') \rangle &= (\delta_{ik}\delta_{jl} + \delta_{il}\delta_{jk})\delta(t - t') \quad . \qquad (2.8) \end{aligned}$$

Thus it has zero mean and no correlation, i.e. a white noise.[1] Dissipative and random force, however, are not independent. They must fulfill a fluctuation-dissipation theorem [74], which results in

$$\omega_D = (\omega_R)^2 \quad , \tag{2.9}$$

and

$$\sigma^2 = 2\gamma_{\mathrm{DPD}} k_B T \quad . \tag{2.10}$$

Only then DPD becomes a proper thermostat to conserve the temperature T. The choice for the weighting functions is important as they will influence the properties of the fluid, by e.g. causing a change in the Schmidt number. The typical choice, which we will also take here, is of the form

$$\omega_R(r_{ij}) = \begin{cases} 1 - \frac{r_{ij}}{r_{\mathrm{cut}}} & r_{ij} < r_{\mathrm{cut}} \\ 0 & r_{ij} \geq r_{\mathrm{cut}} \end{cases} \tag{2.11}$$

and thus saves computation time due to its simplicity. The typical choice for the cutoff is $r_{\mathrm{cut}} = 1$. If one considers a conservative force, it is usually to be taken a soft repulsion in the form

$$\boldsymbol{F}_{C,ij} = a_{ij} \left(1 - \frac{r_{ij}}{r_{\mathrm{cut},c}} \right) \hat{r}_{ij} \quad , \tag{2.12}$$

where the parameter a_{ij} sets the strength and the force acts in the direction of the interparticle-distance, thus $\hat{r}_{ij}$. The linear shape of the force and its usually small cutoff radius $r_{\mathrm{cut},c}$ (which could in principle be different from the general DPD cutoff radius) allows for very fast computation, especially in comparison to other typical repulsive interactions as for instance the WCA potential. The appropriate choice of this interaction is used to set the compressibility of the desired fluid. In this study we omit the conservative interactions completely and thus deal with a DPD fluid that has the thermodynamic properties of an ideal gas.

All interactions are conducted as pairwise forces, i.e. DPD intrinsically fulfills Newton's third law and momentum conservation. Also, all forces are in interparticle distance and thus DPD also conserves angular momentum.

---

[1] Note that in the concrete implementation the time-δ results in another factor $1/\Delta t$.

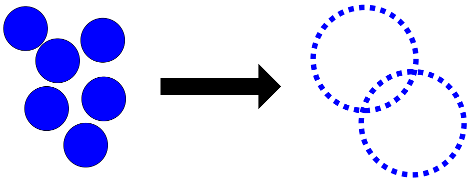

Figure 2.2: Illustration of the coarse-grained DPD particles. Any DPD particle can be considered to be built up of several solvent molecules.

2.2.1 Usefulness of DPD

The application range of DPD as a coarse-grained method is the mesoscale. For this scale, as less as the atomistic details of the macromolecules, also the solvent's atomistic details are mostly of no importance. Additionally there are way more solvent molecules than macromolecules in a typical system. Thus by taking an atomistic approach, most of the computation time goes by for the solvent, which is quite inefficient. The DPD particles can be considered a coarse-grained version of solvent molecules, i.e. a form of penetrable solvent blobs. Hence in addition to the time scale improvement, a necessity for a lower amount of particles to represent the same quantity of solvent works in favor for DPD.

The constantly occurring collisions of solvent molecules with each other and the solutes bring forth the concept of random fluctuations in the solution, which can be quantified by the temperature T. This effect is covered by the random force in DPD. The other effect is an interaction of moving solutes with the background flow field of the solvent, leading to the frictional force in DPD. However, hydrodynamics are only generated, if momentum is a locally conserved quantity. In DPD this is achieved by defining all forces on a pair level. Here lies the core difference to Langevin dynamics, where a global thermostat accounts for fluctuation and dissipation, while the solvent is neglected. Thus DPD intrinsically fulfills the prerequisites to be a coarse-grained solvent model with hydrodynamics. As it comes to Brownian motion of solutes, it is a self-similar process, meaning it does not require an exact ratio of solvent molecules to the solute, but can work with a much lower amount of solvent particles. Additionally, as mentioned in the beginning of this chapter, the hydrodynamics are recovered already for a small amount of solvent molecules as well, so that DPD includes both these concepts in an efficient fashion.

Taking a look onto the actual implementation of DPD as an algorithm, its big strength is its simplicity. DPD can be easily set-up on top of an existing molecular dynamics code. However, the particle-based pairwise interaction model can also be a drawback when it comes to computation speed. In a comparison with Lattice-Boltzmann simulations, Smiatek et al. [77] found DPD to be around nine times slower than Lattice-Boltzmann for a pure fluid. However, when including electrolytes and electrostatic interactions, the overall difference becomes much smaller. So while the pure performance makes Lattice-Boltzmann favorable, DPD still has some advantages that certainly qualify its usage.

Except for modeling a real fluid with certain qualities in a coarse-grained fashion, DPD can be used as a tool for two purposes.

DPD as a Navier-Stokes Solver

One important feature of the Navier-Stokes equations is that they don't ask for the microscopic details of the fluid, thus a coarse-grained model such as DPD can simply be used as a Navier-Stokes solver or to include hydrodynamic interactions between the solutes of interest. In this case the conservative interactions might be removed for further simplicity, resulting in an ideal gas fluid. This is the approach we take in this study. Whereas most fluids one would like to model are incompressible, the DPD ideal gas is not. However, as the considered velocities are usually way below the model's speed of sound $v \ll c_s$, i.e. the Mach number is low, the DPD fluid is effectively incompressible.

DPD as a Thermostat

Alternatively, DPD can simply be seen as an efficient thermostat [78] which is local and works for equilibrium as well as non-equilibrium simulations. In this concept it has been noted that the Gaussian random numbers can be replaced by uniform random numbers as the thermostatic results were the same. [2]

2.3 Properties of DPD

Before continuing to the solution of the other two electrokinetic equations, we first focus a bit more on the details of DPD and some of the crucial properties.

Here it may be worth noting that, even though the interpretation of DPD as a coarse-grained fluid is very common, it can also be derived systematically, as the microscopic derivation of the DPD equations of motion can be realized with Voronoi fluid dynamics [79, 80]. That DPD indeed maintains hydrodynamics, has been studied by Marsh, Backx and Ernst [81] in their 1997 paper on the connection between DPD and the Navier-Stokes equation. They found that the DPD equations are equivalent to a Fokker-Planck equation with three generators representing the conservative, dissipative and fluctuation part. Through an H-theorem it was derived that a DPD fluid approaches the canonical distribution, at least in the time-step limit $\Delta t \to 0$. The resulting momentum equation is a Newtonian Navier-Stokes equation with finite compressibility.

The standard DPD fluid has Schmidt numbers that are gas like, which might be a disadvantage in relation to other simulation techniques and has been discussed in the literature [76, 82]. However, Peters [83] argues that the Schmidt number in principle is related to a single solvent particle and not the DPD blobs, so that a Schmidt number based on the blob diffusivity is rather ill-defined. Also, Schmidt numbers do not need to be of the typical liquid range of 1,000 to lead to the correct dynamics. In the case of polymers, studies of Smiatek et al. (unpublished) have shown that the hydrodynamic

---

[2] Note that by replacing the Gaussian random numbers with uniform random numbers the variance has to be adapted which results in an additional factor $\sqrt{12}$ in σ_{DPD}.

interactions indeed build up fast enough. By measuring the internal vibrational modes of a polymer in solution, it was found that the results fit much better to Zimm scaling than to Rouse scaling, which means that hydrodynamic interactions are present. This would imply that the intra-chain hydrodynamic interactions take place within the time scale of the monomer dynamics and thus fully affect their behavior. Similarly, it was reported in [84] that the Schmidt numbers are large enough in simulations of polymer solutions. Improved Schmidt numbers can be achieved by increasing the cutoff of the DPD interactions or by using different exponents for the weighting functions, which, however, might be undesirable due to the increase in computational effort. A transverse DPD thermostat was proposed by Junghans et al. [85] where the dissipation concept is changed. This method does not conserve angular momentum, however, results in much better Schmidt numbers.

As in any MD scheme, the choice of an appropriate time step in DPD is crucial. Usually one wants to take a larger time step than in conventional MD to have a drastic performance improvement and reach longer time scales. It has been noted that the kinetic temperature has a dependence on the time-step choice and thus different methods have been proposed to remove this problem, including a self-consistent integration scheme [86]. However, also the configurational temperature is of importance and here it seems that all methods proposed so far perform similarly weak [87]. As a result, the standard DPD with an appropriately low time step, e.g. $\Delta t = 0.01$ in this work, might still be the most convenient choice. By means of a Trotter splitting Serrano et al. [88] came up with another integration scheme for the DPD equations of motion. Nowadays, the velocity Verlet scheme is still the most commonly used.

2.3.1 DPD Diffusivity

The properties of the Fokker-Planck equation show two time scales, a kinetic scale for the exponential relaxation of the fluid, and a dissipative scale on which momentum transport is happening. The two time regimes can be found when studying the mean-square displacement (MSD)

$$\mathrm{MSD}(t) = \langle (r(t) - r(t_0))^2 \rangle_N = 6Dt \quad , \tag{2.13}$$

where the averaging is over all N particles in the system.

In a pure DPD fluid with the standard parameters chosen throughout this work, one can find a quadratic time-dependence of the MSD up to around 50 time steps, as shown in Figure 2.3, which corresponds to a ballistic movement of DPD particles, i.e. force free and inertia driven. For larger times the MSD shows a linear time dependence, i.e. the diffusive motion takes over. The decay time of the relaxation also determines the diffusivity of DPD particles as well as the kinetic contribution to the viscosity $\eta_{\mathrm{kin}} = \rho D/2$. While η_{kin} only depends on single-particle distributions, the dissipative contribution to the viscosity depends on the pair-correlations. To determine the correct DPD diffusivity is quite important, as due to the later-on introduced ion-DPD coupling it influences the ion diffusivity as well. D can also be determined with a Green-Kubo relation of

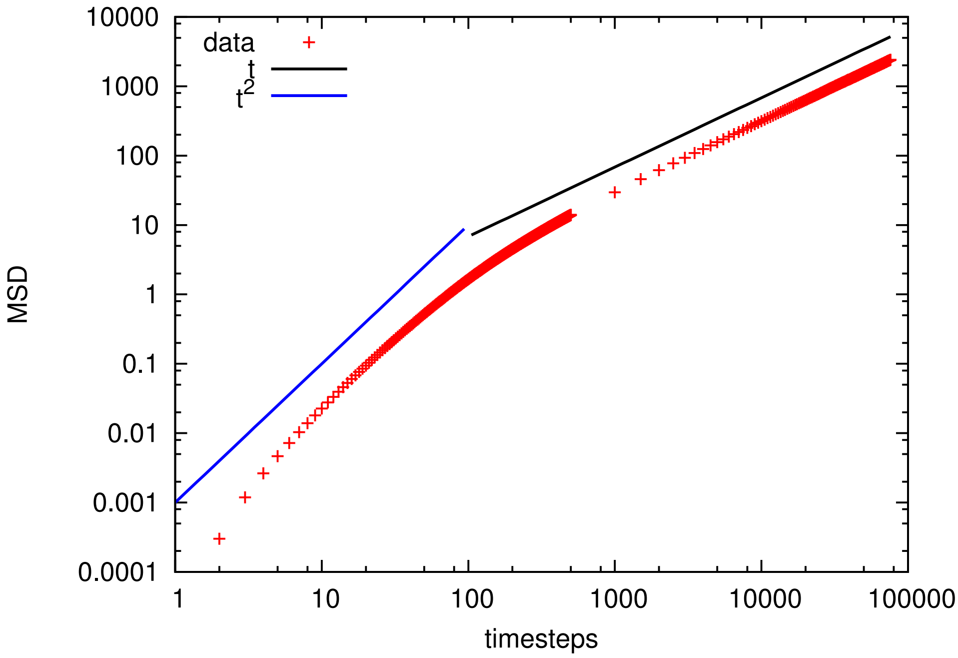

Figure 2.3: Mean square displacement in a DPD fluid in log-log scale. Straight lines show the two time scales.

the velocity autocorrelation function. Here, however, we take the MSD approach by studying a system of a pure DPD fluid, density $\rho_{\text{DPD}} = 3.75$ and size $10 \times 10 \times 10$ with the standard parameters and let it run for 200k steps, i.e. a long enough time to cover the linear behavior in the diffusive regime. D is then obtained by linear regression for the range $> 100\Delta t$, i.e. neglecting the ballistic part. This procedure is repeated 420 times to obtain a mean diffusivity and a mean error:

$$D_{\text{DPD}} = (0.5250 \pm 0.0003) \quad . \tag{2.14}$$

2.3.2 Green-Kubo Relation for the Shear Viscosity

The shear viscosity η_s as one of the transport coefficients is not set directly in DPD. However, by tuning the density, friction coefficient γ_{DPD} and the weighting function including the cutoff distance, one can adjust the shear viscosity to the desired value. We take two approaches to determine the shear viscosity for our standard parameter DPD liquid with density $\rho = 3.75$, friction $\gamma_{DPD} = 5.0$, standard weight function and cutoff $r_{c\text{DPD}} = 1.0$. The first method is to apply a Poiseuille flow. Either from fitting the parabolic profile

$$v_x(z) = \frac{\rho F_x^{\text{ext}}}{2\eta_s} \left(z_B^2 - z^2 + 2\delta_B \, |z_B| \right) \tag{2.15}$$

or from determining the flow maximum $\hat{v}_x$ to get

$$\eta_s = \frac{\rho F_x^{\text{ext}}}{2\hat{v}_x} \tag{2.16}$$

one can obtain the shear viscosity. This can be done even without implementing any boundaries into the system by using the elegant method of periodic Poiseuille flow by Backer et al. [89], where one splits the fully periodic system into two parts of oppositely flow, i.e.

$$\begin{aligned} F_x^{\text{ext}} &> 0 \qquad\qquad , z \geq 0 \\ F_x^{\text{ext}} &< 0 \qquad\qquad , z < 0 \end{aligned} \tag{2.17}$$

such that these two regions act as source of dissipation for each other at their interfaces. That way one obtains a double parabolic profile that can be used for the fit or maximum determination. A more detailed description of the flow methods is described in chapter 4.1.

The second way to determine the shear viscosity is by using a Green-Kubo relation for the off-diagonal elements of the stress tensor

$$\eta_s = \frac{V}{k_B T} \int_{t_0}^{\infty} dt \, \langle \tau_{\alpha\beta}(t) \tau_{\alpha\beta}(t_0) \rangle \quad . \tag{2.18}$$

There are three contributions to the stress tensor in a DPD fluid. The first is the kinetic part, calculated from the particles' velocities. The second is the contribution from dissipative pair interactions and the third is the stochastic pair-interaction part. If one wanted to implement a DPD algorithm with conservative interactions, these would take part here as well. Numerically the integral of the auto-correlation function can be calculated by using the trapezoidal rule (i.e. taking the t_0 value counting half) for a data range of around $[t_0 : t_0 + 200]$ and adding the tail by the integral of a polynomial fit $\sim at^{-b}$.

In the study by Jens Smiatek [90] using the software package ESPResSo, there has been a significant discrepancy between the shear viscosity obtained by the Poiseuille method and the Green-Kubo method, which could not be explained. There also has been controversy about whether the Green-Kubo principle is valid for DPD in general. As it turned out by further investigation, we were able to clarify that the discrepancy was due to a missing implementation of the DPD interactions in the stress-tensor calculations of ESPResSo. Thus only the kinetic stress tensor was calculated. To clarify this point and to obtain a further understanding of the contributions, we ran simulations of a system of size $V = 10 \times 10 \times 10$ with every possible combination of the three contributions, as presented in Table 2.1.

It is important to note that the contribution of the first autocorrelation value at t_0 is significant. Due to the uncorrelated nature of the stochastic force in DPD the stochastic contribution also is dominated totally by the t_0 value. Exactly this contribution is the one explaining the discrepancy between the Green-Kubo and the Poiseuille result discussed

type	η_s	t_0 contr.	variance	sim. steps
only dissipative	0.04212 ± 0.00007	0.002390	0.0001593	72,793,200
only kinetic	1.093 ± 0.006	0.01903	0.001268	87,502,500
only stochastic	0.2820 ± 0.0006	0.2800	0.01866	77,990,800
without dissipative	1.418 ± 0.006	0.2990	0.01993	76,659,400
without kinetic	0.2407 ± 0.0003	0.2824	0.01883	72,054,000
without stochastic	1.138 ± 0.0006	0.02140	0.001427	76,680,500
full (added)	1.417 ± 0.007	0.3014		
ESPResSo 3.11	1.115 ± 0.001	0.0189		100,000,000
condiff	1.380 ± 0.002	0.3014		100,000,000
Poiseuille	1.35 ± 0.01			

Table 2.1: Viscosity results for different combinations of the three contributions. Separately, the contribution of the first data point at t_0 is listed. For comparison we show another result obtained with ESPResSo, another condiff run and a result obtained with Poiseuille flow.

above, as the Green-Kubo result in [90] is $\eta_s = 1.0366 \pm 0.0013$ and the flow result $\eta_s \approx 1.34$. This has also been verified by analyzing the stress tensor calculation in the ESPResSo 3.1.1 source code, where indeed the stochastic and dissipative parts are missing.

2.3.3 Boundary Conditions in DPD

Most solvers for hydrodynamics are constructed to work in a bulk environment. The implementation of boundaries can be rather demanding, depending on the properties they should have and, of course, first of all the shape. An important property is the slippage effect, where many boundary methods can only offer a no-slip condition. However, especially in the regime of nano and micro flows it became apparent that the amount of slip is usually finite [91]. For DPD there exists a method to implement boundaries of arbitrary slip length [75]. Those boundaries can in principle also be arbitrarily shaped, which makes DPD a versatile tool to study flow in complex geometries. While slippage makes the picture more complicated, it can be of advantage when trying to manipulate flow by imposing beneficial boundary conditions.

We start out with the picture of a planar wall in the xy-plane. No-slip means that the velocity profile of the solvent vanishes at the hydrodynamic boundary z_B, i.e.

$$\boldsymbol{v}(z_B) = 0 \quad . \tag{2.19}$$

Partial slip means that there is a net velocity difference between the boundary and the solvent directly adjacent to it. The slip length b can be used to quantify this effect

$$b\frac{\partial \boldsymbol{v}}{\partial z} = \boldsymbol{v}|_{z=z_B} \quad , \tag{2.20}$$

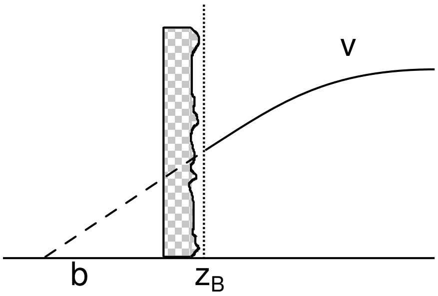

Figure 2.4: Illustration of the partial-slip boundary condition and the meaning of the slip length b.

where z_B is now the effective position of the surface, which does not necessarily coincide with the structural boundary itself. The concept of the slip length b thus is a linear extrapolation of the velocity profile behind the surface and b quantifies the distance where this extrapolation hits zero. This is illustrated in Figure 2.4.

To introduce the tunable-slip boundary condition we consider the DPD fluid layer adjacent to a boundary at $z = 0$. The interaction with the boundary consists of two parts. The first part has to be a repulsion for those particles that get too close to the boundary to make it impermeable. This is achieved by using the purely repulsive Weeks-Chandler-Andersen (WCA) potential

$$V_{WCA}(z) = 4\varepsilon \left[\left(\frac{\sigma}{z}\right)^{12} - \left(\frac{\sigma}{z}\right)^{6} + 0.25 \right] \quad . \tag{2.21}$$

Here σ starts to play the role of the unit length scale. The shift of 0.25 sets the cutoff distance to be $z_{c\ \mathrm{WCA}} = 2^{1/6}$ such that the potential and its first derivative (and thus the force) vanish at the cutoff radius. The advantage of using a "soft" potential instead of a hard-core repulsion is that it does not require a decrease of the DPD time step. However, due to the symmetric nature of the potential in xy-direction, it would only lead to a perfect slip boundary condition. Thus the second contribution to the potential includes a dissipative force

$$\boldsymbol{F}_i^D = -\gamma_L \omega_L(z_i)(\boldsymbol{v}_i - \boldsymbol{v}_{\mathrm{wall}}) \quad , \tag{2.22}$$

that is introduced in a similar fashion as the dissipative force between DPD particles. The wall might in principle have a finite velocity $\boldsymbol{v}_{\mathrm{wall}}$ by itself, for instance in the case of shearing. In order to maintain the correct thermal description at the boundary, a stochastic force fulfilling a fluctuation-dissipation theorem has to be added.

$$\boldsymbol{F}_i^R = \sqrt{2\gamma_L k_B T \omega_L(z)}\ \boldsymbol{\zeta}_i \tag{2.23}$$

The random vector's components $\boldsymbol{\zeta}_k$, $k \epsilon \{x, y, z\}$ are Gaussian random variables with

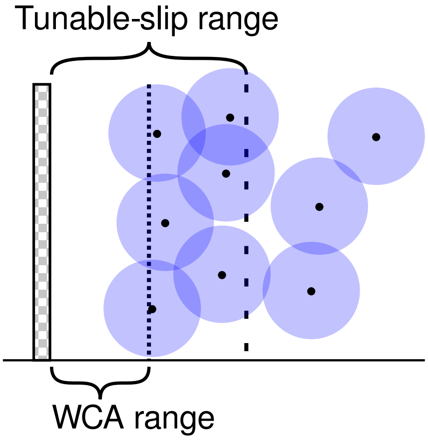

Figure 2.5: Illustration of the viscous layer occurring at the tunable-slip boundary. The WCA repulsion range also sets the position of the hydrodynamic boundary z_B.

zero mean and unit variance.[3] The weighting function ω_L is chosen to be positive definite up to a cutoff distance z_c. The regular choice is a linear weighting function

$$\omega_L(z) = 1 - \frac{z}{z_c} \quad . \tag{2.24}$$

As the WCA repulsion leads to a vacuum layer of about 1 adjacent to the wall, the cutoff z_c for the tunable-slip interaction has to be chosen larger so that the interaction reaches the fluid. The common choice is a cutoff of 2 which leaves a viscous layer of about 1, as sketched in Figure 2.5. By tuning the friction coefficient γ_L adequately, one can obtain all kinds of slippage, ranging from slightly negative slip over no-slip to arbitrary positive slip. One thing to note is that due to the Langevin type character of the tunable-slip interactions there is no momentum conversation in the viscous layer. Hence when evaluating flow behavior, particles in the viscous layer have to be treated with care.

2.4 Convection-Diffusion Equation and Stochastic Processes

The general framework of (convection-)diffusion equations is relevant for many different fields of study and not only limited to physicochemical problems. Hence also a wide range of approaches exist to tackle these kind of equations. However, some solutions rely on the assumption that indeed one term is dominating. A relatively straightforward solution of the equation is possible with a finite-element method [92]. However,

---

[3] For implementation note that one has to add the time step Δt as a factor into the square root. Compare also the fluctuation-dissipation theorem for the DPD forces.

grid-based algorithms show problems in diffusion-dominated systems. Also they have a certain drawback when it comes to complex geometries, which is why we will adopt a different approach in this work [93]. We shift the focus onto the stochastic process that is closely related to the convection-diffusion equation [94, 95]. In this framework a particle-based approach to the density is possible, i.e. a Lagrangian approach. We start out by considering a plain form of a convection-diffusion equation

$$\frac{\partial \rho(\boldsymbol{x},t)}{\partial t} + \boldsymbol{\nabla} \cdot [\boldsymbol{v}(\boldsymbol{x},t)\rho(\boldsymbol{x},t)] = D\nabla^2 \rho(\boldsymbol{x},t) \tag{2.25}$$

The corresponding stochastic process $\boldsymbol{X}(t)$ then describes a stochastic differential equation of the form

$$d\boldsymbol{X}(t) + \boldsymbol{v}(\boldsymbol{X}(t))dt = \sqrt{2D}d\boldsymbol{W}(t) \quad , \tag{2.26}$$

where $\boldsymbol{W}(t)$ is a Wiener process. Its increments are Gaussian random variables

$$\langle \boldsymbol{W}(t) \rangle = 0, \quad \langle \boldsymbol{W}(t)\boldsymbol{W}(t') \rangle = \min(t,t') \tag{2.27}$$

and the resulting fundamental attributes are a zero mean and a unit variance. In the framework of stochastic calculus the velocity term is called a drift. A solution to the convection-diffusion equation can now be found by representing the concentration field ρ by a finite amount of particles that all undergo the stochastic process $\boldsymbol{X}$. These particles, however, only have a pseudo character, as they follow an overdamped dynamics without any pair-correlations. The degree to which they can be interpreted as representatives of 'real' ions, depends on the parameters. While the continuum description of ions does not include any thermal fluctuations, the pseudo-particle description introduces fluctuations in an artificial manner due to the finite number of pseudo-particles that undergo Brownian motion to model diffusion. The nature of these fluctuations, however, is purely artificial and thus has to be considered with care. By increasing the amount of pseudo-particles representing the concentration field, the relative effect of fluctuations is decreased, whereas a decrease of pseudo-particles towards the limit of one particle representing one real particle enhances the fluctuation effects. In that sense both limits can be useful in different situations.

2.4.1 Relationship between the Stochastic Process and the Convection-Diffusion Equation

The relationship between Eq. 2.26 and Eq. 2.25 can be shown in the following way. We start out with a stochastic process $\boldsymbol{X}$ containing a convective term with coefficient $\boldsymbol{A}$ and a diffusive term B

$$d\boldsymbol{X} = -\boldsymbol{A}(\boldsymbol{X})dt + B(\boldsymbol{X})d\boldsymbol{W} \quad . \tag{2.28}$$

If we ask for the distribution of particles at a time $t + \Delta t$, we can formulate the integral equation

$$\rho(\boldsymbol{X}, t+\Delta t) = \int d(\Delta \boldsymbol{X}) \rho(\boldsymbol{X} - \Delta \boldsymbol{X}, t) P(\boldsymbol{X} - \Delta \boldsymbol{X}, \Delta \boldsymbol{X}, \Delta t) \quad . \tag{2.29}$$

Here P is the probability that the density elements shift $\Delta \boldsymbol{X}$ in a time step Δt. Intrinsically we assume a Markovian behavior, as we evaluate P with $\boldsymbol{X} - \Delta \boldsymbol{X}$ only. We can now expand $\boldsymbol{X} - \Delta \boldsymbol{X}$ in a Taylor series around $\boldsymbol{X}$

$$\begin{aligned} \rho(\boldsymbol{X}, t+\Delta t) &= \int d(\Delta \boldsymbol{X}) \Big[\rho(\boldsymbol{X}, t) P(\boldsymbol{X}, \Delta \boldsymbol{X}, \Delta t) \\ &- \Delta \boldsymbol{X} \frac{\partial}{\partial \boldsymbol{X}} \left[\rho(\boldsymbol{X}, t) P(\boldsymbol{X}, \Delta \boldsymbol{X}, \Delta t) \right] \\ &+ \frac{1}{2} (\Delta \boldsymbol{X})^2 \frac{\partial^2}{\partial \boldsymbol{X}^2} \left[\rho(\boldsymbol{X}, t) P(\boldsymbol{X}, \Delta \boldsymbol{X}, \Delta t) \right] \Big] \end{aligned} \tag{2.30}$$

up to second order. As ρ in the first term no longer depends on $\Delta \boldsymbol{X}$, we can use the normalization relation

$$\int d(\Delta \boldsymbol{X}) P(\boldsymbol{X}, \Delta \boldsymbol{X}, \Delta t) = 1 \tag{2.31}$$

for the probability density P. The second and third terms can be expressed by defining $\boldsymbol{A}$ and B in the form

$$\int d(\Delta \boldsymbol{X}) \Delta \boldsymbol{X} P(\boldsymbol{X}, \Delta \boldsymbol{X}, \Delta t) = -\boldsymbol{A}(\boldsymbol{X}) \Delta t \quad , \tag{2.32}$$

and

$$\int d(\Delta \boldsymbol{X}) (\Delta \boldsymbol{X})^2 P(\boldsymbol{X}, \Delta \boldsymbol{X}, \Delta t) = (B(\boldsymbol{X}))^2 \Delta t \quad . \tag{2.33}$$

Terms $(\Delta t)^2$ will vanish for $\Delta t \to dt \to 0$ and thus are left out. Now one can change the order of differentiation and integration and relocate the terms in the form

$$\begin{aligned} \rho(\boldsymbol{X}, t+\Delta t) - \rho(\boldsymbol{X}, t) &= -\frac{\partial}{\partial \boldsymbol{X}} \left[\boldsymbol{A}(\boldsymbol{X}) \rho(\boldsymbol{X}, t) \right] \Delta t \\ &+ \frac{1}{2} \frac{\partial^2}{\partial \boldsymbol{X}^2} \left[(B(\boldsymbol{X}))^2 \rho(\boldsymbol{X}, t) \right] \Delta t \quad , \end{aligned} \tag{2.34}$$

and hence take the limit $\Delta t \longrightarrow dt$ to arrive at

$$\frac{\partial}{\partial t} \rho(\boldsymbol{x}, t) = -\frac{\partial}{\partial \boldsymbol{x}} \left[\boldsymbol{A}(\boldsymbol{x}) \rho(\boldsymbol{x}, t) \right] + \frac{\partial^2}{\partial \boldsymbol{x}^2} \left[\frac{1}{2} (\boldsymbol{B}(\boldsymbol{x}))^2 \rho(\boldsymbol{x}, t) \right] \quad . \tag{2.35}$$

If we now consider $B(\boldsymbol{x}) = const.$ and identify

$$\boldsymbol{A} = \boldsymbol{v} \tag{2.36}$$

$$\frac{1}{2}B^2 = D \ , \tag{2.37}$$

we end up with the original convection-diffusion equation 2.25.

2.4.2 Integration Schemes

In this section we focus on two methods to integrate the stochastic process in Eq. 2.26. The simplest is the Euler scheme (also called Euler-Maruyama), where the differential dt is simply approximated by a finite time step Δt and quantities are evaluated at time t

$$\boldsymbol{X}(t+\Delta t) = \boldsymbol{X}(t) + \boldsymbol{v}(\boldsymbol{X}(t))\Delta t + \sqrt{2D}\Delta\boldsymbol{W}(t) \ \ . \tag{2.38}$$

The increment $\Delta\boldsymbol{W}(t) = \boldsymbol{W}(t+\Delta t) - \boldsymbol{W}(t)$ is the Gaussian random variable described above in Eq. 2.27 with variance Δt [4].

Any integration scheme should be compared in its convergence to the exact solution. However, there are two convergence concepts. The first is the so-called **strong** convergence. If we consider an integration with an approximative scheme $\boldsymbol{X}(t)$ up to time $t_{\max}$, it converges to the correct solution $\boldsymbol{X}_C$ with order $v > 0$ at $t_{\max}$ if there exists a positive constant c so that for sufficiently small Δt

$$\left\langle |\boldsymbol{X}_C(t_{\max}) - \boldsymbol{X}(t_{\max})|^2 \right\rangle^{1/2} \leq c(\Delta t)^v \ \ . \tag{2.39}$$

The angular brackets indicate an averaging over different trajectories, which is necessary due to the stochastic character of the variable. Strong convergence is a necessary feature if one is interested in the actual trajectories of the particles describing the stochastic process. However, most of the times, and in particular in our case, the particles are just a representation of a mean-field and thus do not need to have exact trajectories but should yield the correct concentration field ρ.

The second concept is the **weak** convergence. An integration scheme is referred to as weakly convergent with order $v > 0$ at time $t_{\max}$ to the correct solution $\boldsymbol{X}_C$, if for all sufficiently smooth functions $g : \mathbb{R}^d \to \mathbb{R}$ (d being the dimensionality of the integration space) with polynomial growth, there exists a positive constant c_g such that for sufficiently small Δt

$$|\langle g(\boldsymbol{X}_C(t_{\max}))\rangle - \langle g(\boldsymbol{X}(t_{\max}))\rangle| \leq c_g(\Delta t)^v \ \ . \tag{2.40}$$

In the deterministic case without any diffusive motion both concepts are identical, which can be shown by choosing $g(\boldsymbol{X}) = X_i, \ \ i \in \{1, ..., d\}$.

If the coefficients in the Euler scheme fulfill certain conditions [96] it has a strong convergence order of 1/2 and a weak convergence order of one, similar to the general

---

[4] similar to DPD this requires a factor $\sqrt{\Delta t}$ in the numerical implementation.

convergence order in the purely deterministic case. Higher order schemes can now be constructed taking the Euler method as the starting point [97]. Here we want to mention only one other scheme which is of the predictor-corrector or Runge-Kutta type.

The Heun method is obtained when introducing an intermediate step into the Euler scheme so that the integrand is evaluated twice per time step

$$\boldsymbol{X}_P(t+\Delta t) = \boldsymbol{X}(t) + \boldsymbol{v}(\boldsymbol{X}(t))\Delta t + \sqrt{2D}\Delta \boldsymbol{W}(t) \tag{2.41}$$

$$\boldsymbol{X}(t+\Delta t) = \boldsymbol{X}(t) + \frac{1}{2}\left(\boldsymbol{v}(\boldsymbol{X}) + \boldsymbol{v}(\boldsymbol{X}_P)\right)\Delta t + \sqrt{2D}\Delta \boldsymbol{W}(t) \quad . \tag{2.42}$$

Thus one first calculates a predicted position $\boldsymbol{X}_P$ for all particles, where one evaluates the field $\boldsymbol{v}$ again and takes the average field for the actual integration step. The Wiener increment must be the same. The Heun scheme is second-order weakly convergent, which makes it a good alternative if one desires higher accuracy.

According to the literature [96], the Euler scheme performs well as long as the coefficients, i.e. the velocity field, do not vary too much. Nowadays the Euler scheme is still the most common method in Brownian dynamics simulations. While with the Heun scheme in principle one could gain one convergence order, it has the apparent drawback that the coefficients, i.e. the velocity field (which here stands representatively for both the solvent velocity field and the electrostatic force field), have to be calculated twice per time step. Thus in an application, where the computation time matters, like in the case of this study, it might be favorable to stick to the Euler method and accept the lower convergence order. A detailed comparison of the two schemes in the actual algorithm is presented in section A.1 of the appendix.

As previously mentioned the velocity $\boldsymbol{v}$ in this section stands for both the solvent velocity field and the electrostatic interactions. Due to the different nature and the fact that the electrostatic forces are later-on transferred to the DPD particles for the coupling, the terms are treated separately in the algorithm, i.e.

$$d\boldsymbol{X} + \boldsymbol{v}dt - zD\boldsymbol{\nabla}\hat{\Phi}dt = \sqrt{2D}d\boldsymbol{W} \quad . \tag{2.43}$$

2.5 Solution of the Poisson Equation - The Particle Mesh Method

Most of this chapter is based on Hockney and Eastwood's book [98], the paper by Deserno and Holm [99] and the chapter by Arnold in [100]. Some of the relations are given for one-dimensional geometries. However, their three-dimensional counterparts are in straight analogy.

One of the typical approaches to solve the Poisson equation in a periodic boundary situation is to make use of the Fourier transform (FT)

$$
\begin{aligned}
\triangle\Phi(x) &= -4\pi\rho(x) \\
\text{(FT)} \Longrightarrow -k^2\tilde{\phi}(k) &= -4\pi\tilde{\rho}(k) \\
\tilde{\Phi}(k) &= \frac{4\pi}{k^2}\tilde{\rho}(k) \\
&= \tilde{G}(k)\tilde{\rho}(k) \quad . \qquad (2.44)
\end{aligned}
$$

This way the differential operator is turned into a simple multiplication and one deals with a system of linear equations. By solving for $\tilde{\Phi}$ and back transforming into real space, one obtains the electrostatic potential. The term $\tilde{G}(k) = 4\pi/k^2$ is also the k-space Green's function to the Poisson equation. Its real-space counterpart $G(x)$ can in principle also be used to obtain the potential by convolution with the charge density

$$\Phi(x) = [G * \rho](x) \quad . \qquad (2.45)$$

2.5.1 The Ewald Summation

The Ewald technique [101] is a smart way to split long-ranged pairwise interactions between particles in a periodic geometry. Typically it is applied to the Coulomb forces. The center of interest is the electrostatic energy

$$U = \frac{1}{2}\sum_{R=0}^{\infty}\sum_{\boldsymbol{m}^2=R}\sum_{i,j=1}^{N}{}' \frac{q_i q_j}{|\boldsymbol{r}_{ij} + \boldsymbol{m}L|} \quad , \qquad (2.46)$$

where all pair interactions are summed up over every periodic image of the box in distance R from the origin and the $'$ stands for the exclusion of self interactions. m is an integer vector for the shift into the according image box. Here and in the continuity of this chapter we assume a cubic simulation box

$$V = L^3 \qquad (2.47)$$

for simplicity. However, all the formulas in this chapter can be adapted to allow for rectangular boxes and the final algorithm allows for them as well. The sum in Eq. 2.46 has the flaw that it is only conditionally convergent, i.e. the result is dependent on the summation order. Usually one would choose a spherical summation. In some cases another summation scheme might be useful, which will be discussed with the ELC algorithm in section 2.5.3. The idea behind the Ewald summation is now to split the actual point-charges into a screened charge and a smeared charge of opposite sign. A smearing of the charges in Gaussian shape can be represented by

$$\gamma(\boldsymbol{x}) = (\alpha/\sqrt{\pi})^3 \; e^{-\alpha^2 x^2} \quad . \qquad (2.48)$$

Here α is the width of the Gaussian and the prefactor is chosen for normalization. Mathematically, the point charges as δ-functions are split such that

$$\delta(\boldsymbol{x}) = \underbrace{\gamma(\boldsymbol{x})}_{\text{k-space part}} + \underbrace{[\delta(\boldsymbol{x}) - \gamma(\boldsymbol{x})]}_{\text{real-space part}} \quad . \tag{2.49}$$

The first part of the right hand side is now representing smeared particles. Without the tricky point-shape it is possible to solve the Poisson equation for this part in k-space. The second part represents the point particles screened by a Gaussian charge of opposite sign. This way the actual pair interaction will have a much stronger decay. Thus it is no longer of infinite range. This part may then be calculated in real space. The separation into two contributions is a feature of the linear nature of the electrostatics formalism.

Important for the purpose of this work is only the k-space part. Due to the pseudo-character of ions, they do not possess point charges, but, however, require a smeared charge distribution. For this purpose we pick the Gaussian shape, just as in the splitting procedure. Thus the parameter α naturally defines the size of the pseudo-particles. The real-space part can be neglected as it is only a correction to get back to point-particles. However, it is exactly this correction where the pair correlations are taken into account. By disregarding it we automatically enter the mean-field description of electrostatics. Applying the Fourier transform concept described above, the k-space contribution to the electrostatic energy reads

$$U^{(k)} = \frac{1}{2V} \sum_{\boldsymbol{k} \neq 0} \frac{4\pi}{k^2} e^{-k^2/(4\alpha^2)} \left|\tilde{\rho}(\boldsymbol{k})\right|^2 \quad . \tag{2.50}$$

Differentiation, either in real space or better in k-space by $-i\boldsymbol{k}$ results in the electrostatic field. As a feature of this approach one can manually add the correct correlations for specific charge types, as e.g. solutes like polyelectrolytes, by adding the real-space contribution for them and thus transforming them into point-charges.

2.5.2 Mesh-based Poisson Solver

In principle one could use the k-space part of the Ewald summation as the Poisson solver. However, the scaling of the Ewald technique is of order $O(N^{3/2})$ with the number of charged particles N, if the optimal splitting into real-space and k-space part is chosen. This scaling is not the best one achievable and thus the Ewald technique can be outperformed quickly by grid-based methods when dealing with higher amounts of charges. As a rough estimate an Ewald summation stays competitive up to $N = 300$. However, in this work we make use of a grid-based approach. If one considers a discrete system, i.e. a grid, one can make use of the Fast Fourier Transform (FFT) to transform the Poisson equation into k-space. There exist highly optimized algorithms for the FFT, namely in this case the FFTW library [5], which can readily be used in the C/C++ environment. The speed of this method is determined by the amount of grid points N_p considered and

---

[5] Fastest Fourier Transform in the West, http://www.fftw.org

scales like $N_p \log(N_p)$. But as the increase in charge and system size/grid size is usually proportional, one can directly compare this scaling to the one of the Ewald summation. The discrete character of the mesh approach asks for a change in the Green's function, which can be constructed from the stencil used for differentiation on the grid [102].

For a particle based system as in our case, one has to think of a way to introduce a grid structure into the system in order to use the approach described above. An assignment scheme is used to transfer the particles' charges onto the grid for the calculation. The field is then evaluated on the grid and then reassigned to the particles. The process of transporting the density on the mesh can be described with the integral

$$\rho_M(x_p) = \frac{1}{h}\int_0^L dx\ W(x - x_p)\rho(x) \quad , \tag{2.51}$$

here presented in the one-dimensional form for simplification. An extension to three dimensions is straightforward. The density $\rho(x)$ is carried onto the grid points x_p with a spacing h by a convolution over the entire system with a weighting function $W(x)$. This weighting function must fulfill several conditions, as described in [99]:

1. charge conservation - the fractions of a particle's charge distributed among the grid points must sum up to its total charge.
2. finite and small support - i.e. the weighting function should only distribute to grid points in the vicinity of the particle as otherwise the computational cost is increased.
3. localization of discretization errors - if particles are more separated from each other, the discretization error in the electric force should be smaller.
4. smoothness - a continuously varying weighting function balances the grid discretization.
5. a similarly small support in k-space - as the amount of k vectors is limited, it should decay rapidly in k-space as well, to minimize aliasing errors.
6. easy and transparent implementation.

The simplest approach would be the nearest grid point scheme (NGP), where each charge is assigned to the nearest grid point available. This scheme, however, does not fulfill all the criterion described above. However, it is a good starting point for a first order charge assignment (cao 1)

$$W_1(x) = \chi_{[-\frac{1}{2},\frac{1}{2}]} = \begin{cases} 1, & -\frac{1}{2} \leq x < \frac{1}{2} \\ 0, & \text{otherwise} \quad . \end{cases} \tag{2.52}$$

Increasing the assignment scheme order, one starts to take into account the two nearest grid points in each direction, and then more and more as the order increases. A

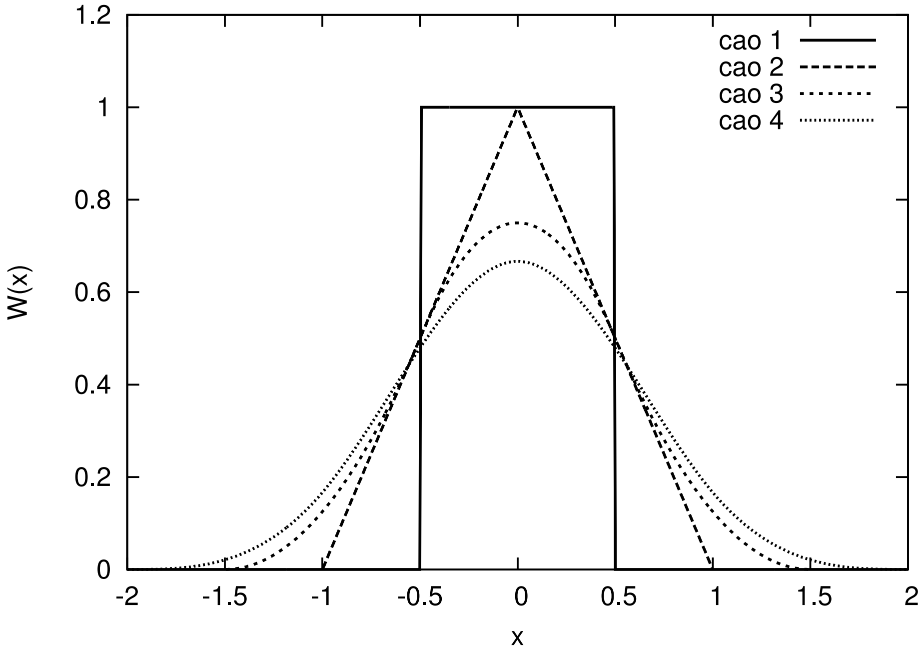

Figure 2.6: Series of cardinal B-splines as charge assignment functions. Increasing the assignment order leads to smoother assignments but larger support.

choice for the weight function is a convolution of the simple step function used in the NGP

$$W_a(x) = [W_{a-1} * W_1](x) \quad , \tag{2.53}$$

where the a-th order assignment function is made up of a convolutions of W_1. This set of functions is called cardinal B-splines. The series is illustrated in Figure 2.6.

Their Fourier-transformed structure

$$\tilde{W}_a(k) = h \left(\frac{\sin(kh/2)}{kh/2} \right)^a \tag{2.54}$$

is rather simple and the real-space implementation is easily done with piecewise polynomials. Further details including a table of this representation up to order seven can be found in [99]. The cardinal B-spline assignment is the original choice by Hockney and Eastwood [98] in their P3M method. Similar methods such as PME and SPME use different assignment schemes. An important thing to note for the assignment scheme is that the back assignment of electric field from the grid onto the particles should be carried out with the exact same assignment scheme in order to guarantee momentum conservation.

By introducing the assignment function and taking into account the extension of the charges, i.e. their smearing, an error is transported onto the grid. It has been shown that this error can be minimized by modification of the Green's function in Eq. 2.44 to a so-called optimal Green's function G_{opt} that takes into account the assignment scheme, the size of the charges and the specific type of differentiation operator used. Luckily it is only necessary to know the k-space shape of G_{opt}, which according to Hockney and Eastwood is

$$\tilde{G}_{\text{opt}}(\boldsymbol{k}) = \frac{\tilde{\boldsymbol{D}}(\boldsymbol{k}) \cdot \sum_{\boldsymbol{m}\in\mathbb{Z}^3} \tilde{U}^2\left(\boldsymbol{k} + \frac{2\pi}{h}\boldsymbol{m}\right) \tilde{\boldsymbol{R}}\left(\boldsymbol{k} + \frac{2\pi}{h}\boldsymbol{m}\right)}{\left|\tilde{\boldsymbol{D}}(\boldsymbol{k})\right|^2 \left[\sum_{\boldsymbol{m}\in\mathbb{Z}^3} \tilde{U}^2\left(\boldsymbol{k} + \frac{2\pi}{h}\boldsymbol{m}\right)\right]^2} \quad . \tag{2.55}$$

Here $\tilde{\boldsymbol{D}}(\boldsymbol{k})$ is the k-space version of the used differentiation operator, $\tilde{U} = \tilde{W}(k)/h^3$ is the k-space version of the assignment function divided by the one-cell volume. $\tilde{\boldsymbol{R}}(\boldsymbol{k})$ is the true reference force that is to be modeled with the grid approach, i.e.

$$\tilde{\boldsymbol{R}}(\boldsymbol{k}) = -i\boldsymbol{k}\tilde{G}(\boldsymbol{k})\tilde{\gamma}^2(\boldsymbol{k}) \tag{2.56}$$

with the true Green's function in convolution with the charged particles shape and the differentiation operator $-i\boldsymbol{k}$. This rather complicated structure has to replace the ordinary Green's function to obtain a minimized error in the force. A different shape is obtained when trying to optimize the energy instead of the force. At this point it has to be noted that there is a deviation in the approach by Holm and Deserno, who use $\tilde{\gamma}^1$ in Eq. 2.56 instead. The reason is that they view the k-space part of P3M as an interaction between a γ-smeared particle and a point charge. In the original approach, however, Hockney and Eastwood take it to be the interaction between two smeared charges, just as we want to define it for our purpose. We will later comment on the particle shape in section 2.8. For now we have

$$\tilde{\gamma}(\boldsymbol{k}) = \exp(-k^2/4\alpha^2) \quad . \tag{2.57}$$

The nice feature of the obtained Green's function is that it can be precalculated once the grid parameters are known at the beginning and thus produces no computational overhead. The general outline for the mesh-based Poisson solver goes like:

0. (precalculate the Green's function)
1. assign the charges onto the mesh to obtain ρ_M
2. transform ρ_M into k-space
3. multiply with $\tilde{G}_{\text{opt}}(\boldsymbol{k})$
4. multiply with $-i\boldsymbol{k}$ for the differentiation
5. transform back into real space
6. reassign the electric field back to the particles

Both the speed and the accuracy of the method are set by the assignment order and the grid spacing. Thus a smart choice of both parameters can lead to an improved performance. An extensive test is presented in section A.2 in the appendix.

2.5.3 Electrostatic Layer Correction

One of the underlying principles of FFT-based Poisson solvers is that they assume periodic boundary conditions (PBC). While PBC are certainly useful especially to study the bulk behavior and to reduce finite-size effects, many problems do not offer a full periodicity. The implementation of boundaries in one direction would be a simple example of such kind, where one ends up with a quasi 2D-periodic system. Short-ranged interactions with a certain cutoff radius are not affected by this, as one just has to introduce a gap behind the boundaries to make sure that no particle is interacting with an image of another particle behind the boundaries. However, for long-range interactions the cutoff argument does not hold and thus an alternative way to obtain boundary conditions other than periodic is necessary.

For electrostatics there are methods that work in 2D geometries, such as MMM2D [103]. The scaling of MMM2D with particle number is $O(N^{5/3})$. Thus it can be more efficient to stick to the original solver and add an additionally calculated correction-term. This is the approach of the electrostatic layer correction (ELC) [104], which we want to sketch here briefly. The main idea is to first calculate the fully periodic electrostatics with the underlying FFT-based solver and then systematically subtract those contributions that occurred due to the wrongly-assumed periodicity in the non-periodic direction.

In the standard form the Ewald summation has a summation order that is spherical in space, i.e. the contributions to the sum are in an order depending on the distance of the image box to the original box. As the sum is only conditionally convergent, a change in the summation order requires additional changes.

Lets assume a box of size $V = L_x \times L_y \times L_z$ that is non-periodic in z-direction, perhaps due to boundaries at positions $z_1 = 0$ and $z_2 = H < L_z$ and with its origin in $(0,0,0)$. The best summation order for such a quasi-2D periodic system is to sum in layers, i.e. first taking the original box and all image boxes with $z = 0$ and then adding consequently the other layers in the order of their z-distance to the original box. This leads to a change in the Ewald formula, namely the dipole term

$$U_d = \frac{2\pi}{(1+2\varepsilon_r')V}\left(\sum_i q_i \boldsymbol{r}_i\right)^2 \quad , \tag{2.58}$$

where ε_r' is the dielectric constant in infinite distance (assuming $\varepsilon_r = 1$ inside the box). Usually one assumes metallic boundary conditions, i.e. $\varepsilon_r' = \infty$ and thus the dipole term can be neglected. However, in a slab-wise summation order this no longer holds and a correction term is necessary

$$U_d = \frac{2\pi}{V}\left(\sum_i q_i z_i\right)^2 \quad . \tag{2.59}$$

The nice property of the slab-wise summation order is the 'symmetry' in z-direction. Images in far-apart layers above and below the original box cancel each other out, as they have the same distance to the original box and this distance is large enough so that the

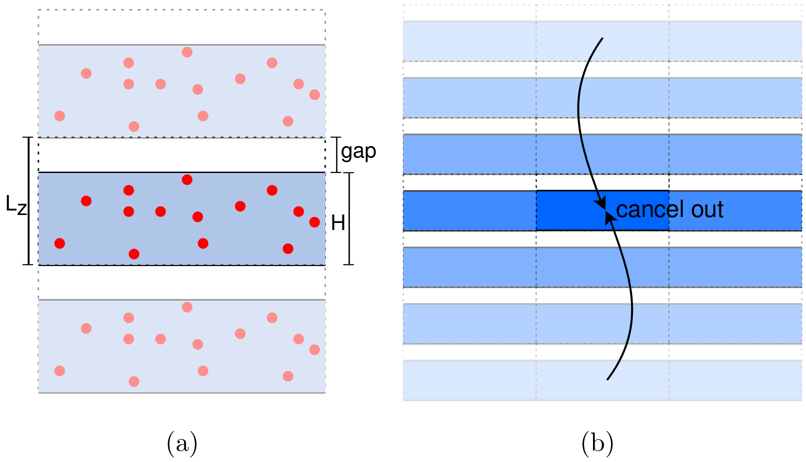

Figure 2.7: Illustration of the slab-wise geometry. (a) shows the gap on top of the confined volume of height H, which reoccurs in the periodic images. (b) shows how in distant images the collective of charges appears almost as homogeneous and thus cancel out with an image of the opposite side.

slabs appear as being almost homogeneous. This is the approach by Yeh and Berkowitz [105]. By inserting a gap above the upper boundary and assuming the cancel-out effect one already has a good approximation for the quasi-2D periodic electrostatics. This approach is illustrated in Figure 2.7. The error made with this approximation decays exponentially with the gap size.

Large gap sizes, however, require artificially large mesh sizes for the Poisson solver, so that the calculation is slowed down. ELC comes into play right there with the goal to require only small gaps, but calculate the correction exactly, instead of using an approximation. Additionally, ELC provides an error estimation formula which is not the case for the plain Yeh-Berkowitz approach. It is important to note for the slab-wise correction approaches that the error is not uniformly distributed, but is highest close to the boundaries, which is not advantageous as most often particles in the layer adjacent to the boundaries are the most important in their behavior. Hence tuning ELC to high accuracy is desirable. The scaling of ELC is $O(NR_{\max})$, where $R_{\max}$ is a cutoff radius for the infinite sums in the correction term. In the case of condiff particles this can be a drawback for systems with high particle-per-charge numbers N_q. The observation during the course of this study was that in the worst case ELC roughly doubles the computational effort of the electrostatics, which is an acceptable result.

Even though we simulate boundaries and thus dielectric interfaces, we will not deal with image charge effects in this study. There exist methods to include image effects [106, 107], however, the additional computational effort would somewhat double the electrostatics part another time. For our purposes this is neither feasible nor are the image effects of utmost importance in the current scope.

2.6 The Condiff Algorithm

Putting all components together, the final algorithm proceeds in the following manner:

Single Step

1. Leap Frog step 1 (update velocities by $\Delta t/2$)
2. initialize forces
3. apply boundary conditions
4. (if necessary) build neighbor lists, cell lists
5. compute DPD interactions
6. compute Lennard-Jones, harmonic, FENE, Yukawa interactions
7. boundary interactions for real particles
8. condiff step
9. Leap Frog step 2 (update velocities by $\Delta t/2$, positions by Δt)
10. (if evaluation step) analyze.

Condiff Step

1. initialize pseudo-ions
2. (if necessary) calculate the velocity grid
3. assign charges to grid
4. calculate electric field in k-space
5. add ELC corrections
6. add external field
7. assign electric force to monomers
8. assign electric force and velocity to pseudo-ions
9. boundary interactions for pseudo-ions
10. Heun step 1 (update to predictor positions)
11. assign charges to grid
12. calculate electric field in k-space

13. add ELC corrections
14. add external field
15. assign electric force and velocity to pseudo-ions
16. Heun step 2 (average motion and update to corrected positions)
17. assign electric force grid
18. assign electric force to DPD particles.

When the Euler scheme is used instead of the Heun scheme, the condiff step is basically reduced by cutting out steps 11-16. In the end the whole condiff procedure can be looked at as an additional interaction in a regular MD scheme, but with a more sophisticated computation process. As mentioned in chapter 2.3, the DPD fluid has a ballistic regime, in which the mean velocity is constant. One could take an advantage of this time scale separation for an improvement of the algorithm, since in principle the solvent velocity field has only to be calculated once and will in good approximation not change over the ballistic time scale. Therefore step 2 of the condiff step is noted with the comment “if necessary”.

2.7 Details on the Ion-DPD Coupling

By choice of the right coupling method we have to ensure on the one hand, that the flow velocity of the DPD particles is correctly transmitted to the pseudo-particles and their convective motion, and on the other hand, that the electric force felt by the pseudo-ions is transmitted correctly onto the DPD particles (step 18), as they are constantly being dragged along with the ions in an electric field.

2.7.1 Velocity Coupling

Every communication between the DPD particles and the pseudo-particles is performed by means of the grid, i.e. a quantity to be transmitted is put onto the grid first and from there distributed to the other species. That way all coupling processes follow the same procedure that is used in the electrostatic solver. For the velocity coupling this means the following:

1. assign velocity and density (number) of DPD particles to the grid
2. normalize velocity by dividing by the DPD number density
3. distribute normalized velocity from grid onto pseudo-particles.

The second step creates a locally averaged velocity field, which ensures that the condiff particles move with the local average velocity, while individual DPD particles could be faster or slower. It is important, however, that the collective velocity in the local volume is the one the pseudo-particles feel.

node	DPD density	force
m_1	$W(m_1, s_1) \cdot 1 + W(m1, s_2) \cdot 1$	$W(m_1, q_1) \cdot F(q_1) + W(m_1, q_2) \cdot F(q_2)$
m_2	$W(m_2, s_1) \cdot 1 + W(m2, s_2) \cdot 1$	$W(m_2, q_1) \cdot F(q_1) + W(m_2, q_2) \cdot F(q_2)$

Table 2.2: Quantities as they are transmitted onto the nodes (with the appropriate weighting).

2.7.2 Force Coupling

The force coupling is a little more complicated than the velocity coupling, as there are in principle many ways to normalize the force field. The way it is done in the condiff algorithm is the following:

1. assign electric field E from grid to pseudo-ions
2. multiply by pseudo-ion charge $\Rightarrow$ electric force F
3. assign F from each pseudo-ion onto the grid
4. normalize force field by DPD number density
5. distribute normalized force field from grid to DPD particles.

The first two steps are quite obvious, as they are necessary for the pseudo-particle motion itself. The third step ensures that the coupling is started from each pseudo-particle separately, i.e. we start out with a quantity defined on the pseudo-particle level, namely the electric force F. Another possibility would be to calculate the force field directly on the grid level by multiplying the electric field and the charge density. This attempt, however, did not lead to suitable DPD density profiles.

Step four is maybe the most subtle one. The idea behind it is that we have to conserve momentum, i.e. the force on the pseudo-particles has to be exactly the same as the force transferred to the DPD particles. The reason is that the DPD particles represent the total mass density and not only the solvent, i.e. they also represent the mass belonging to the charges represented by the pseudo-ions. In the simplest form one could think of a one-to-one correspondence between a DPD particle and a pseudo-particle, which leads back to the idea of Groot [9]. As the forces are distributed onto the DPD particles weighted by their contribution to the individual nodes, a prior normalization to the local DPD density on the node thus ensures that the total force is conserved. The whole process is illustrated in Figure 2.8.

Table 2.2 expresses how the quantities arrive at the nodes in the example of figure 2.8. Here the weighting function W is normalized so that

$$W(m_1, x) + W(m_2, x) = 1 \quad . \tag{2.60}$$

Thus we can write the conservation of force in the following manner:

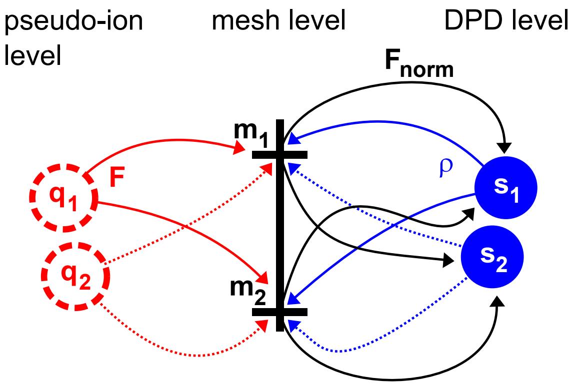

Figure 2.8: Cartoon of the force coupling. The electric forces of the pseudo-ions q_1 *and* q_2 *are assigned to the grid points* m_1 *and* m_2*, where it is divided by the DPD density. From there the normalized force is distributed onto the DPD particles* s_1 *and* s_2*.*

$$\begin{aligned}
F_{tot} &= F(q_1) + F(q_2) && (2.61)\\
&= \underbrace{W(m_1,q_1)F(q_1) + W(m_1,q_2)F(q_2)}_{F(m_1)} + \underbrace{W(m_2,q_1)F(q_1) + W(m_2,q_2)F(q_2)}_{F(m_2)} && (2.62)\\
&= F(m_1) + F(m_2) && (2.63)\\
&= \underbrace{\frac{W(m_1,s_1)F(m_1)}{W(m_1,s_1)+W(m_1,s_2)} + \frac{W(m_2,s_1)F(m_2)}{W(m_2,s_1)+W(m_2,s_2)}}_{F(s_1)}\\
&+ \underbrace{\frac{W(m_1,s_2)F(m_1)}{W(m_1,s_1)+W(m_1,s_2)} + \frac{W(m_2,s_2)F(m_2)}{W(m_2,s_1)+W(m_2,s_2)}}_{F(s_2)} && (2.64)\\
&= F(s_1) + F(s_2) \quad . && (2.65)
\end{aligned}$$

From Eq. 2.61 to Eq. 2.62 the forces are distributed from the pseudo-ions onto the grid by multiplication with the appropriate weight function. Hence we can define the force values on the nodes, as in Eq. 2.63. In the next step the forces are weighted and normalized with the DPD weight functions to Eq. 2.64 and thus distributed onto the DPD particles by defining the force on each particle as in Eq. 2.65. In the end, both steps that introduce the weight functions are simply a multiplication by 1 (Eq. 2.60).

Other ways to normalize the forces were also investigated, for instance to distribute both the original force field and the DPD density from the grid to the DPD particles and normalize there. In the numerical test it turned out that only the procedure described above was leading to the correct force coupling. The tests were also performed with externally applied electric forces. Here it also turned out that charge assignment order 1 is not sufficient to maintain the coupling, regardless of the grid size.

2.8 Standard Parameters for the Simulations

While several parameters can be varied in the algorithm, in this work we concentrate mostly on one parameter set throughout, to keep the data comparable. Also this parameter set has shown to produce a reasonable combination of performance and accuracy. The standard DPD density is mostly chosen to be

$$\rho_{\mathrm{DPD}} = 3.75 \quad . \tag{2.66}$$

This value has been used in many previous studies, as is it high enough to ensure a rather homogeneous distribution of particles throughout the system. The standard DPD parameters are

$$\begin{aligned} \gamma_{\mathrm{DPD}} &= 5.0 & (2.67)\\ r_{\mathrm{cut}} &= 1.0 & (2.68)\\ \omega_R(r) &= (1 - r/r_{\mathrm{cut}}) & (2.69)\\ F_C &= 0 \quad , & (2.70) \end{aligned}$$

so there are no conservative interactions and we deal with a pure ideal-gas type fluid. The temperature will be set to unity throughout these studies

$$T = 1 \quad . \tag{2.71}$$

For the condiff algorithm we first choose a width of the pseudo-charges by setting

$$\alpha = 1/\sqrt{2} \quad . \tag{2.72}$$

The width of the particles results from the particle-mesh algorithm to solve the electrostatics. Further details can be found in chapter 2.5.2. The smearing function in k-space has the form

$$\tilde{\gamma}(\boldsymbol{k}) = \exp(-k^2/4\alpha^2) \quad . \tag{2.73}$$

For the size of the pseudo-ions this means that their Gaussian shape has a real-space width

$$2r_{\mathrm{ion}} = \alpha^{-1} = \sqrt{2} \quad . \tag{2.74}$$

The diffusivity of the pseudo-ions is set by the diffusion constant D, which is taken equal for all ion species

$$D = 0.26 \quad . \tag{2.75}$$

This corresponds roughly to half the diffusivity of a DPD particle in this parameter set, $D \approx D_{\mathrm{DPD}}/2$, as described in section 2.3.1 (Eq. 2.14). The lower value has been chosen as it leads to an improved behavior at the boundaries. Much higher values lead to higher penetration rates, which slows down the algorithm, as those moves have to be rejected. Also a lower D results in a better ratio of charge to momentum transport. It is important to note that D also influences the strength of the electrostatic interactions between the pseudo-ions (see chapter 2.4 about the convection-diffusion equation).

The Bjerrum length is chosen to be unity as well

$$l_B = 1 \quad , \tag{2.76}$$

which sets the length scale of the system. The number N_q sets the amount of pseudo-particles representing one charge unit q. It is mostly taken to be

$$N_q = 1 \quad , \tag{2.77}$$

however, sometimes we choose $N_q = 10$ to obtain smoother profiles. The standard parameters for the grid, namely the charge assignment order (cao) and the grid spacing, are

$$\mathrm{cao} = 3 \tag{2.78}$$

$$a_{\mathrm{grid}} = 10\sigma/12 \quad . \tag{2.79}$$

This means that on the grid-level a particle has an influence range of 3 grid points or 2.5 in real units in each spatial dimension. This is also the maximum distance over which a DPD particle and a pseudo-ion can have a 'direct' correlation with each other. Thus the DPD particle's velocity will be assigned partly in the grid range from which the pseudo-ion obtains its velocity, and on the other hand the pseudo-ion's electrostatic force will be partly assigned in the grid range from which the DPD particle obtains its electrostatic force. The product cao × a_{grid} or better to say the ratio cao/grid size is therefore influencing the local coupling of pseudo-ions and DPD particles, which is further explained and illustrated in section A.4 of the appendix. In general, it is crucial that the grid size is accompanied by an appropriate assignment order. Choosing a large grid size, i.e. a high mesh refinement, and a low assignment order, can lead to cases where pseudo-particles have no DPD particles in their vicinity. In those cases the force coupling is not working properly. Thus a good parameter set has to ensure a coverage of all pseudo-particles with DPD density. A natural choice would be to take the grid spacing in the order of magnitude of the typical DPD particle distances (i.e. the particle diameters) and an assignment order that spreads the coupling range to 1-2 particle diameters in all directions.

Chapter 3

Tests and Discussion

Overview

In this chapter we deal with the applicability of the condiff algorithm. First we summarize the results of tests performed to determine the optimal parameter set and to study the behavior and results of the algorithm in controlled situations. Further details on these points are presented in the appendix. The first applications of the algorithm deal with the electro-osmotic flow, where we intent to compare the results to theoretical predictions of the Poisson-Boltzmann theory, as well as explicit-ion simulations. Furthermore we compare the condiff algorithm to other DPD based models published in the recent past. A detailed performance measurement follows, where we compare to the software package ESPResSo. Finally, we summarize the algorithm and give a short outlook into possible further improvements.

3.1 Summary of Tests

In principle, the condiff algorithm allows for different integration schemes for the stochastic process resembling the convection-diffusion equation. In this study we focus on the Euler and Heun method. While the latter requires a higher computational effort, it also yields a higher accuracy at a given time step. A detailed comparison can be found in section A.1. The conclusion is that both schemes are suitable, while it can be beneficial to choose the Euler scheme due to the better performance. Significant deviations have only been found for ion profiles close to boundaries, where, however, both schemes still follow the theoretical predictions of the Poisson-Boltzmann theory, as will be shown in section 3.2. A reduction of the time step below $\Delta t = 0.01$ leads to improved results. Due to the drawback of increased computational effort, it is, however, only recommendable in situations which require very accurate density profiles close to boundaries or, for instance, in quantitative comparisons with explicit-ion simulations.

The electrostatic part of the algorithm involves the charge assignment order and the grid spacing as free parameters that had to be optimized by means of various tests with different systems. For the particle-mesh Poisson solver it became apparent that with the standard parameters one obtains an accuracy of the order of 10^{-2}. More details can be found in a comparison of different mesh sizes and charge assignment orders (cao) presented in section A.2.

The pseudo-particle representation of the ion-concentration field involves the parameter N_q, which defines the number of pseudo-particles representing a unit charge. In chapter A.3 we present some tests, where it shows that $N_q > 1$ can lead to improved equilibration times of density profiles. Whenever dealing with a very low ionic concentration, it can thus be favorable to increase N_q. While we mostly choose $N_q = 1$ throughout this study, we show that higher values do not lead to deviations, especially in the shape of density profiles close to boundaries.

The choice of the assignment order and grid spacing not only determines the accuracy of the electrostatics, but also how the coupling between DPD fluid and pseudo-ions is managed. The coupling of the two components is studied extensively, with the results presented in section A.4. Both the comparison of density profiles and the study of radial-distribution functions lead to the conclusion that the standard parameters maintain the coupling in most situations encountered. Other combinations of mesh sizes and assignment orders have also been tested. Attention should be paid to situations of high charge gradients, such as in systems confined between charged walls with a high load of counterions in the solution and little or no salt to increase the screening. In these cases, an appropriate choice becomes important. It has been observed that the DPD density can overshoot close to the boundaries due to the strong electrostatic coupling to the pseudo-ions. Such an overshoot is rather unphysical, as the DPD density represents the combination of solvent and ion concentration and thus should never deviate that much from the shape determined by the ion profile. A different coupling scheme is presented in section A.4.8, where we additionally transfer the boundary repulsion felt by the pseudo-ions to the DPD particles in order to balance out the strong electrostatic attraction. The result is a flatter DPD profile, which then, however, is not any longer interpretable as a representation of the total density. Yet the most important effects, namely the coupling and force transmission, are maintained.

3.2 Counterion-induced Electro-osmotic Flow

As a simple test case for the algorithm we choose the electro-osmotic flow (EOF) in a pure counterion solution. This phenomenon occurs if counterions dissociate from an interface, which then is charged. Applying an electric field leads to a movement of the counterions and hence a flow of the solution. In the thesis by Jens Smiatek [90] it was shown that a coarse-grained MD simulation with tunable slip boundaries can reproduce the analytic result for the charge profile and the flow velocity profile obtained from Poisson-Boltzmann (PB) theory. Our test case directly builds on this study.

3.2.1 Analytical Results

The Poisson-Boltzmann equation for a single charge component reads

$$\triangle\Phi(\boldsymbol{r}) = -\frac{Ze}{\varepsilon_r}\rho_0 \exp\left(-\frac{Ze}{k_B T}\Phi(\boldsymbol{r})\right) \tag{3.1}$$

with the electrostatic potential Φ, and the charge density ρ_c expressed by a Boltzmann distribution. The solution for the density [90, 108] can be derived

$$\rho_c(z) = \frac{\rho_0}{\cos^2(\kappa z)} \quad , \tag{3.2}$$

with ρ_0 being the charge density in the center of the slit channel and

$$\kappa = \sqrt{\frac{(Ze)^2\rho_0}{2\varepsilon_r k_B T}} \tag{3.3}$$

the screening constant[1].

The flow inside the slit channel by an external field applied in positive x-direction can be determined from the Stokes equation. Here we include the partial-slip boundary conditions

$$v_x(z) = -\frac{\varepsilon_r k_B T}{Ze\eta_s} E_x \left[\log(\cos^2(\kappa z_B)) - \log(\cos^2(\kappa z)) - 2\kappa\delta_B \tan(\kappa z_B)\right] \quad . \tag{3.4}$$

The prefactor includes the shear viscosity of the fluid η_s. As a reminder, z_B is the position of the hydrodynamic boundary and δ_B the slip length.

3.2.2 Simulation

We take a box of size 10 × 10 × 15 and place the two boundaries at $z_1 = 0$ and $z_2 = 10$, so that we obtain a penetrable volume of 10 × 10 × 8 and a gap for the ELC calculation of 5σ. The system is filled with a DPD density of $\rho_{\mathrm{DPD}} = 3.75$ (3000 particles) and a counterion density of $\rho_c = 0.0125$ (100 particles with $N_q = 10$ to smoothen the charge density). It is not necessary to set the surface charge explicitly, as the resulting potential for two equally charged surfaces would be constant throughout the channel. We apply the tunable-slip boundary conditions with three different friction values and resulting slip lengths.

γ_L	b
5.26	0
1.0	1.21
0.5	2.65

---

[1] Note that κ is not the usual Debye screening constant. $\varepsilon_r = \frac{1}{4\pi}$ in our units.

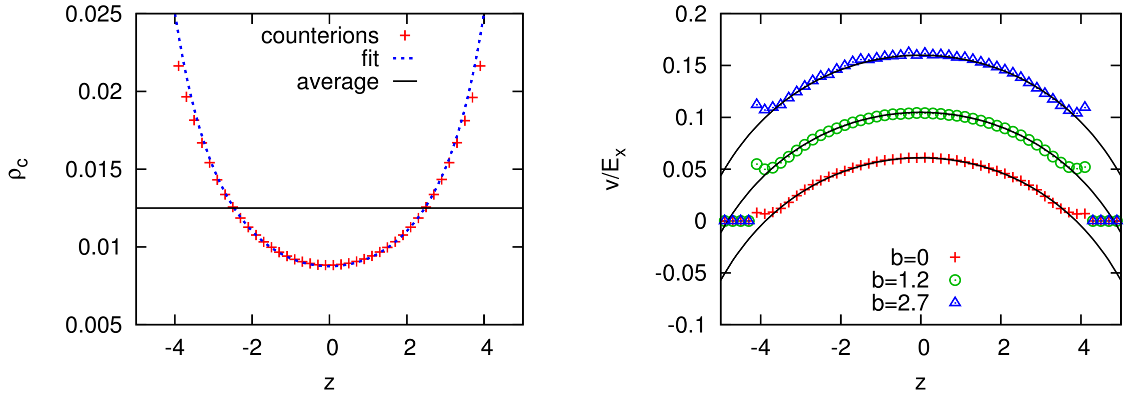

(a) (b)

Figure 3.1: Comparison to Poisson-Boltzmann theory. (a) shows the counterion distribution (PB result as blue dashed line), (b) the reduced flow velocity for three different slip lengths (with the PB results as black lines)

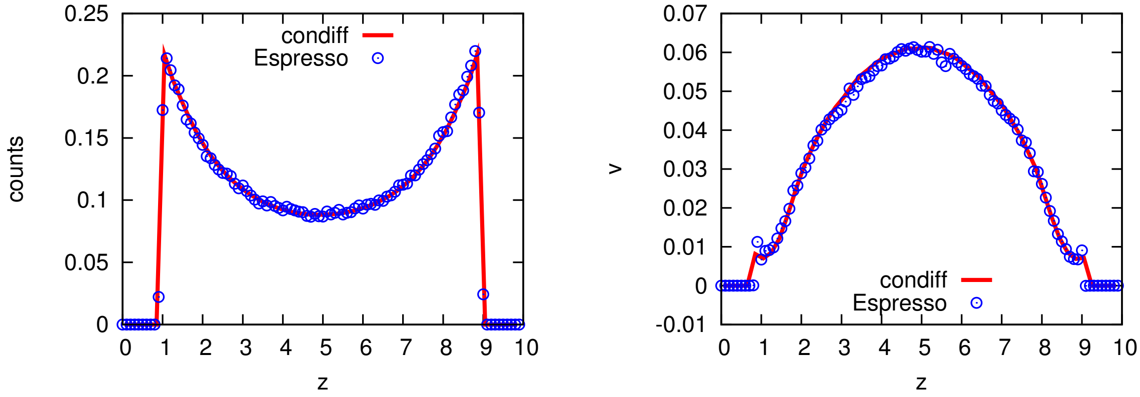

(a) density (b) velocity

Figure 3.2: Comparison of counterion-induced EOF run with condiff and ESPResSo. A system of size $10 \times 10 \times 8$ *with* $\rho_c = 0.0125$ *and an external field* $E = 1.0$ *has been studied. (a) shows the counterion profile, (b) shows the resulting velocity.*

The system is allowed to equilibrate first and then to reach steady-state flow within 200k steps with applied electric field. Thereupon we accumulate the charge and flow profile over a period of roughly 20M steps, writing out every 50 steps. The position of the hydrodynamic boundary measured from the channel center is $z_B = 3.88$. Both z_B and b were determined by additionally running plane Couette and plane Poiseuille simulations as described in chapter 5.2.2. All other parameters were kept at the standard values. After equilibration, the counterion distribution can be compared to the Poisson-Boltzmann result of Eq. 3.2. The only remaining fit parameter is the density in the center ρ_0.

Figure 3.1a shows that the profile overall agrees very well with the PB theory, with some deviations close to the boundaries. Here the actual character of the repulsion appears to be important. With the equilibrated system, the EOF is started by imposing an electric field $E_x = 0.1$. The field strength is chosen small enough to stay in the linear-response regime. After reaching steady state, all three flow profiles can be compared to their corresponding PB result of Eq. 3.4. There is no fit parameter, as ρ_0 has been determined in Fig. 3.1a. Figure 3.1b indicates that all three flow profiles agree nicely with the theoretical prediction. During this study it became apparent that small uncertainties in b, z_B and η_s can lead to systematic deviations in the magnitude of $5 - 10\%$. Hence the parameter set has been determined separately for each of the three cases.

3.2.3 Comparison to ESPResSo

Many of the simulations performed with the condiff program have been accompanied by test simulations with the software package ESPResSo, to check for consistency and clarify possible differences to explicit-ion simulations. Figure 3.2 shows the comparison for the counterion-induced EOF, as presented in the previous paragraph. Both the counterion distribution and the resulting flow profile agree nicely.

3.3 EOF in the Presence of Salt

The test case can be extended to salt solutions by adding cations and anions. While there is no exact analytical formula in the Poisson-Boltzmann limit for this case, an approximation in the Debye-Hückel limit and with the limitation to no-slip boundary conditions yields [90]

$$v_x(z) = -\frac{\varepsilon_r \zeta}{\eta_s} E_x \left(e^{-\kappa(z+z_B)} + e^{-\kappa(z_B - z)} - 1 - e^{-2\kappa z_B} \right) \quad . \tag{3.5}$$

Here ζ is the zeta potential of the surface and κ is the regular inverse Debye length. We try four different salt concentrations with a net charge density of $\rho_{\text{net}} = 0.0125$ to mimic the charged surfaces: $\rho_{\text{salt}} = 0.0125$ (100 coions, 200 counterions, $N_q = 10$), $\rho_{\text{salt}} = 0.03125$ (250 coions, 350 counterions, $N_q = 10$), $\rho_{\text{salt}} = 0.06875$ (550 coions, 650 counterions, $N_q = 10$) and $\rho_{\text{salt}} = 0.08125$ (650 coions, 750 counterions, $N_q = 10$). For the high salt concentrations the electric field has to be increased accordingly due to the low net charge and the high screening inside the channel. Otherwise the flow would be hidden in the thermal fluctuations and much longer runtimes would become necessary.

The results shown in Figure 3.3 indicate a good qualitative agreement, whereas quantitatively the theoretical prediction underestimates the flow, similarly to the results in [90] for explicit-ion simulations. Also, the typical plug-flow profile for the high concentrations is more pronounced in the simulation data than in the theory.

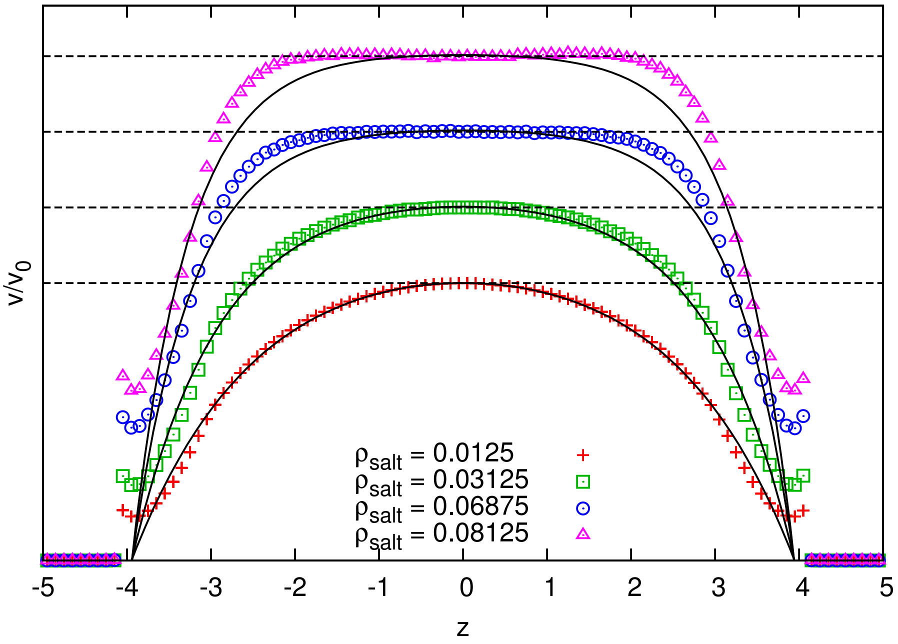

Figure 3.3: Normalized flow profile for various salt concentrations and corresponding results of Eq. 3.5. The scale has been changed for each curve to enhance the visibility, starting at 0 and with the dashed line representing unity.

3.3.1 Comparison to ESPResSo

Next we perform a quantitative comparison to explicit-ion simulations for EOF in the presence of salt. For this purpose we pick a system with a penetrable volume of $V = 10 \times 10 \times 16$, with the boundaries positioned at $z_1 = 0$ and $z_2 = 18$. 6130 DPD particles lead to a DPD density of $\rho_{\text{DPD}} = 3.83125$, and a surface charge of $\sigma = 0.25$ is put onto the boundaries by means of frozen charge units. The slit is filled with ion concentrations of $\rho_- = 0.05625$ (90 counterions) and $\rho_+ = 0.025$ (40 coions). We apply an external field of strength $E_x = 1$ and choose no-slip boundary conditions by setting $\gamma_L = 5.26$. The resulting flow is plug like, which simplifies the determination of the mobility. For the simulations performed with ESPResSo we adapt the DPD density as explicit ions additionally count to the total density.

In [21] Smiatek et al. derived a relation between the flow velocity and the occurring electrostatic potential $\Phi(z)$

$$v_x(z) = \frac{E_x}{4\pi\eta_s}\Phi(z) + v_{\text{EOF}} \quad , \tag{3.6}$$

which allows us to compare in detail the electrostatic conditions inside the slit and the resulting solvent flow. There is a second relation regarding the mobility

$$M_{\text{EOF}} = v_{\text{EOF}}/E_x = -\frac{1}{4\pi}\Phi_B/\eta_s \quad , \tag{3.7}$$

with $\Phi_B = \Phi(z_B)$ the potential at the hydrodynamic boundary, i.e. the zeta potential. We determine $\Phi(z)$ by measuring the electrostatic field inside the slit with the help of a test charge, and then integrating the profile starting from the center of the slit. Figure 3.4 shows a comparison of the ion and charge profiles in the slit for the condiff algorithm using the Euler scheme with ESPResSo. In both cases there is charge neutrality in the center of the channel, however the distribution of ions adjacent to the boundaries differs. The net-charge profiles in (b) show that while the ESPResSo system has a higher net charge close to the boundary, there is a slightly higher net charge in the range $[-7 : -5]$ in the condiff case, before both approach zero in the center of the slit. The resulting plug flow profiles are shown in Figure 3.5, where a significant deviation for the mobilities is visible. This shows that minor changes in the charge profiles can already lead to considerable differences in the resulting flow. By determining v_{EOF} and with the help of Eq. 3.6 we can compare the electrostatic potential to the velocity profiles. Even though the two simulation methods lead to different flow profiles, both seem to be consistent with the theoretical prediction. Figure 3.5b shows the electrostatic potentials, which mostly agree, except for the range close to the boundaries, where the actual type of surface charge begins to matter. Here point-charges lead to a strong increase. The results on Φ_B from Eq. 3.7 are drawn with straight lines, where we can thus compare with the position of the hydrodynamic boundaries, which is done in the blow-up. For the condiff simulation the prediction would be $z = 8.00 \pm 0.01$ (averaged over both sides of the slit), which agrees with an expected z_b of about $z_B = 7.9 \pm 0.1$. For the ESPResSo system the prediction is $z = 7.73 \pm 0.05$, which is slightly lower. The data obtained with ESPResSo still lacks statistics, as fluctuations are visible in almost all graphs, so that we expect an improved match for Φ_B and z_B with a larger sample. Yet the general context is still deductible and the consistency of potential and flow profile are visible in both simulations.

For a second test we chose the smaller channel used in section 3.2 for the counterion-induced EOF. At this point we also include a comparison of the Euler and Heun integration schemes for the condiff algorithm, as the resulting flow profiles differ. The discussion of the results can be found in the appendix in A.1.5.

3.4 Comparison to other DPD-based Methods

In the context of the DPD method, there have been two suggestions on how to introduce efficient electrostatic calculations. In principle, in explicit ion simulations one would usually add ions in the form of WCA-repulsive particles with a point charge. Those particles would also take part in the DPD interactions to couple them to the fluid flow and the local temperature. Then one would solve the electrostatics following a method of choice; mostly Ewald sum or particle-mesh techniques are used. This approach is what is called 'explicit ion simulations' throughout this work and is e.g. done with ESPResSo. Groot [9] in 2003 suggested a method that introduces mean-field electrostatics into a DPD liquid by setting up some DPD particles with smeared-out charges. The charges have to be smeared since the DPD particles have no hard-core repulsion and thus opposite charges would just collapse on top of each other. In his approach he also uses the conservative,

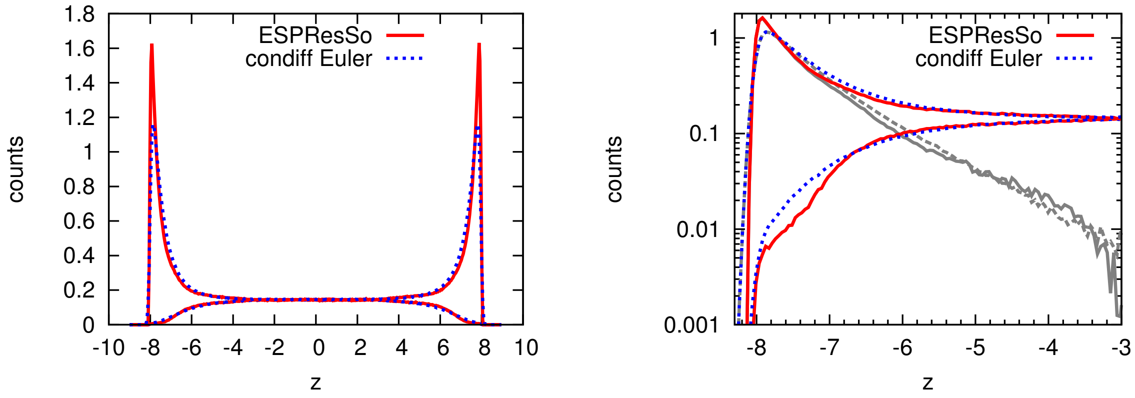

(a) (b)

Figure 3.4: Comparison of ion profiles inside the slit. (b) shows a blow-up of the boundary area, where the net-charge profile is shown by gray lines (dashed for condiff, straight for ESPResSo).

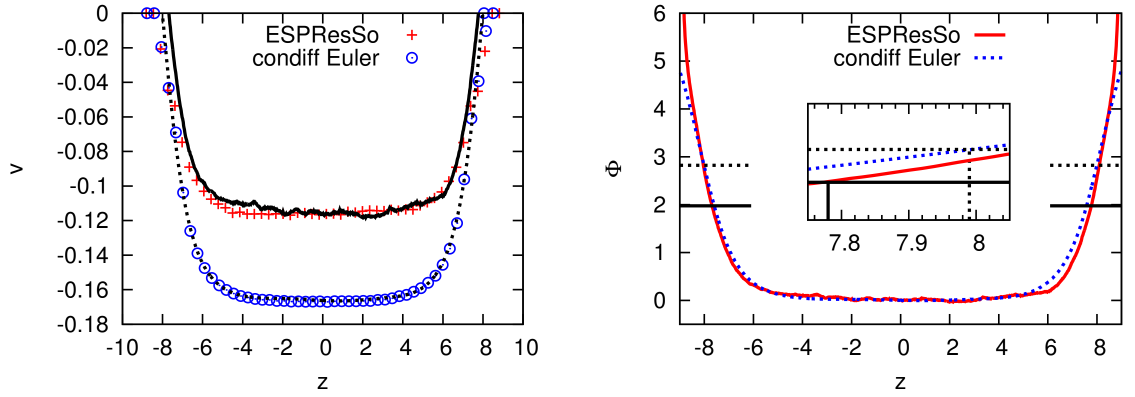

(a) (b)

Figure 3.5: Comparison of resulting flow profiles and electrostatic potentials. (a) shows the plug flow together with the prediction of Eq. 3.6, (b) shows the potentials, where the straight lines are the Φ_B values determined with Eq. 3.7 from the mobilities.

repulsive DPD interactions, since the goal is to mimic explicitly the behavior of water. He chooses a method to solve the electrostatics that goes back to the paper of Beckers et al. [109]. The mesh part is calculated in real-space by a successive overrelaxation scheme (SOR) instead of a Fourier-space approach. The short-ranged real-space part is replaced by the DPD conservative interaction with appropriate parameters. The biggest advantage of the SOR scheme is that it automatically incorporates dielectric inhomogeneities inside the system, as the dielectric constant ε enters locally. Thus it is especially useful for simulations of interfaces. The disadvantage is that SOR schemes are relatively costly in terms of computational effort. The other method was published by González-Melchor et al. [10] in 2006. Here the authors follow the same concept, but choose an Ewald sum approach to the electrostatics. Due to the same problem with the point-charge description they introduce a smearing function for the charge and approximate the resulting real space interactions.

In both of these methods there is a strict coupling of charge to a specific DPD particle. This is not the case in the condiff method presented in this study. In principle the charge-density field and the solvent are independent quantities. Thus we are also able to choose the diffusivity of our pseudo-ions independent of the properties of the DPD fluid, which can be an advantage in certain situations. Out of the test cases they present, we here want to focus on two of them, namely the distribution around a single charged plane and a simple bulk electrolyte.

3.4.1 Single Charged Plane in a Salt Solution

First we consider a periodic system of size $10 \times 10 \times 20$ with a single charged plane at $z = 10$ and surface charge density $\sigma = -0.1$. The plane has no repulsive interactions and is modeled by a set of a hundred frozen charged particles aligned in an array. The system is filled with DPD particles at a density $\rho_{\mathrm{DPD}} = 3.0$ and with a salt solution, $\rho_+ = 0.015$ (30 counterions) and $\rho_- = 0.01$ (20 coions). Due to the periodicity this system is almost equivalent to the slit channel considered in section 3.2 for the EOF. However, the periodicity and the missing repulsive character of the wall will inherently produce deviations, especially close to the plane.

To compare the electrostatic potential Φ, we use a test particle to measure the electric field in the equilibrated system and average over the whole sample, measuring every 50 steps of 7.5M steps runtime after equilibration. From the Poisson-Boltzmann theory one knows that the potential should have a structure

$$\Phi(z) = a \exp(-\kappa z) + a \exp(\kappa(x - 20)) + \Phi_\infty \quad . \tag{3.8}$$

Here a is the amplitude of the potential and κ is the resulting inverse screening length. These parameters are obtained by fit. However, as we only obtain the electric field, we use

$$E(z) = +\kappa a \exp(-\kappa z) - \kappa a \exp(\kappa(x - 20)) \quad . \tag{3.9}$$

The result for the screening parameter is $\kappa = 0.571 \pm 0.005$, in agreement with Groot's result. Figure 3.6 shows the electric field and the fit from which κ has been obtained. The ion distributions should follow an exponential in the form $\rho_+ = c \exp(-\Phi(z))$ and $\rho_- = c \exp(\Phi(z))$. The constant c can be obtained from the mean salt concentration far away from the single plane, in this case in the range $6 < z < 14$. The result $c = 0.01184$ again resembles Groot's result. Now one can take the logarithm of the ion densities to compare them to the potential in the form $-\log(\rho_+/c) = \log(\rho_-/c) = \Phi$. The result is shown in Figure 3.7, where it shows that they clearly agree very well.

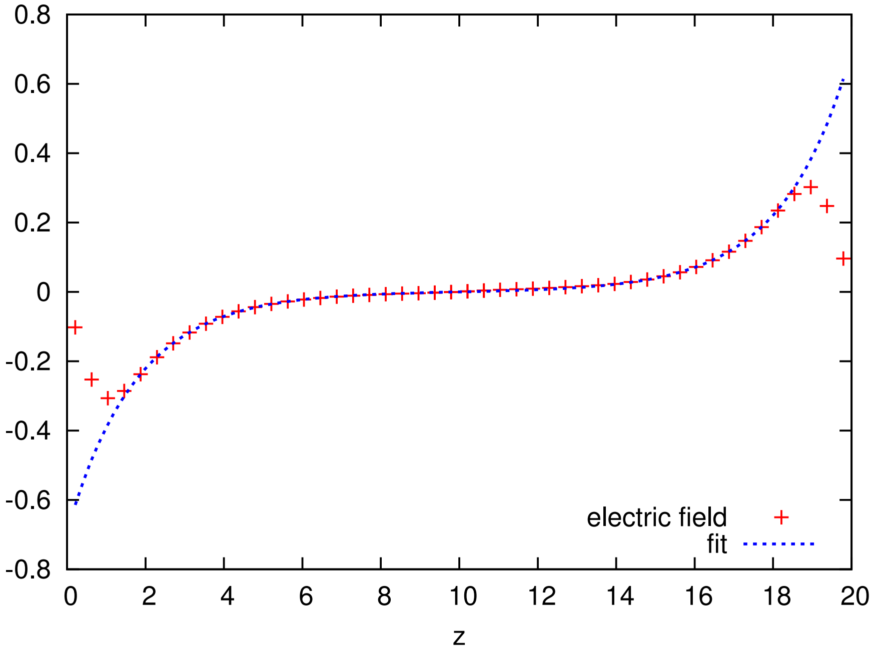

Figure 3.6: Electric field and fit by Equation 3.9 for a single charged plane in a salt solution. Deviations start to increase close to the boundary.

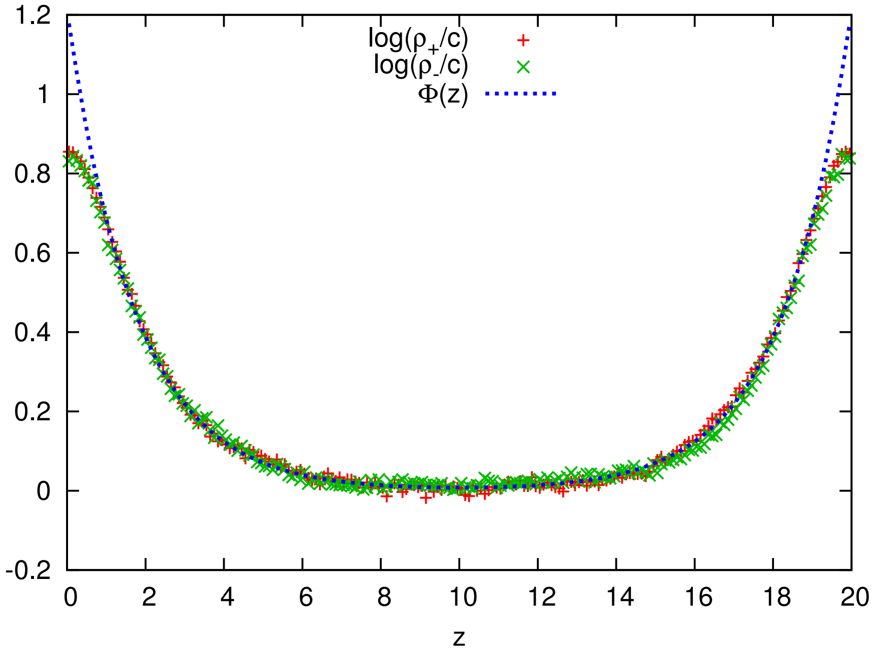

Figure 3.7: Potential and logarithms of ion densities in the single plane system.

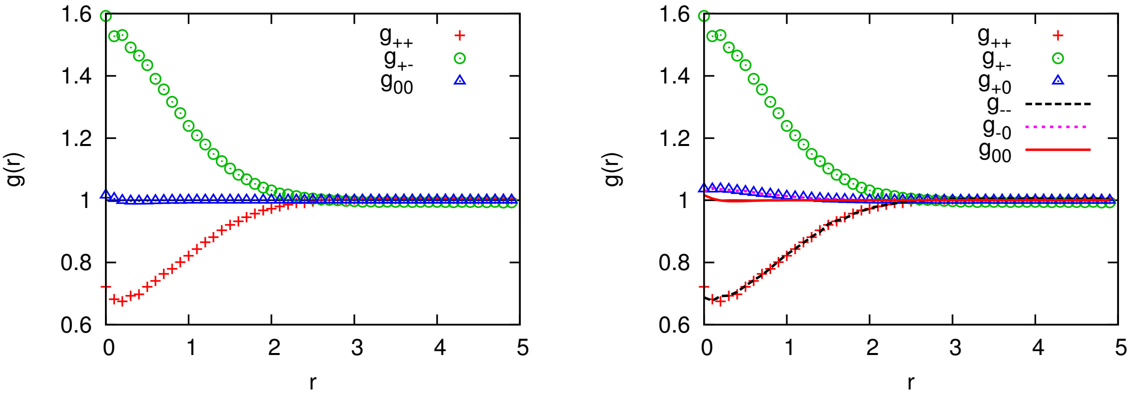

(a) (b)

Figure 3.8: Radial distribution functions for a bulk electrolyte. (a) shows the correlation between fluid particles, equally charged and oppositely charged particles. (b) shows a collection of all RDFs.

3.4.2 Bulk Electrolyte

In the bulk electrolyte Groot specifically looked at the correlation relations of the ion species and solvent particles. Therefore a direct comparison is not possible, as we not only neglect all ion correlations but also do not use any conservative DPD interaction. Thus we can show with this test case that indeed there is no correlation. Figure 3.8a shows the radial distribution function (RDF) for DPD particles (g_{00}), the positive charge RDF (g_{++}) and the cross-RDF between oppositely charged particles (g_{+-}) for comparison with Groot's result. In (b) all RDFs are shown together. The DPD particles (g_{00}) show no increase in the RDF at all except for a small deviation close to $r = 0$ which is also noted in [110]. Thus they are distributed totally homogeneously in the bulk. There is a small increase in g_{+0} and g_{-0}, i.e. a small increase if DPD density close to a charge. This corresponds to the fact that the DPD particles represent the full density and not only the solvent itself, as also described in section A.4 about the boundary effects.

3.5 Performance Test

One major objective in developing the algorithm was to gain efficiency for simulations of mesoscopic systems with high salt concentrations compared to standard coarse-grained MD simulations. When speaking about performance, however, one nowadays also has to deal with parallelization. While in principle the parallelizability of the algorithm should be comparable to plain MD algorithms, in this study we have no intention to compete with highly optimized parallel MD codes. On the other hand, the focus of this study lies on studying rather small systems. Such systems contain particle numbers of certainly below one million, roughly saying more in the ten thousands. Thus single core runs, or shared-memory parallelized runs are applicable.

In order to measure the performance of the algorithm, we compare it to the ESPResSo software package, which is a widely used program in soft matter. For a detailed comparison we create three model systems and run each simulation for ten thousand time steps in single-core mode.

1. **pure DPD solvent**
   - $V = 10 \times 10 \times 10$
   - 3750 particles
2. **monovalent salt solution**
   - $V = 10 \times 10 \times 10$
   - 100 cations/anions
   - $\kappa_D = 1.585$
   - condiff: 3750 DPD particles
ESPResSo: 3550 DPD particles
   - condiff: pm with grid $12 \times 12 \times 12$, cao 3
ESPResSo: optimized P3M, accuracy 0.01
3. **confined polyelectrolyte solution**
   - $V_{\text{box}} = 10 \times 10 \times 17$
   - boundaries at $z = 0$,$z = 12$
   - $V_{\text{accessible}} = 10 \times 10 \times 10$
   - 10×10 charged monomers
   - harmonic bonds $K = 30$, $R = 2^{1/6}$
   - monomer WCA repulsion, $\sigma = 1$, $\varepsilon = 1$
   - 50 coions
   - 150 counterions
   - condiff: 3750 DPD particles
ESPResSo: 3550 DPD particles
   - condiff: PM with grid $12 \times 12 \times 20$, cao 3
ESPResSo: optimized P3M, accuracy 0.01
   - ELC on, accuracy 0.01

In the ESPResSo systems we decrease the DPD particle number according to the amount of ions, as those are real particles. Also, ions and monomers interact via the WCA potential with standard parameters. ESPResSo's P3M is optimized with the "tunev2" command, and there is an additional warm-up time with capped forces for the ESPResSo systems, as the WCA repulsion may be too strong initially. The tuning is

	pure DPD	salt solution	confined polyelectrolytes
condiff Euler	33.2s	55.1s	60.0s
condiff Heun	33.1s	58.7s	66.3s
ESPResSo 3.0.2	45.3s	93.2s	164.5s
ESPResSo 3.1.1	45.0s	74.8s	99.7s

Table 3.1: Runtime results for 10k steps with condiff and ESPResSo. All times are averaged over 20 samples and initialization times are subtracted.

performed several times to obtain the best result. As there has been an improvement in the electrostatics algorithm for ESPResSo in the newer versions, we also compare to an older version (3.0.2) that resembles the state at the beginning of this study. The accuracy for the P3M was chosen to be 0.01 as the condiff algorithm obtains a similar accuracy (although not for point particles of course). The Verlet skin or neighbor-list cutoff was set to 0.4 for all systems.

Since ESPResSo usually takes longer to initialize the simulation, we subtract the initialization-time, which is measured separately. An average of 20 runtime measurements is performed with the UNIX command “time” (user time), which is accurate enough for the time scale expected for 10k steps. The test computer is an Intel Core i7 860 at 2.8GHz, with 16GB memory. We use GCC 4.4.3 for compilation with the “-O3” flag.

The results shown in Table 3.1 state that for the condiff program already the pure DPD system is much faster, which can be a result of the way it is implemented. Another reason could be that the way ESPResSo is written is to incorporate a much higher load of additional features. Those were not activated for this purpose, however, the general structure may influence the performance. For the salt system we see that the difference between Euler and Heun is quite small, which shows that the main effort is related to the DPD particles. Additionally to the runtime necessary for the 10k DPD steps, the velocity assignment takes a large part. The difference to ESPResSo 3.0.2 is quite high, which takes about 160% in comparison to Heun and 170% in comparison to Euler. The newer version of ESPResSo performs much better, as it saves almost 20s. Still the condiff program is faster in total and also if one compares the pure runtime required for the salt (by subtracting the pure DPD times). In the polyelectrolyte system the difference between Euler and Heun becomes more apparent, as the additional boundary interactions and especially ELC sum up. A 10% gain in speed is possible by reducing the algorithm to Euler. The comparison to the old ESPResSo is quite dramatic. The condiff program saves a factor of 2.5 (2.7 respectively with Euler) in runtime. The factor becomes even larger when subtracting the pure DPD time. However, the difference becomes much smaller for the new version, which performs about 50% (66%) worse than the condiff program.

This shows that the condiff algorithm is capable of outperforming explicit ion simulations when going for high charge concentrations. This measurement also illustrates the motivation for new electrohydrodynamic simulation methods, as the runtime increase for such small systems with charge concentration is quite high. When the work on the

	Euler	Heun
DPD	30%	22%
neighbor lists	19%	17%
condiff step	46%	51%
assign velocity grid	15%	14%
assign force to DPD	14%	13%
electrostatics	9%	17%

Table 3.2: Runtime profiling of the condiff algorithm with Euler and Heun scheme. The profiling was done with valgrind's callgrind option for runtime of 1k steps.

condiff algorithm was started in 2010, ESPResSo was in version 2.2.0b, which we also benchmarked for the salt solution. The result was 111s, i.e. even much slower than the version 3.0.2. The improvement in ESPResSo is partly due to the adapted distribution of computing time to the real-space and k-space part. By decreasing the real-space cutoff to a value that is similar to the other interaction cutoffs in the system, the neighbor lists are much smaller and hence the real-space contribution produces less overhead in comparison to the condiff algorithm.

In Table 3.2 we show the results of a code profiling. With the "callgrind" option of "valgrind" one can get an overview of the internal time distribution of the code. Here we ran the polyelectrolyte system for 1k steps. With the Euler scheme, the DPD takes up to 50% of the runtime, as the neighbor lists are mainly for the DPD algorithm. The condiff step takes about 46%, but still the main part of it is related to the DPD particles, as the velocity grid assignment and the force assignment to the DPD particles takes 29% (of those 46%) themselves. A similar picture shows up for the Heun scheme. Here, however, the electrostatics with 17% take a larger part than in the Euler case with only 9%. The electrostatic layer correction takes 2.2% for Heun and 1.2% for Euler. However, this value is largely particle number and accuracy dependent, and can easily range to times comparable to the particle-mesh electrostatics itself.

3.5.1 Performance on Electro-osmotic Flow Simulations

Besides the benchmark with the model systems, we also did comparisons in the actual applications of the algorithm. The simulations performed for the electro-osmotic flow over superhydrophobic surfaces described in chapter 5 were quite demanding due to the large system size required and the amount of charges involved to obtain an appropriate screening length. While we performed the simulations in shared-memory parallelized form, we also did some comparisons between serial runs with the condiff algorithm and ESPResSo. From a sample of 10 runs we averaged the runtime for 1000 steps. The results are shown in Table 3.3. As the DPD implementation in the condiff program is already faster than the one in ESPResSo, we show the runtimes for a system without electrostatics as well. The P3M in ESPResSo was tuned to an accuracy of 10^{-2} to keep it comparable with the condiff accuracy. As the optimization of the P3M parameters is very crucial for the runtime, we performed the tuning several times to ensure that we

	condiff method	ESPResSo 3.1.1
full	545s (15%)	3519s (100%)
uncharged	371s (11%)	506s (14%)

Table 3.3: Runtime comparison for 1000 steps, averaged over 10 runs on a AMD Opteron(TM) Processor 6272, 2100MHz machine. Runtimes of the pure DPD system are shown for comparison. All runtimes are single-core and without analysis and initialization time.

have the best parameter set.

The comparison shows that one gains a factor of six in speedup with the condiff method. The pure improvement in the electrostatics part is about 17×. This result should be representative for studies of rather large systems, which nowadays become more and more common, as complexity increases. Thus the result underscores the importance of improving and developing new efficient algorithms for electrohydrodynamics to reduce computational cost and make large, complex systems accessible.

3.6 Further Performance Improvements

The test with different parameter sets and the comparison of the Euler and Heun scheme have shown that slight performance improvements are possible within the condiff algorithm. However, as the profiling in the previous section has shown, the pure DPD calculations (interactions + neighbor lists) take about 50% of the computation time. Thus even with an improvement on the condiff side, the algorithm would always be limited by DPD as the current bottleneck. This is somewhat the reverse situation from what we were starting out with in the beginning. Except for the particle-mesh and the DPD part, the current source code of the condiff program is not yet optimized. Thus a small improvement in the magnitude of $\leq 10\%$ appears possible.

3.6.1 Ballistic Time Regime

Ironically the DPD particles also take the largest time in the condiff part, due to the velocity grid assignment and the force coupling. The former with a percentage of 15%, however, can be reduced systematically in equilibrium situations. As mentioned in chapter 2.3.1 and shown in Figure 2.3, the DPD particles enter a ballistic regime that lasts for about 50 time steps with presumably constant local velocity. Thus one could calculate the velocity grid only every next time step, e.g. every 40th, so that the computational effort would reduce to $1/40 \cdot 15\%$. Attempts with this ballistic velocity grid have been made. However, it turned out that in non-equilibrium situations, e.g. in an external electric field, the force transfer to the DPD particles became inconsistent and momentum was lost. The reason is that the force coupling requires an up-to-date DPD density grid, to normalize the forces correctly. Yet the DPD density grid is assigned together with the velocity grid, as it takes the same effort. Also, problems with the ballistic-regime reduction or any other kind of assignment reduction occur if WCA-repulsive boundaries

system	Heun	Euler	grid-based	grid-based 2x mesh
salt solution	87s	81s	61s	101s
polyelectrolyte slit	103s	92s	69s	138s

Table 3.4: Overview of performance results for the condiff algorithm with a Heun and an Euler scheme in comparison to a grid-based approach. The runtime for 10.000 steps was measured on an AMD Opteron(TM) 6272 processor at 2100MHz. On the grid-based runtimes, charge and force assignment times have been subtracted.

are included. Due to fluctuations close to the vacuum layer an up-to-date density profile is essential for the normalization.

3.6.2 Reduced Assignment Order for DPD

The most direct solution to reduce the assignment time of the DPD particles would be to minimize the corresponding assignment order to cao 1 without changing the pseudo-ion cao. With the standard parameters, there would be about 2 DPD particles per cell, i.e. there might be grid points without any DPD velocity/density assignment. Therefore one could for instance increase the pseudo-ion assignment order appropriately to ensure the coupling, which does not lead to much computational overhead. The approach of different assignment orders could, however, be problematic because of momentum conservation. No attempts have been made in this study to investigate in this direction.

3.6.3 Grid-based Approach to the Convection-Diffusion Equation

A more drastic possibility for a performance improvement would be to remove the pseudo-particle description of the ion-density fields and represent them on a grid, similar to [12]. Without implementing such a solver, we can model it by reducing the charge assignment order to 1. This way the particles contribute to only one node, i.e. they behave for the electrostatics as if they were on the grid, but they can still move freely. Then, by removing the overhead produced by the assignment, one has a good estimate for the pure-grid method. However, the velocity assignment from the DPD particles will in this approach still be necessary.

A good estimate for the assignment overhead can be achieved by comparing profiles created with the “callgrind” option of “valgrind” on a short run of the system. As explained in chapter A.2, a lower charge assignment order should be accompanied by a higher grid resolution, as the electrostatic forces otherwise are too approximative. Thus we start a second run of the grid-based systems with the mesh size doubled. The results in Table 3.4 show that a switch to a grid-based method could indeed lead to a significant performance improvement of around 1/3, however, with the result of a lower accuracy. Increasing the grid resolution also increases the computation time drastically, such that a doubling already exceeds the condiff time. Hence a particle-based algorithm can perform better than a grid-based algorithm, as one can choose a smaller grid for the Poisson solver and balance it by a higher charge assignment order.

3.7 Summary and Outlook

With Regards to Explicit-Ion Simulations

During the course of this study the condiff algorithm with its dynamic mean-field treatment of charges has proven to perform well in applications that were typically suited for explicit-ion simulations. Its performance and accuracy are very satisfactory, always in comparison to the latter. With the new tuning version of P3M in ESPResSo (current version 3.1.2) the real-space calculations are generally reduced and more load is put into the FFT calculations, thus also reducing the interaction ranges and the size of the Verlet lists. All this considerably improves the performance of explicit-ion simulations and hence simultaneously diminishes the speedup gained by the condiff method. With everything put into perspective, the condiff algorithm is still faster, which especially showed during the simulations performed for the electro-osmotic flow on superhydrophobic surfaces in chapter 5.

Another advantage of the condiff algorithm over explicit-ion simulations is that it does not require excluded-volume interactions for charges. If ions are considered as point charges, they require an excluded volume interaction to prevent overlapping. However, this usually makes the ions artificially large, as particle diameters cannot be reduced much below unity. A side effect is that unphysical layering can occur, whenever strong charge concentrations appear, such as close to charged boundaries. Also the mismatch in particle sizes could in principle have artificial effects on the behavior of macromolecules. The pseudo character of ions in the condiff method also leads to much shorter equilibration times, where system warm-ups with capped interactions are only necessary for very concentrated polymer solutions. A drawback of the condiff method is that it is not capable of simulating conditions under which strong correlations become important, e.g. in electrolytes containing multivalent ions at low concentrations.

With Regards to Other Methods

Besides the explicit-ion methods, other effective methods have been proposed in the recent past, which we want to separate into three categories. The first-category methods differ in their treatment of solvent and charges in either explicit/implicit manner. In the context of electrophoresis some methods neglect explicit ions and account for electrostatics in the Debye-Hückel approximation with an additional friction term in the coupling to a LB fluid [3], or by assigning an effective charge onto MPCD particles surrounding a charged bead [4]. A similar idea has also been introduced for DPD [5]. Other approaches include coupled continuum-particle methods [6] and implicit solvent models [7, 8]. In strong contrast to all these methods the condiff algorithm includes full hydrodynamics and Poisson-Nernst-Planck level electrostatics, i.e. there is no assumption of equilibrated charge distributions.

Secondly, similar methods involving DPD in combination with smeared charges have been proposed [9, 10], which have been discussed in section 3.4. Here, the main difference is in their approach charges and DPD particles are joined directly instead of freely coupled. In contrast, the condiff algorithm allows for different ion diffusivities.

Thirdly, lattice-based solvers of the electrokinetic equations have been proposed, [11, 12]. Here, the still somewhat controversial coupling of macromolecules and colloidal particles could be seen as a drawback, as well as the implementation of boundaries. Both these points are relatively straightforward in a particle-based approach, such as the condiff algorithm. An additional disadvantage is that these methods do not account for thermal fluctuations, which limits their application to scales on which diffusion by Brownian motion is insignificant.

Possible Extensions

Of course the algorithm still allows for various extensions. To include the effect of dielectric contrast is certainly one possibility, which may especially become important at interfaces and boundaries. As an additional feature to the electrostatic layering correction ELC, which has been used throughout this work when dealing with quasi two-dimensional geometries, Tyagi et al. developed a correction to account for the image charge effect on boundaries with different dielectric constant [106]. This idea was then taken further to work in a universal way with different kinds of electrostatic solvers [107]. With these approaches it becomes possible to study the effect of dielectric contrast, especially in electro-osmotic flows. However, those corrections are more important in the case of multivalent ions and thus have not been accounted for in this work. In principle the particle-mesh electrostatics could also be combined with a successive-overrelaxation (SOR) scheme instead of the FFT solver, which allows for locally varying dielectricity, but is generally slower. Thus we come to the idea of varying dielectricities inside the solution, which also has its validity. In the current version of the algorithm the entire system is treated as if it had a homogeneous dielectricity ε. However, as the typical model would be an aqueous solution, polarization effects might occur depending on the local charge distribution. In the framework of self-consistent field theories this has recently been tackled [111]. The solvation energy of ions, which might not be constant due to the local behavior of the solvent is certainly also an important aspect [112, 113] that could be included into the algorithm in a future version.

CHAPTER 4

Polyelectrolyte Solutions

Even though polymer and polyelectrolyte solutions have been studied for several decades, they are still a topic of ongoing research, not only because of the manifold industrial applications of polymers. When speaking about solutions, various concentration regimes are of interest, starting with polymer melts and concentrated solutions with the focus on materials science, down to more dilute solutions with emphasis on DNA/RNA transport or drug delivery by transport polymers. Protein-folding is another biophysical problem that comes into play.

An important topic closely connected to polymers and polyelectrolytes is the concept of lubrication. The very fundamental question behind the scene is what makes something slippery. In nature, the answer often involves polymers and especially polyelectrolytes. Speaking in a more general framework, the addition of polymers to a liquid can alter the viscous behavior drastically. Concepts such as shear thickening and shear thinning come into play. The question of lubrication is maybe equally important for understanding biological mechanisms, such as the motion of joints, as in engineering applications, where optimizations of lubrication processes can lead to enhanced lifetime and stability of components as well as increased efficiencies [114].

Thus there is a strong motivation to characterize the rheology of solutions, for instance by means of simulations. The study of polymer solutions in non-equilibrium situations, i.e. flow or shear motion, leaves a wide parameter range to be explored. A multitude of experimental and simulational studies on the dynamics of polymers in solution have been performed, and theoretical approaches have been developed as well (e.g. [115, 116]). Special attention is paid to the comparison of the dilute and semidilute regime, including the concentration dependence of viscosity, described by the phenomenological Fuoss law. Similarly important is the direct comparison of neutral polymer and polyelectrolytes and the question of how the electrostatics change the situation, macroscopically as well as microscopically. Worthwhile to mention are the peak in the scattering function for semidilute polyelectrolytes and the different scaling of the correlation length and the relaxation times [117]. The addition of salt to the solution can lead to screening effects and should therefore work as a link between the two primary cases. However, multivalent ions can lead to rather different results, such as gelation processes [118].

From a theoretical and simulational point of view it is of strong interest to establish how important hydrodynamic interactions are under various circumstances, as well as whether approximations such as the Debye-Hückel or Poisson-Boltzmann electrostatics are applicable. The latter point is directly related to the role of counterions and their dynamics. In this context, it is important to mention the primary electroviscous effect, which is the contribution to the viscosity that originates in the deformation of the counterion cloud around a charged solute, e.g. a polyelectrolyte.

Many simulational studies of polymer rheology have been performed under bulk conditions, e.g. by means of Lees-Edwards boundary conditions [119, 27]. On the other hand people are also interested in bound systems with adsorbed polymers, such as polymer brushes and their lubrication effects [120, 121, 122, 123]. Before proceeding, we want to mention some references to former studies that stand in close relation to ours. To this date, simulations of polyelectrolyte solutions including fully the electrostatics and hydrodynamics are still somewhat rare, mostly due to the computational effort involved. Carrillo et al. [124] studied polyelectrolytes in equilibrium under addition of salt. Stoltz et al. [53] present studies of dilute polyelectrolytes under shear using Brownian dynamics with hydrodynamics and electrostatics by means of Ewald techniques. Large scale simulations of neutral-polymer rheology in semidilute solutions have been performed with the MPCD method [125]. One should also mention studies of single polyelectrolyte chains in Brownian dynamics [126], including hydrodynamics and Debye-Hückel electrostatics. Recent reviews of the theoretical and simulational side can be found in [47, 49]. Related experimental studies of the viscoelasticity of polyelectrolytes include publications such as [48], where the addition of salt [127, 128, 129] and dilute and semidilute solutions [130, 131] have been studied, as well as comparisons to scaling theories and the Rouse model [132] have been performed.

The condiff algorithm has an advantage over explicit-ion simulations in highly concentrated ionic systems, which is why the method is extremely suitable for the study of semidilute solutions, thus being able to fill the gap of simulational studies in this regime. Hereby we also show the applicability of the new method to the study of macromolecules in solution, which should motivate further studies in the near future. Lastly we want to clarify the role of electrostatics in the rheology of polyelectrolytes. We will therefore also conduct simulations of uncharged chains, as well as of charged chains with a so-called Yukawa potential, which resembles the Debye-Hückel electrostatics, so that we can compare directly to a model that does not incorporate counterion retardation effects. Contrary to bulk studies, we intentionally make use of boundary-induced shear flow but study pure solutions without tethering of molecules. The use of two opposite boundaries instead of periodic boundary conditions resembles the situation encountered for instance in thin films or joints. Thus we put the finite-size effects apparent in simulations to our advantage by concentrating on systems of such finite size.

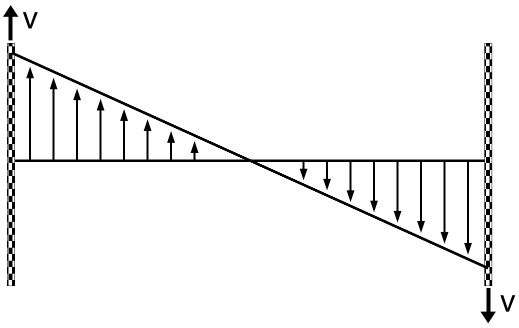

Figure 4.1: Illustration of the plane Couette flow.

4.1 Measuring the Shear Viscosity

We first describe the non-equilibrium simulation techniques used to study the polyelectrolyte solutions and determine their viscous behavior. The viscosity of a fluid can be measured by comparing its flow behavior to the theoretical predictions of certain model flows that have a simple nature. Similarly to experimental rheology, where viscometers may work with a linear flow profile or a capillary flow, those two flow types can also be used in simulations. The underlying principle is to measure both shear rate and stress to obtain the viscosity from the relation

$$\tau = \eta(\dot{\gamma})\dot{\gamma} \quad . \tag{4.1}$$

4.1.1 Couette Flow

The plane Couette flow is obtained when a fluid is confined between two planar and parallel boundaries that move with a velocity difference in opposite directions, thus creating a shear flow by dragging the fluid along. In the case of a homogeneous density, the resulting velocity profile is linear, as also described later on in section 5.2.2. The linear velocity profile leads to a constant shear rate

$$\dot{\gamma}(z) = \frac{\Delta v}{H} = const. \quad , \tag{4.2}$$

with Δv the velocity difference at the two hydrodynamic boundaries and H their distance. The stress can either be measured directly, i.e. with help of the virial theorem, or it can be calculated from the force the fluid exerts onto the boundaries

$$\tau = \frac{F}{A} \quad , \tag{4.3}$$

where the force acts in opposite flow direction and A is the boundary area. With the use of tunable-slip boundaries this force can be measured by accumulating the dissipative and random forces over a period of time, once a steady state flow has been reached

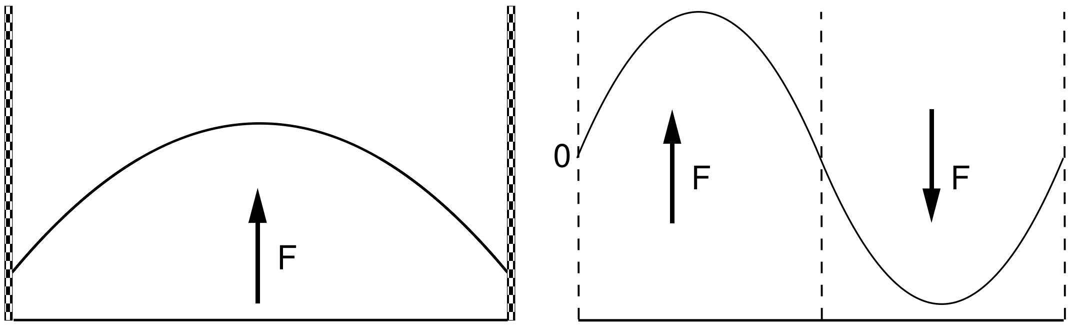

(a) Plane Poiseuille (b) periodic Poiseuille

Figure 4.2: Illustration of Poiseuille flow with and without boundaries.

$$\eta = \frac{FH}{A\Delta v} \quad . \tag{4.4}$$

Couette flow can also be artificially imposed by the usage of Lees-Edwards boundary conditions [119, 27]. This is of advantage when studying bulk properties, as no boundaries are required. However, the stress then has to be calculated on its own terms, which is challenging for long-range interactions. In the case of particle-mesh electrostatics it also requires an adaption of the rectangular mesh to the deformed periodic images.

4.1.2 Poiseuille Flow

Plane Poiseuille flow is obtained when imposing a parallel, constant force on a fluid confined between two plates. We define the geometry such that the confinement takes place in z-direction and the force acts in positive x-direction. In the case of a homogeneous density the resulting velocity profile is parabolic for Newtonian liquids. An alternative geometry without any boundaries can be constructed by splitting the simulation box in half and imposing the same force in two opposite directions [89]. The resulting flow profile can then in principle also be averaged over both flow directions. In this method, the boundary condition obtained at the interfaces is no-slip, as the velocity intercepts zero to change signs.

With a non-parabolic velocity profile for a non-Newtonian fluid, also the shear-rate profile becomes nonlinear. Thus it must be calculated by derivation

$$\dot{\gamma} = \frac{\partial v(z)}{\partial z} \quad . \tag{4.5}$$

The stress profile can be calculated from a virial expression [133] by considering the local velocity and force distribution. However, the original formulation requires all interactions to be pairwise. In our case, however, the electrostatic force is a mean-field force and thus has no pairwise shape. With a different formulation of the stress/pressure tensor and by taking into account the proper symmetry, i.e. we are only interest in a

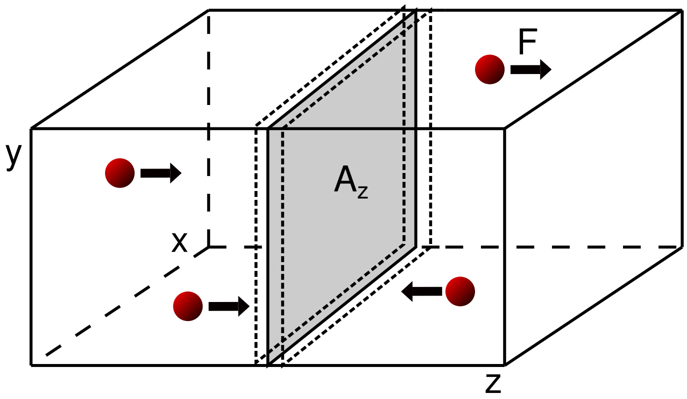

Figure 4.3: Illustration of the stress measurement in slabs across the system. The kinetic contribution comes from particles present in the volume around the plane A_z, while all particles contribute to the force part by whether they are left or right of the plane.

one-dimensional profile of the stress, the required components of τ can be calculated following [134, 135]

$$\bar{\tau}_{xz}(z) = \frac{1}{2A_z\Delta z}\left\langle \sum_{i\in(\Delta V=2A_z\Delta z)} m_i v_{ix} v_{iz} \right\rangle \tag{4.6}$$

$$+ \frac{1}{2A_z}\left\langle \sum_{i=1}^{N} F_{ix} sgn(z_i - z) \right\rangle \quad . \tag{4.7}$$

The equation is illustrated in Figure 4.3. All particles are either on the left or right side of a plane A_z and thus contribute with the corresponding sign to the force part of the virial sum, while the particles in a small volume around A_z of width $2\Delta z$ contribute with their velocity as well. Finally the time averages are taken to obtain the mean stress profile. In the case of the condiff method only the DPD particles and monomers have to be considered, as the condiff particles themselves are of pseudo character. Thus the electrostatic contributions are included through the transmission to the DPD particles.

At this point we note that the original formula (Eq. 19 in [135]) is valid for $\tau_{xz}(z)$, while we need $\tau_{zx}(z)$. In most situations, the stress tensor is symmetric, i.e.

$$\tau_{zx} = \tau_{xz} \quad . \tag{4.8}$$

On the particle level this becomes apparent when considering the different interactions, which are in principle isotropic.

In practice the Poiseuille procedure to calculate the shear viscosity works mainly as outlined in [136]. First the obtained stress is compared to the expected linear profile for Poiseuille geometries. The velocity profile is fitted by cubic splines and even-order polynomials to calculate the first derivative as in Eq. 4.5. The shear-viscosity is then

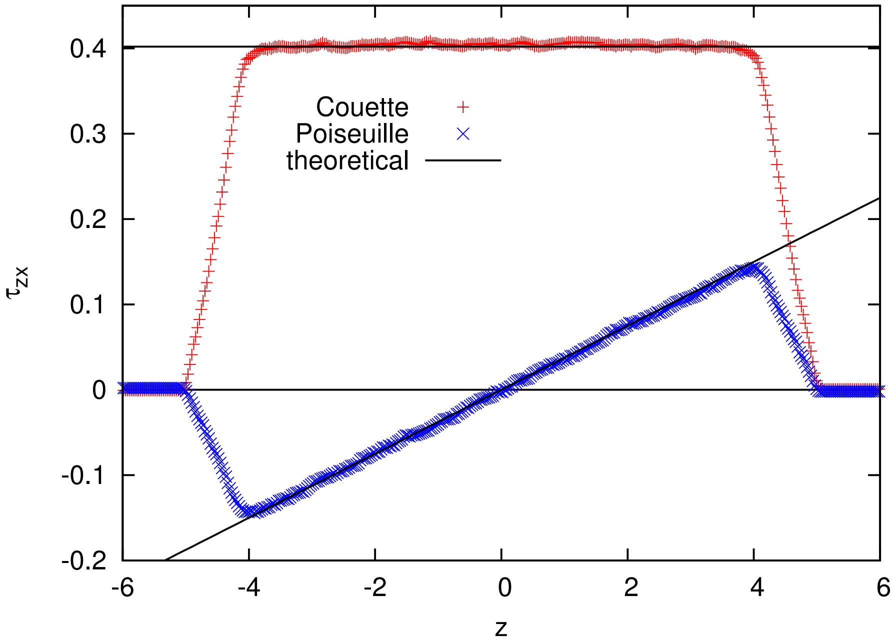

Figure 4.4: Stress component τ_{zx} for a Couette and a Poiseuille flow of a pure DPD fluid.

obtained with the use of Eq. 4.1. For the stress it is of advantage to work with the theoretical relation in Eq. 4.10 instead of the measured profile to decrease statistical fluctuations.

The advantage of the Poiseuille geometry is that one can cover a wide range of different shear rates with just one flow profile. On the other hand the Couette geometry requires only the information about the boundary force to calculate the viscosity, as the shear rate is imposed and deviations cancel out as a system average is taken. Thus both methods are legitimate to use, which allows us to compare the results.

Testing the Stress Measurement

Prior to applying the stress formalism to the Poiseuille flow, we consider a test case of a pure DPD fluid in confinement, applying both a Couette and a Poiseuille flow. For the simple DPD fluid, the stress can be calculated from the shear rate due to the Newtonian behavior. In the Couette flow we obtain a constant stress

$$\tau_{zx}(z) = \eta \frac{\Delta v}{H} \quad , \tag{4.9}$$

and for the Poiseuille flow the stress profile should be linear

$$\tau_{zx}(z) = F\rho z \quad . \tag{4.10}$$

The results are compared to the predictions in Figure 4.4. In both flow geometries the calculated stress agrees with the theory, thus confirming Equation 4.6.

4.2 Polyelectrolyte Model

In thus study the polyelectrolytes are described by bead-spring chains of length $N_m = 20$ with a charge fraction of 1, i.e. every bead is charged with $q = -1$. The beads interact via a WCA repulsion with $\sigma = 1$, $\varepsilon = 1$ for the excluded volume interactions and are connected by a harmonic spring with the parameters

$$r_0 = 2^{1/6} \approx 1.1225 \tag{4.11}$$

$$K = 30 \quad . \tag{4.12}$$

With this parameter set it is ensured that there is no chain crossing. All monomers take part in the DPD interactions and are penetrable by the ideal-gas DPD particles. They are accompanied by the appropriate amount of counterions, represented by pseudo-particles with $z_c = 1$, to ensure charge neutrality. Additionally, we can add salt by introducing coions and increasing the counterion concentration.

4.3 Single-Polymer Properties

Before investigating the full solution, we consider single polyelectrolytes to collect their equilibrium properties. Therefore we run a simulation of a polyelectrolyte and 20 counterions in a system of size 25.2^3 with fully periodic boundary conditions, which corresponds to a concentration $c = 0.00125$ ($\approx 1/40$ of the pure solution described below). The simulation ran for about 2M steps for equilibration and another 7M for sampling. We determine the end-to-end distance R_e, the radius of gyration R_g, the hydrodynamic radius R_h and the bond length b

$$R_e = 11.823 \pm 0.008 \tag{4.13}$$

$$R_g = 4.312 \pm 0.002 \tag{4.14}$$

$$R_h = 3.730 \pm 0.001 \tag{4.15}$$

$$b = 1.2683 \pm 0.0001 \quad . \tag{4.16}$$

With the single-polymer data, we can determine the overlap concentration (in monomers) for the solution according to Eq. 1.49

$$\text{from } R_g \quad c^\star = 0.0596 \tag{4.17}$$

$$(\text{from } R_e \quad c^\star = 0.0029) \quad . \tag{4.18}$$

	N_{pol}	N_{mon}	N_+	N_-	N_{DPD}	c	κ	ρ
pure	80	1600	1600	0	120k	0.053	0.813	4.000
uncharged (**un**)	80	1600	0	0	120k	0.053	0.000	4.000
Yukawa 1 (resembling pure)(**yuk1**)	80	1600	0	0	120k	0.053	0.8	4.000
with salt (**ws**)	80	1600	3200	1600	120k	0.053	1.409	4.000
Yukawa 2 (resembling with salt) (**yuk2**)	80	1600	0	0	120k	0.053	1.25	4.000
higher concentration (**hc**)	160	3200	3200	0	120k	0.105	1.150	4.053
higher concentration with salt (**hc ws**)	160	3200	4800	1600	120k	0.105	1.627	4.053
even higher concentration with salt (**ehc ws**)	240	4800	5400	1600	120k	0.158	1.818	4.105

Table 4.1: Overview of the simulated concentrations and introduction of the abbreviations. The systems contain N_{pol} polymers consisting of N_{mon} monomers. Counterions add up to N_+ and coions to N_-. Additionally there are N_{DPD} particles, which add up with the monomer concentration c to the total density ρ. The inverse Debye length κ results from the ion concentrations.

4.4 System Sizes

The system geometry is set to $40 \times 10 \times 45$ with the boundaries at $z_1 = 0$ and $z_2 = 40$ (or measured from the center $z_1 = -20$, $z_2 = 20$ respectively), leaving a penetrable volume

$$V = 40 \times 10 \times 38 \quad . \tag{4.19}$$

Table 4.1 lists all the different concentrations and polymer systems considered for the simulations. The volume is filled with a DPD fluid of constant density. N_{pol} polymers (charged/ uncharged) are added, corresponding to N_{mon} monomers in total. For charge neutrality N_c counterions are introduced, and in some cases salt is added in the form of N_s cations and N_s anions. The monomers and the DPD particles add up to the full density ρ. Additionally, we can directly calculate the inverse Debye screening length κ from the ion concentration

$$\kappa = \sqrt{4\pi \frac{N_c + 2N_s}{V}} \quad . \tag{4.20}$$

For the Yukawa systems, κ as listed in Table 4.1 is an input parameter, which has been determined by comparing conformational data, which will be presented in section 4.5. Comparing to the overlap concentration evaluated in the previous section, the systems with $c = 0.053$ are already close to the semi-dilute regime, but still in the dilute regime. The systems with higher concentration are deep in the semi-dilute regime.

4.5 Determination of the Debye Length

To compare our simulation method to an implicit salt model in the Debye-Hückel limit, we can make use of the Yukawa-type pair potential for charged monomers

$$V(r_{12}) = l_B k_B T q_1 q_2 \frac{\exp(-\kappa r_{12})}{r_{12}} \quad , \tag{4.21}$$

with $r_{12} = |\boldsymbol{r}_1 - \boldsymbol{r}_2|$. The Debye screening length $\lambda_D = \kappa^{-1}$ is the only free parameter of the Yukawa potential, as the strength of the potential is determined by the interacting charges and the Bjerrum length, which all are fixed. The salt density in the solution is then described effectively by a screening of the potential with the screening length κ^{-1}. The exponential decay allows for a local cutoff r_{cut}, which makes the Debye-Hückel electrostatics much faster than any other method. However, one completely loses the explicit description of ions, which corresponds to the assumption that all surrounding ions relax infinitely fast, when a monomer is disturbed. While in principle we can use Eq. 1.33 to calculate κ, it also makes sense to run test simulations in which we vary κ systematically to find the appropriate value by comparing conformational properties of the polyelectrolytes with the condiff result. These simulations are performed in bulk and equilibrium. Quantities used for comparison are the end-to-end distance R_e, the radius of gyration R_g, the hydrodynamic radius R_h, the average bond length b and the static structure factor $S(k)$.

By increasing the salt density, or $\kappa \to \infty$, we reach the totally screened case, i.e. corresponding to neutral polymers without electrostatics. Decreasing the salt density, or $\kappa \to 0$, leads to the plain electrostatics without any screening. As we use two different salt concentrations in this study, we obtain two Yukawa parameter sets. Firstly we take $\rho_s = 0$, the case with counterions only, which also has a corresponding screening length due to screening by the counterions and the monomers themselves. Secondly we have $\rho_s = \rho_m$, the case with equal salt and monomer concentration. All simulations are performed with an equilibration time of 4M steps and a measurement time of 4M steps writing out every 100 steps.

Figure 4.5 shows the results for different quantities that characterize the chain conformation. We compare different values of κ to the results of bulk simulations with the condiff algorithm for the counterions-only situation and the one with salt, represented by black solid and blue dashed lines respectively. In comparing the different quantities, they yield different recommendations for κ. This means that there is not a direct correspondence of a single κ value with the conformations. It seems that the two collective parameters R_g and R_h recommend a lower κ than the two pair-related parameters, R_e and bond length b. Thus, for further clarification, we also look into the single-chain structure factor.

Figure 4.7 shows the structure factor for the counterions-only case, where the best fitting values are $\kappa = 0.8$ and $\kappa = 0.85$. Figure 4.8 shows the results for the with-salt case. Here the best fitting values are $\kappa = 1.2$ and $\kappa = 1.3$.

Concluding the analysis, we choose the following values for the two Yukawa systems, as already listed in Table 4.1:

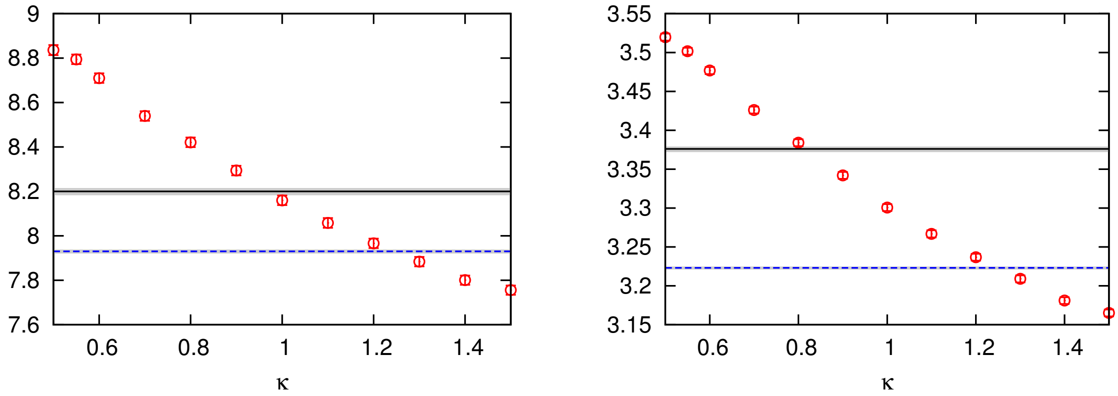

(a) R_e (b) R_g

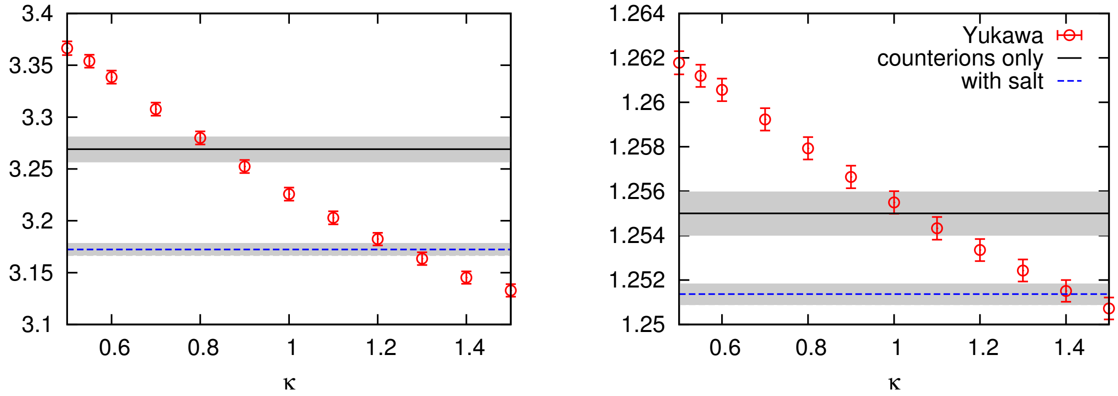

(c) R_h (d) b

Figure 4.5: Conformation quantities for different salt concentrations measured in κ in comparison to the condiff values marked by lines. The gray areas mark the error range. Shown are the end-to-end distance (a), the radius of gyration (b), the hydrodynamic radius (c), and the bond length (d).

$$\text{counterions only} \qquad \kappa = 0.8 \tag{4.22}$$

$$\text{with salt} \qquad \kappa = 1.25 \quad . \tag{4.23}$$

In all simulations the cutoff radius has been set to $r_c = 9.0$. Table 4.2 lists again the conformation results for the chosen values and their condiff counterparts.

For the counterions-only case we performed an additional test by doubling the chain length. The results are listed in Table 4.3. Here the recommended κ for R_e agrees with the R_g and R_h predictions, but the bond length still deviates.

The result $\kappa = 0.8$ also agrees well with the calculated one from Eq. 1.33, $\kappa = 0.81$. In the with-salt case the theoretical value would be $\kappa = 1.41$, hence there is a larger discrepancy. Interestingly this value agrees with the bond-length result in Figure 4.5d.

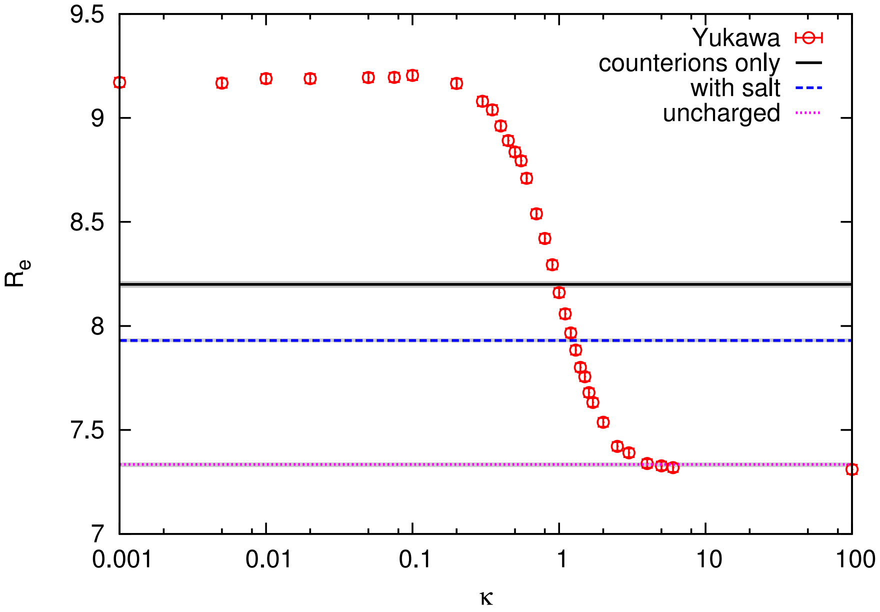

Figure 4.6: End-to-end distance in full range of tested κ (red symbols) and condiff results for counterions only, with salt, and completely uncharged polymers. The gray areas mark the error range.

	R_e	R_g	R_h	b
$\kappa = 0.8$	8.421 ± 0.009	3.384 ± 0.002	3.280 ± 0.006	1.2579 ± 0.0005
condiff pure	8.200 ± 0.013	3.376 ± 0.003	3.269 ± 0.010	1.2549 ± 0.0008
$\kappa = 1.2$	7.966 ± 0.009	3.237 ± 0.002	3.182 ± 0.006	1.2534 ± 0.0005
condiff with salt	7.930 ± 0.008	3.223 ± 0.002	3.172 ± 0.006	1.2514 ± 0.0005

Table 4.2: Conformational results for the chosen κ values and the corresponding condiff simulations.

Finally we can look at a wider range of κ and compare with the neutral polymers. Figure 4.6 shows the R_e data that saturates both for high κ, and $\kappa \longrightarrow 0$, showing agreement with the R_e obtained for neutral polymers.

κ	R_e	R_g	R_h	b
0.8	19.303 ± 0.031	9.759 ± 0.013	4.484 ± 0.007	1.2586 ± 0.0005
0.85	19.494 ± 0.032	9.732 ± 0.013	4.462 ± 0.007	1.2580 ± 0.0005
0.9	19.491 ± 0.031	9.681 ± 0.013	4.442 ± 0.007	1.2573 ± 0.0005
condiff	19.329 ± 0.028	9.728 ± 0.012	4.473 ± 0.007	1.2566 ± 0.0005

Table 4.3: Results for longer chains ($N_m = 40$) in the counterions-only case and comparison to the closest κ values.

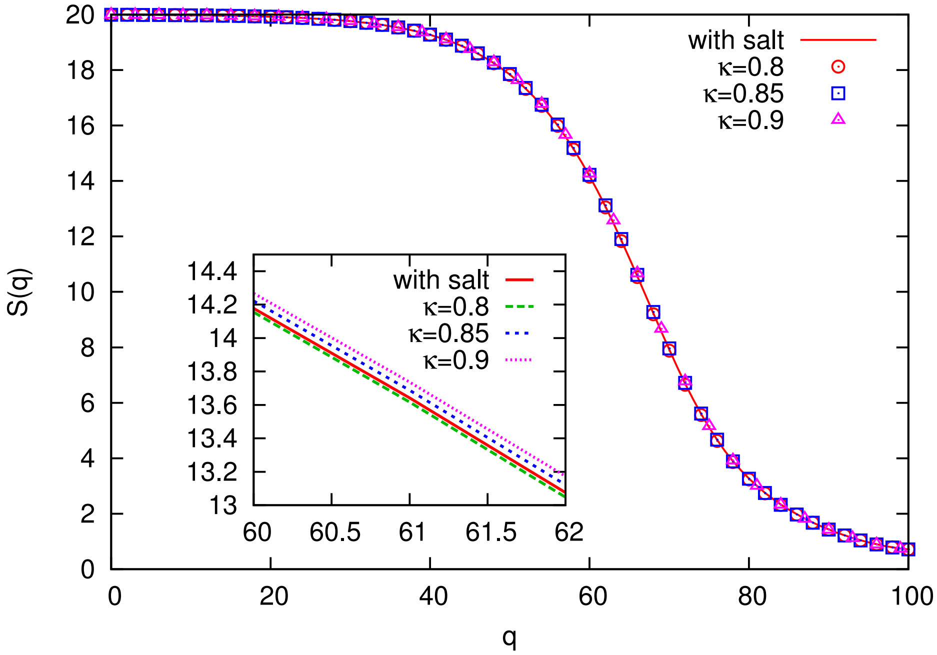

Figure 4.7: Single polymer structure factor for the counterions-only case and the three best-fitting Yukawa curves. The inset shows a blow up with the typical trend.

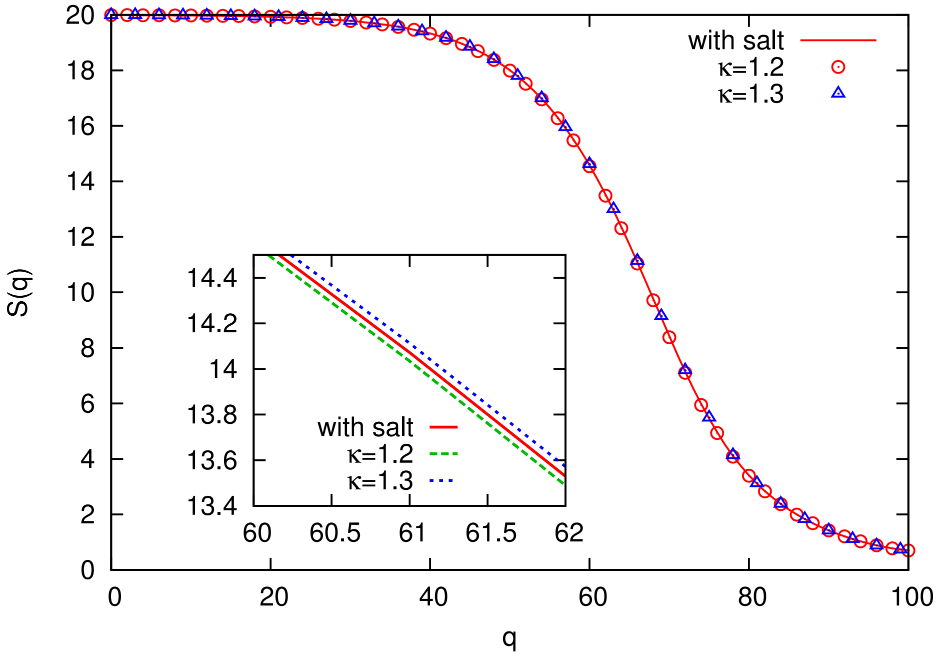

Figure 4.8: Single polymer structure factor for the with-salt case and the two best-fitting Yukawa curves. The inset shows a blow up with the typical trend.

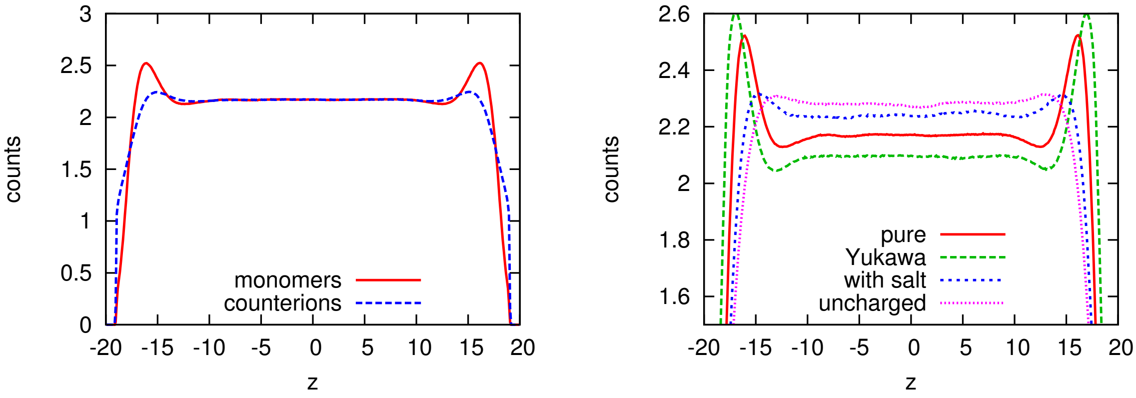

(a) pure, monomers + counterions

(b) monomers

Figure 4.9: Equilibrium profiles in the slit. (a) shows the pure polyelectrolyte system, (b) shows the monomer profiles for various systems.

4.6 Equilibrium Properties

4.6.1 Profiles

We start out with studying the equilibrium properties in the confined situation by comparing the resulting monomer and counterion profiles inside the slit. Figure 4.9a shows the profiles for the pure polyelectrolyte system. First we note that there is an effective attraction of monomers to the boundaries, which is not visible for individual ions in a pure salt solution and must therefore be related to the chain structure. There is charge neutrality in the central region, while the counterions distribute somewhat differently at the boundaries, showing a depletion up to the monomer peak and then peaking themselves. In (b) we compare the monomer profiles for the systems of low concentration. In contrast to the pure polyelectrolyte case, the neutral chains show a strong depletion. In the case with salt the monomer peaks are strongly decreased and moved towards the center, leaving a depletion zone. The Yukawa polymers show a similar peak behavior as the pure polyelectrolytes, but the peak is stronger and closer to the boundaries, showing no depletion.

While this peak structure also affects the total density profile, the deviation is extremely small as the DPD density dominates (the total density in terms of the above histogram would be around 160). Therefore we can still assume a homogeneous total-density profile, which is essential for the viscosity evaluation. However, we need to keep the approximative character in mind.

4.6.2 Chain Conformations

As we expect the boundaries to influence the conformations strongly, we only consider polymers that are fully in the range

	R_{e0}	ΔR_{e0}	R_{g0}	ΔR_{g0}	R_{h0}	ΔR_{h0}	b_0	Δb_0
pure	8.33	0.02	3.352	0.005	3.255	0.016	1.254	0.001
Yukawa 1 (yuk1)	8.42	0.02	3.382	0.004	3.277	0.016	1.258	0.001
with salt (ws)	7.85	0.03	3.202	0.006	3.160	0.022	1.251	0.002
Yukawa 2 (yuk2)	7.88	0.01	3.211	0.002	3.166	0.008	1.252	0.001
uncharged (un)	7.30	0.02	3.019	0.004	3.027	0.015	1.243	0.001

Table 4.4: Equilibrium properties of the different polymer solutions.

	R_{e0}	ΔR_{e0}	R_{g0}	ΔR_{g0}	R_{h0}	ΔR_{h0}	b_0	Δb_0
pure	8.33	0.02	3.352	0.005	3.255	0.016	1.254	0.001
with salt (ws)	7.85	0.03	3.202	0.006	3.160	0.022	1.251	0.002
higher concentration (hc)	7.60	0.03	3.130	0.005	3.116	0.018	1.249	0.001
higher concentration with salt (hc ws)	7.39	0.03	3.064	0.006	3.072	0.020	1.248	0.002
even higher concentration with salt (ehc ws)	7.11	0.03	2.971	0.005	3.005	0.018	1.244	0.001

Table 4.5: Equilibrium conformations for the different polyelectrolyte/salt concentrations.

$$z_1 + 6 \leq z < z_2 + 6 \tag{4.24}$$

for the calculation of the chain properties.

Tables 4.4 and 4.5 summarize all obtained equilibrium conformations of the polymer systems. Even though the quantities were only sampled in the center of the channel, there is already a clearly visible change due to the confinement, when comparing to the bulk results in Table 4.2. Also, the Yukawa polymers deviate stronger from their condiff counterparts. The uncharged chains have a smaller size as well as a slightly smaller bond length b, which is to be expected due to the missing intrachain electrostatic repulsions.

4.6.3 Longest Relaxation Times

By studying the equilibrium behavior of the polymers, we obtain useful information about the time scale of the single-chain dynamics. The longest relaxation time τ can for instance be extracted from the R_e autocorrelation function, which should decay exponentially.

Table 4.6 summarizes the results for τ. In general it shows that the determination of relaxation times requires a very large sample size, as the errors are still quite high. It seems that the uncharged chains have the shortest relaxation times, thus having the fastest dynamics. They are followed by the Yukawa 2 chains, where the long-ranged electrostatics are strongly screened. Yet the results for the polyelectrolytes with screening by salt do not resemble this result. Similarly the Yukawa 1 and pure cases do not match. The higher concentrated systems do not show a slower dynamics, while the system with

system	τ	sim. steps
pure	30.5 ± 4.0	7.77M
uncharged (un)	23.0 ± 3.0	20.1M
with salt (ws)	28.0 ± 6.0	7.36M
Yukawa 1 (yuk1)	25.0 ± 3.0	8.95M
Yukawa 2 (yuk2)	23.5 ± 3.0	9.29M
higher concentration (hc)	29.0 ± 4.5	7.31M
higher concentration with salt (hc ws)	30.0 ± 3.5	7.38M
even higher concentration with salt (ehc ws)	69.5 ± 7.5	6.95M

Table 4.6: Relaxation times τ extracted from the R_e autocorrelation functions by an exponential fit. The sample size is given by the simulation time, writing out every 50 steps.

even higher concentration (ehc ws) significantly deviates from any other system, as the relaxation time is more than doubled. However, the value has also been extracted from the smallest sample. Therefore we cannot draw any meaningful conclusions about the dependence on concentration.

4.7 Couette Flow - Conformational Changes

When shear flow is imposed, the polymers will respond by a change in their conformation. Such changes can have two origins, where the change of spatial distribution of the monomers is the interesting one, including the alignment of polymers with the shear flow and the stretching of chains. As a second origin an extension of bonds is possible, in the limits given by the stiffness of the bond interactions. As we are dealing with harmonic bonds instead of the finitely extensible FENE bonds, the bond-extension effect should be cared about. Therefore we take the pure polyelectrolyte system as a model system to study the bond length.

As shown in Figure 4.10 the bond length b changes only slightly with shear rate. Similarly, the ratio R_e/b shows that the polymers are extending disproportionately to the increase in b. Hence the bonds are stiff enough for the applied shear rates and conformational changes are predominantly visible in R_e, R_g, R_h.

4.7.1 Comparison with Uncharged and Yukawa Chains

Having characterized the equilibrium data we can look at the conformational changes with shear rate $\dot{\gamma}$ by studying the change in R_g, shown in Figure 4.11. For low shear rates the Yukawa polymers resemble their condiff counterparts fairly well, however, with increasing shear rate they underestimate the chain stretching significantly. The situation

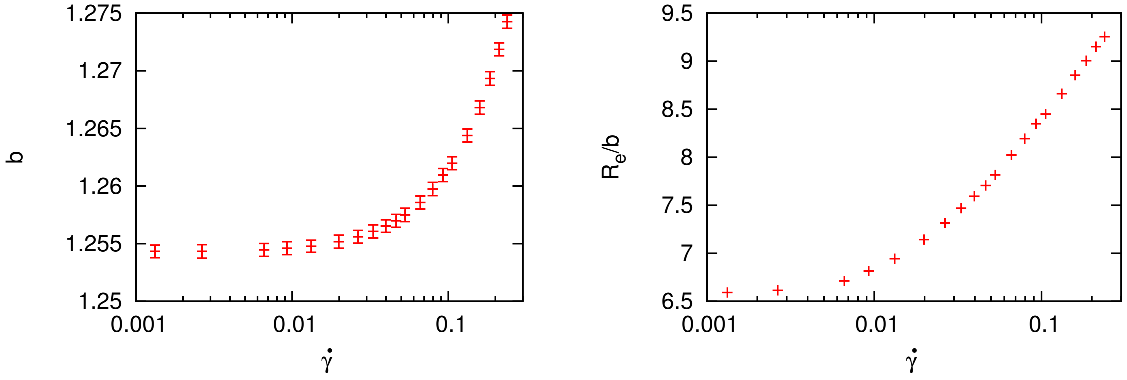

(a) (b)

Figure 4.10: Illustration of the bond stretching. (a) shows the bond length b over shear rate, and (b) the ratio of end-to-end distance and bond length.

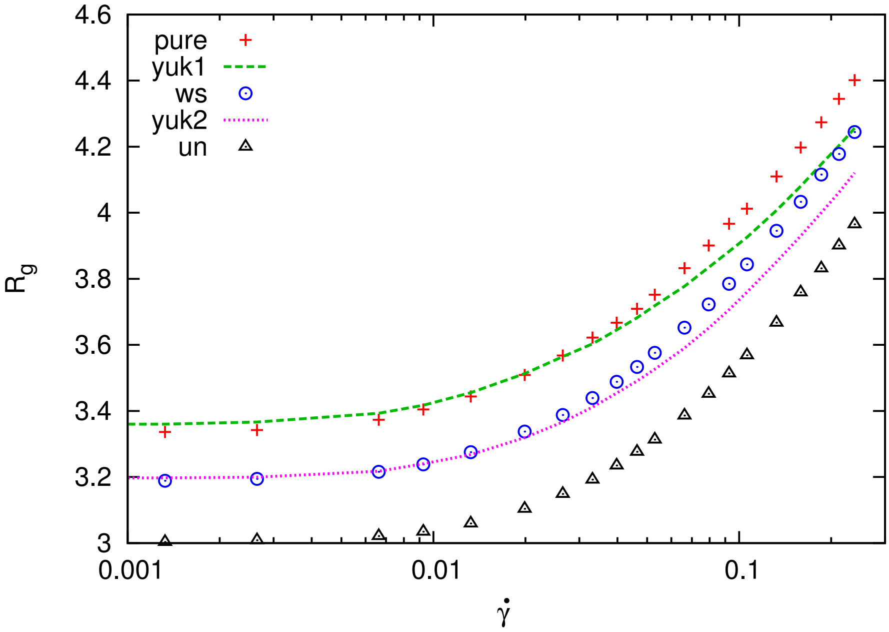

Figure 4.11: R_g over shear rate for the different polymers at low concentration.

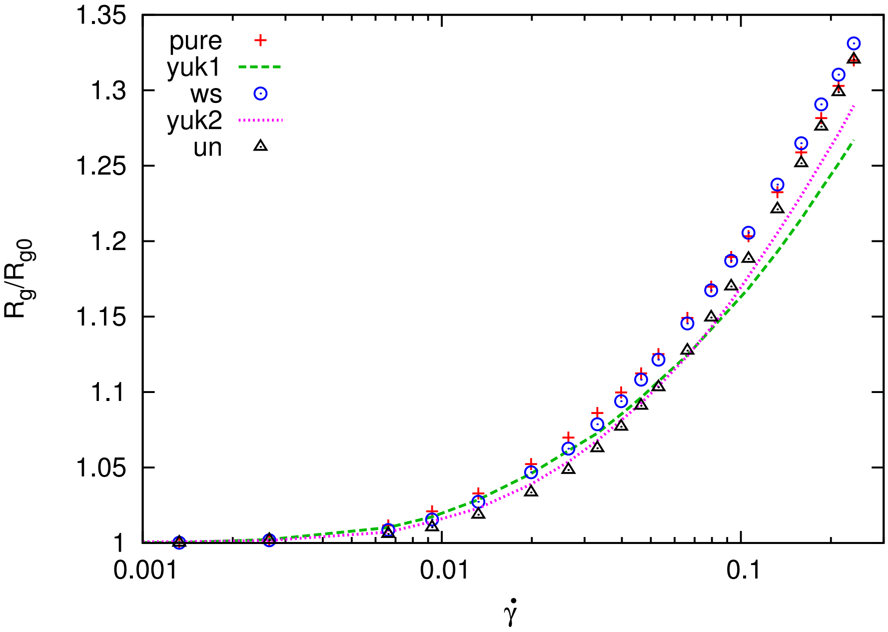

Figure 4.12: Relative change in R_g over shear rate for the different polymers.

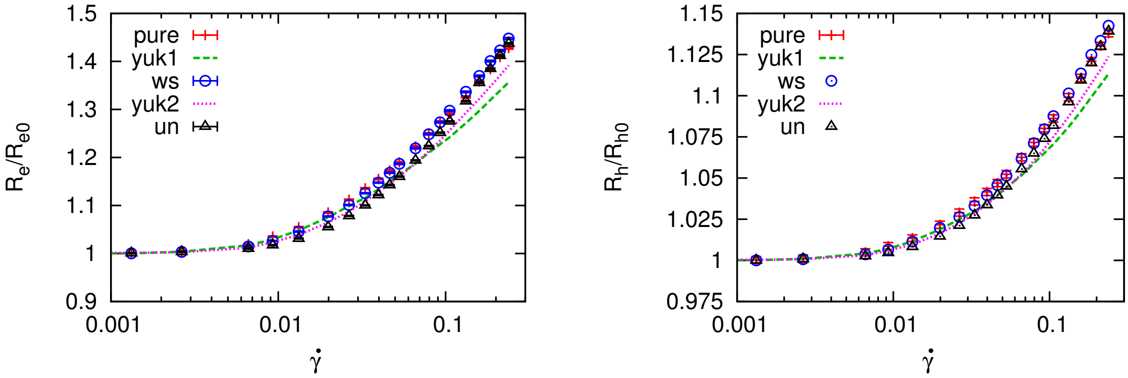

(a) (b)

Figure 4.13: Relative change in R_e and R_h. In (b), error bars for R_h are only shown for one curve to enhance the visibility.

seems to be a little better for the case with salt. Further comparisons are possible when looking into the relative changes of R_g, as shown in Figure 4.12.

For the low shear-rate regime $\dot{\gamma} < 0.01$ there is almost no change in the conformation for any system. From there on also the individual behavior differs. The uncharged chains seem to stretch less for intermediate $\dot{\gamma}$, and then slightly more. The same behavior can be seen in the end-to-end distance and the hydrodynamic radius, illustrated in Figure 4.13.

Overall, the Yukawa description of polymers fails in the high shear regime for the pure polyelectrolyte + counterion case, whereas it appears to be slightly more accurate in the situation with salt. Apparently there are stronger stretching effects that are not captured appropriately by the Yukawa model. While this does not seem to be a crucial shortcoming in our case, it might certainly be a stronger effect for longer chains. Lastly we note that the pure and with-salt polymers behave almost identically, except for a crossover at about $\dot{\gamma} = 0.1$, visible in Figure 4.12 and also slightly visible in Figure 4.13a and b. Thus the salt seems to reduce conformational changes for moderate shear rates up to the point where the effect vanishes and thus the chains extend more, in relation to the case without salt. For much higher shear rates outside the measured range one would expect the salt to become irrelevant.

4.7.2 Changes with Concentration and Addition of Salt

With increasing polymer concentration the chains collapse further. While additional polyelectrolytes are able to screen electrostatic repulsions, the decrease in size is larger than the analogous decrease with salt. Hence this is a direct effect of reaching the overlap regime, which can be nicely seen in the change from 'pure' to 'ws' (with salt) and to 'hc' (higher concentration) in the low shear-rate regime of Figure 4.14a. For higher shear rates the difference between 'ws' and 'hc' becomes smaller, i.e. the more stretched the polymers become, the less the importance of the actual screening source (other chains, or salt). In Figure 4.14b the relative change is plotted, where the order of the curves is just reverse, i.e. the higher-density system shows the strongest relative chain stretching, as it started out with the smallest size. The Yukawa description of the with-salt case fails both in the absolute and relative for high shear rates.

Similar comparisons have been made with the cases of 'higher concentration with salt' and 'even higher concentration with salt', where no additional effects have been visible, which have not yet been covered with the comparison pure to 'hc'/'ws'. Therefore these cases are omitted here, but are presented together with the other cases in the appendix in section A.5.

4.7.3 Gyration tensor

Instead of studying the scalar conformational quantities, one can also evaluate the gyration tensor and thus obtain detailed information about the stretching process. Figure 4.15 shows the diagonal components of G in a comparison between the pure, Yukawa and neutral-polymer case, with the y-axis held in logarithmic representation. In the low shear

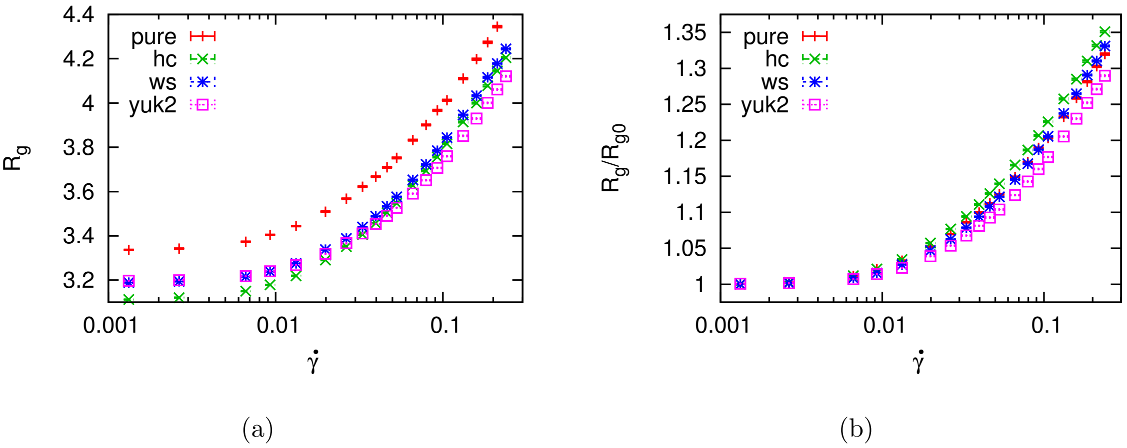

(a) (b)

Figure 4.14: Radius of gyration in comparison between the pure case and the cases with higher concentration and with salt (plus the corresponding Yukawa result). (a) shows the absolute R_g, (b) shows a relative values normalized by the equilibrium value.

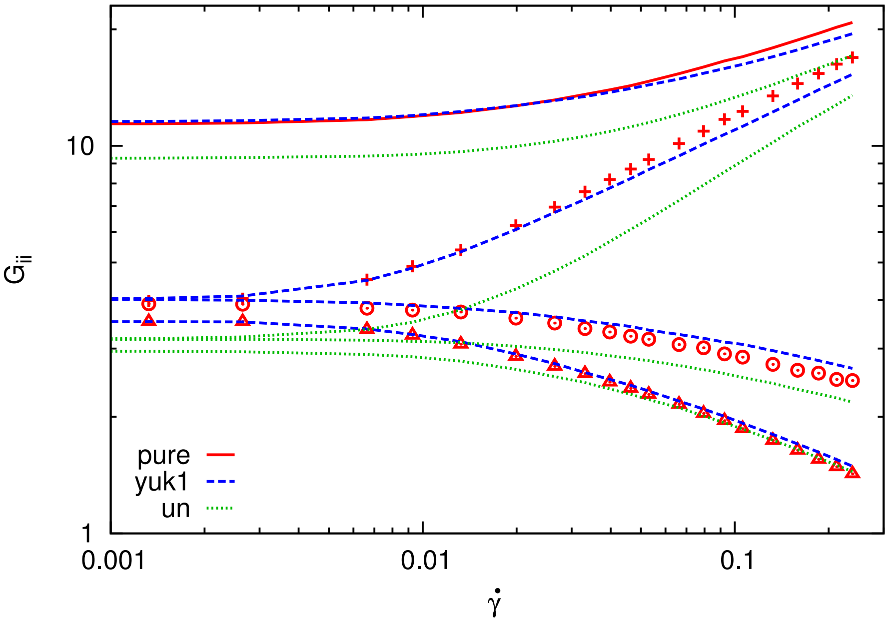

Figure 4.15: Gyration-tensor components over shear rate, comparison of the pure case with the Yukawa and neutral-polymer case. From top to bottom, the first lines show R_g^2 as a reference. G_{xx} (shear-direction) has a positive slope and is represented by crosses. G_{yy} is the largest one with negative slope, represented by circles. G_{zz} (boundary direction) is the lowest curve, represented by triangles. Note the logarithmic scale on the y-axis.

regime the xx and yy-components agree with each other, for any of the three systems, with the zz-component being slightly lower. This is in agreement with the observation that the boundaries decrease the chains already in equilibrium, even though we only evaluate the chains in the center of the slit. In all three cases there is chain stretching, i.e. a clear extension of the xx-component (crosses) is visible. The Yukawa curve shows a much lower slope, while the neutral-polymer curve starts out lower, but has a higher slope, showing that neutral chains stretch faster for high shear rates. Thus for very high shear rates all chains should reach a similar stretching level, that is independent of the electrostatics. The decrease in the yy and zz-component has different slopes, with the yy-component having the smaller one. This observation agrees with the results in Ref. [125]. For all three cases the zz-component shows a fairly good agreement in the high shear-rate regime, where the neutral-polymer curve converges towards the 'pure' result. Hence the combined shear and confinement effects are somewhat stronger than the intrinsic differences in the chain description. Overall, the Yukawa description underestimates the slope in all three components.

Figure 4.16 shows the same kind of comparison, but for the cases with salt and with higher concentration. This time the y-scale is linear. Interesting is the direct comparison of 'hc' and 'ws'. While the course of R_g shows a convergence for high shear rates, the xx-component shows that the stretching is somewhat non-uniform. For low shear rates the 'ws' curve is slightly higher, which changes for intermediate shear rates. Finally, for high shear rates there is another crossover and thus the chains with salt are slightly further extended. The other two components show a somewhat monotonic picture, where the 'hc' values are always below the 'ws' ones, in accordance to the generally smaller R_g. The situation might change for very high shear rates.

4.8 Viscosity

4.8.1 Solvent Properties

Before we investigate the rheology of polymer solutions, we start out with a pure DPD fluid to determine the solvent properties. Both the Couette flow and the Poiseuille flow are used. The DPD results will then be the reference to determine the reduced viscosity

$$\eta_{\mathrm{red}} = \frac{\eta - \eta_s}{\eta_s} \quad , \tag{4.25}$$

which is a measure for the contribution of chains, relative to the viscosity that a pure solvent of the same density would have. To obtain a better comparison between systems of different total density, we investigate all occurring ρ in separate DPD simulations, using the Poiseuille and periodic Poiseuille flow. Representatively we discuss the case $\rho = 3.947$ (120k particles), where also Couette results are available. From the Couette flow we can determine η_s by averaging over the range of $\dot{\gamma}$ we apply. Each data point is an average of four individual runs of about 2M steps after reaching steady-state. Therefore

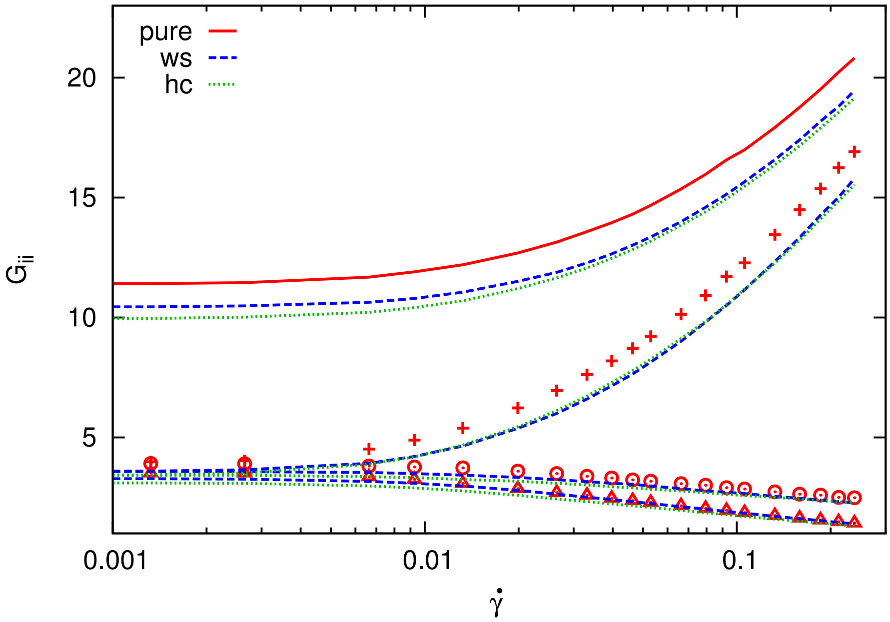

(a)

Figure 4.16: Gyration-tensor components over shear rate, comparison of the pure case with the cases with salt and with higher concentration. From top to bottom, the first lines show R_g^2 as a reference. G_{xx} (shear-direction) has a positive slope and is represented by crosses. G_{yy} is the largest one with negative slope, represented by circles. G_{zz} (boundary direction) is the lowest curve, represented by triangles.

the low-shear regime is left out due to the strong fluctuations. The resulting average shear viscosity is $\eta_s = 1.395 \pm 0.015$.

The Poiseuille flow results in a shear viscosity of $\eta_s = 1.3948 \pm 0.0005$, which agrees nicely. The applied external force of $F = 0.01$ leads to a maximum velocity of $v_{\text{max}} \approx 5$, which is high enough do reduce fluctuations. The evaluation was performed with ten individual runs of 2.5M steps after reaching steady-state, using Eq. 2.15. While the Poiseuille result appears more accurate, it should be noted that η_s is very sensitive to small changes in z_B and δ_B, so that a determination to more than two digits is almost not applicable, three at the most. Here, both calculations were done with the set of slip parameters

$$z_B = \frac{37.75}{2}, \qquad \delta_B = 0 \quad , \tag{4.26}$$

which will be used further on. Table 4.7 lists all obtained η_s values that will be used to calculate η_{red}.

N	ρ	η_s
120k	3.947	1.395
121.6k	4.000	1.404
123.2k	4.053	1.411
124.8k	4.105	1.419

Table 4.7: Solvent viscosities for different DPD densities, used to calculate the reduced viscosities.

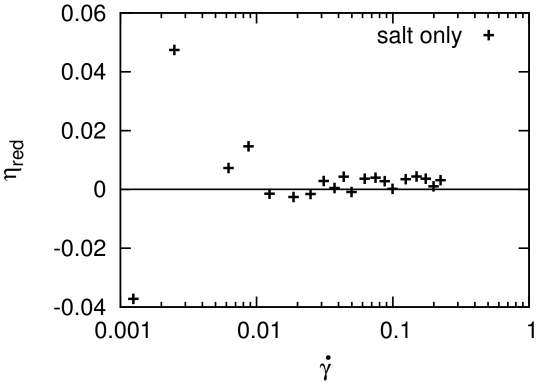

Figure 4.17: Reduced viscosity for a pure electrolyte solution. The deviations are in the same fluctuation range as in the DPD fluid.

4.8.2 Pure Electrolyte Solution

The addition of salt to the DPD fluid should not influence the Newtonian behavior. As the boundaries are neutral, there is no double layer and thus the charge distribution is homogeneous. Therefore the DPD particles are mostly undisturbed. Figure 4.17 shows the resulting reduced viscosity values for different shear rates, obtained with the Couette method. The overall deviation is in the error range of η_s, except for the two lowest shear-rate values, which deviate due to the statistical fluctuations in the force measurements.

Thus the inclusion of salt does not lead to rheological changes by itself. However, ions will have an impact on the polyelectrolytes due to screening effects and the primary electroviscous effect.

4.8.3 Couette Results

Figure 4.18 shows the Couette results for the reduced viscosities. Even though all η_{red} have been calculated with the appropriate DPD result for the total density, there is a clear shift that must be related to the monomer characteristics, as it increases with concentration. One could estimate that all curves continue to zero for $\dot{\gamma} > 1$. The cause for the general shift might be the excluded volume interactions, which somewhat blow up the volume fraction in comparison to the ideal-gas DPD fluid. All systems show shear thinning over the entire shear range. The data for the low shear regime $\dot{\gamma} < 0.01$ still lack statistics, even though the boundary force was sampled over $\sim 15M$ steps. Here the thermal fluctuations are too strong to obtain results with reasonable computational effort. It is expected that for very low shear rates Newtonian behavior sets in, leading to a plateau in η_{red}.

Figure 4.19 zooms in on the low-concentrated systems. Here the neutral chains show the least shear thinning. The remaining systems show a similar slope, where both Yukawa systems generally underestimate the viscosity. Thus they can reproduce the qualitative character of the condiff systems quite well, though lacking quantitative agreement. This might be directly related to the mismatch in the conformations, which to a certain degree is already caused by the boundaries, as seen in the equilibrium situation. Deviations might occur in the low shear regime, which, however, lacks clarity due to the statistics. Interestingly the with-salt curve clings to the pure curve for high shear rates, but shows deviations for low shear rates. There might even be a transition for $\dot{\gamma} \approx 0.2$, which could correspond to the crossover in R_g/R_{g0} in Figure 4.12.

4.8.4 Poiseuille Results

A comparison between the Poiseuille and Couette results is shown in Figure 4.20 for the pure case. The Poiseuille viscosity has been determined with several individual simulations with different driving force and two channel widths. While the agreement is fairly good in the regime around $\dot{\gamma} = 0.1$, the Poiseuille method fails in the intermediate shear-rate regime.

The low shear regime has not been covered with the Poiseuille method, as very low forces are required which results in long simulation times. Overall, the Poiseuille method requires similarly long runtimes as simulations in the low shear-rate regime with the Couette flow. Therefore a detailed comparison between the two methods is rather demanding for such large systems and more extensive simulations are required to yield accurate results.

4.9 Counterion Diffusivity

To clarify further the role of the counterions in the non-equilibrium situations, we modify the ion diffusivity in the pure system from $D = 0.26$ to $D = 0.13$ and $D = 0.53$. By studying the Couette flow, we can compare the conformational changes as well as the rheology. Both are presented in Figure 4.21. In the end-to-end distance in (a) all three curves start out with almost identical equilibrium values. With increasing shear rate deviations occur, where the lower diffusivity leads to a slightly stronger stretching. The reduced viscosity in (b) shows in accordance to the general trend that larger conformations result in larger η-contributions. Unfortunately the statistics for the low shear-rate regime are not sufficient for a conclusion. However, it appears that the general trend for the curves is to converge, as the green circles indicate.

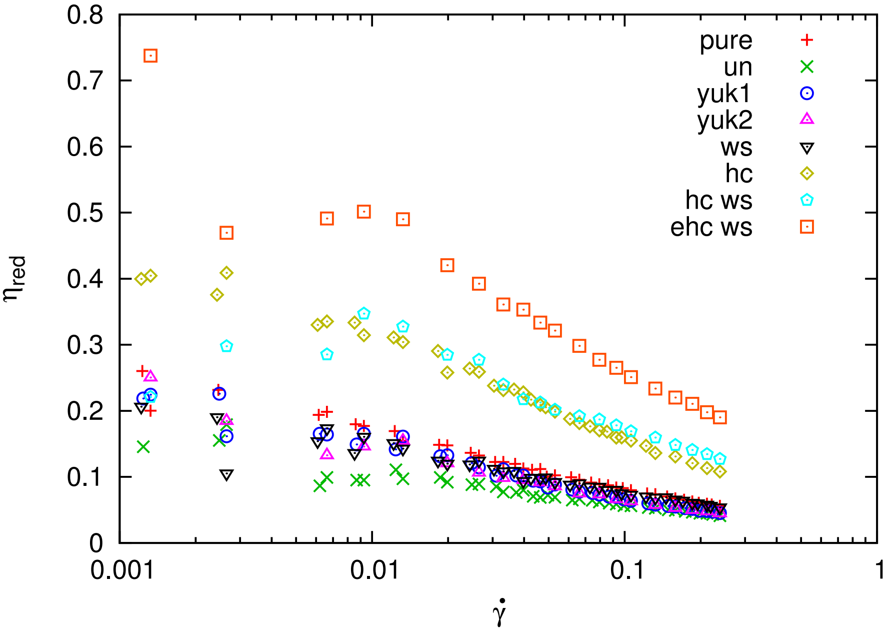

Figure 4.18: Reduced viscosity for different systems, determined with Couette flow.

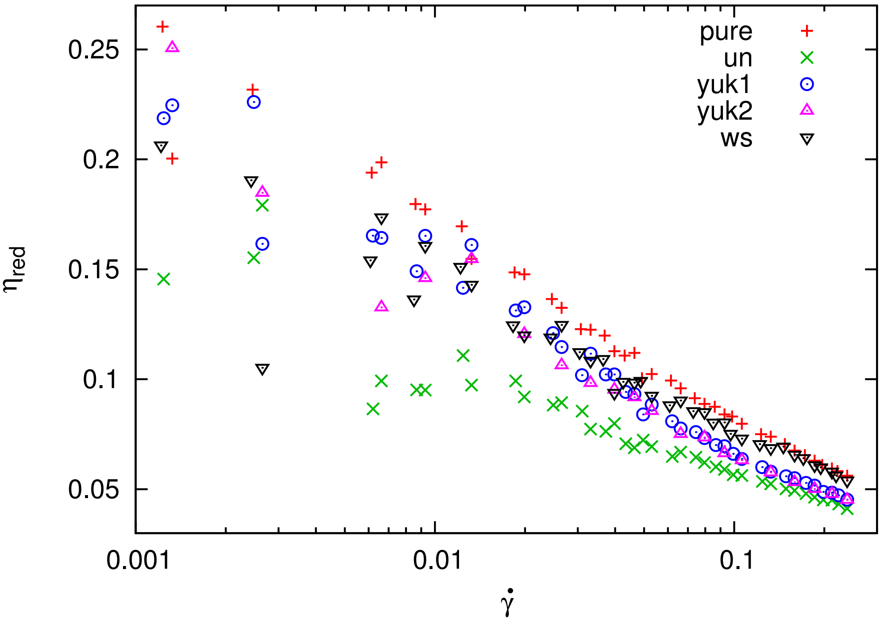

Figure 4.19: Reduced viscosity for the low-concentrated systems (same data as in Fig. 4.18 in different representation).

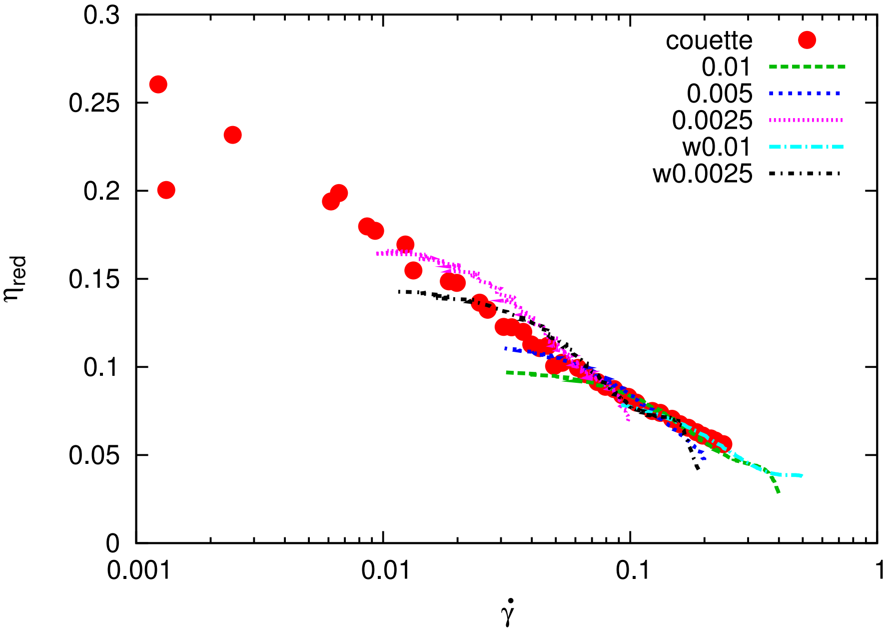

Figure 4.20: Reduced viscosity as a result of Couette and Poiseuille measurements. The Poiseuille flow has been induced with several force values, using a slit of regular width ($H = 38$) and a wider one (w, $H = 57$).

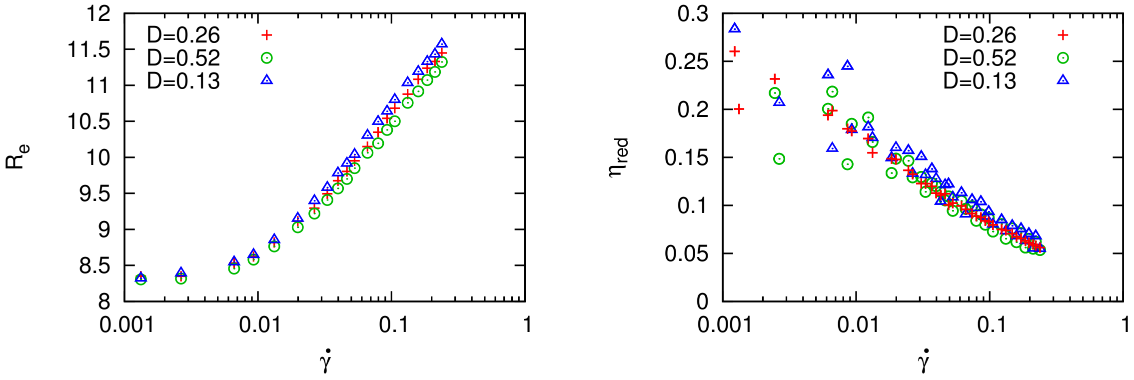

(a) (b)

Figure 4.21: End-to-end distance (a) and viscosity (b) for the pure system with different diffusivities.

4.10 Data in Terms of Wi and Pe

While presenting all data versus the shear rate $\dot{\gamma}$ has the benefit of giving a geometrical interpretation in terms of the system's scales, one could also use either the Péclet number Pe or the Weissenberg number Wi instead of $\dot{\gamma}$. The former relates the shear motion to the model parameters and the strength of the thermal fluctuations [53]

$$\mathrm{Pe} = \frac{\xi \dot{\gamma} \sigma^2}{k_B T} \quad , \tag{4.27}$$

with $\sigma = 1$ the bead diameter and $\xi = 6\pi\eta\sigma/2$ the Stokes friction for a single bead. The latter relates the shear motion to the polymer time scale

$$\mathrm{Wi} = \tau \dot{\gamma} \quad , \tag{4.28}$$

with τ the longest relaxation time. Therefore Wi gives information about whether the single chains are able to relax their conformation in the time scale given by the shear rate. The linear-response regime is thus found in the low Wi range, while Wi > 1 states that the chains are distorted strongly by the shear motion. We calculate Pe with help of the pure DPD system's viscosity of Table 4.7

$$c = 0.053 \quad (\eta_s = 1.404) \quad \Longrightarrow \quad \mathrm{Pe} = 13.232\dot{\gamma} \tag{4.29}$$

$$c = 0.105 \quad (\eta_s = 1.411) \quad \Longrightarrow \quad \mathrm{Pe} = 13.298\dot{\gamma} \tag{4.30}$$

$$c = 0.158 \quad (\eta_s = 1.419) \quad \Longrightarrow \quad \mathrm{Pe} = 13.374\dot{\gamma} \quad . \tag{4.31}$$

As there is only a slight difference in the viscosity for the different concentrations and thus in the Péclet numbers, there is no need for extra plots versus Pe. Figure 4.22 shows the R_g and η_{red} data in terms of the Weissenberg number, where in section 4.6.3 τ has been determined separately for each system. The main difference to a plot versus $\dot{\gamma}$ as in Fig. 4.11 and Fig. 4.18 is that the R_g curves seem to run together for high shear rates, showing the relation between the individual stretching processes.

In Ref. [125], Huang et al. found a universal scaling law of $\eta(\dot{\gamma})/\eta(0)$ with a concentration dependent Wi for the case of neutral polymers. In our case, however, it appears that the low shear rate data is too noisy to make reasonable estimates of $\eta(0)$.

4.11 Finite Size Effects

In general the shear motion of the boundaries leads to a stretching of the polymers in the solution. Thus it is important that the simulation box is large enough so that a fully stretched polymer does not predominantly interact, let alone overlap, with itself, which would lead to finite size effects. On the other hand there is a clear finite size effect originating in the confinement, which has been reduced by only evaluating conformational properties of polymers in the central area of the slit. Here we test four different system sizes, namely $L = 10, 20, 30, 40$ for a penetrable volume $L \times 20 \times 38$, where $L = 10$ is only

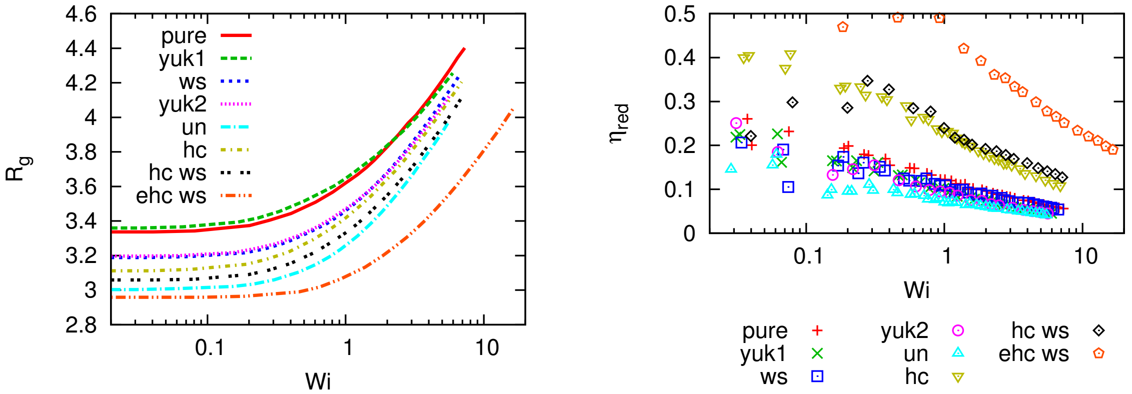

(a) (b)

Figure 4.22: Radius of gyration (a) and reduced viscosity (b) versus the Weissenberg number.

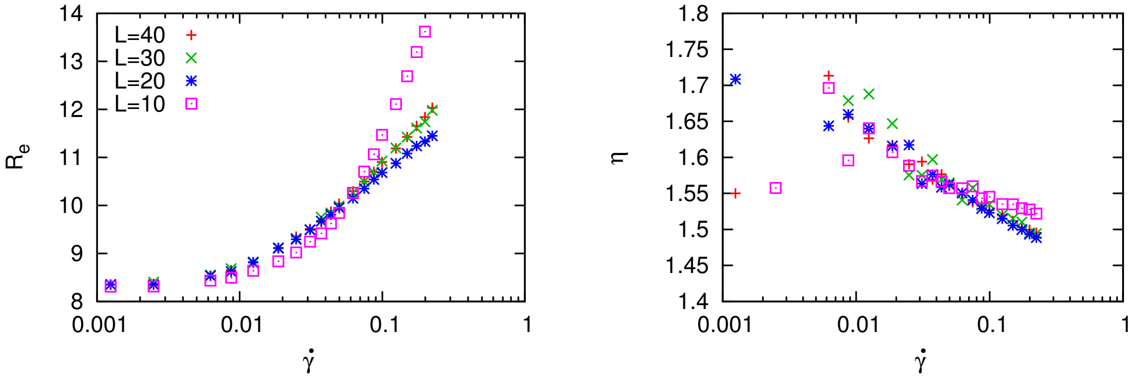

(a) (b)

Figure 4.23: End-to-end distance (a) and viscosity (b) for a pure polyelectrolyte solution with different box lengths to visualize the finite size effects.

academically motivated as it is of the same magnitude as the typical R_e in equilibrium. We take the pure polyelectrolyte system for the test and compare R_e and η, presented in Figure 4.23. For the low shear regime, R_e shows almost no L-dependence. The finite size comes into play once the stretching increases in the moderate shear regime. Especially the system with $L = 10$ shows strong deviations, once $R_e \approx L$. The $L = 20$ system starts to fail for high shear rates, showing that stretched polymers of $R_e \approx 12$ already self-interact over a range $L = 20$. The two larger system sizes do not show any significant deviation from each other. Hence $L = 40$ seems to be sufficient for our purposes. It has been observed that the effects in $L = 20$ reduce for the more concentrated systems, which may be due to the collective screening of the polymers. When looking into the viscosity in Figure 4.23b, there is only a clear deviation of $L = 10$ for high shear rates. Other than that, the viscosity data agrees fairly well. Yet the data for $L = 30$ lacks statistics, as this was only a test run. In conclusion, the smaller system sizes could only be applicable for viscosity measurements, at least in a low shear regime.

4.12 Polyelectrolytes in a Thin Film

The behavior of polymers in confinement can differ greatly from the bulk. Minor effects of the boundaries have been visible in the previous sections, where the conformations slightly changed, even though we have neglected all chains located close to the boundaries and have focused on the center of the slit. We now shift our focus to the study of strong confinement, i.e. polyelectrolyte solutions confined in very thin slit channels, creating a so-called thin film geometry. With the transition in geometry also the terminology changes, as the study of the viscous behavior in thin films is not called rheology, but tribology. The study of shearing motions of thin films is of strong interest, as it is motivated both biologically as well as by industrial applications. A prominent example of the former is the functionality of synovial joints, and of the latter the reduction of wearing in bearings, to enhance the life time of components.

The study of thin film properties is of a broader, more general interest and not only limited to polymer solutions. For instance, when confined in films of nanometer size, certain liquids can show behavior that is more likely for a solid or a liquid crystal [137]. Yet there is also a specific interest in the study of polymers at interfaces [138]. In a thin film, polymers behave differently as boundary effects become dominant, leaving the chains strongly compressed. Thus significant conformational changes and also changes in the viscous behavior are expected. Experimental measurements of polyelectrolyte solutions show that for large channel heights, $H > 6R_g$, the viscosity resembles the bulk value. However, as the separation between the surfaces is decreased, the viscosity also decreases until it converges to a minimum for channel heights of $H \approx 0.5R_g$ [139].

In general there are two types of situations to be encountered for the polymers. On the one hand people study polymers grafted onto surfaces, i.e. polymer brushes. Here strong differences have been encountered between uncharged and charged polymers [120]. On the other hand people are also interest in solutions of free polymers. In polyelectrolyte thin films confined between charged surfaces chains get adsorbed, so that a setting similar to the polymer brushes is created with a polyelectrolyte layer adjacent to the surface. However, as the adsorption energy is of the order of k_BT, chains are easily dragged away in shear flow, thus creating a more flexible environment than a polymer brush. An experimental study has shown that such a situation can be favorable, as those polyelectrolytes that are teared away by the shearing motion are generally replaced in a so-called self-healing process by free polyelectrolytes [140], while grafted polymer brushes cannot be fixed that easily. Another study showed that a high salt concentration can decrease the lubricative character of a polyelectrolyte thin film significantly [141]. Also, studies are performed to discover possible polymer candidates for enhanced lubrication [142].

In the framework of the condiff algorithm we want to seize the motivation given by the experiments and study the behavior of solutions of linear polyelectrolytes under strong confinement between planar walls with focus on the lubricative changes due to the

L_x	L_y	H	$c_{N=500}$	$c_{N=1000}$
50	20	10.0 (12.0)	0.05	0.1
50	20	7.5 (9.5)	0.0667	0.1333
50	20	5.0 (7.0)	0.1	0.2

Table 4.8: List of the channel geometries, where H stands for the actually penetrable volume due to the WCA repulsion of the boundaries. The boundary spacing is given in brackets. Also the resulting monomer concentrations are shown.

polyelectrolyte chains. From a simulational point of view, the study of small, confined systems is also advantageous as occurring finite-size effects are no longer artificial but gain a physical meaning. In experiments on thin films, the lubricative behavior is usually determined with the help of a surface-force apparatus. In our simulations we employ the tunable-slip boundaries in order to calculate the viscous forces due to the shearing motion of boundaries. Additionally we study the conformational changes of the chains and distributions inside the thin film. Due to the spatial asymmetry, conformational quantities should be treated in tensorial form. By systematically varying the film height, surface properties and concentrations of polyelectrolytes and salt, we can derive a picture of the general behavior of polyelectrolyte thin films and determine their lubricative properties. The data presented in this section is still in a preliminary state as the study is still ongoing. However, principal results are already deducible and a comparison of charged and uncharged surfaces is presented.

4.12.1 System Settings

We start out with three different slit sizes listed in Table 4.8 where the x-direction will be the shear direction and the z-direction is the one in which the confinement takes place. A fourth system size of $H = 2.5$ has also been studied, however, resulted in very strong layering effects of monomers and will be omitted in the following.

As before, the polyelectrolytes have a chain length of $N_m = 20$ and we will consider two monomer concentrations in each geometry, where always

$$N = 500 \tag{4.32}$$

$$N = 1000 \ . \tag{4.33}$$

The resulting concentrations are also shown in Table 4.8. Additionally, the appropriate amount of counterions N_{cp} is put into the system. As the resulting monomer concentrations are quite high, we adapt the DPD density such that the total density is kept constant

$$c + \rho_{\text{DPD}} = \rho = 3.75 \ . \tag{4.34}$$

This way the systems stay directly comparable to a pure DPD system of the same density, which we will also investigate. As we want to include polymer adsorption, we choose a surface charge σ of opposite sign, which can be modeled in two different ways. The first way is to assume homogeneously charged surfaces. This can be achieved by including the corresponding counterions N_{cw} in the solution. The resulting net charge results in the same electrostatics as with homogeneously charged surfaces. The second way is to put charges explicitly onto the surface in the form of frozen pseudo-ions. A comparison of preliminary results for both situations showed no difference in charge profiles, polymer conformations and flow properties. Thus, we stick to the homogeneous description and leave a comparison to the explicit description for future studies. By choosing

$$\sigma = 0.25 \tag{4.35}$$

we realize one system where each surface-charge unit has one corresponding monomer of opposite charge ($N = 500$) and one case with twice as many monomers ($N = 1000$). The second case ensures that there is never a complete adsorption, while the first one in principle allows for a high percentage, up to complete adsorption. The polymers are placed into the system by means of a self-avoiding random walk. Then the systems are allowed to equilibrate. The applied shear rates vary in the range $\dot{\gamma} \in [0, 1]$, where the velocity difference is applied through the tunable-slip boundaries with a friction of $\gamma_L = 5.26$ to maintain no-slip conditions. By measuring the resulting tunable-slip forces we can extract the viscous response of the solution. As the polymers are strongly confined and in principle also entangled, a bond-breaking criterion has to be defined for the high shear rates, as the harmonic bonds in principle could extend infinitely. Thus we will set the maximum bond length to

$$b_{\max} = 3.0 \quad . \tag{4.36}$$

If a monomer-monomer pair exceeds this value in the course of the simulation, the run is stopped. Indeed in most cases the bonds 'break' for $\dot{\gamma} = 1$.

4.12.2 Concentration and Flow Profiles

At first we take a look at the monomer distribution inside the channel as well as the distribution of ions. In the equilibrium situation we compare the case 'with' and 'without' surface charge. Additionally we show the behavior of neutral polymers to estimate the effect of the electrostatics.

All profiles are collected in Figure 4.24 for an overview. Generally, the main difference in all figures is that charged walls lead to adsorption, while neutral walls lead to a depletion, which is somewhat independent of the type of polymer (charged or uncharged). However, the two profiles deviate in the central area of the slit. In the case of charged surfaces one can observe some kind of shoulder effect on the peaks close to the boundaries. The shoulders become more pronounced for the higher concentration. For $N = 500$ and $H = 10$, all monomers are adsorbed to the surface, as the profile hits zero in the center. Interestingly the width of the depletion layer for uncharged surfaces is similar to the position of the shoulders. Like in the equilibrium profiles in section 4.6.1, the neutral

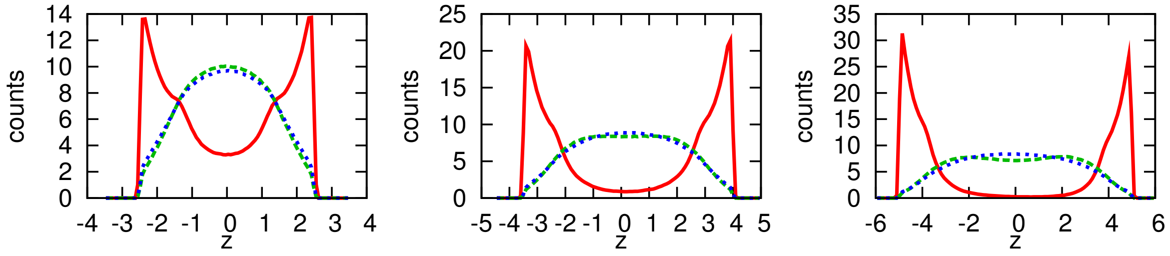

(a) $H = 5$ (b) $H = 7.5$ (c) $H = 10$

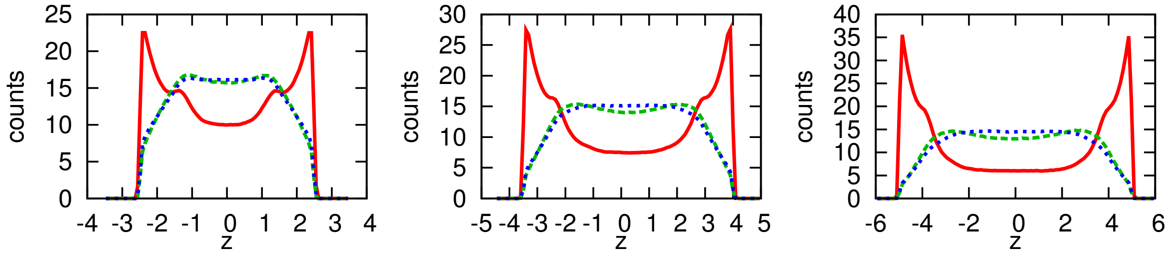

(d) $H = 5$ (e) $H = 7.5$ (f) $H = 10$

Figure 4.24: Thin-film monomer profiles for different slit heights H. (a)-(d) show the case $N = 500$, (e)-(h) show $N = 1000$. Compared are the profiles for charged walls (red lines), neutral walls (green dashed lines) and neutral polymers with neutral walls (blue dotted lines).

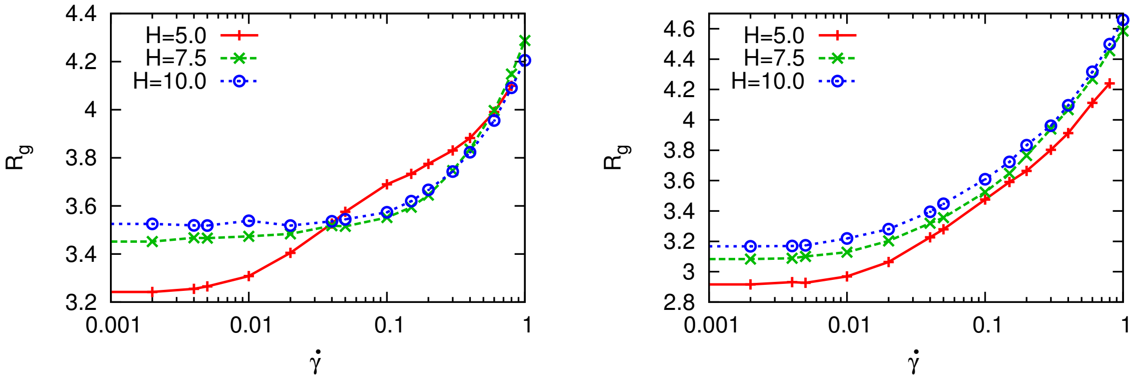

(a) $N = 500$ (b) $N = 1000$

Figure 4.25: Radius of gyration versus shear rate for the different slit heights. (a) shows the case of 500 monomers, (b) of 1000 respectively.

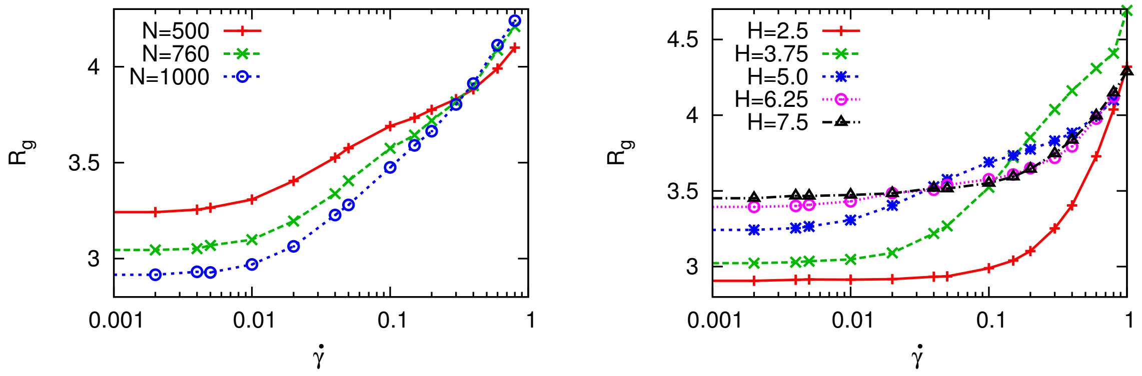

(a) $H = 5$ (b) $N = 500$

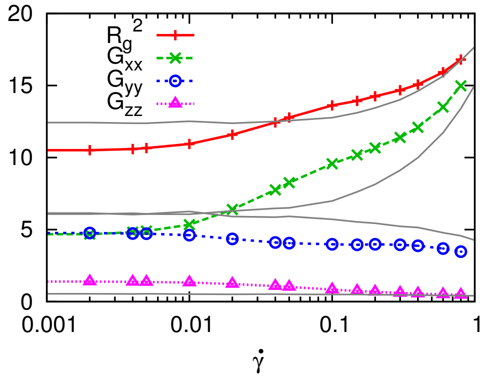

(c)

Figure 4.26: Radius of gyration with focus on the '$N = 500$, $H = 5$' system. (a) shows a comparison between different concentrations, (b) shows varying system heights. (c) shows the gyration-tensor components, where the gray lines are drawn for comparison for the '$N = 500$, $H = 10$' system.

boundaries still lead to a small excess of monomers adjacent to the depletion layer, leaving a small dip in the center.

4.12.3 Conformational Changes

For the conformational properties we focus on the charged-surface case. Figure 4.25 shows the R_g data for the three heights. Comparing the curves in (a) and (b), it becomes apparent that there is a significant deviation of the '$N = 500$, $H = 5$' system, which shows a crossover, while all the other curves have a similar slope. Generally, in the low shear range the conformations stay rather constant, where this range is shorter for the more concentrated systems in (b), showing that the higher concentration retains collective conformational changes.

To study the crossover for $N = 500$, $H = 5$' a little further, we try intermediate systems and compare the results, as done in Figure 4.26. In (a) we can see that all systems with height $H = 5$ but different concentrations seem to have a singular interception point. Figure 4.26b shows $N = 500$ with different intermediate heights, where the deviating behavior is clearly visible for $H = 5$ and $H = 3.75$, while the $H = 6.25$ curve is already aligned to the ones of larger height. Thus the crossover effect seems to be a unique phenomenon happening for a specific range of channel height, in relation to the monomer concentration, and presumably also to the chain length. Finally, in Figure 4.26c we can study the individual gyration-tensor components G_{ii} of the '$N = 500$, $H = 5$' system, where the gray lines are drawn to enable a comparison to the '$N = 500$, $H = 10$' system as a reference. Comparing the components, the zz-component is clearly decreased, which states that the chains align along the boundary directions. Interestingly, there is a shear threshold of $\dot{\gamma} \approx 0.005$ after which the xx- and yy-component split apart, where the former resembles the expected chain stretching in shear direction. This behavior can be compared to the Couette study of section 4.7.3, Figure 4.15, where the splitting sets in at a similar shear rate. In comparison to the $H = 10$ system, the yy-components stays rather constant instead of decreasing, which seems to be related to the clearly different slope in the xx-component and the resulting R_g curve. Thus in the smaller channel the polymers appear to be stacked in y-direction, whereas they are more freely arranged for $H = 10$.

4.12.4 Forces

To extract the contribution of the polyelectrolytes to the system's response, we define a reduced force in terms of the actually measured force F and the result from the system without polyelectrolytes F_0

$$F_{\text{red}} = \frac{F - F_0}{F_0} \quad . \tag{4.37}$$

The reduced force is thus a substitution for the reduced viscosity, which cannot be calculated accurately due to the strongly inhomogeneous total-density profile. However, the general trends of the viscous behavior are perfectly visible in the force itself.

Figure 4.27 shows the results in a comparison between charged and neutral surfaces. The data in the low shear-regime still lacks statistics. For high shear rates both cases agree mostly, for $N = 500$ and $N = 1000$ respectively. For smaller shear rates there appear deviations that should be explained a little further. In the case $H = 5$ (a) it seems that charged surfaces lead to a stronger force contribution for both concentrations. In the case $H = 7.5$ (b) the trend flips for $N = 500$. Similarly, for $H = 10$ (c) the neutral-surface values are higher for both concentrations. Thus there seems to be a transition somewhere in the concentration range

$$\frac{500}{50 \times 20 \times 7.5} < c < \frac{1000}{50 \times 20 \times 7.5} \quad . \tag{4.38}$$

Hence it appears that in the low shear regime the surface charge can lead to less lubrication for very thin films. This effect might be related to the wall-counterions re-

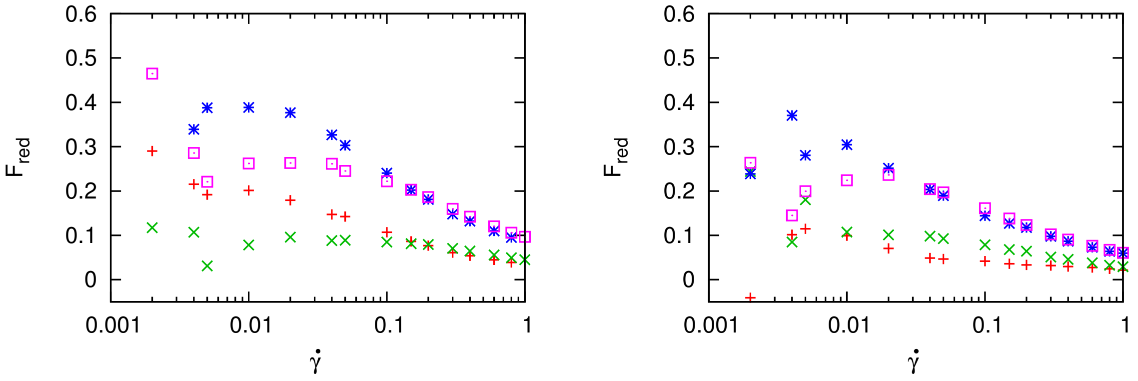

(a) $H = 5$

(b) $H = 7.5$

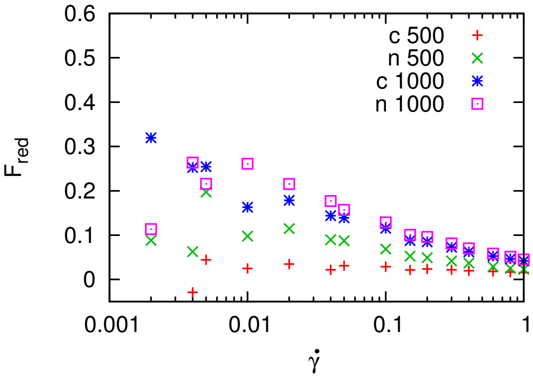

(c) $H = 10$

Figure 4.27: Reduced boundary forces over shear rate for charged [c] and neutral [n] surfaces, comparing monomer numbers $N = 500$ *and* $N = 1000$.

leased into the film and thus screening the electrostatic interactions, resulting in different conformations, or to the difference in adsorption and depletion.

4.12.5 Bridging

As the polymer chains are in principle long enough to be adsorbed to both surfaces at once, such configurations are of special interest due to the presumably large contribution to shear resistance. We can define a polymer as adsorbed to a surface if one of its monomers is inside the viscous layer of the given boundary, i.e. interacting with it by means of the tunable-slip forces. The definition of bridging then follows directly if a second monomer is in the viscous layer of the opposite boundary. Thus we can count the amount of free, adsorbed and bridging polymers and relate the ratio to the viscous response of the system.

Figure 4.28 shows the amount of bridging polymers for the case of structured surface charge. We can see that for $H = 10$ almost no polymers are in contact to both surfaces,

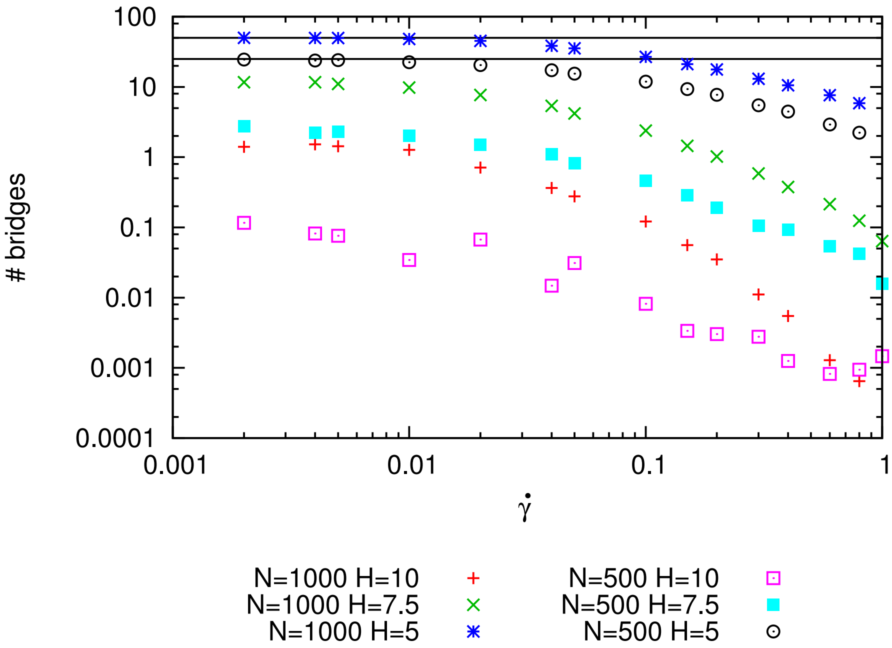

Figure 4.28: Amount of bridging chains (adsorbed on both surfaces) in the case of structured surface charge. The black horizontal lines mark 25 and 50, which is the number of polymers for $N = 500$ *and* $N = 1000$*.*

were for $N = 1000$ it is at least ≈ 2. For $N = 500$ this makes sense, as the monomer profile showed zero concentration in the center (see Figure 4.24). With increasing shear rate the bridging reduces further in all cases. For $H = 7.5$ we obtain about ≈ 3 and ≈ 10 bridges, whereas for $H = 5$ all polymers bridge the walls, at least in the low shear regime. Hence the chains cannot be aligned in layers to begin with. This changes for high shear rates, where the chains begin to extend in shear direction and thus the bridging is reduced.

4.12.6 Outlook

We have started to investigate thin films of polyelectrolytes in slits of different size and with charged/ uncharged boundaries. Up to now there seem to be clear deviations for the two boundary types. Neutral boundaries lead to depletion of polyelectrolytes, while charged boundaries lead to adsorption. There are also strong deviations in the change of conformations with shear rate. The viscous forces measured with both surface types seem to be in different relations depending on the film height. More simulations with structured surface charges will be performed in the near future to have a third case for comparison. Then it would be interesting to relate the bridging between boundaries to effects on the viscous force. Also, the crossover behavior for '$N = 500$, $H = 5$' might have an effect on the force. An amplification of the effects might be possible by switching to longer chains. Also, comparisons to uncharged chains and cases with higher salt concentrations are possible.

Chapter 5

Electro-osmotic Flow on Superhydrophobic Surfaces

5.1 Theoretical Background

In recent years the scientific interest in microfluidic devices has grown rapidly. Approaching the nano-regime, the concept of electro-osmotic flow plays an increasing role, as generating pressure-driven flows becomes problematic for very narrow channels on the submicron scale. In such situations the viscosity of the solution often prohibits the desired flow rates. Instead of using pressure gradients, electro-osmotic flow on the other hand is induced by an external electric field, which additionally has the advantage of being easily controllable. Hence so-called electro-hydrodynamic pumps have been developed [143, 144] that use electric forces and have no mechanically moving parts. Also, such microfluidic flows can be used in terms of electrokinetic batteries [145].

5.1.1 First Principles

The flow rate is physically described by the mobility M, which is the ratio of applied field and resulting velocity

$$M = -\frac{U}{E} \quad . \tag{5.1}$$

In the case of a simple slit geometry with an electrolyte solution confined between two charged surfaces of surface charge q_s and the electrostatics described on the Debye-Hückel level, M can be estimated by the Smoluchowski formula

$$M = \frac{q_s}{\eta\kappa} \quad , \tag{5.2}$$

with η the solvent viscosity. This equation assumes sticky boundaries, such that the velocity profile vanishes there. As described earlier in chapter 3.2, this is not always correct as slippage may appear, which is especially true for nanoscale geometries. As the apparent slip effect can modify the flow considerably, the specific character of the surfaces comes into play as a control parameter. The Smoluchowski formula in the case of slippage has to be modified

$$M = \frac{q_s}{\eta\kappa}\left(1 + \kappa b\right) \quad , \tag{5.3}$$

where an additional term enters with the slip length b.

5.1.2 Superhydrophobic Surfaces

The increase in mobility due to pure slippage on surfaces is limited. Slip lengths can be of the order of tens of nanometers [146, 147, 148], while typical Debye lengths are of the order of nanometers as well, leading to a mobility increase of about one order of magnitude. Here the concept of superhydrophobic surfaces gives opportunity for further improvements. The idea is to no longer shape the surfaces in a homogeneous way, but to cut slots for so-called gas sectors, which results in a dramatic enhancement of the slippage effect. In this situation the different slippage on the actual surface material, in many cases mica, and the gas sectors combines into an effective slip length b_{eff}, which can be as large as several microns [149, 150, 151].

5.1.3 Theoretical Predictions

By breaking the isotropy of the surfaces, the slip length is no longer a scalar quantity but obtains a tensorial character, which by no means is simple to derive. Theoretical attempts have been made concentrating on symmetric geometries, such as the stripe pattern on which we will focus in this study. The surface is constructed by placing a pattern of solid and gaseous stripes in x-direction, with the stripes extending infinitely in the y-direction. By assuming no-slip conditions for the solid stripes, we obtain a periodic slip/no-slip pattern in the xy-plane.

The theoretical predictions obtained by Belyaev et al. [152] are based on flow over a single surface in a system which is semi-infinite in z-direction. This is analogous to the assumption that the periodicity L of the stripe pattern is much smaller than the height of the actual microfluidic channel. By applying the Debye-Hückel approximation to the electrostatics and assuming an electric double layer that is rather thin

$$\kappa L \ll 1 \quad , \tag{5.4}$$

they were able to predict the components of the 2×2 slip-length tensor $\boldsymbol{b}_{\text{eff}}$ and thus of the mobility tensor, by dividing into flows in x-direction, i.e. transverse to the stripe pattern, and y-direction, i.e. parallel to the stripe pattern, as illustrated in Figure 5.2. We mark the solid, no-slip stripe with index 1 and the gas-sector with index 2, i.e. their surface-charge densities are accordingly named q_1 and q_2 and we use b to describe the slip on the gas sectors. The surface fraction can be expressed in the form

$$\phi_1 + \phi_2 = 1 \quad , \tag{5.5}$$

where only one component, e.g. ϕ_2, is required to describe the surface ratio in calculations. In this formulation, the mobility tensor can be expressed as

$$\boldsymbol{M} = M_0 \cdot \left[\boldsymbol{I} + \frac{\boldsymbol{b}_{\text{eff}}}{b} \left(\frac{q_2}{q_1}(1 + \kappa b) - 1 \right) \right] \quad . \tag{5.6}$$

Here, M_0 is the classical Smoluchowski value of Equation 5.2 for simple no-slip surfaces with the parameters of the solid stripes and $\boldsymbol{I}$ is the 2×2 unit matrix. The eigenvalues of $\boldsymbol{b}_{\text{eff}}$

$$\begin{pmatrix} b_{\text{eff}}^{\perp} & 0 \\ 0 & b_{\text{eff}}^{\parallel} \end{pmatrix} \tag{5.7}$$

can be determined numerically, or by the approximative formulas

$$b_{\text{eff}}^{\perp} \simeq \frac{L}{2\pi} \frac{\ln[\sec(\frac{\pi\phi_2}{2})]}{1 + \frac{L}{2\pi b} \ln[\sec(\frac{\pi\phi_2}{2}) + \tan(\frac{\pi\phi_2}{2})]} \tag{5.8}$$

$$b_{\text{eff}}^{\parallel} \simeq \frac{L}{\pi} \frac{\ln[\sec(\frac{\pi\phi_2}{2})]}{1 + \frac{L}{\pi b} \ln[\sec(\frac{\pi\phi_2}{2}) + \tan(\frac{\pi\phi_2}{2})]} \quad . \tag{5.9}$$

The resulting mobility can be quite diverse due to the rich parameter space consisting of ϕ_2, b, q_1 and q_2. Details of the theoretical predictions will be discussed later on, when the simulation data are evaluated.

5.1.4 Simulation Details

With the numerical results at hand, it became desirable to verify them by means of mesoscopic simulations. In particular since the calculations were performed on the Debye-Hückel level of electrostatics, a comparison to a more sophisticated level could give valuable information about the applicability and the range of validity of the theory. The problem of electro-osmotic flow had been successfully studied with a combined DPD explicit-ion approach [77, 90] in the past. In this specific problem, however, the geometry requires for fairly large simulation boxes, as there are three different length scales involved, namely first of all the thickness of the electric double layer κ^{-1} and the periodicity of the pattern L. Thirdly there is the height of the channel H, which has to be considered as we cannot deal with a semi-infinite situation like in the theoretical approach. Hence one would like to reduce κ to be able to have a small L and H and thus a smaller box. However, keeping the double layer as small as possible still increases the computational effort as this requires a fairly high amount of salt to be dealt with. Thus the application of the condiff method instead of explicit charges is of obvious advantage.

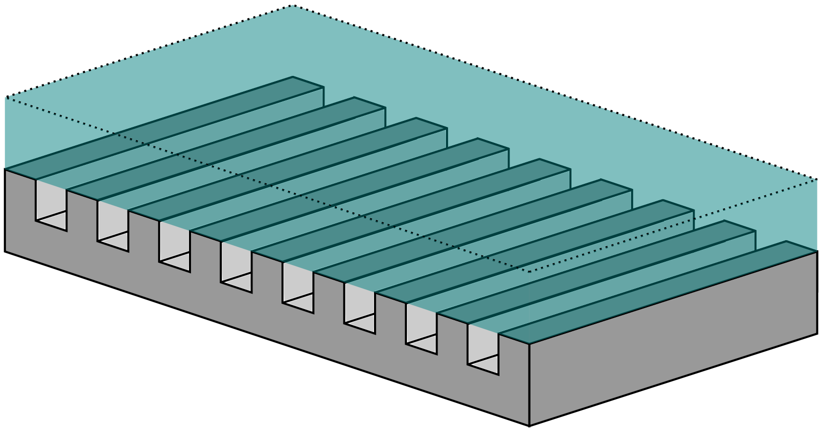

Figure 5.1: Illustration of a superhydrophobic surface with gas sectors.

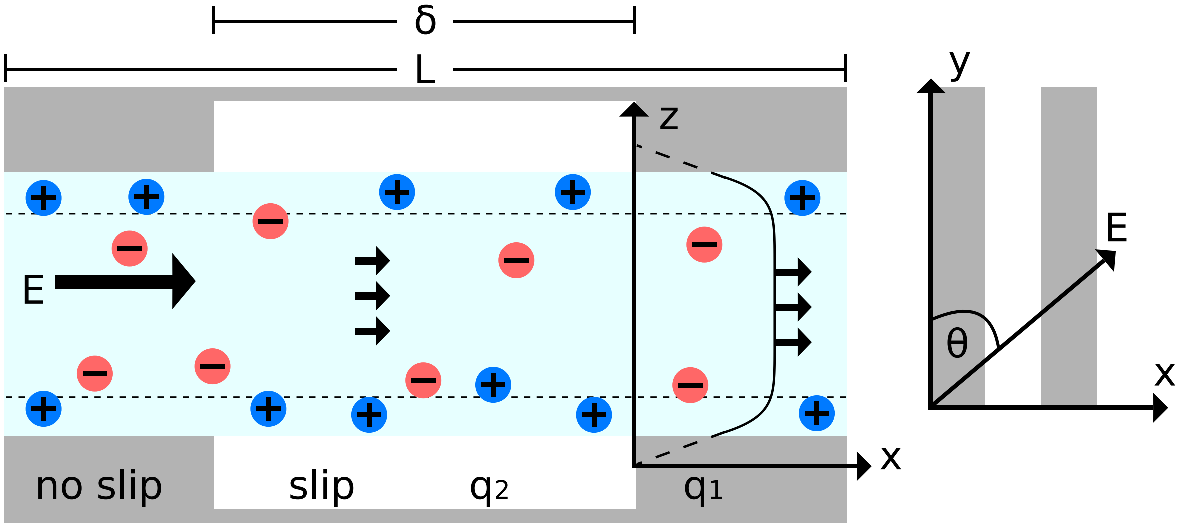

Figure 5.2: Illustration of the slit geometry. The electrolyte solution is confined between two plates with sections of different slippage and different surface charge q_1 and q_2, one representing the substrate material and the other representing the gas sectors in the slots. The sector width δ leads to a periodic pattern, where the simulation box resembles one such unit of length L. By applying an electric field, a plug-flow profile is established where the finite slippage effects can be described by an effective slip length. The right cartoon shows the stripe pattern in the xy-plane, illustrating that the flow direction can be chosen by setting an angle Θ accordingly, $\Theta = \pi/2$ meaning transverse flow and $\Theta = 0$ meaning parallel flow.

case	q_1	q_2	ϕ_2	b (in gas sector)
A	0.5	0	0.5	varying
B	0.25	0.25	0.5	varying
C	0.25	-0.25	0.5	varying
D	0.25	-0.25	varying	13.31

Table 5.1: Overview of the parameters in the four studied cases. In all situations $\kappa = 1.01$.

Some of the simulations have been repeated with coarse-grained molecular dynamics and explicit charges. A comparison of the results and especially of the runtimes will be presented at a later point in this chapter.

We start out with a simulation box of size $50 \times 20 \times 55$, so that we obtain a wide slit by placing the boundaries at $z = 0$ and $z = 50$. Due to the WCA repulsion, the resulting penetrable volume is $50 \times 20 \times 48$. The additional empty gap of size 5 is necessary for the electrostatic layer correction. The system is split in x-direction into two parts of different surface charge and slip length. The left part of the boundaries is equipped with a no-slip boundary condition by the choice $\gamma_L = 5.26$ and the right part is taken to have a varying slip length b. The surface charge is modeled by frozen particles sitting directly on the boundary in a $(1\sigma, 1\sigma)$ mesh, charged with the appropriate charge fraction. The DPD fluid with density $\rho_{\text{DPD}} = 3.75$ is set up with the standard parameters. As we encountered a problem with ELC in the case of uncharged slip areas, only the dipole-correction term is taken. This is further described in section 5.4. All simulations have been performed on the MOGON cluster at the Universität Mainz, equipped with AMD Opteron(TM) Processor 6272 at 2100MHz. The simulations ran in shared-memory parallelization with OpenMP in clusters of eight threads. Due to the low electric field, rather long simulation times were necessary to reach steady-state flow. Also, the runtime for averaging the flow profile had to be long due to the fluctuations that are similarly strong as the driving force. Error bars are obtained by means of a block analysis of the samples.

We will distinguish between four different cases throughout this study, by which we follow the approach of Belyaev et al. [152]. The case A consists of a charged no-slip area with $q_1 = 0.5$ and an uncharged gas-sector, $q_2 = 0$, of same size, i.e. $\phi_1 = \phi_2 = 0.5$. In case B we deal with a uniformly charged surface, $q_1 = q_2 = 0.25$, where again $\phi_1 = \phi_2 = 0.5$. The case C is a modification, where the two areas are now oppositely charged, i.e. $q_1 = -q_2 = -0.25$. In all three cases we vary the slip length b of the gas sector in a range $b/L \in [0 : 10,000]$ and study the change in mobility. In case D we take the geometry of case C, but vary the surface fraction ϕ_2 systematically with a fixed $b = 13.31$. Table 5.1 again summarizes the four parameter sets. All systems are filled with the appropriate amount of counterions N_c and salt ions N_s, so that we end up with

$$\kappa = \sqrt{4\pi \frac{N_c + 2N_s}{V}} = 1.01 \quad . \tag{5.10}$$

5.2 Slip Length Determination

Before studying the electro-osmotic flow, we first have to determine the relation between the friction parameter γ_L involved in the tunable-slip boundary interactions and the resulting slip length. While the tunable-slip boundary method is capable of modeling any desired slippage on the boundaries, there exists only an approximate analytical formula for the slip length b as a function of the friction parameter. The actual slip length can be calculated from studying the system in flow situations that can be expressed analytically, allowing the slip length to be extracted accurately.

5.2.1 Analytical Formula

The analytical formula, which was derived in the work of Jens Smiatek [90] leads to

$$b(\gamma_L) = \frac{2}{\alpha(\gamma_L)} - \frac{7}{15} - \frac{19\alpha(\gamma_L)}{1800} + \frac{293\alpha(\gamma_L)^2}{772625} + ... \tag{5.11}$$

with

$$\alpha(\gamma_L) = \frac{\rho\gamma_L}{2\eta_s} \quad . \tag{5.12}$$

The formula works reasonably well for large slip lengths, but becomes worse in the limit $b \to 0$.

5.2.2 Flow Profile Method

In the context of simulations, the slip length can be determined by studying both the Poiseuille and the Couette flow in the system and combining the obtained flow properties. We take the same geometry but leave out the stripe pattern, such that the flow occurs in x-direction and the system is confined by the boundaries in z-direction, hence due to symmetry there is only a z-dependence. We start out with the analysis of a homogeneous density in the slit. This assumption will be discussed later on. From the Stokes equation, the Poiseuille flow is determined by the solution of

$$\eta_s \partial_z^2 v(z) = -\rho F^{\mathrm{ext}} \quad , \tag{5.13}$$

with the external force driving the flow. Solving this equation with the partial-slip boundary condition

$$v(z)|_{z=z_B} = b \left(\frac{\partial v(z)}{\partial z} \right)_{z=z_B} \tag{5.14}$$

by double integration leads to

$$v(z) = \frac{\rho F^{\mathrm{ext}}}{2\eta_s} \left(z_B^2 - z^2 + 2bz_B \right) \quad , \tag{5.15}$$

with the quadratic dependence on z and the well-known parabolic flow profile.

The plane Couette flow is induced by oppositely directed movement of the boundaries with a velocity v_0 and $-v_0$. The Stokes equation becomes

$$\eta_s \partial_z^2 v(z) = 0 \tag{5.16}$$

and the boundary condition is

$$v_0 \mp v(z)|_{z=\pm z_B} = b \left. \frac{\partial v(z)}{\partial z} \right|_{z=\pm z_B} \quad . \tag{5.17}$$

The solution leads to the well-known linear flow profile

$$v(z) = \frac{z v_0}{z_B + b} \quad . \tag{5.18}$$

As the slip length b in both cases appears together with the position of the hydrodynamic boundary z_B, they are both required. Thus we perform a parabolic/linear fit

$$\begin{aligned} v_p(z) &= A_p(z-0)^2 + B_p && (5.19) \\ v_c(z) &= A_c z + 0 && (5.20) \end{aligned}$$

and can determine both the slip length b and the hydrodynamic boundary position z_B from the fit parameters

$$\begin{aligned} b &= \sqrt{\frac{v_0^2}{A_c^2} + \frac{B_p}{A_p}} && (5.21) \\ z_B &= \frac{v_0}{A_c} - b \quad . && (5.22) \end{aligned}$$

One difficulty occurs in the range of small slip lengths, starting with $\gamma_L \approx 1$, when the term under the square root may become negative. In this case one can make the assumption that the hydrodynamic boundary position stays constant for any γ_L and determine it from simulations with smaller γ_L. Then one can calculate the slip length using the constant z_B value

$$b = -\frac{B_p}{2A_p z_B} - \frac{1}{2} z_B \quad . \tag{5.23}$$

5.2.3 Results

We are especially interested in the friction value that gives a no-slip boundary condition. As the reference system, we take the settings of the no-slip area in the case B described later, i.e. a surface charge density of $q_1 = 0.25$. As we need very accurate flow profiles,

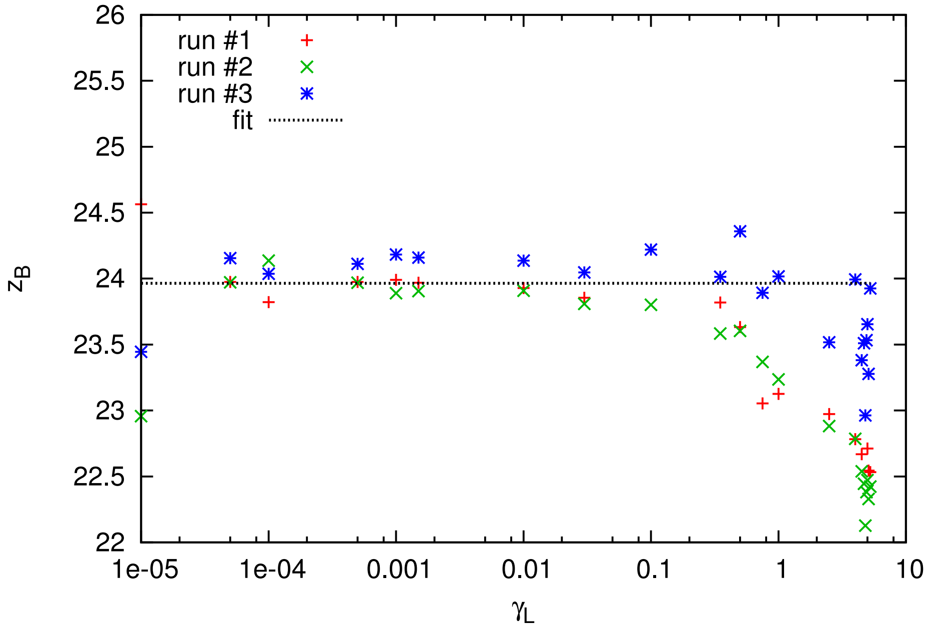

Figure 5.3: Determination of the hydrodynamic boundary position in the three runs. The fit is done with a constant.

we try to speed up the simulations by reducing the system size in y-direction to end up with an effective volume of $50 \times 4 \times 48$. We take $F^{\text{ext}} = 0.01$ and $v_0 = 2.5$ as standard values, however, allowing higher Couette velocities in the case of higher slip lengths. The reason is that for high slippage the flow profiles become extremely flat and therefore highly perturbed by thermal fluctuations. Therefore it is convenient to increase v_0 to obtain better averages . An equilibration time of at least 12M steps is allowed to let the system reach its steady state. Then we average the flow profiles three times consecutively over >7M steps measuring every 100 steps. The flow profiles are fitted by considering only the range $[-22.5, 22.5]$, i.e. leaving out 1.5 adjacent to each boundary. Due to the problem with the negative term under the square root we determine the hydrodynamic boundary position first.

Figure 5.3 shows the resulting values for z_B, where it is quite obvious that the data becomes untrustworthy for $\gamma_L > 0.5$. Thus we fit a constant to the range $[5 \cdot 10^{-5} : 0.5]$, and we obtain

$$z_B = 23.96 \quad . \tag{5.24}$$

Thus the channel has an actual width of $2z_B = 47.92$, which is close to the assumed 48 and definitely in the error range as seen in Figure 5.3. However, this also indicates that even with large samples it can be quite tricky to determine z_B an thus b accurately.

If we now assume a fixed z_B with varying γ_L, we can calculate b easily with Eq. (5.23). Table 5.2 shows the resulting slip lengths, where the values for γ_L have been chosen arbitrarily to cover a certain range.

Up to $\gamma_L = 2.5$ the relative errors were quite low. For larger γ_L it becomes difficult

γ_L	b	b/L
0.00001	137066.92	2741.338
0.00005	28399.80	567.996
0.0001	14275.16	285.503
0.0005	2836.90	56.738
0.001	1418.40	28.368
0.0015	945.93	18.919
0.01	141.91	2.838
0.03	47.08	0.942
0.1	13.9	0.278
0.35	3.75	0.075
1	1.1	0.022
2.5	0.26	0.005
5.26	0.000	0.000

Table 5.2: Collection of the applied γ_L and the corresponding slip lengths for the gas sectors up.

to determine an exact b as one is approaching the no-slip case. Relative errors become quite large and the determination of the exact no-slip value is not feasible. Simulations of pure DPD liquids in smaller channels led in other studies [153] to the result

$$\gamma_L = 5.26 \Rightarrow b = 0 \tag{5.25}$$

for the no-slip case. Thus we continue with $\gamma_L = 5.26$ as the no-slip parameter. A further investigation of the area around $b = 0$ will be presented in the next section.

5.2.4 Charged and Uncharged Systems

When dealing with charged solutions and charged boundaries, the assumption of homogeneous density no longer holds true. Due to the charged surface there will be an increase in density adjacent to the walls coming from the counterions. This is a local effect, so that the overall parabolic/linear shape of the flow profiles is only perturbed in the proximity of the boundaries. However, due to the locally higher density, there is also a larger interaction with the boundaries in the viscous layer. The result is that the same γ_L can lead to smaller slip lengths than in the pure DPD case. Before quantifying the effect, we first want to take a look into the distribution of ions and the flow profile in the Poiseuille case.

Figure 5.4a shows the density profiles in the charged case and for a neutral system. As the salt density in this study is quite high, the relative increase at the boundaries is lower than e.g. for the pure counterion systems discussed in chapter 3.2. Here it reaches about 8%, where about 1% is already a pure DPD-boundary effect, as visible for the neutral system and also noted in section A.4. The resulting flow profiles in (b) differ slightly in the maximum velocity, where the charged system is a little slower. This is the direct result of the increased density at the boundaries, as dissipation increases as

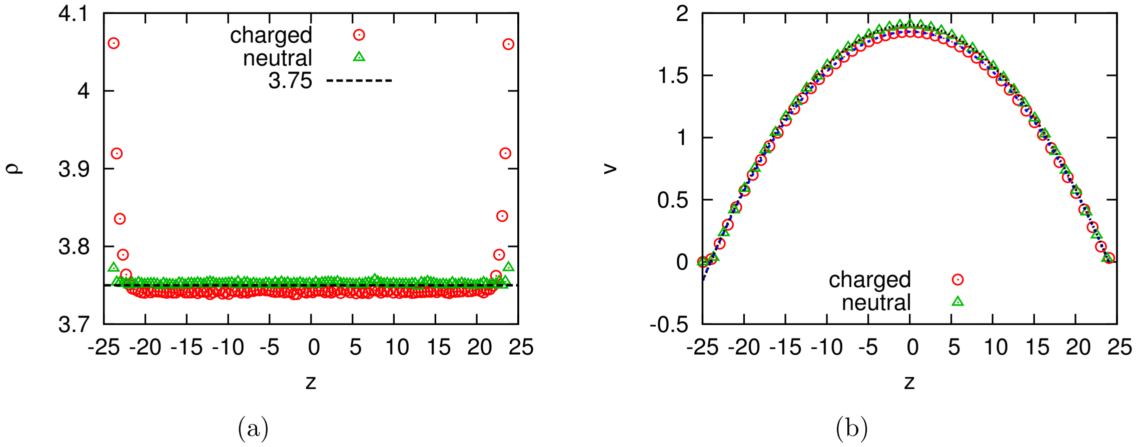

Figure 5.4: Comparison of Poiseuille flow in a charged and an uncharged system with $F = 0.0025$*. (a) shows the difference in the density profile with the increase at the boundaries due to the counterions. (b) shows the changes in the flow profile.*

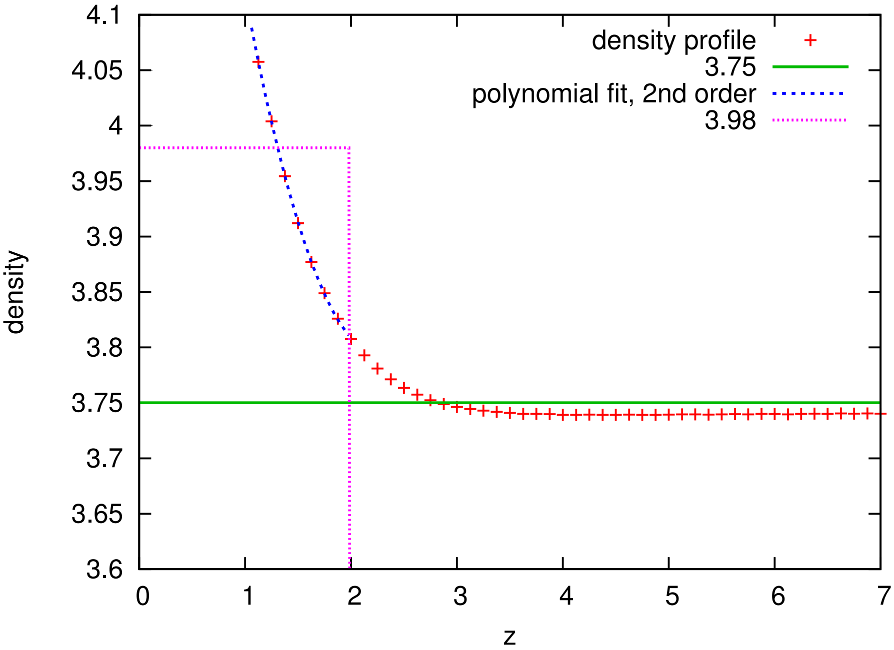

Figure 5.5: Density profile at the boundary. 3.75 is the average system density, 3.98 is the mean density in the viscous layer determined from Eq. (5.26).

well. However, the final deviation is quite low. Fitting the velocity profiles in 5.4b with a parabolic curve, the charged profile shows stronger deviations away from the center, which is also due to the inhomogeneous density.

5.2.5 Estimation of the Effect of the Density Increase

When comparing the slip lengths, over a large range of the friction parameter γ_L there is basically no difference between the uncharged and charged systems. However, when approaching the no-slip condition the charged system shows the expected tendency to lower slip lengths. We now estimate the effect of the increased density by modifying the analytical formula. Therefore we first approximate the density in the viscous layer by a polynomial of second order $P_2(z) = a + bz + cz^2$. To go by importance, we multiply with the tunable-slip weighting function $\omega(z) = 1 - \frac{z}{2}$, to calculate a mean density in the viscous layer

$$\bar{\rho} = \frac{1}{\int_1^2 \omega(z)dz} \int_1^2 P_2(z)\omega(z)dz \quad . \tag{5.26}$$

In this case the result is $\bar{\rho} = 3.98$. We can plug this density into the analytical formula for the slip length, given in the form of Eq. 5.11, instead of using the homogeneous value $\rho = 3.75$. Then we compare with the simulation data, shown in Figure 5.6. In any case, the formula has to be adapted, as it does not predict the no-slip crossover correctly. Therefore we shift it with a constant offset. For the pure DPD case, the offset is taken from the results at $\gamma_L = 5.26$. For the charged case we take the approach to fit the analytic formula (using the calculated mean density) via a constant offset to the data in the range $[1 : 5.26]$. The parameter for no-slip is then obtained from the zero-crossing, with the result $\gamma_L = 4.5$. The deviation between the charged and uncharged case is shown in Figure 5.7.

The modified analytical formula and the simulation results agree well over the entire range of positive b, so that it is legitimate to use the formula to calculate any additional slip lengths not measured by simulation. The result on the exact no-slip parameter is still a little controversial. Additionally the uncertainty of z_B comes into play, as described in the previous section. This analysis has been performed after the initial simulations, in which we had started out with $\gamma_L = 5.26$. However, the actual deviation from no-slip was insignificantly low, as $\gamma_L = 5.26$ leads to $b \approx -0.01$. Therefore we will proceed with the original value $\gamma_L = 5.26$ instead of using $\gamma_L = 4.5$.

5.3 Simulation Results and Comparison to Theory

Figure 5.8 shows an exemplary flow profile used to determine the mobility. Here it is a case B system (homogeneously charged surface) with a relatively high slip length, thus the strong jump in velocity at the boundaries. We determine the velocity by fitting a constant to the central region of the slit. All systems were equilibrated first and then

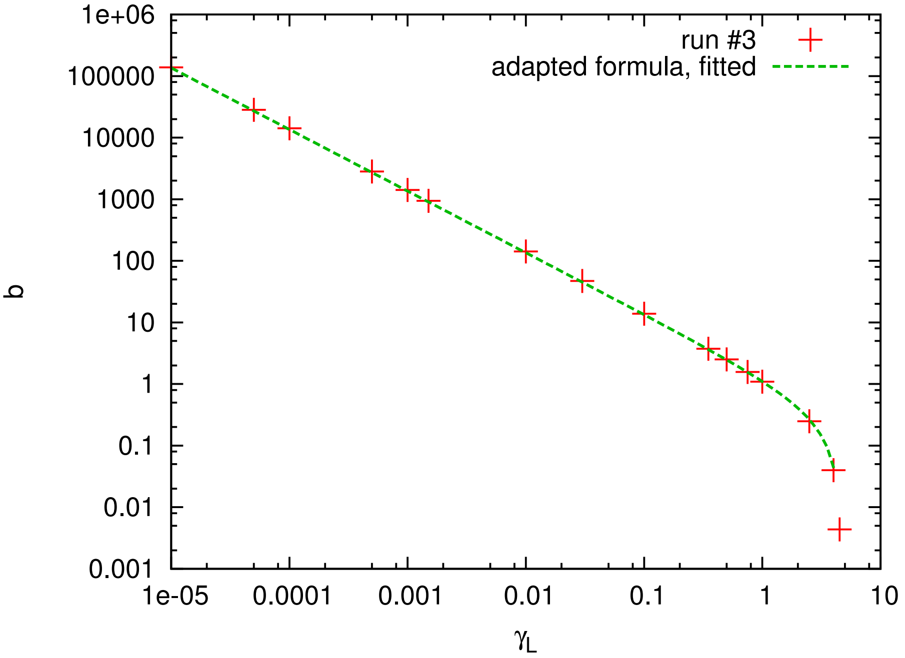

Figure 5.6: Slip length versus boundary friction γ_L in logarithmic scale. The figure shows the overall agreement of the adapted theoretical formula (Eq. 5.11 with $\bar{\rho}$) and the data.

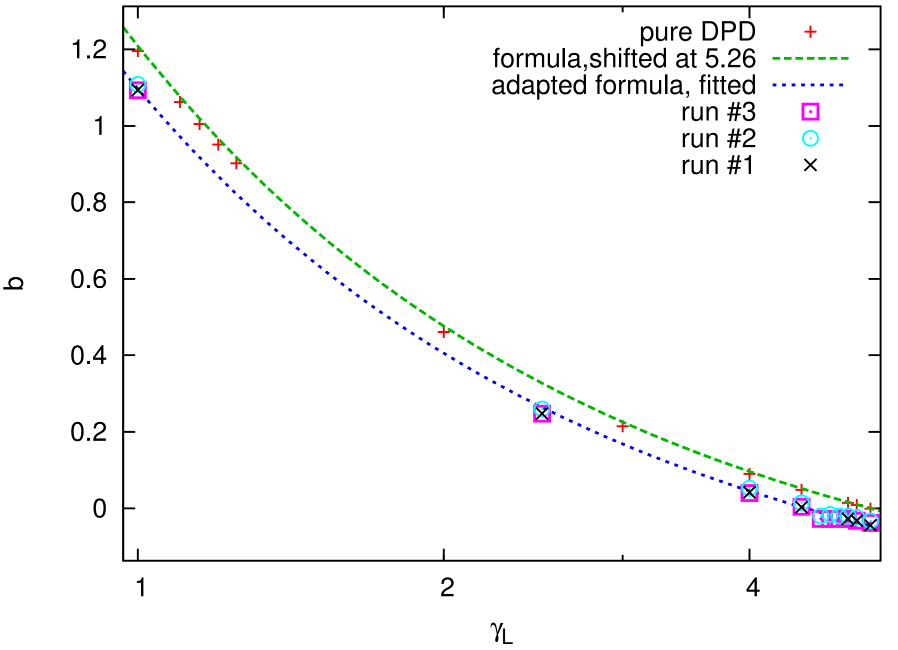

Figure 5.7: Deviations of the pure DPD results from the charged system in the range close to the no-slip condition. The x-axis is held in logarithmic scale. Also shown is original formula (Eq. 5.11) for the pure DPD data and the adapted formula (Eq. 5.11 with $\bar{\rho}$) for the results with charges.

simulated until reaching steady-state flow, which dependent on the parameters took up to 5M steps. The profiles were then averaged over a range up to $\sim 6M$ steps, sampling every 100 steps. As a runtime estimate, it took about 5 days to perform 1.5M steps. Because of the overall worse statistics in case A, these systems ran additionally for another 3M steps.

Figure 5.9 shows the results for the cases A, B, C and D as listed in Table 5.1. As the deviations in A require some further investigations, we will first focus on the other ones. The simulations done for cases B and C both agree with the theoretical predictions of [152]. Qualitatively, the agreement is quite visible, while the quantitative agreement is also quite well, considering that there is no fit parameter involved. The homogeneously charged surface in case B, meaning that the gas sectors themselves carry charge, is actually not an unlikely condition [154]. The result is a strong enhancement of flow in parallel direction, i.e. along the stripes, while the enhancement in perpendicular direction is not that high. Also the simulations predict a larger difference between the two components than the theory does. The case C with the oppositely charged areas is quite interesting. Here the mobility starts out at zero, as the two opposite flow processes compete with each other. As the slip length increases, the flow on slippery sectors dominates, which results in negative mobilities. Here again the longitudinal flow shows a much stronger enhancement, which again is more pronounced in the simulations than in the theory. Figure 5.9d shows case D, i.e. the surface-fraction dependence of case C, where the gas-sector area ϕ_2 is increased from 0% to 100%, here for a certain fixed slip length of $b/L \approx 0.27$. One can observe that the flow starts out positive and then changes sign once the gas-sectors become dominant. This inversion can already take place for very small surface fractions ϕ_2, depending on the slip length. This results in a very rich diversity of possible flow situations, depending on the surface parameters.

The case A of uncharged slip areas is shown in Fig. 5.9a. As flow can only originate close to a charged surface area, the theory predicts a general inhibition of flow in comparison to a homogeneous surface, regardless of the direction. Thus for $b \approx 0$, the mobility is just half of M_0. In this situation the uncharged area only slows down the flow. As the slip length is increased, the influence of the uncharged area decreases just like the dissipation, so that the curves saturate at $M/M_0 = 1$. However, the increase is different for longitudinal and transverse flow, where the latter is predicted to be favored. In the simulational data the transverse flow seems to agree to this prediction, whereas the longitudinal direction behaves quite differently. While it still saturates, the threshold lies at about $M/M_0 = 1.35$, i.e. clearly higher than M_0.

Thus we want to investigate this case a little more in detail. We start out by looking into the ion distributions along the two surface areas, which are shown for the equilibrium situation in Figure 5.10 by red symbols. The curves are produced by counting all ions that stay in the viscous layer (2σ from the boundaries). As anticipated, there is a strong accumulation of counterions close to the charged surfaces in $[0 : 25]$. For the uncharged area $[25 : 50]$ one would expect a charge neutral situation. However, this is only the case for a short range in the center, i.e. around $x = 37.5$, as the counterions from the charged area are hanging over into the neutral area on both edges. This overhanging effect might

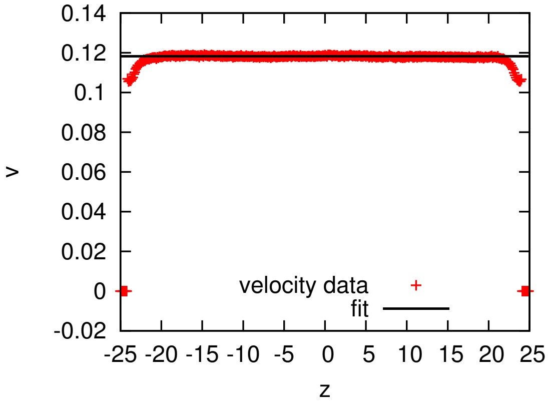

Figure 5.8: Exemplary flow profile and fit. Here it is case B with $b = 1418.4$ *and flow in y-direction (parallel flow).*

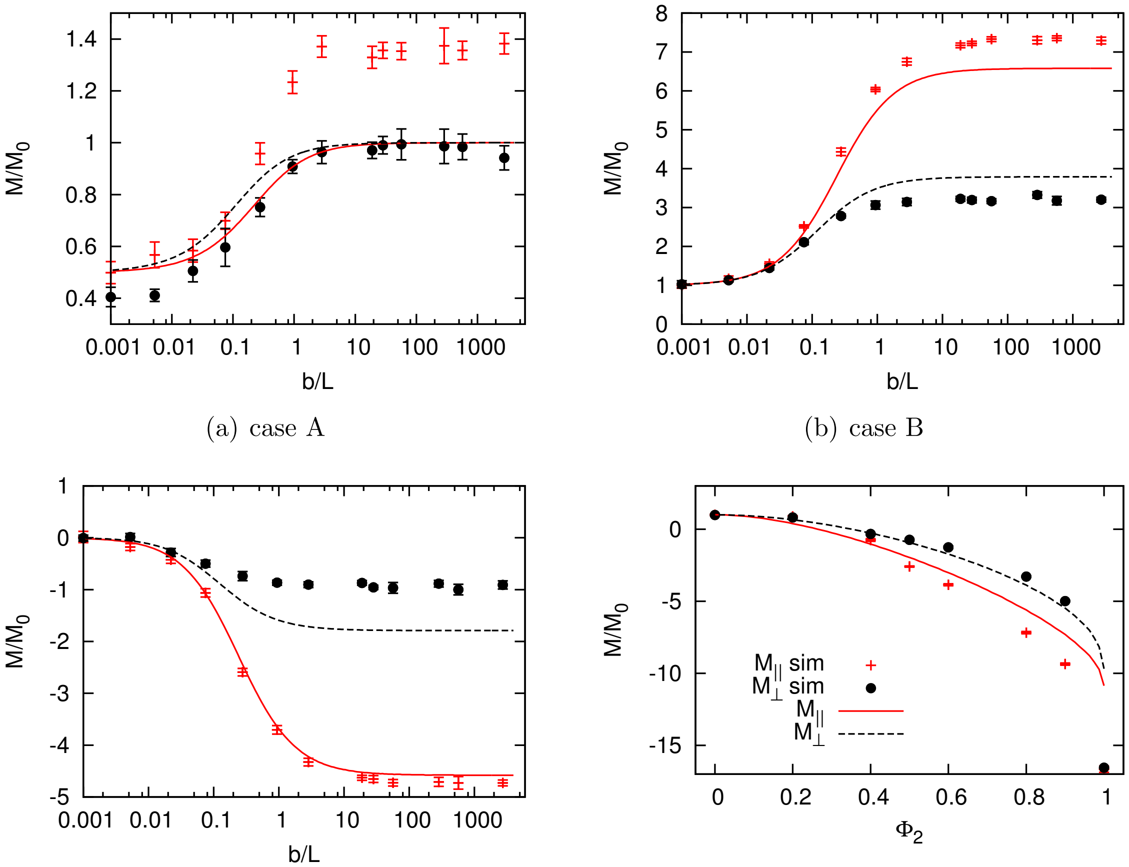

(a) case A (b) case B

(c) case C (d) ϕ_2-dependence of C

Figure 5.9: The normalized mobility of the three different cases (a,b,c). The plots show both the theoretical and simulation results of the normalized mobility over slip length for flows in perpendicular and parallel direction. The area-fraction dependence of system C shown in (d).

be the reason for the qualitative difference to the theoretical predictions in Figure 5.9a, since the theory includes the approximation of a clear cut between the two areas and not such a smooth transition.

Once the charge neutrality is broken in the neutral area, the flow benefits from its large slip length. A charge in the slippery area can produce a larger contribution to the flow than in the no-slip area, due to the lower dissipation. Speaking of single charges, if the flow is induced in the transverse direction, these charges will hit the charge-neutral area around $x = 37.5$ and the no-slip area in their motion and thus are slowed down again. In summary, the effect will be the same. For longitudinal fields, however, these charges experience a constantly high slip in flow direction, thus contribute strongly to the flow. Once in the large slip-length regime of Figure 5.9a, the increase in mobility is ultimately limited by the friction in the no-slip area, so that the curve saturates.

5.3.1 Case A with Reduced Charged Stripe

To test whether the overhanging effect is responsible for the strong deviations in the mobilities, we investigate the case A with a reduced surface charge by removing two rows of charges in y-direction at each of the two edges of the no-slip area, as illustrated in Figure 5.11. That way the charged area $[2 : 23]$ is centered in the no-slip area $[0 : 25]$ and the overhanging should be decreased. The resulting ion distributions are also shown in Figure 5.10, represented by the black lines. Indeed the overhanging is reduced and the neutral area increased. The resulting mobilities are shown in Figure 5.12 in comparison to the original theoretical data, where we have to distinguish two normalizations. The first one in (a) uses the original M_0. The result of a reduced charged stripe is that both mobilities are decreased in the high slip-length regime. As there is still a small overhanging visible in Figure 5.10, the longitudinal mobilities still exceed M_0. However, they appear to agree better with the theoretical prediction than their transverse counterparts. In Figure 5.12b a scaled mobility is shown, where the original M_0 is decreased by a factor $21/25$ due the subtraction of four rows of charges. For this normalization the transverse data agrees quite nicely, while the longitudinal data shows an excess that is comparable to the original one in Figure 5.9a.

Important for the interpretation is also the behavior for $b \to 0$. The theoretically predicted $M = 0.5M_0$ is originally only fulfilled for longitudinal flow (Figure 5.9a). The transverse mobility seems to be reduced in this case. When looking into the scaled and unscaled comparison of Figure 5.12, the deviation seems to be dependent. The unscaled mobility seems to be the appropriate one for the longitudinal flow, as the mobility hits 0.5 and agrees overall better than in the scaled plot. The transverse mobility, however, shows exactly the opposite behavior, with a much better agreement in the scaled case and $M = 0.5M_0$ for $b \to 0$. Hence it appears that the two flow directions have different reference systems, where the longitudinal flow should be referred to a homogeneous-surface system with the original charge, and the transverse flow should be referred to a homogeneous-surface system with the reduced charge of $21/25$.

Besides this detailed view on the individual mobilities, there is still the issue that

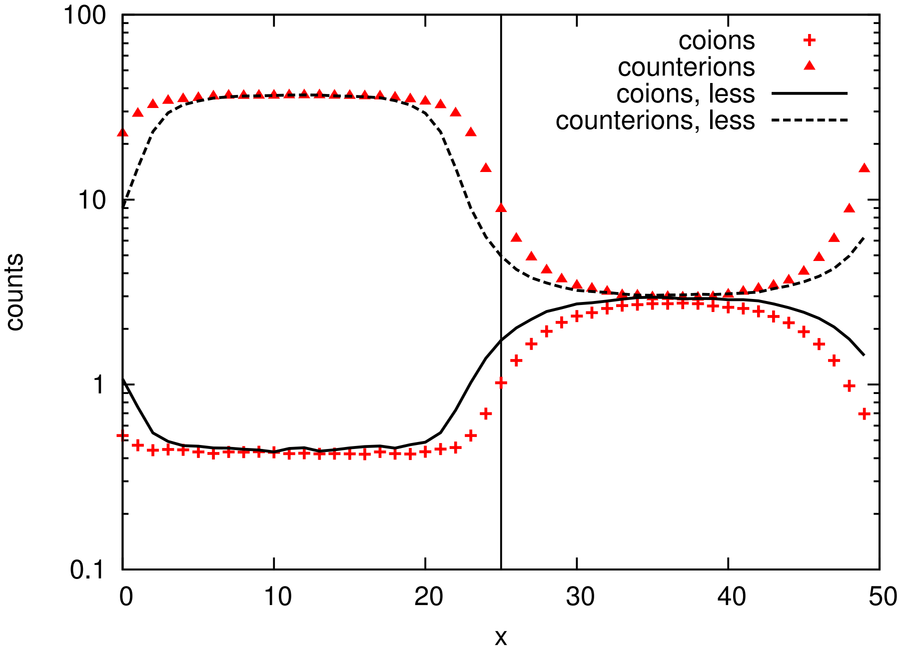

Figure 5.10: Ion distribution (logarithmic) adjacent to the boundaries for the case A with full surface charge and reduced surface charge (less). The overlap into the uncharged area [25:50] is reduced due to the reduction of surface charge close the edges in the 'less' case.

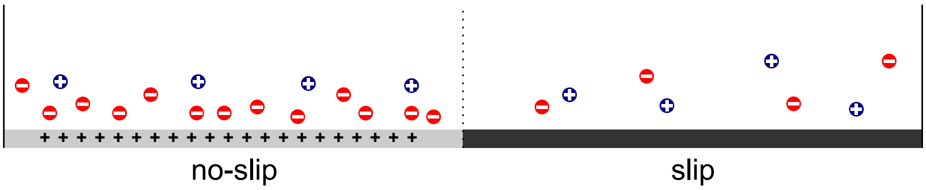

Figure 5.11: Illustration of the reduced surface charge, where the charged area $[2:23]$ *is embedded into the no-slip area* $[0:25]$.

the theory predicts the longitudinal flow to be generally weaker than the transverse flow, which is not validated by the simulations, even with the presumably correct normalizations. Hence the results encourages further theoretical attempts that do not incorporate the clear-cut assumption.

5.4 Effect of ELC

During the study of the stripe systems it became apparent that the electrostatic-layer correction has a limited applicability for the system sizes we consider. For the case A we observed that the ion distributions along the boundaries do not neutralize in the uncharged area at all, if the full ELC is activated. By switching off the additional terms and only using the dipole-correction, the neutral regime as in Figure 5.13 was again

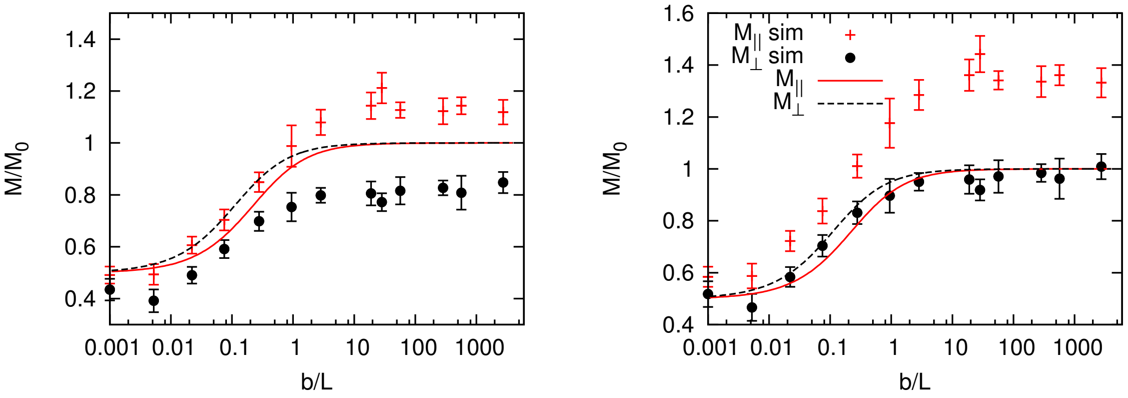

(a) unscaled (b) scaled

Figure 5.12: Mobility results of case A with a reduced surface charge. (a) shows the results normalized with the original M_0*, while (b) shows the results with a scaled down normalization of* $21/25 \cdot M_0$.

obtained.

The non-neutrality had also a large effect on the mobilities. Figure 5.14 shows the results with ELC activated, compared to the original simulation data and the theoretical predictions. One can see a clear increase for both flow directions. This also reinforces the observations made of the overhanging, as the ELC results with no charge neutrality whatsoever somewhat give an upper limit for the deviations from the case of a perfectly charge-neutral slip area.

For the cases B and C, the electrostatic-layer correction did not lead to pronounced deviations, neither in the ion distributions, nor in the mobilities.

5.5 Linear Response Regime

By testing different field strengths, we encountered that E not only determines the flow quantitatively, but can also lead to qualitative changes. For a comparison we tried two different values, i.e. $E = 1$ and $E = 0.1$. In earlier studies of electrically driven systems [90, 155] it has been observed that the latter field strength is well in the linear-response regime, while the former is quite high and leads to non-linear effects.

Non-linear effects are quite prominent in the study of case A with high electric field. In the Debye-Hückel limit it is assumed that the electric double layer stays undisturbed. Additionally the theoretical prediction assumes that the double layer is formed only in the charged area, whereas the uncharged, slippery area stays neutral. While the overhanging effect already disturbs this assumption, a high field strength can distort the ion distributions even further as ions are pushed in flow direction and thus into the neutral area. This effect is illustrated in Figure 5.15, where the distribution of ions adjacent to the walls across the x-direction is shown in the equilibrium situation as well as with both field strengths applied.

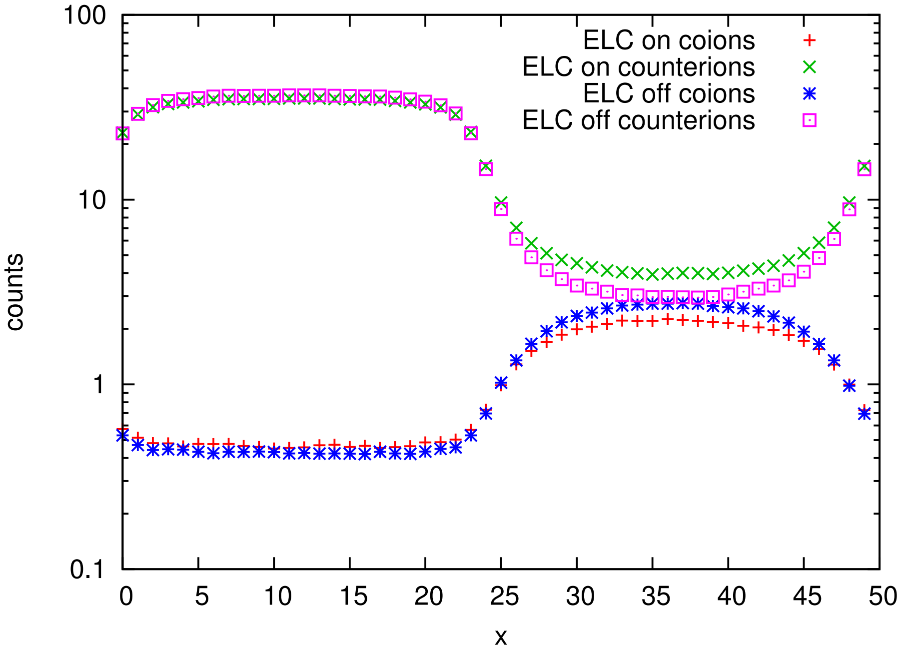

Figure 5.13: Ion distribution along the x-direction close to the boundaries with ELC activated and deactivated.

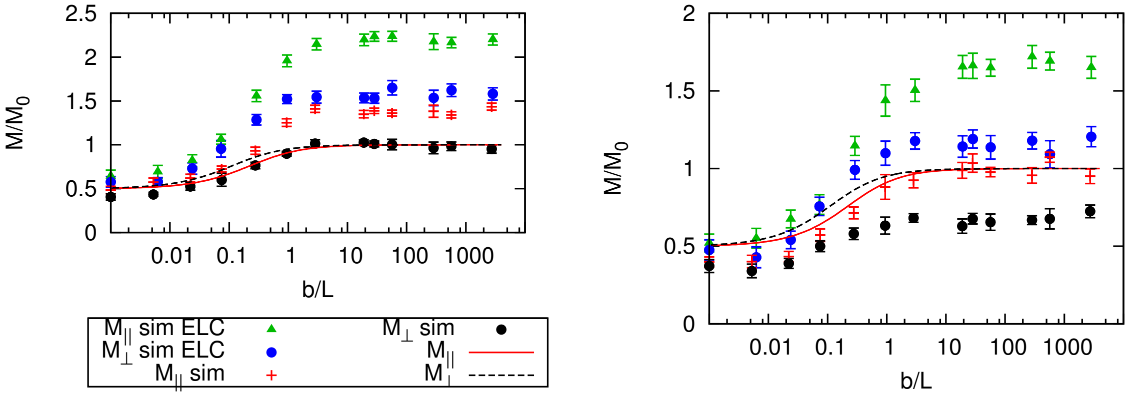

(a) case A

(b) case A reduced charge

Figure 5.14: Comparison of the results with ELC turned on/off for the case A with full surface charge (a) and reduced surface charge (b).

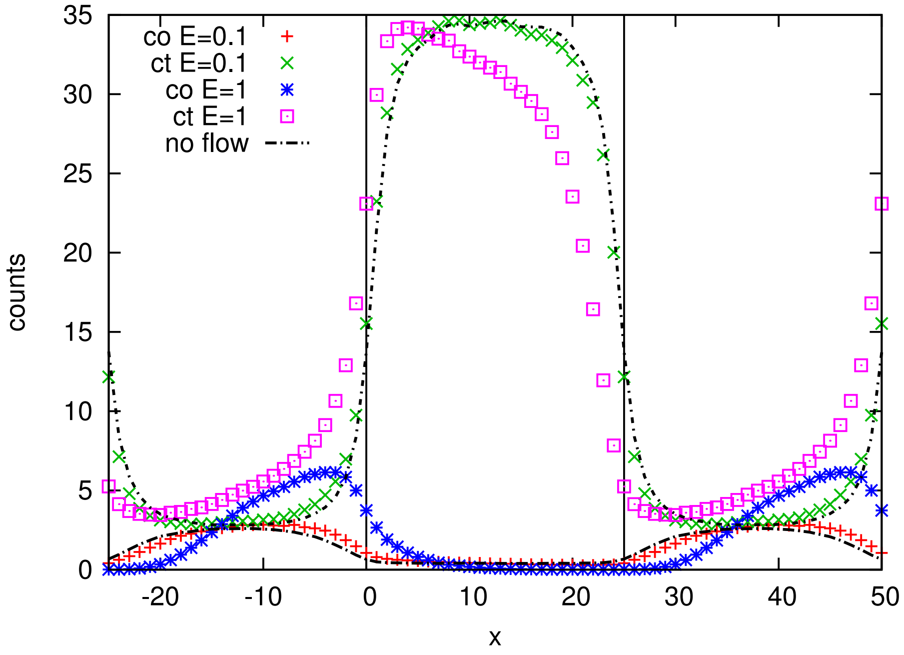

Figure 5.15: Ion distribution adjacent to the walls for field strengths $E = 1$, $E = 0.1$ and no field. While the lower field only slightly disturbs the ion distribution, the higher field leads to a strong deviation from equilibrium.

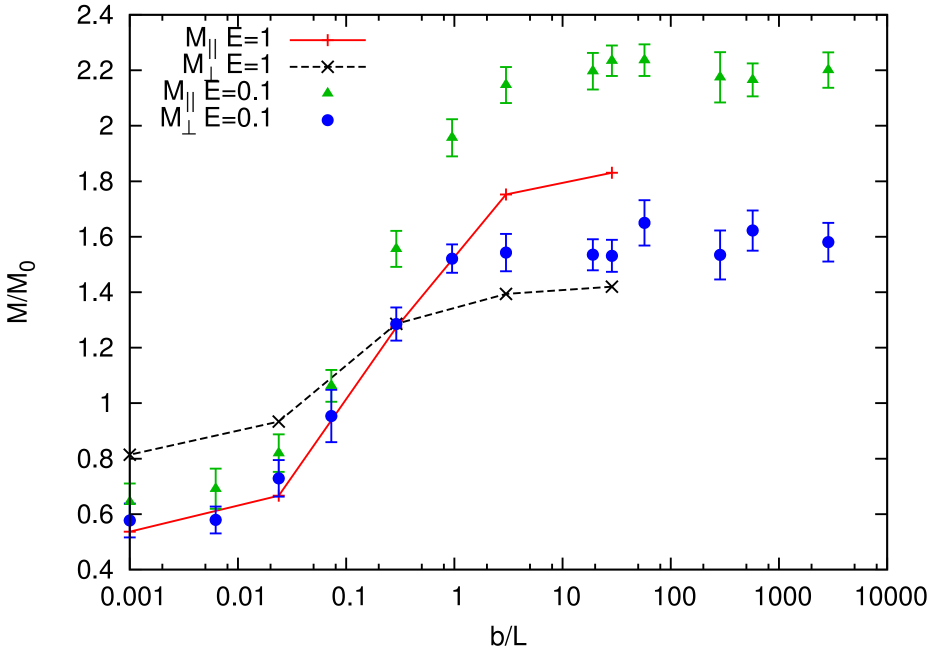

Figure 5.16: Mobility plot for $E = 1$ and $E = 0.1$ (data is produced with ELC).

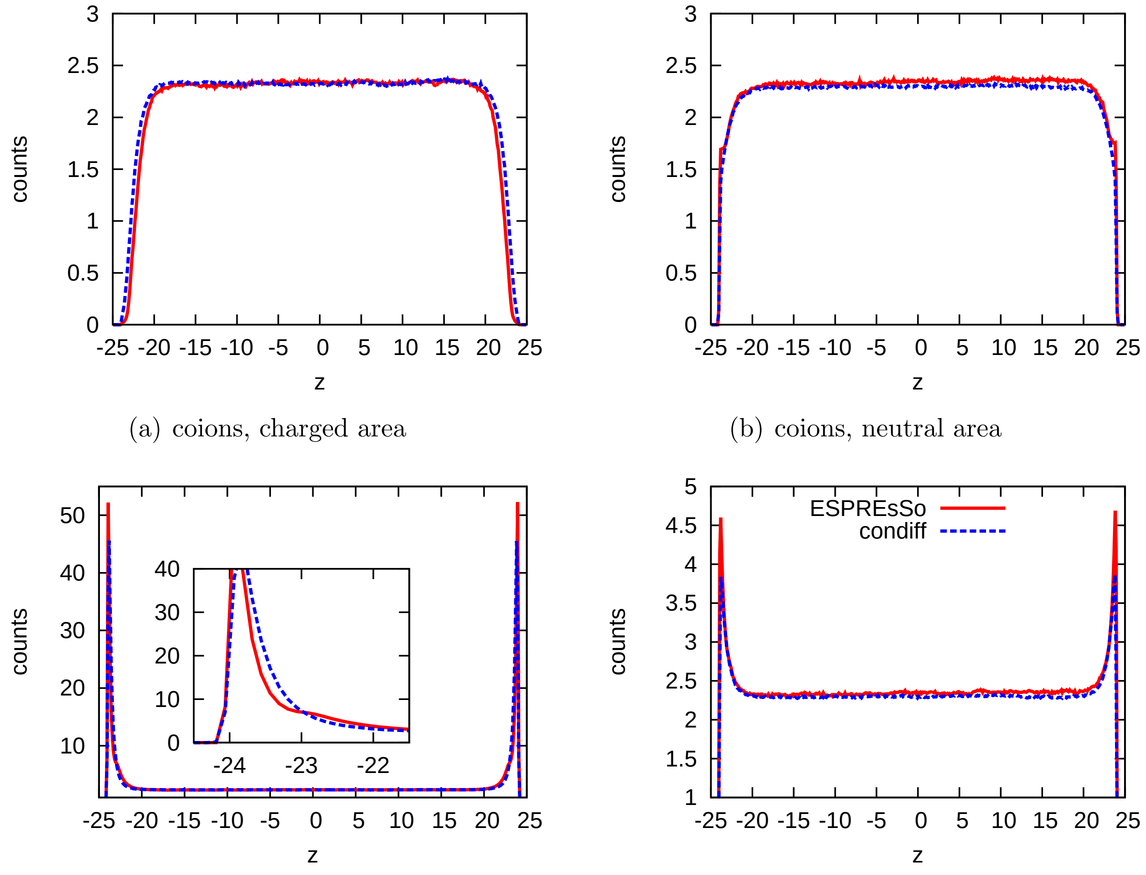

(a) coions, charged area (b) coions, neutral area

(c) counterions, charged area (d) counterions, neutral area

Figure 5.17: Comparison of ion profiles for explicit-ion simulations performed with ESPResSo and the condiff results for case A. Simulation were performed without solvent.

The distortion also has a dramatic effect on the mobility. The resulting M for the higher field is shown in Figure 5.16 in comparison to the one obtained in the linear regime. In this comparison ELC was turned on, so the data should only be viewed in a qualitative fashion. The biggest difference resulting from the higher field strength is the crossover in the mobilities, which is neither predicted by theory nor seen in the linear-response regime.

5.6 Comparison to ESPResSo

To verify our results, we also performed some simulations with explicit charges for the equilibrium charge distributions in the case A system. As hydrodynamic interactions are not required to obtain the equilibrium results, the explicit ion simulations were performed with a Langevin thermostat instead of a DPD solvent to speed up the simulations. Figure 5.17 shows the resulting profiles across the channel.

For the coions (a and b) there are slight deviations close to the boundaries, where

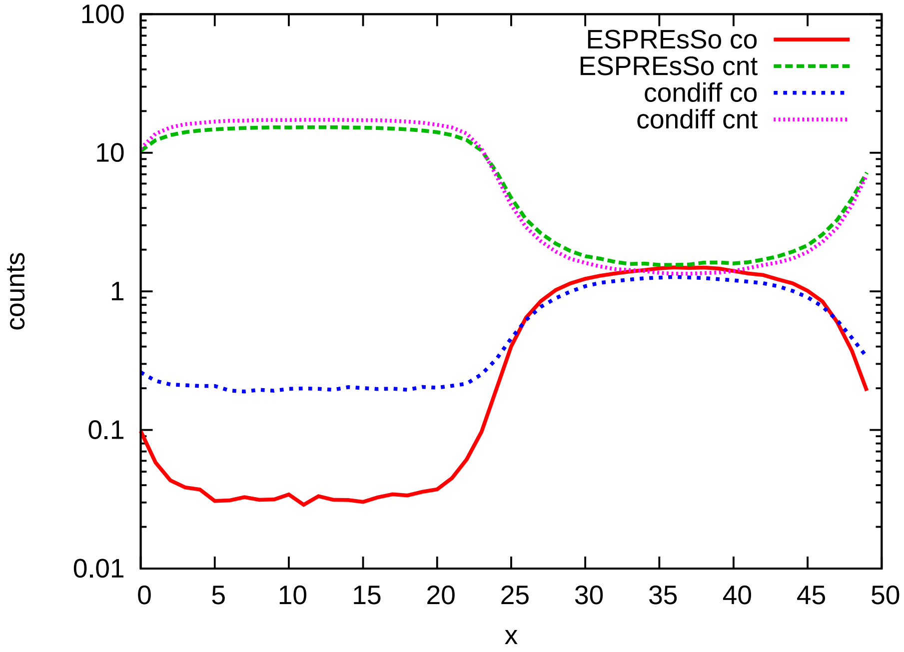

Figure 5.18: Ion profile ina 2σ stripe along the x-direction adjacent to the boundaries for an explicit-ion simulation and a condiff simulation. Both coions (co) and counterions (cnt) are shown in the charged-surface area [0 : 25] *and the uncharged area* [25 : 50]*. The counts on the y-scale are held logarithmic. Simulations were performed without solvent.*

the depletion is a bit stronger for the explicit ions in the uncharged area (b) and thus the amount of coions increases in the charged area. There, however, one can see a jump in the profile close to the boundaries that is not visible for the pseudo-ions. Also, the profile does not seem to be fully equilibrated, as there is a slight increase in density for $z > 5$. A similar increase is visible for the counterions in (d). The counterion profiles show that explicit ions distribute closer to the boundaries, both in the charged (c) and uncharged (d) area. However, in the charged area layering occurs, as can be seen in the blow-up in (c), where a shoulder appears in the ESPResSo profile. The layering could also be the reason for the stronger depletion in (a). The jump in (b) might be an effect of a weaker layering in the uncharged area, as the counterion peak (d) is smaller.

We can also take a look into the ion distribution along the x-direction adjacent to the walls, shown in Figure 5.18. The differences in the coion distributions are more pronounced in the logarithmic scale. Similar to the earlier observations, both simulations appear to reach neutrality in the uncharged-surface area only in a small range around $z = 37.5$. As mentioned before, ELC had to be reduced to the dipole correction to maintain this behavior. We modified the ESPResSo source code accordingly. Overall, the agreement is satisfactory.

A comparison of driven systems including the DPD solvent had to be performed with reduced system size due to the long computation times. The results are presented in section 3.3.1. The deviations in the ion profiles also lead to different mobilities for the two simulation methods. However, both results are consistent with the corresponding electrostatics. Also, in the comparison to the theory we only use relative mobilities. Thus we would expect similar mobility curves from the explicit-ion simulations.

Additionally we performed short simulations of a full "case A" system with ESPResSo for a detailed runtime comparison. The results and the related discussion are presented in chapter 3.5.1.

5.7 Discussion of κ

The comparison of the simulation results with the theoretical predictions shows a good qualitative agreement, except for the case A with its potential limitations in the theoretical description. Similarly to the questionable applicability of the Debye-Hückel approximation for that case, we also should discuss the applicability in the other cases, as the quantitative agreement is not too profound.

The Debye-Hückel approximation is in general strongly limited by the surface charge and salt concentration, as it starts to fail for high zeta potentials. However, the exponential form of the charge profiles in the channel is usually still maintained, but a different type of screening constant should be used for the description. In this case it is a so-called surface screening constant κ_s (see [21] and references therein). The change of κ directly affects the mobility, as the Smoluchowski formula with slip correction directly depends on the screening length

$$M = M_0(1 + \kappa b) \quad , \tag{5.27}$$

with $M_0 = q/(\kappa\eta)$. While the Debye screening constant can be calculated from the ion concentrations inside the system, the surface screening constant can be determined either from the potential Φ or from the total charge distribution

$$\sum_c (Z_c e)\rho_c(z) \propto \frac{\partial^2 \Phi(z)}{\partial z^2} \propto [\exp(\kappa_s z) + \exp(-\kappa_s z)] \quad . \tag{5.28}$$

By fitting the sum of the exponential functions to the charge profile in the range close to the surface, one can determine κ_s. With this method we analyze the case B of homogeneous surface charge. Figure 5.19 shows the charge profile and two types of exponential fits. To obtain the best possible data, we combined all available profile samples of the case B. The first fit is performed over the range [1 : 5] and results in $\kappa_s = 1.5$, where there is a visible deviation for $z \approx 1$ and for $z > 3$. As the fit turned out to be quite sensitive with regards to the initial parameter sets and the fit range, we tried various other combinations in the same manner, with the best results for $\kappa_s \in [1.3 : 1.6]$. The second fit with a fixed $\kappa_s \equiv \kappa_{DB} = 1.01$ was performed over a wider range of [2.5 : 10], as this improved the result. However, there is still a clear deviation for $z < 2.5$, showing that the charge profile is increasing too strongly in contrast to the Debye-Hückel prediction. Yet altogether it appears that the profile is not well described by an exponential as in Eq. 5.28. Even though the whole fit procedure is quite delicate due to the large changes in magnitude in the fit range, we can at least assume that $\kappa_s > \kappa_{DB}$.

There is another approach to determine κ by using Eq. 5.27 itself. The equation is applicable to the situations of a homogeneous surface, i.e. constant surface charge and constant slip length b. By evaluating it for two different slip lengths, one can compare the resulting κ and viscosity η. Writing 5.27 in the form

$$\eta = \frac{q}{\kappa M}\left(1 + \kappa b\right) \quad , \tag{5.29}$$

one can vary κ systematically to match the two resulting viscosities. For this purpose we compare two mobilities of case D for $\phi_2 = 0$ and $\phi_2 = 1$, where $b = 0$ and $b = 13.31$:

$M(0)$	$M(13.31)$	κ	η
0.1514	2.574	1.14	1.38

The comparison leads to a moderately increased screening length, while the viscosity is slightly higher than the pure DPD viscosity ($\eta = 1.35$). A similar increase in the measured viscosity was observed for the counterion-induced electro-osmotic flow in chapter 3.2, where the velocity profiles fit much better, if η was determined directly in the electrolyte solution and not with a pure DPD fluid. The origin of the deviation is the slight inhomogeneity at the boundaries, which results in a higher effective viscosity. The whole determination procedure of the viscosity and the slip lengths is the main error source in this approach, as small changes in η and b can already lead to strong changes in κ (for instance, shifting the no-slip condition $b = 0 \rightarrow b = 0.1$ would result in $\kappa = 1.38$ and $\eta = 1.36$).

In conclusion, both approaches to determine κ favor higher values than the original κ_{DB}, but lead to clearly different results. As a final remark we state that a simple change in κ is not able to improve the overall quantitative agreement. Therefore we plot the theoretical curves with both κ values in Figure 5.20. While $\kappa = 1.5$ clearly overestimates the simulation data, $\kappa = 1.14$ shows a remarkably well agreement for the longitudinal mobility component. But on the other hand it becomes obvious that a change due to κ is systematic to both components of M, which is also visible in Eq. 5.6 (or simply Eq. 5.27). As a result, an improvement in one component automatically leads to a setback in the other component, for any of the four cases. Therefore there must be another factor of uncertainty, similarly significant as the effect of κ.

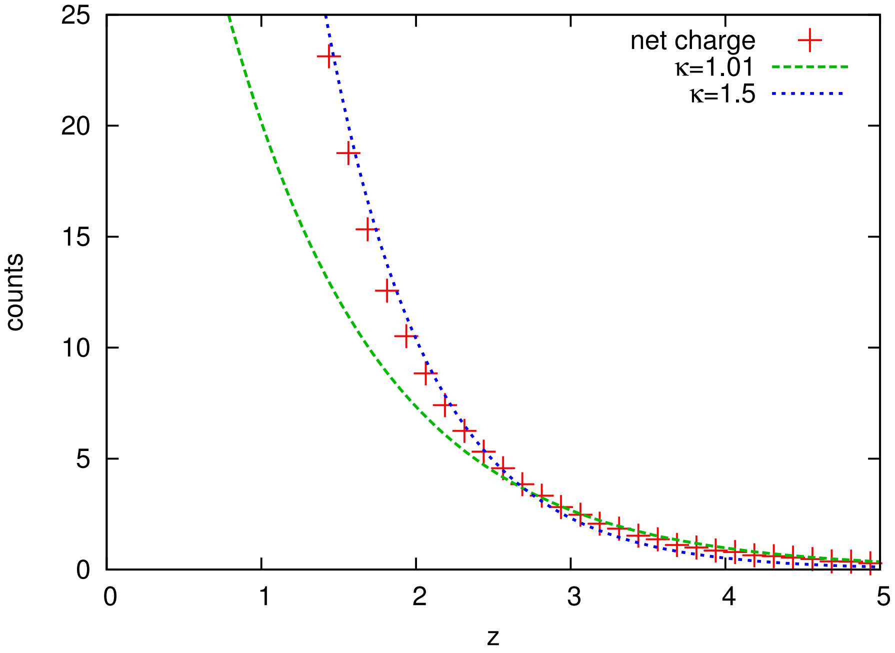

Figure 5.19: Charge profile at surface in case B, averaged over all runs dependent on distance to surface z. Fits of Eq. 5.28 with an optimized $\kappa = 1.5$ *and the original* $\kappa_{DB} = 1.01$ *are shown. The first fit was done over the range* $[1:5]$ *and the second over* $[2.5:10]$.

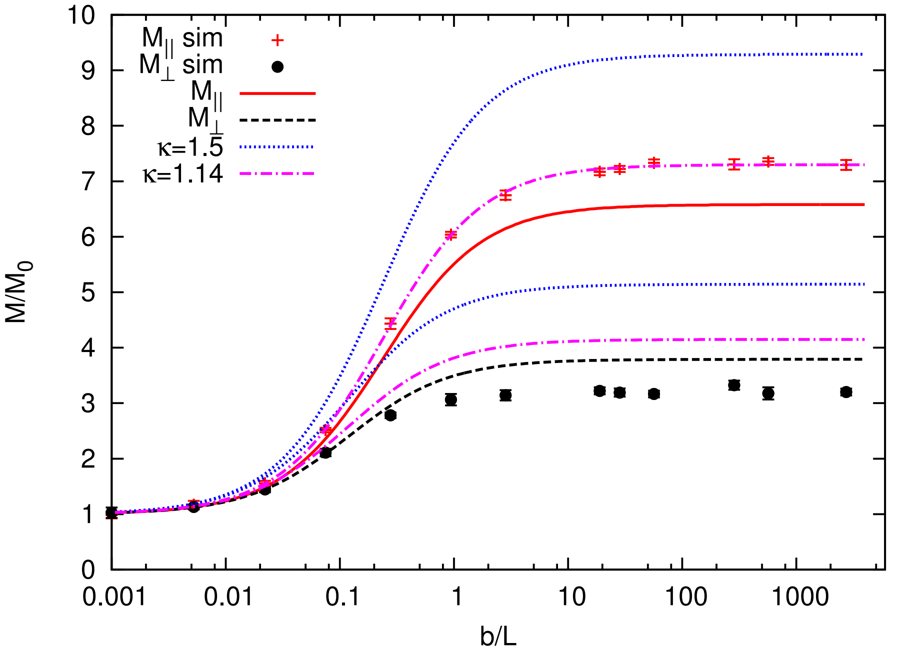

Figure 5.20: Mobility for case B with homogeneous surface charge. The theoretical predictions are shown with the original $\kappa = 1.01$ *and additionally* $\kappa = 1.5$ *and* $\kappa = 1.14$*, as determined in this section.*

CONCLUSION

The focus of this study was to develop a novel algorithm, to solve the electrokinetic equations. The condiff algorithm was constructed step by step, starting with the dissipative particle dynamics (DPD) method to solve the Navier-Stokes equation. The DPD fluid is the foundation, which maintains hydrodynamics and acts as a local thermostat. On top of that we put the ionic concentration fields following the convection-diffusion equation, which are represented by means of pseudo-particles describing a stochastic process, in which they are coupled to the DPD fluid. The coupling works in both ways, such that on the one hand fluid flow leads to convection of the pseudo-ions, and on the other hand electrostatic forces are transmitted to the DPD fluid through the pseudo-ions. Lastly, a fast particle-mesh algorithm is used to solve the Poisson equation and calculate the electrostatic interactions. Macromolecules such as polymers or colloidal particles are easily implemented due to the particle representation. The same holds true for boundaries that can in principle be arbitrarily shaped, which is a great advantage over lattice-based models. The algorithm has been tested extensively, and results have been compared to other simulation methods and theoretical predictions, resulting in very good agreement. The possible parameter space has been explored widely and we found limitations for very high charge gradients, such as close to strongly charged boundaries, where the mesh refinement has to be adjusted accordingly. A detailed comparison of condiff's performance with explicit-ion simulations performed with the software package ESPResSo showed a considerable speedup of > 6 for cases of high salt concentrations. An interim discussion on the condiff method was given in chapter 3.7.

The algorithm was then applied to the study of polyelectrolyte solutions confined in slit channels. The behavior of the charged polymers was studied in different concentrations in the dilute and semidilute regime, and with the addition of salt. Both equilibrium and non-equilibrium were covered. Additionally, we compared all results to a Debye-Hückel description of electrostatics and the case of neutral polymers, where the former appears to be fairly applicable, except for the high shear rates $\dot{\gamma} > 0.5$. Both plane

Couette and Poiseuille flow were used to study the shear thinning, where both data sets agreed. However, we discover certain limitations for the low shear regime, where the statistics were generally too weak to allow substantial interpretations. The study was then extended to very narrow slits in order to study thin-film behavior of very concentrated polyelectrolyte solutions. We again encountered shear-thinning under Couette flow, where a height and concentration-dependent deviation between the case of charged surfaces and uncharged surfaces occurred. Also, a specific combination of concentration and system height led to a crossover in the conformation behavior with shear rate, stating that there seems to be a different alignment process of chains with shear flow.

As a second application of the algorithm we studied the electro-osmotic flow over superhydrophobic surfaces. An electrolyte solution with fairly high concentration and thus small screening length was placed between two superhydrophobic surfaces. The surfaces were modeled by dividing them into two stripes, one of no-slip and one of adjustable slippage. Different cases of surface charge were investigated, and we determined the mobilities from the plug flow occurring due to the applied electric field. A detailed comparison to theoretical predictions led to a very good agreement, both for flow parallel to the stripe pattern and also transverse. Deviations from the theory have been found for the case of charged no-slip areas and uncharged slip areas, which we traced back to an overhanging of counterions from the proximity of the charged area into the uncharged area, leading thus to a different flow behavior. This effect had not been covered in the theoretical work based on the Debye-Hückel approximation, given that they assume perfectly formed ion profiles. We obtained an improved match by decreasing the surface charge at the edges, discovering that the two flow directions appear to require a different normalization of mobilities. For consistency in the study, we compared to field strengths beyond the linear-response regime as well as explicit-ion simulations with ESPResSo.

All together we can conclude that the developed condiff algorithm is suitable for mesoscopic studies of charged macromolecules as well as electrolyte solutions in confinement. In both cases it has an advantage over lattice-based methods regarding the implementability. Its improved performance becomes especially beneficial for highly concentrated systems and large system sizes. A drawback of the condiff method is that it neglects ion-ion correlations, which, however, lose importance in more concentrated systems such as under physiological conditions. All components of the algorithm are in principle parallelizable which should make the algorithm highly interesting to large-scale parallel simulations. As a next step, a future implementation into the software package ESPResSo is planned. This way the algorithm becomes accessible to a broad scientific community and should enable various simulational studies that so far have been limited due to the computational effort involved.

APPENDIX

A.1 Comparison of the Euler and Heun Method

One straightforward way to accelerate the algorithm is to switch from the two-step Heun method to a one-step Euler-Maruyama method. The Euler scheme is used widely in Brownian dynamics, where the stochastic process is in principle the same. Such a switch would instantly reduce the condiff and electrostatic part almost by half, as one no longer needs to calculate the electrostatic field twice. However, one needs to determine and compare the accuracy of both approaches to legitimate such a downgrade. A first performance comparison is shown in Table 3.4 (in section 3.6) for two reference systems. The Euler scheme saves about 5-10% in the salt solution, and the polyelectrolyte system.

A.1.1 Pure Diffusion

To compare the two schemes regarding their accuracy we start out with a pure set up of condiff particles with no interactions. The system size is $10 \times 10 \times 10$ filled with 200 particles and the diffusivity is set to $D = 0.26$. By running the system for $t = 10^5$ with different time steps Δt, one can determine the resulting diffusivity from a linear fit of the mean square displacement. Each simulation is repeated 1000 times to obtain an average.

The results are collected in Table A.1. In general, both methods lead to deviations that are lower than 1% and are mostly covered by the error range. Thus in the case of free diffusion there are no significant differences to be expected.

A.1.2 Equilibration in a Slit Channel

By now it appears that both methods are well suited to describe the free motion of condiff particles, but we must investigate their behavior when coupled to the DPD fluid. For

Δt	Heun	Euler
0.005	$(0.017 \pm 0.156)\%$	$(0.223 \pm 0.138)\%$
0.01	$(0.147 \pm 0.164)\%$	$(0.004 \pm 0.159)\%$
0.02	$(0.151 \pm 0.159)\%$	$(0.060 \pm 0.152)\%$
0.03	$(0.381 \pm 0.154)\%$	$(0.009 \pm 0.161)\%$
0.05	$(0.134 \pm 0.164)\%$	$(0.257 \pm 0.154)\%$
0.1	$(0.209 \pm 0.157)\%$	$(0.062 \pm 0.157)\%$
0.2	$(0.226 \pm 0.157)\%$	$(0.145 \pm 0.156)\%$
0.5	$(0.074 \pm 0.152)\%$	$(0.017 \pm 0.157)\%$
1	$(0.123 \pm 0.153)\%$	$(0.234 \pm 0.156)\%$

Table A.1: Relative deviation of the resulting diffusivity for the Euler and Heun methods with different time steps, averaged over 1000 runs of $t = 10^5$.

this purpose we take a slit geometry of $10 \times 10 \times 15$ with walls at $z = 0$ and $z = 10$, filled with a DPD fluid of density $\rho_{\mathrm{DPD}} = 3.75$, and place 100 pseudo-ions randomly on the $z = 5$ plane as the start configuration. From there we observe the equilibration process, where the ions finally end up in the distribution described by the PB theory (section 3.2). Both the Heun and Euler methods are used on 100 single runs to get an average for each sample step.

Figure A.1 shows a sample of the several distributions during the equilibration process. The decay of the peak seems to happen similarly fast for both methods. However, when the ions at the boundaries just start to accumulate, the accumulation is faster in the Heun method. Furthermore, the final, equilibrated distribution for the Heun method has a stronger increase at the boundaries, which is presumably also the reason why it deviated from the Euler system in the build up. An explanation could be related to the rather hard WCA repulsion of the boundaries. In the Heun method the particles approach the boundary in a somewhat smoother way due to the predictor step that can decrease the drastic repulsion a little, so that they ultimately can arrange themselves a bit closer to the wall.

We study this confinement effect further by looking at a special system, which has the same amount of DPD particles and pseudo-particles. Figure A.2 shows the profiles close to a boundary in a slit channel with surface charge, integrated with both the Euler and Heun scheme.

The two step Heun scheme leads to a larger agglomeration of ions close to the boundary that peaks strongly at about $z = 1$. The Euler scheme leads to a smoother ion profile, with a peak at about $z = 1.05$ from the boundary, but reaching further into the repulsive zone. The DPD profiles, however, are almost unaffected from this change in the ion distribution. While the range around the peak seems to be identical, there must be a minor difference, somewhat hidden in the logarithmic scale, as one can see a different slope occurring for $z > 1.2$. The wall repulsion reaches up to $z = 1.12$. For comparison we also draw the ion distribution for an Euler system with time step $\Delta t = 0.001$. This allows us to estimate the time-step effect, which is in the same range as the deviation

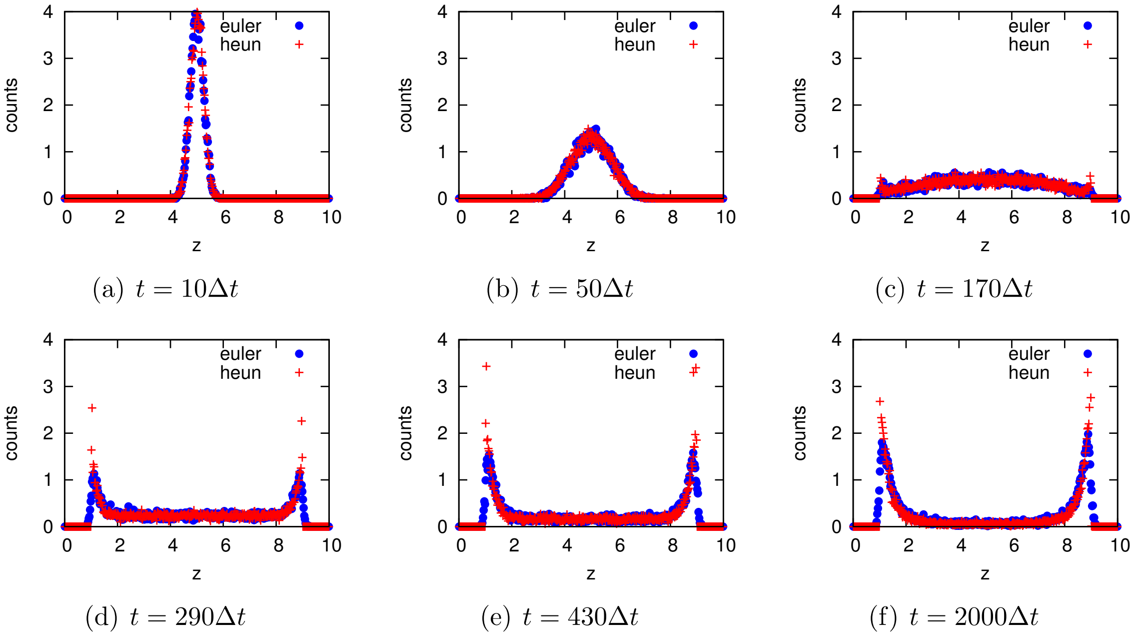

(a) $t = 10\Delta t$ (b) $t = 50\Delta t$ (c) $t = 170\Delta t$

(d) $t = 290\Delta t$ (e) $t = 430\Delta t$ (f) $t = 2000\Delta t$

Figure A.1: Comparison of the counterion distributions inside the slit at different times for the Heun and Euler integration.

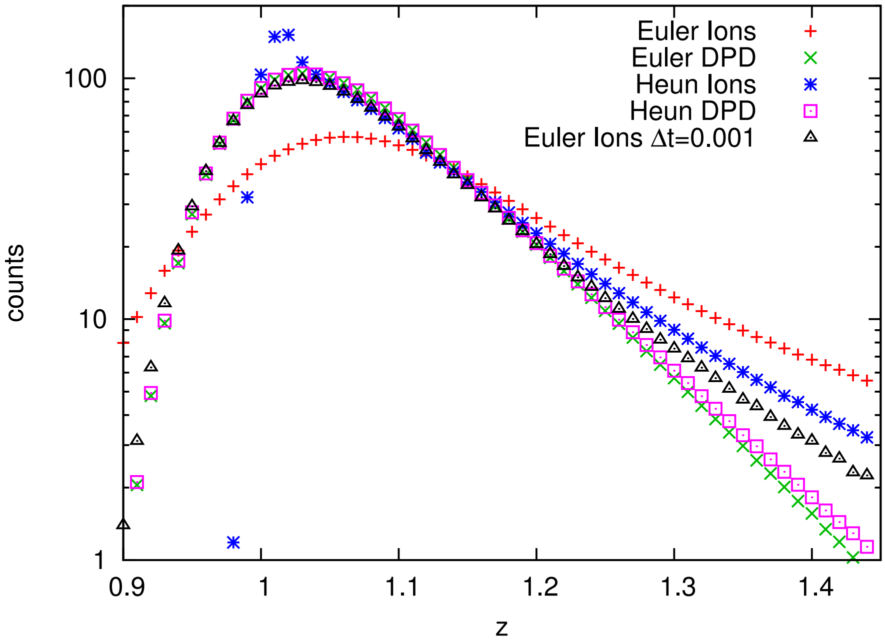

Figure A.2: Comparison of ion and DPD profiles close to a boundary at $z = 0$ for the two integration methods. The counts on the y-axis are shown in logarithmic scale.

Euler to Heun.

Equilibration in a Flow Situation

We also performed a similar study of the equilibration process in a flow situation. In that set-up the DPD particles are manipulated such that they do not feel the boundary repulsion, and an external driving force is switched on to let them flow in boundary direction. The pseudo-ions are then dragged along and distribute at the boundary as they are stopped by the repulsion. In this convection-dominated situation, the Heun and Euler method behaved again similarly and there was no clear deviation except for the difference in the final distribution, similar to the one described above.

A.1.3 Radial Distribution Functions

The local effects in the bulk are quite small. Radial distribution functions for ion-ion pairs and ion-DPD pairs are almost identical down to short distances, were statistical fluctuations set in, as shown in Figure A.3.

A.1.4 Time-Step Effects for Boundary Repulsions

One difference between the Heun and Euler method lies in the behavior of particles close to a repulsive boundary. Due to the relatively hard WCA repulsion, the overdamped dynamics becomes strongly time-step dependent. For instance, when such a potential is used in a Brownian dynamics simulation, usually a time step of $\Delta t = 0.001$ is applied. Here we study the density profile close to a boundary, where we take a system of penetrable volume $10 \times 10 \times 8$ with a charge density $\rho_c = 0.0625$, represented by $N = 1000$ pseudo-ions with $N_q = 20$. Figure A.4 shows the corresponding profiles close to the boundaries for different time steps in the range $\Delta t = 0.001 - 0.02$ and both Euler and Heun. For the Euler method (simple lines) one has a systematic improvement. For Heun (lines with symbols) one observes peak structure occurring for the large time steps down to $\Delta t = 0.0075$, which seems to be an artifact and only becomes visible for very fine histograms. However, studying $\Delta t = 0.01$ with different concentrations up to $\rho_c = 1.25$, it disappeared already for moderate concentrations.

For $\Delta t < 0.01$, the profiles agree mostly in the range $[1.05 : 1.4]$. Thus in a case, where the actual profile close to a boundary is of importance, the time step should be appropriately small. In the context of this study, however, it is not convenient to reduce the time step considerably below $\Delta t = 0.01$ other than for small systems. Shorter time steps would strongly increase the computational effort. As an estimation we can take the profiling results of section 3.5, wherein the Euler step consumed a fraction of 15% of the runtime (24% for Heun). This portion would increase with the same factor the time step is decreased by. Thus with regards to efficiency, the choice of time steps is limited.

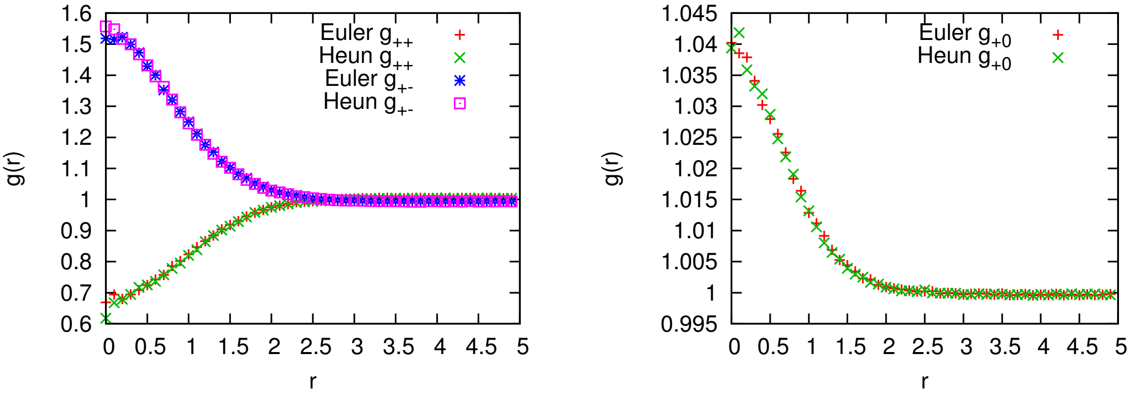

(a) (b)

Figure A.3: Radial distribution functions for Euler and Heun integration in a bulk electrolyte. (a) shows the ion-ion pairs, and (b) shows the ion-DPD pairs.

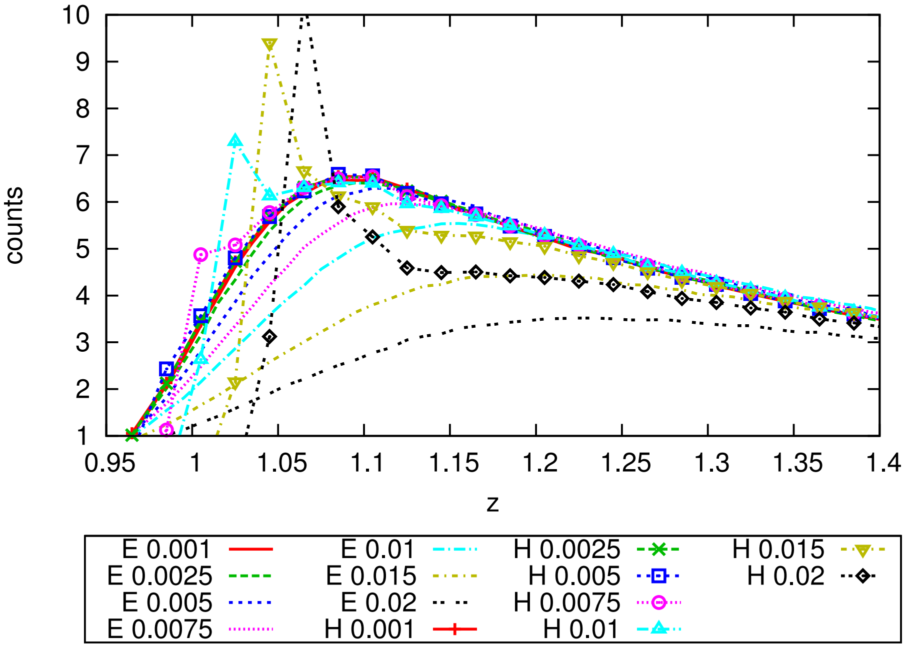

Figure A.4: Pseudo-ion profiles close to the boundaries for various time steps, comparing Euler (E) and Heun (H).

A.1.5 Comparison of Electro-osmotic Flow

Similar to the test presented in section 3.3.1 we can compare the electro-osmotic flow in the presence of salt for the two integration methods. Additionally we include results of simulations with ESPResSo. We pick a system of size $V = 10 \times 10 \times 8$ with boundaries at $z_1 = 0$ and $z_2 = 10$. The volume is filled with $\rho_{\text{DPD}} = 3.75$ (3000 DPD particles), $\rho_- = 0.05375$ (43 counterions) and $\rho_+ = 0.02875$ (23 coions), while the surface charge is $\sigma = 0.1$, represented by frozen charge units. We apply an external field of $E_x = 1$ to induce the flow and compare the resulting ion and flow profiles, as well as the electrostatic potential obtained with a test-charge method.

Figure A.5 shows the resulting ion profiles with a blow-up in (b). In accordance to the previous results, the Euler method leads to slightly lower counterion peaks, which is easily visible in (b). Yet there is also a difference between the Heun profile and the ESPResSo result. If desired, the match should improve with the use of lower time steps, as encountered in the previous section. In the coion profile obtained with ESPResSo there seems to be a shoulder effect close to the boundaries that is not visible in the condiff profiles. The resulting velocities are shown in Figure A.6a, together with a plot of the electrostatic potential Φ_B in the channel. Here the same method was applied as in section 3.3.1. The obtained mobilities predict the hydrodynamic boundaries through the zeta potential Φ_B to be at $z = 3.74 \pm 0.11$ for ESPResSo, $z = 3.971 \pm 0.005$ for condiff Euler, and $z = 3.978 \pm 0.005$ for condiff Heun as indicated in (b). The actual position has been determined to $z_B = 3.88 \pm 0.10$. Thus both condiff results agree within the error range. The ESPResSo data clearly lacks statistics, which is why the analysis has to be seen qualitatively. The reason is that the low charge concentrations lead to strong relative fluctuations, which require very high sample sizes. In the condiff simulations the situation was improved by setting $N_q = 10$.

Concluding the analysis presented in this chapter, it appears legitimate to choose the Euler method and benefit from the better performance. The only possibly problematic aspect is the behavior at boundaries, where the ion profiles are a bit reduced in the vicinity, but still follow the theoretical predictions (see chapter 3.2). However, both schemes have been applied equally often throughout this study, also in direct comparison, and no further discrepancies have been observed. In the case of flow the actual integration method and chosen time step lead to differences in the ion profiles, which then also lead to deviations in the flow profiles. Both integration schemes do not match with the explicit-ion result, yet the Heun scheme already performs better than the Euler scheme. However, both show consistency regarding the connection of flow and charge distribution, as the analysis of Figures A.6a,b indicates.

A.2 Accuracy of Particle-Mesh Electrostatics

The accuracy of particle-mesh Ewald techniques is largely determined by the set of parameters chosen, which includes the charge assignment, the grid size and the parameter α which determines the smearing of the charges or the splitting into real-space and k-

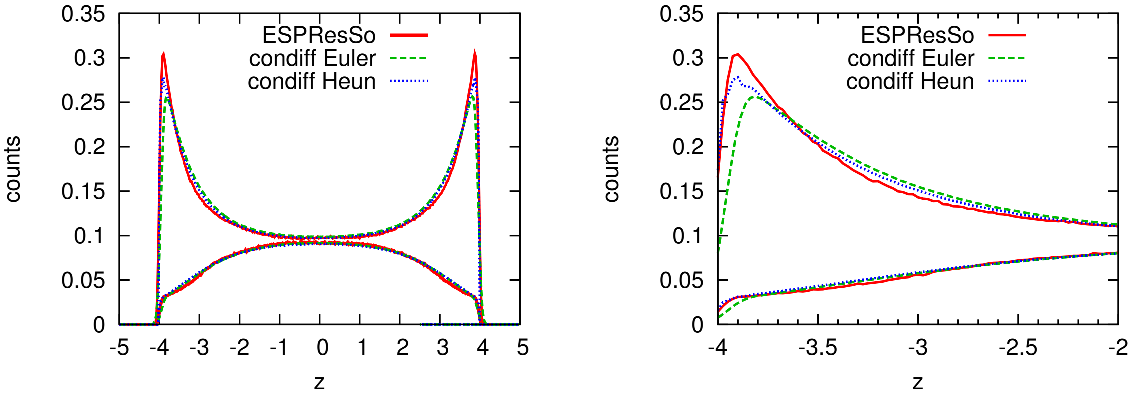

(a) (b)

Figure A.5: Comparison of ion profiles inside the slit. (b) shows a blow-up of the boundary area, where the net-charge profile is shown by gray lines (dashed for condiff, straight for ESPResSo).

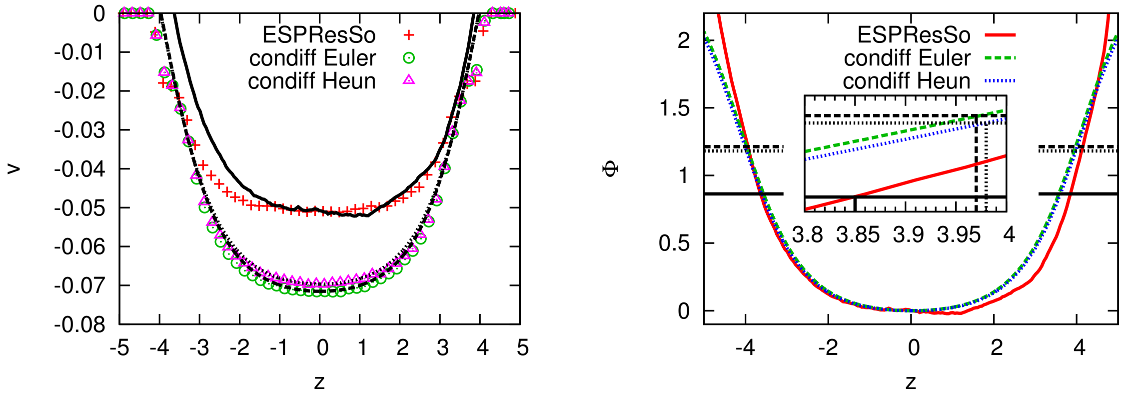

(a) (b)

Figure A.6: Comparison of resulting flow profiles and electrostatic potentials. (a) shows the plug flow together with the prediction of Eq. 3.6, (b) shows the potentials, where the straight lines are the Φ_B values determined with Eq. 3.7 from the mobilities.

space contributions. There exists a sophisticated scheme to calculate the rms error of the electrostatic force calculations in particle-mesh methods that goes back to the work of Hockney and Eastwood [98]. Petersen [156] determined an estimate for the k-space error. Deserno and Holm reviewed the whole particle-mesh technique and gave a recipe to implement such methods and calculate errors [99, 157].

The optimal Green's function to use for the k-space calculation is determined from a functional which includes the charge assignment scheme. The same functional can be used to calculate the error in the force determined in the way

$$Q = \frac{1}{h^3} \int_{h^3} d^3 r_1 \int_{L^3} d^3 r \, [\boldsymbol{F}(\boldsymbol{r}, \boldsymbol{r}_1) - \boldsymbol{R}(\boldsymbol{r})]^2 \quad . \tag{A.2.1}$$

Here $\boldsymbol{F}$ is the Fourier-space part of the electrostatic interactions of two charge units at positions $\boldsymbol{r}_1$ and $\boldsymbol{r}_1 + \boldsymbol{r}$ calculated from the particle-mesh method and $\boldsymbol{R}$ is the corresponding reference force. L stands for the system size if it is cubic and h for the grid spacing. From there the error can be estimated to

$$\Delta F^{(k)} \approx \sum_{i=1}^{N} q_i^2 \sqrt{\frac{Q}{NL^3}} \tag{A.2.2}$$

for N charged particles in the cubic system. Additionally there is an error contribution from the real-space part that was derived by Kolafa and Perram [158]

$$\Delta F^{(r)} \approx \frac{2\sum_{i=1}^{N} q_i^2}{\sqrt{N r_{\max} L^3}} \exp(-\alpha^2 r_{\max}^2) \quad , \tag{A.2.3}$$

where $r_{\max}$ is the cutoff radius for the interaction.

In our case, however, we have a slightly different situation. While the smearing of charges in the original particle-mesh method is a tool to obtain the two contributions, in our case the smeared charges are real, i.e. we do not deal with point charges. The choice of the appropriate α is therefore a choice of the simulation model and not of accuracy. A simple way to estimate the electrostatic-force error in this case can be to compare the particle-mesh calculation with a k-space only Ewald sum, where $k_{\max}$ is taken to be very large [99]

$$\Delta F = \sqrt{\frac{1}{N} \sum_{i=1}^{N} (\boldsymbol{F}_i - \boldsymbol{F}_i^{\text{Ewald}})^2} \quad . \tag{A.2.4}$$

The comparison tool is compiled separately. Since a rather simple version of the Ewald summation is implemented, the box has to be cubic for comparison (or better to say: the Ewald algorithm takes the system size in x-direction to be the cube's length).

A.2.1 Two Charged Particles

First we consider a system of size 20 × 20 × 20 with a positive and a negative particle in various distances to each other. We choose $\alpha = 1$ for the size of the particles. For the mesh size we start with the typical 12 per 10σ size and different charge assignment orders and compare to a case of double mesh size.

mesh size	cao
24^3	1
24^3	2
24^3	3
48^3	2
48^3	3

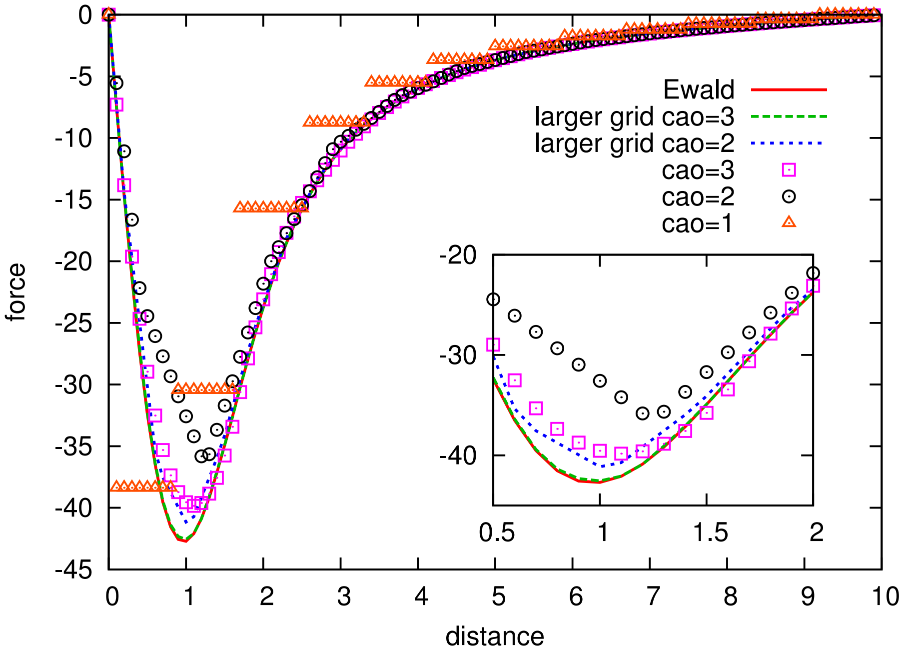

Figure A.7: Electrostatic force for a two-particle system. The accurate Ewald result is compared to approximations by the particle-mesh method. The inset shows a detailed view on the deviation at particle overlap.

The Ewald summation with which we compare has a k-space cutoff of $n_{\max} = 150$ which is considerably high. The resulting curves are shown in Figure A.7. Except for the case cao 1 all curves agree in the long-range behavior. Larger deviations appear when the particles start to overlap, around $r < 2.5$. Here one can either choose a higher grid size or a higher charge assignment order. The case with mesh 48^3 and cao 3 reproduces the Ewald result almost perfectly.

It is important to note that the accuracy of individual dimensions is not independent. A larger grid in perpendicular directions can lead to a higher accuracy in the current dimension. This might be a consequence of the charge assignment. Thus, one should always try to have the same grid-spacing in each direction, to keep the mesh description isotropic.

A.2.2 Randomly Distributed Salt Solution

The next test case is a prototype of a system that will be of interest. We consider a salt solution with $N_+ = N+ = 100$ ions in a system of size 10^3. The ions are placed randomly and we calculate the rms-force difference to the Ewald result.

Table A.2 lists the different cases. With standard settings (mesh 12^3 cao 3) the order of the error is about $O(10^{-2})$. An improvement is clearly visible when increasing the mesh, which results in a jump of about an order of magnitude. It also shows that cao 1 is never a good choice. However, a higher grid size also leads to a higher computational effort

mesh size	cao	rms error
12^3	1	$4.39 \cdot 10^{-01}$
12^3	2	$9.87 \cdot 10^{-02}$
12^3	3	$3.80 \cdot 10^{-02}$
24^3	1	$2.22 \cdot 10^{-01}$
24^3	2	$1.83 \cdot 10^{-02}$
24^3	3	$2.93 \cdot 10^{-03}$

Table A.2: List of rms errors in the electrostatic calculations for a salt solution with different assignment order and mesh size.

for the field calculation, while a higher charge assignment order leads to an additional computational increase for the velocity assignment.

A.3 Test of the Parameter N_q

Next we discuss the influence of the number of pseudo-particles representing the concentration field, N_q, where in principle there are two possible limits. On the one hand one could reduce the amount of pseudo-particle to obtain a one-to-one correspondence between particles and charge units, which means $N_q = 1$. On the other hand one could increase the amount of particles and work with higher N_q. By increasing the amount of particles to represent a unit charge, the fluctuations that are inherent to the particle model average out, and one approaches a continuum description. Thus the parameter N_q determines the fraction with which pseudo-ions count to one charge unit. This means that when assigning charges to the grid, every charge unit of a pseudo-particle is divided by N_q. However, when calculating the force onto a particle, the full charge has to be accounted for in each particle. In an illustrative example one could look at a group of ten pseudo-particles representing one unit charge, i.e. $N_q = 10$, sitting close together. As on a more coarse level they would be represented by just one single particle, they should, as a collective, reproduce the motion this particle would make. Thus they need the same amount of force, and not a force scaled by $1/N_q$. Then in the final stage, when the force onto the DPD particles is calculated, the scaling must be included again.

To check whether the algorithm works fine in that sense, we look at a test system of a counterion solution between two charged walls and compare the obtained profiles in equilibrium and in flow. The penetrable volume of $10 \times 10 \times 8$ is filled with 3750 DPD particles and 50 charge units, i.e. $\rho_{\mathrm{DPD}} = 4.6875$ and $\rho_c = 0.0625$. In this test we use the following N_q values

N_q	# pseudo-ions
1	50
2	100
10	500
50	2500
75	3750

The last value corresponds to $N_{\text{DPD}} = N_{\text{pseudo-ions}}$. As a side note it is worth mentioning that the agreement for different N_q was tested with both the Euler and Heun scheme. Figure A.8 shows the resulting profiles in equilibrium. For the counterions in (a) the profiles agree very well, with the only difference that the statistics improve with N_q as fluctuations decrease. The improvement is already visible for very short run times. Figure A.8b shows the increase of DPD density at the boundaries, which states that N_q appears to have no effect on the DPD particles, neither in magnitude, nor in terms of overall noisiness.

The correct force coupling can additionally be verified by applying an external electric field and comparing the DPD flow profiles. The resulting flow profiles are shown in Figure A.9. The overall agreement of the velocities is quite visible, which confirms that the parameter N_q only has an effect on the local charge fluctuations.

A.4 Effects of Boundaries and Charge Gradients

During the study of the counterion-induced electro-osmotic flow, described in chapter 3.2, a certain limitation of the algorithm was encountered for strong gradients in the ion density. Considering such a system confined between two equally charged plates, filled with solvent and one ion species, i.e. the counterions, one can observe the typical aggregation of counterions close to the boundaries that is also well described by the Poisson-Boltzmann theory. However, as the ion density and the DPD density are coupled, there is also an increase in DPD particles close to the boundaries. This is in a way reasonable, in that the DPD particles do not only represent the solvent, but the total density $\rho = \rho_s + \rho_c$. Similarly, in an explicit-ion simulation with DPD one would count the total density as DPD density plus counterion density as the counterions themselves take part in the DPD interactions. By subtracting the latter, one obtains the neutral solvent density that should be homogeneous over the whole slit, which can be understood by looking into the Navier-Stokes equation (Eq. 1.4). However, by studying a pure DPD fluid, it becomes apparent that there are small deviations directly at the boundaries that only show up through the statistical fluctuations after very long run times. Figure A.10 shows the small increase close to the boundaries that is in the 1% range. There is also a small layering visible hidden in the fluctuations of the constant range. Both effects might be caused by the finite time step. The latter phenomenon shows an alignment of particles, which is also visible in radial-distribution functions, as described in section 3.4.2, and also in [88, 110].

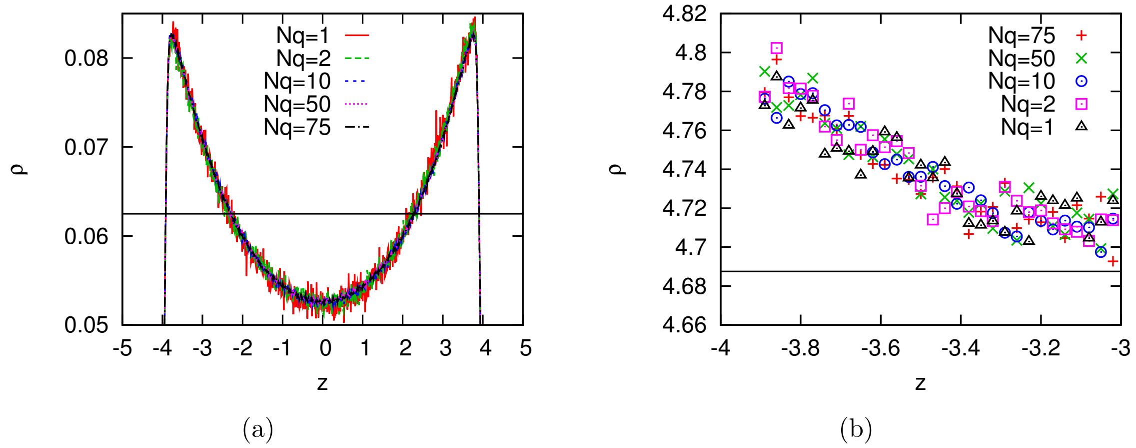

(a) (b)

Figure A.8: Equilibrium profiles of a counterion-solution in a slit channel, with different amounts of pseudo-particles per unit charge, N_q. (a) shows the charge density in the channel, where the black horizontal line represents the mean, (b) shows a blow-up of the boundary region for the DPD density, where again the black line shows the mean of the entire system.

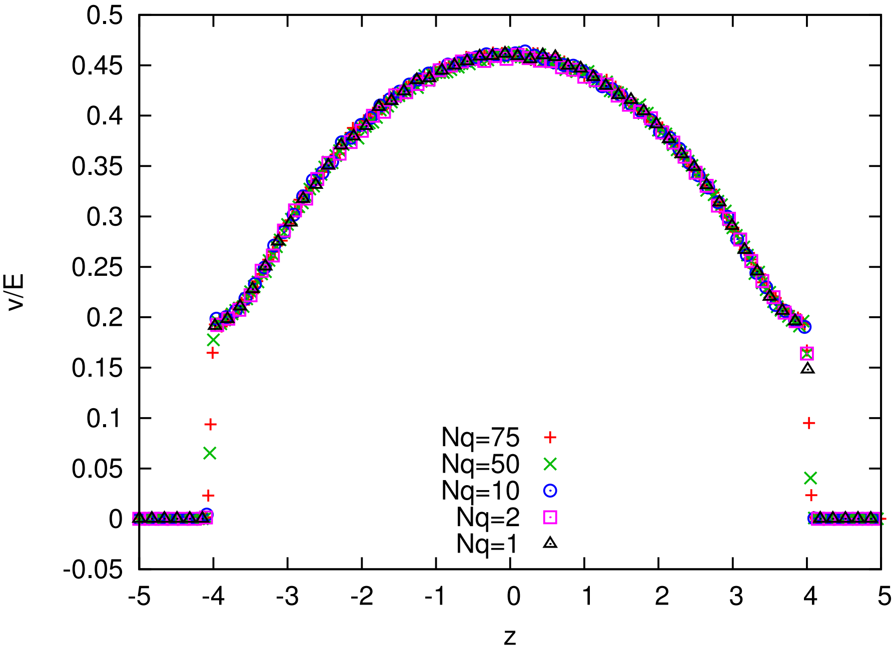

Figure A.9: Velocity profiles of a counterion-solution in a slit channel, with different amounts of pseudo-particles per unit charge, N_q. For better visibility only a selection of data points is plotted, as they otherwise overlap strongly.

In the following we study some situations with mismatched density profiles and gather all influencing factors. We will take the profile in Figure A.10 to be the standard neutral profile instead of assuming a homogeneous one, whenever comparing ion and DPD profiles in confinement.

A.4.1 DPD Overshoot at Charged Walls

In the system described in chapter 3.2 with a counterion solution between two charged plates, the relative shape of the DPD profile is directly dependent on the absolute counterion density ρ_c. Here we start out with two systems, $\rho_c = 0.03125$ and $\rho_c = 0.0625$ (i.e. 25 and 50 charge units in a $10 \times 10 \times 8$ volume). For a direct comparison, we subtract the profile of Figure A.10 (scaled appropriately by $(3750 - 25(50))/3750$) to obtain a reduced DPD profile that should resemble the counterion profile. At these relatively low charge densities this is indeed the case, as it is illustrated in Figure A.11.

In both figures the reduced DPD profile is only marginally increased at the boundaries. However, the general trend is already visible. For higher charge concentrations, the counterion density still follows the Poisson-Boltzmann prediction, but the DPD density shows a clear overshoot close to the boundaries. The resulting neutral profiles are shown in Figure A.12, obtained by subtracting the counterion density from the DPD density. The overshoot effect becomes absurdly strong when going to very high charge densities, so that in the end almost all DPD particles are dragged to the boundaries for $\rho_c \geq 1$. By means of extensive tests with different parameter sets for the grid, it became apparent that the shape of the DPD profile depends on the assignment order and the grid size. More details on this will be presented in section A.4.5.

A test with different wall repulsions shows that the overshoot is fairly independent of the type of wall considered for the pseudo-ions. Figure A.13b shows the ion and reduced DPD profiles in a comparison between the original WCA repulsion, a weaker version with $\varepsilon = 0.25$ and an implementation of the hard walls described in [159]. In all three cases the DPD particles still deal with the $\varepsilon = 1$ WCA repulsion. While there seems to be almost no difference between the regular WCA case and the hard walls, the smaller WCA repulsion reduces the vacuum layer for the counterions. Such a mismatch is in general rather unphysical, but should be of no concern for this purpose. In any case the change in the DPD profile is only marginal, which shows that the cause for the overshoot cannot be a very local effect. This will indeed be confirmed when looking at different mesh parameters later on.

With the rather strange behavior at high ρ_c up to this point, we wanted to clarify the reasons by looking further into the ion-DPD coupling. For this purpose we start out with some other simulation geometries that lead to gradients in the profiles.

A.4.2 DPD Undershoot at a Penetrable Plane

A simple test case for the coupling of the densities is to consider a charged, but penetrable plate in a periodic system. This geometry can be modeled by freezing some charges along a plane at $z = 0$ and filling the system with the appropriate amount of counterions to

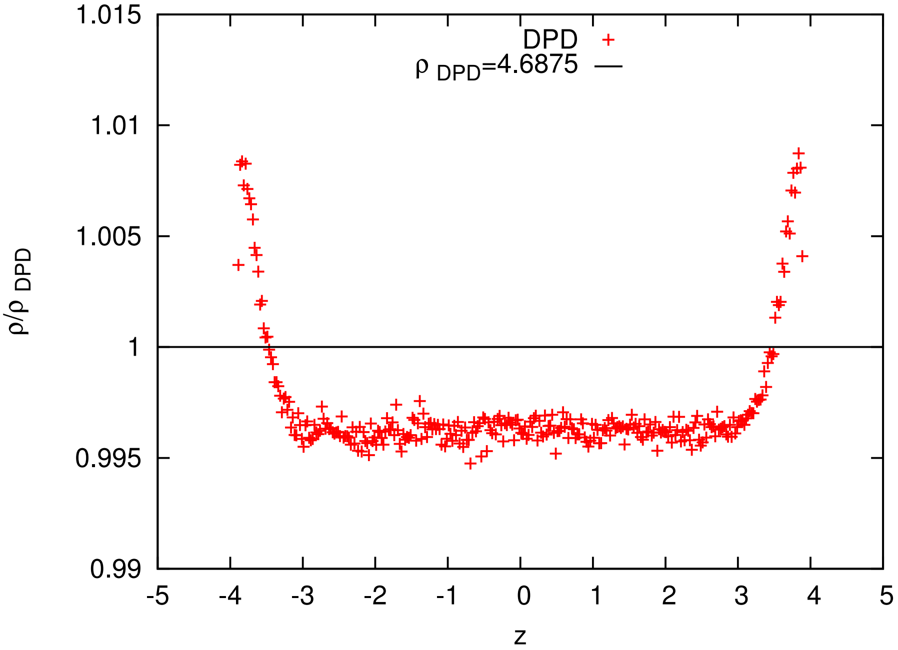

Figure A.10: Pure DPD fluid confined between two walls. The density is normalized to show the relative deviations close to the boundaries. The profile is averaged over 5M steps, sampling every 50 steps.

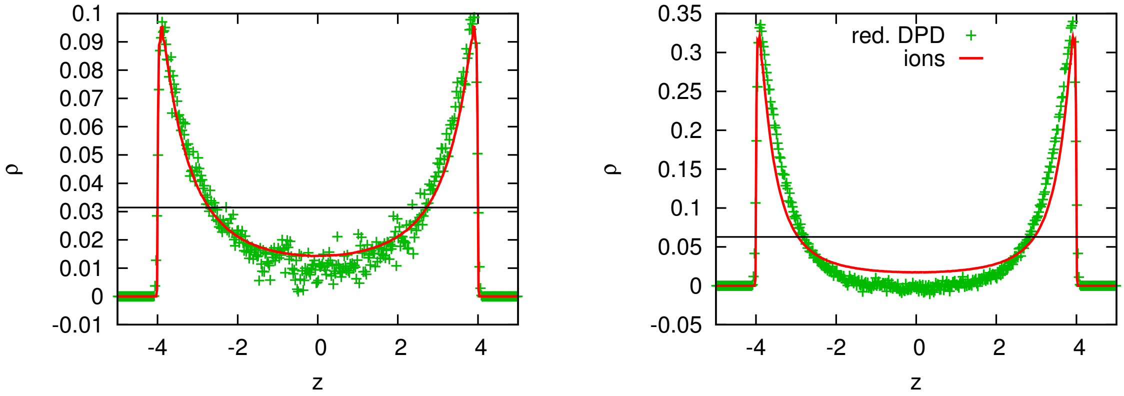

(a) $\rho_c = 0.03125$

(b) $\rho_c = 0.0625$

Figure A.11: Counterion and reduced DPD profiles between two charged plates. The DPD profile has been modified by subtracting the neutral profile of Fig. A.10 scaled to the according density. The black line shows the average counterion density which thus is also the average DPD density. The profiles are averaged over 200k samples in $50\Delta t$ *distance.*

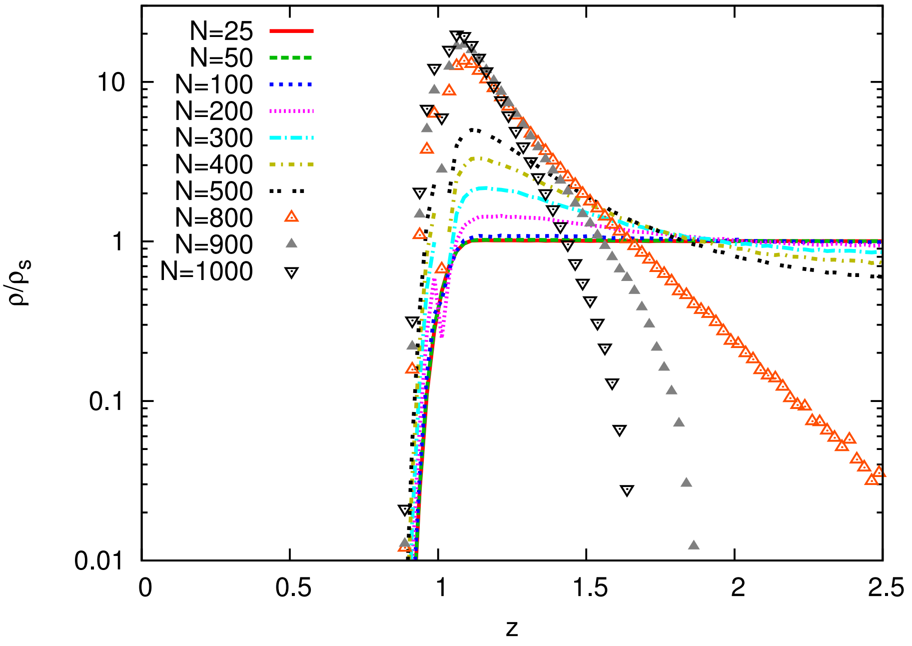

Figure A.12: Neutral profiles (DPD minus counterions) close to the boundary for various counterion densities ranging from $\rho_c = 25/800 = 0.03125$ to $\rho_c = 1.25$.

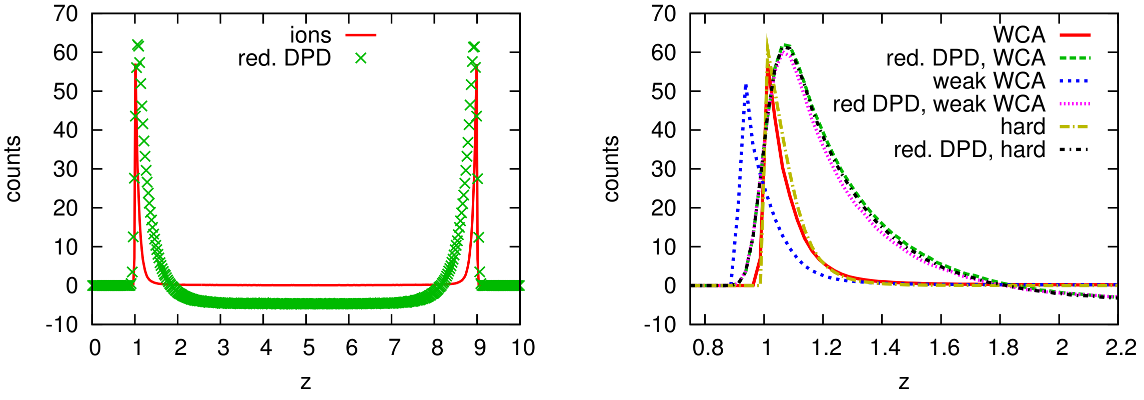

(a)

(b)

Figure A.13: Profiles for $\rho_c = 0.625$. (a) shows the original counterion and reduced DPD profile, where the overshoot is quite visible. (b) compares the effects of three different boundaries.

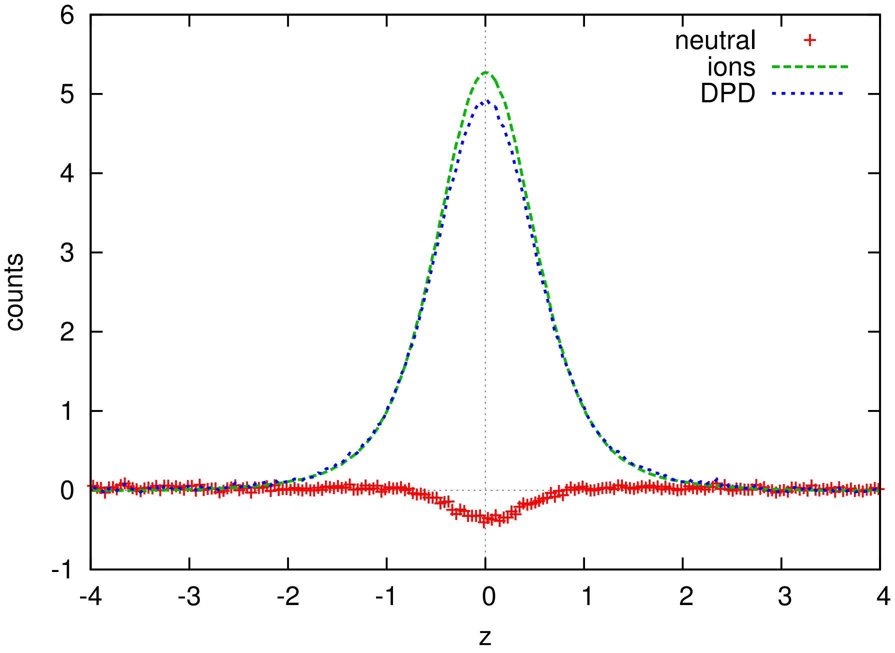

Figure A.14: Density profiles in a periodic system with a charged, penetrable plane at $z = 0$. *The plane with a surface charge of* $\sigma = 2$ *is represented by fixed pseudo-ions. Counterions with a density of* $\rho_c = 0.25$ *distribute around it and influence the local DPD profile. All profiles are shifted to zero.*

balance the charge. In this case the counterions are allowed to freely distribute around the charged plane and the DPD density will follow. The benefit is that there are no boundary effects disturbing the coupling. In Figure A.14 the result is shown for a counterion density of $\rho_c = 0.25$, which is relatively high for such a system. One can see a clear misfit between the counterion density and DPD density that are both shifted to zero far away from the plane. The result of this mismatch is a negative dip in the neutral density, obtained by subtracting the counterion profile from the DPD profile. By comparing other density values, it became apparent that the dip increases monotonically with the charge density. Test runs have been made up to $\rho_c = 1.25$.

A.4.3 Distribution in an External Potential

To simplify the situation even more, we replace the frozen-charge plane and study coupling and mutual increase of densities by applying an inhomogeneous external electric field to trap ions in a subvolume and observe the according increase in DPD density. With a quadratic potential well at $z = 0$ in a system of size $10 \times 10 \times 20$ filled with just one sort of ions, we obtain a linear force driving the ions towards the very center. Since the ions will fulfill a Boltzmann law in equilibrium, the resulting profiles should be Gaussian. It is reasonable to expect the same behavior for the DPD profiles, where the Gaussian should have the same width but different amplitude and an offset due to

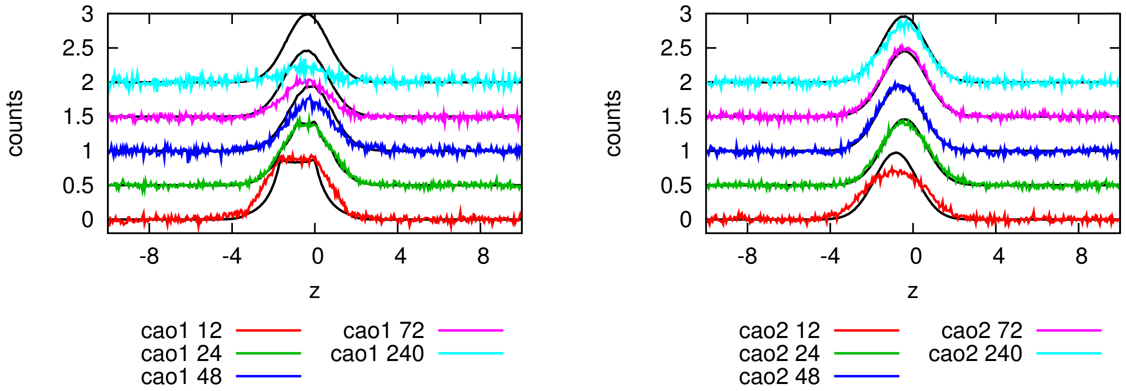

(a) cao 1 (b) cao 2

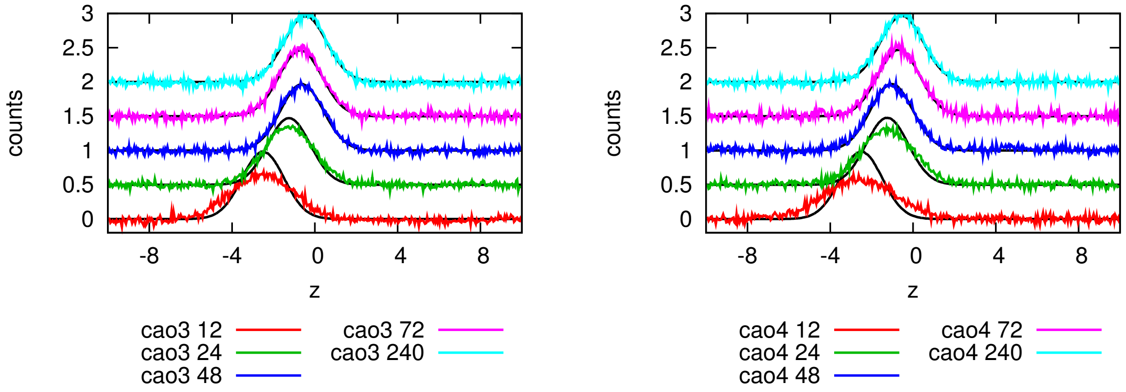

(c) cao 3 (d) cao 4

Figure A.15: Ion profiles (black lines) and according DPD profiles shifted to match in the homogeneous region for different assignment orders and grid sizes. Each pair is shifted by 0.5 for better visibility.

the neutral density. To test the effect of different parameters, we try charge assignment orders (cao) up to 4 and different grid sizes. Figure A.15 summarizes all results.

For cao 1 it requires a relatively fine grid to even obtain a smooth ion profile (black lines), as otherwise the external force is distributed too coarse. Very fine grids, however, are not useful, as then the ion-DPD coupling fails. More details on cao 1 can be found in Figure A.16. In A.15b,c,d it generally shows that cao $2, 3, 4$ are appropriate as long as the grid size is at least 24, which is also the standard grid spacing throughout this study. A grid of size 48 appears to produce the best results independently of the assignment order. The shift of the peak with increasing mesh size is an artifact of the discrete nature, as the external electric force has been plugged in on the grid level. It should, however, be of no concern due to the periodicity.

Finally we fit the ion profiles with Gaussians, which works out very well for any ion profile except the deformed ones with cao 1. In accordance to the relations to be presented in section A.4.7, also the DPD profiles should be Gaussian, which is why we

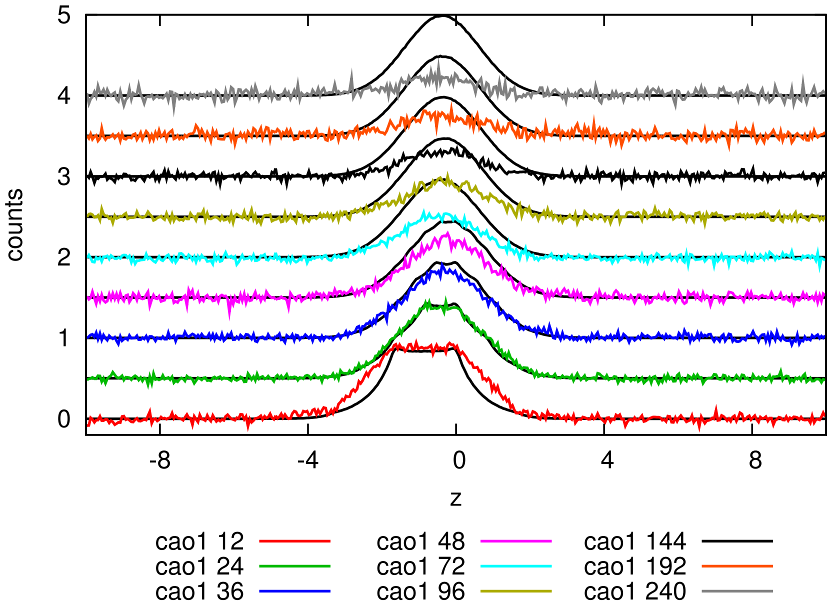

Figure A.16: Ion profiles (black lines) and according DPD profiles shifted to match in the homogeneous region for different grid sizes and charge assignment order one. Each pair is shifted by 0.5 for better visibility.

take the fit for the ions and modify it accordingly

$$\begin{aligned} f_{\text{ion}}(z) &= A\exp(-B(z-C)^2) && \text{(A.4.5)} \\ f_{\text{DPD}}(z) &= f_{\text{ion}}(z)\cdot D + E \quad . && \text{(A.4.6)} \end{aligned}$$

The agreement to the DPD profiles is quite well for the intermediate and large grid sizes, but not for grid size 12. Some illustrative results are shown in Figure A.17.

A.4.4 Tests with a High Load of Pseudo-Particles

We can further try to clarify whether the effect is also related to the overall density mismatch, as there are usually more DPD particles than ions. As an extreme case we study systems with $N_c = N_{\text{DPD}} = 3750$, but change the valence z_c of the ions. The penetrable volume is $10 \times 10 \times 8$, so that the number density is fixed to $\rho_c = 4.6875$, but since $z_c \leq 1$ we arrive at the following charge densities:

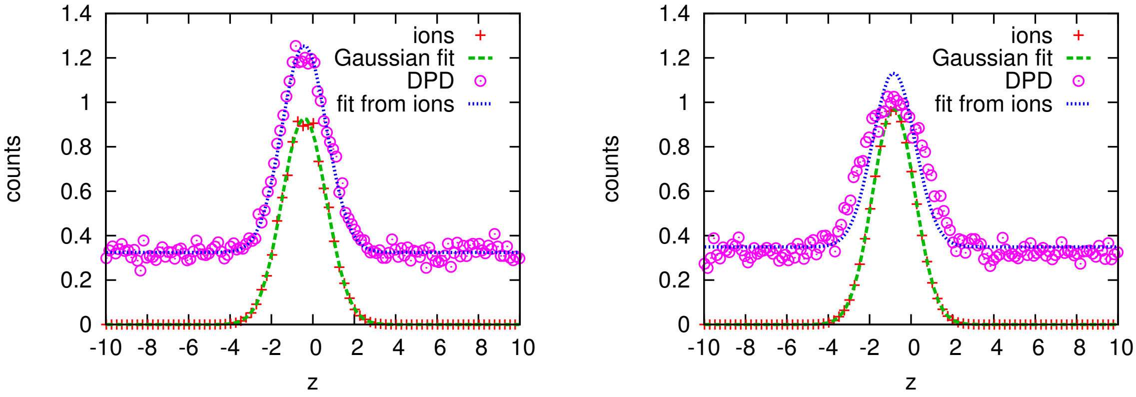

(a) cao 1, grid 24

(b) cao 2, grid 12

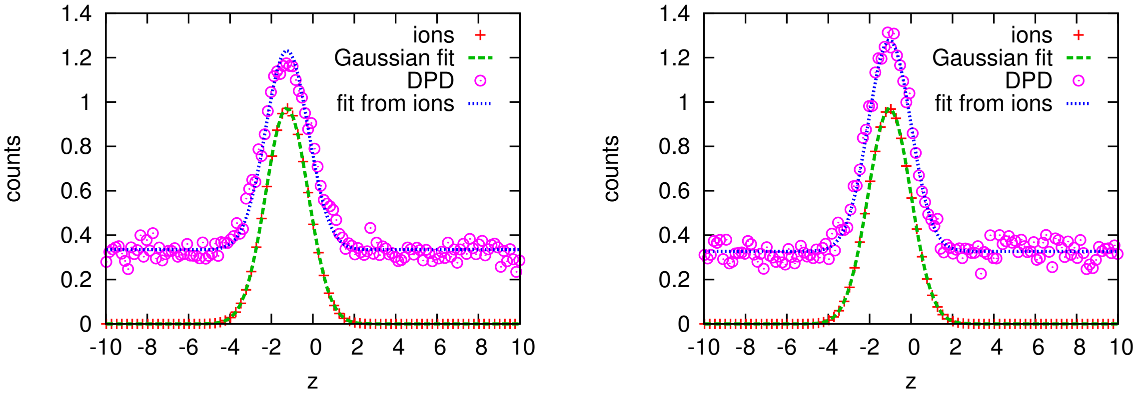

(c) cao 3, grid 24

(d) cao 4, grid 48

Figure A.17: Ion profiles and Gaussian fit together with the according DPD profiles (shifted) and the adapted fit function for different combinations of cao and grid size.

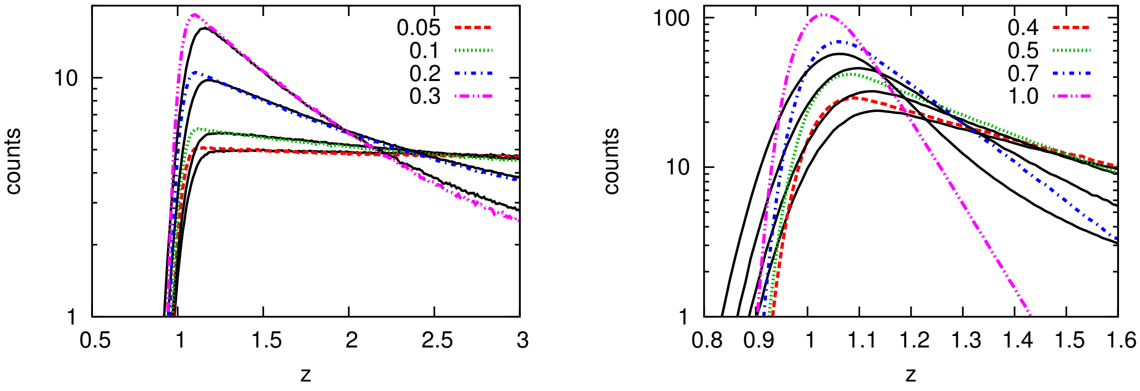

(a)

(b)

Figure A.18: Ion profiles (black lines) and DPD profiles for $N_c = N_{DPD}$ and different valencies. For $z_c = 1$ and $z_c = 0.7$ all DPD particles are dragged away from the center.

z_c	$\rho_q = z_c \rho_c$
0.05	0.234375
0.1	0.46875
0.2	0.9375
0.3	1.40625
0.4	1.875
0.5	2.34375
0.7	3.28125
1.0	4.6875

The DPD overshoot can thus be studied systematically with the increase in z_c. Figure A.18 shows all ion profiles (black lines) and the according DPD profiles, both held in logarithmic scale. Even the lowest valency, $z_c = 0.05$ leads to a relative high charge density, comparable to the ones studied earlier in this chapter. Ideally the DPD and ion curves should agree, as the number density is identical. The agreement, however, becomes worse with increasing z_c. For $z_c = 0.7$ and $z_c = 1.0$ the force on the DPD particles is so absurdly high that they vanish from the center of the slit, thus showing the limitations of the algorithm in this parameter set.

A.4.5 Improvement with Mesh Refinement

The whole overshoot phenomenon somewhat states that there is an imbalance in attraction and repulsion for the DPD particles. The attraction is given by the electrostatic forces of the counterions, which are the strongest close to the boundaries, where the electric field is the highest and also the largest amount of pseudo-ions are located to transport the force. The repulsion is governed by two effects, namely the WCA repulsion of the boundaries, ending at $z = 2^{1/6} \approx 1.122$, and the chemical potential gradient due to the particle overload. By increasing the grid size and keeping the assignment order constant, one effectively reduces the attraction-range for the DPD particles. This improves the situation, as shown in Figure A.19. There we take the system of size $10 \times 10 \times 15$ with boundaries at $z = 0$ and $z = 10$ and penetrable volume $10 \times 10 \times 8$, 3750 DPD particles and 500 pseudo-ions. The DPD overshoot is studied with different grid sizes and assignment orders, where all profiles are shifted to zero in the center of the channel, to directly compare them. We first note that there is never a direct resemblance of the two profiles, as the DPD peaks are generally wider. A pure increase of the mesh refinement in z-direction is already capable of reducing the overshoot sufficiently, but requires a factor 10 in the mesh size as a comparison of the first two curves shows [1]. Similarly, an increase in mesh size combined with an increase in assignment order does not lead to satisfactory changes. The best combination would be achieved for cao 3 with a grid in the range $12 \times 12 \times 18$ to $48 \times 48 \times 72$, i.e. a grid spacing of $10/12 \geq a \geq 10/48 \approx 0.2$. For the smallest value the coupling range would be reduced by a factor of four. However,

---

[1] Note that for the Poisson solver the grid spacing should preferably be kept constant in all directions.

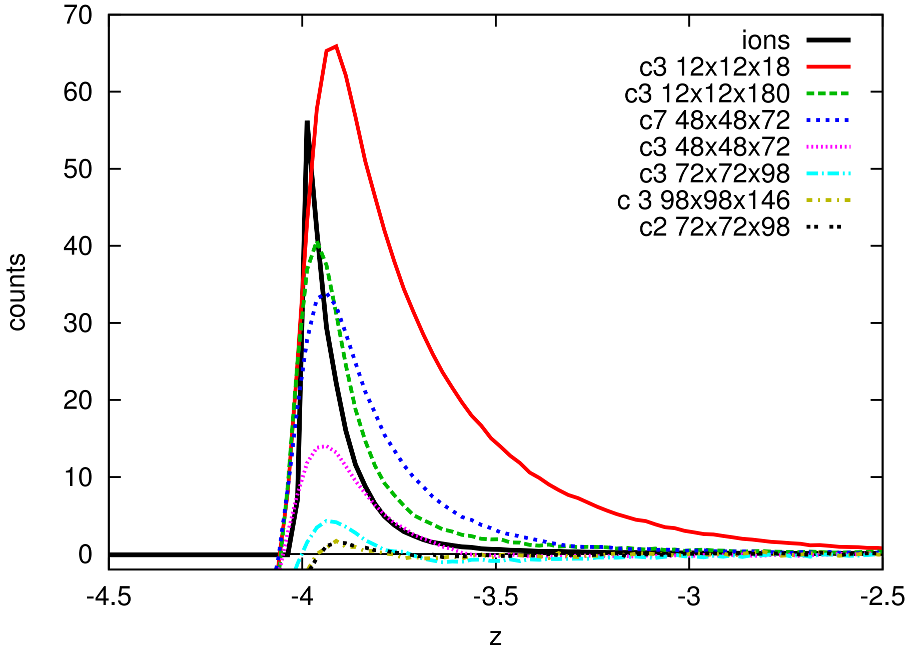

Figure A.19: DPD profiles in comparison to the ion profile (solid black line) to study the DPD overshoot. The grid sizes and charge assignment orders (c2,c3,c7) are varied systematically, listed in the order of the peak height. All profiles are shifted to zero in the center.

the drawback of a very fine mesh is that the coupling becomes leaky, so that there are occasions, where some pseudo-ions are in no contact to DPD particles. Yet the more the coupling is reduced, the lower the DPD curve becomes. The choice for the grid parameters is therefore strongly limited by the demand for a reduction of coupling-range to decrease attraction effects and a fully covering coupling procedure that does not leave particles out consistently.

Whenever a high charge gradient occurs, i.e. there is a strong attraction/repulsion, this becomes crucial. In most other situations the standard parameters as described in chapter 2.8 are applicable. Also, for the functionality of the algorithm the profiles do not need to match perfectly in the real space, but need to result in agreement on the grid level, as the coupling and momentum transport is happening there. Therefore we study the density profiles on the grid for the promising range of mesh sizes. Figure A.20 shows the resulting profiles on grid level and in real space. On the grid level the DPD profile has been modified by subtraction of the neutral solvent part, i.e. $\rho_n = \rho_{\mathrm{DPD}} - \rho_c$ (here assumed to be constant for simplicity). For the real space curves both profiles have been shifted to zero in the very center, which essentially has the same effect, but leads to a shifted scale. On the grid level (red-blue curves) the best agreement is achieved arguably either in (c),(g) or (h). In (g) and (h) for grid spacing $a = 10/32$ and $a = 10/36$ the peaks agree fairly well, but there is a small continuous DPD excess in the center of the slit. For $a = 10/28$ in (c) this excess vanishes, whereas the DPD overshoot is visible both on the grid level as well as in the real-space profile in (f). On the grid level, it shows that the DPD density reduces strongly into the negative for the very first and very last row, stating that there is a strong imbalance in the densities. However, the mismatch averages out, as there are always other grid points in z-direction involved due to the assignment-order and additionally there is the underlying neutral part to compensate minor mismatches.

A.4.6 Radial Distribution Functions

The coupling effect of pseudo-ions and DPD particles can also be seen in the radial distribution functions (RDF) of a simple bulk electrolyte system. Figure A.21a shows g_{+0}, i.e. the distribution of DPD particles around positively charged pseudo-ions in a bulk electrolyte with the following concentrations:

ρ_+	N_+
0.025	25
0.05	50
0.1	100
0.2	200

In A.21b the system of size 10^3 with $\rho_+ = 0.1$ is taken with four different parameter sets, [cao 2, grid 12^3], [cao 3, grid 12^3], [cao 3, grid 24^3] and [cao 3, grid 48^3]. For the systems in A.21a [cao 3, grid 12^3] was used. An increase in salt concentration does not show a quantitative difference in the arrangement of DPD particles. There is just a slight change close to $r = 0$. The reason might simply be that the averaging improves with the number of pseudo-ions, as there are more particles to overlap with. The overall increase is of a magnitude of around 0.035. The part (b) of the figure, however, shows a stronger deviation for different parameter sets. It seems that the combination reducing the ratio cao/grid size is increasing the correlation between pseudo-ions and DPD particles. The effect is quite local, as for $r > 1$, i.e. distances larger than the particle diameters, the deviations diminish.

Figure A.21b also stands in relation to the results in Figure A.15. Comparing the parameter sets [cao 2/3, grid 24] one can see that the lower cao enhances the DPD increase and leads to a better fit of the two profiles. Also the comparison [cao 3, grid 24/48] is in agreement with A.21b. A doubling of grid size leads to an improvement in the fit of the profiles, as the DPD profile increases as well. It is possible to directly compare both figures, since here we deal with grid spacing $10\sigma/12$ $(10\sigma/24)$ and in Figure A.15 it was $20\sigma/24$ $(20\sigma/48)$. An even larger grid as in Figure A.21b for [cao 3, grid 48] leads to a stronger, but slimmer peak, i.e. the correlation becomes more localized with increased mesh size, as the coupling range decreases.

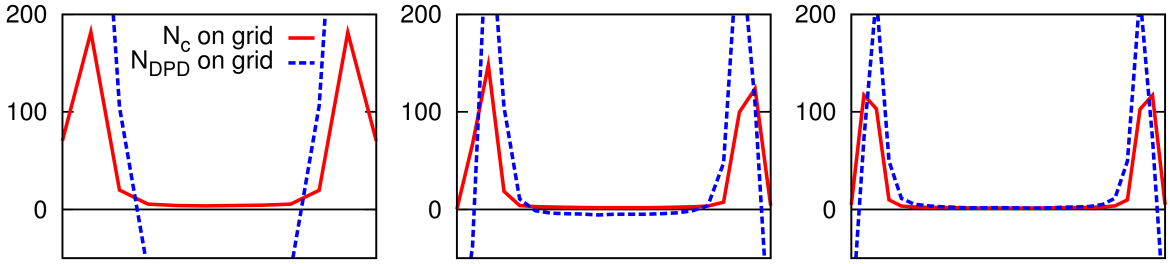

(a) 12 on mesh (b) 24 on mesh (c) 28 on mesh

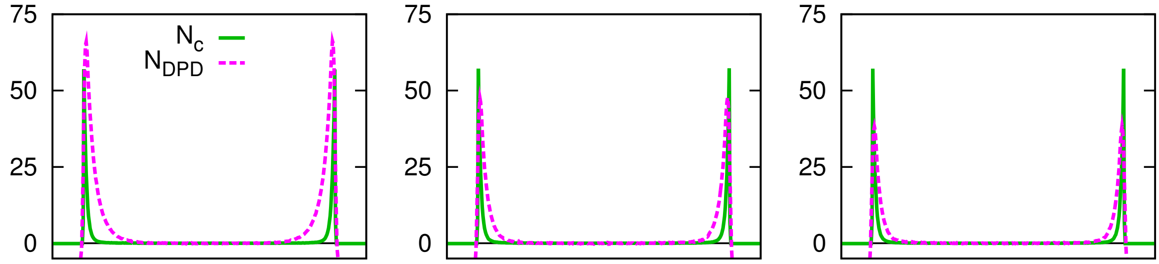

(d) 12 profile (e) 24 profile (f) 28 profile

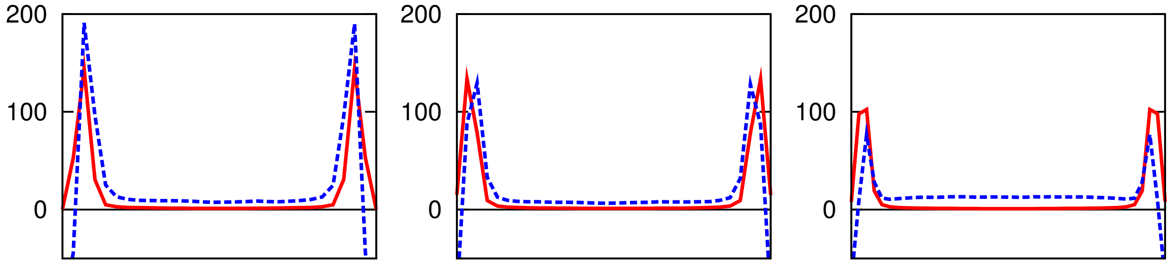

(g) 32 on mesh (h) 36 on mesh (i) 48 on mesh

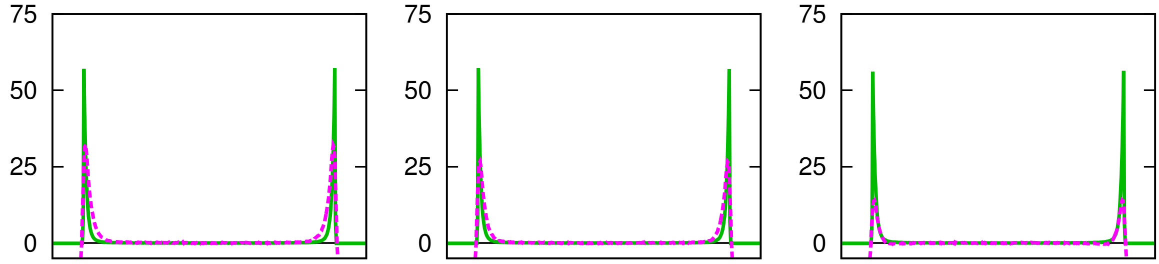

(j) 32 profile (k) 36 profile (l) 48 profile

Figure A.20: Comparison of different mesh sizes (named after x-direction) and the resulting DPD and ion profiles on the grid level and in real-space. The DPD profiles on grid level are reduced by the neutral solvent density (assumed to be homogeneous), and in real-space both profiles are shifted to zero in the center to investigate the overlap.

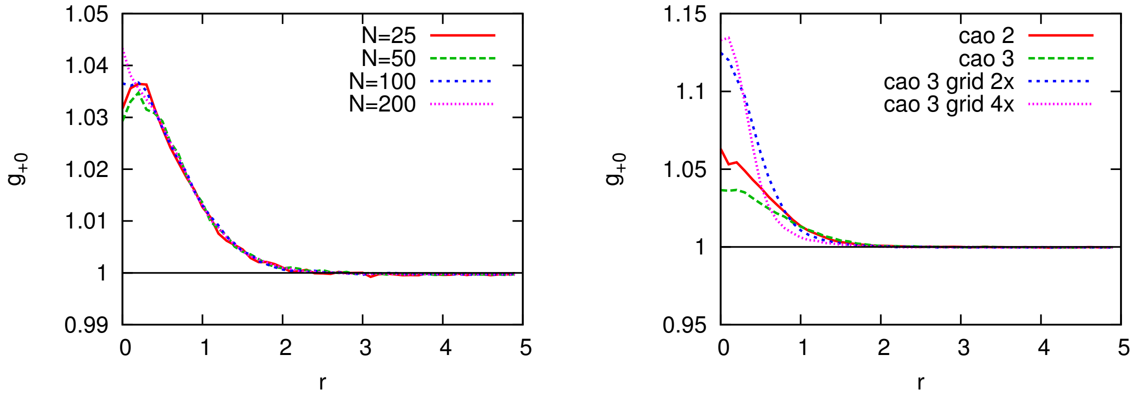

(a) (b)

Figure A.21: RDF of DPD particles and positive pseudo-ions. (a) compares different salt concentrations. (b) shows three different parameter sets for the algorithm.

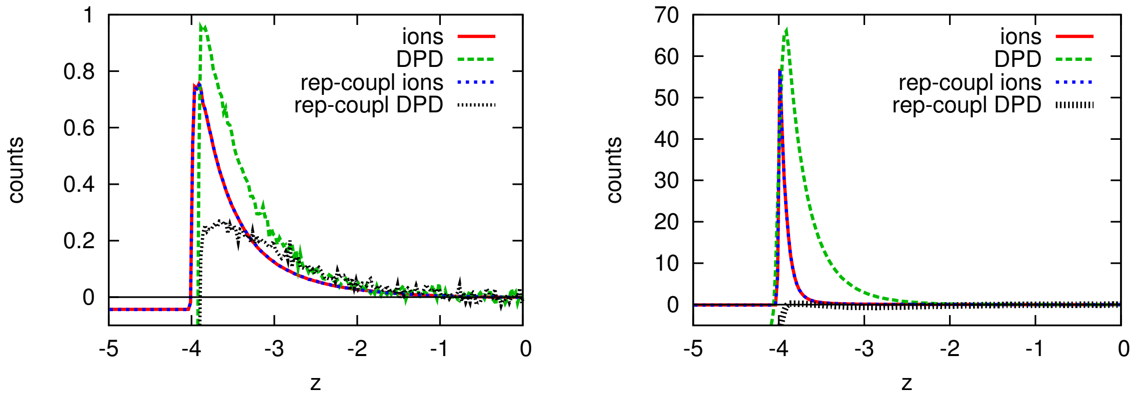

(a) $\rho_c = 0.0625$ (b) $\rho_c = 0.625$

Figure A.22: Ion and reduced DPD profiles for a coupling scheme that includes the repulsive boundary forces to decrease the overshoot effect in comparison to the original profiles.

A.4.7 Force-Coupling Relations

The problem with the excess or shortage of DPD density in certain areas of high counterion density must be related to the coupling term in the Navier-Stokes equation, acting on the DPD particles as an additional force. As described earlier, the DPD particles play the role of the total mass density in the system, i.e.

$$\rho_{\text{DPD}} = \rho_s + \rho_c \tag{A.4.7}$$

with the neutral solvent density ρ_s and the total charge density ρ_c. In the simplest case the charge density is only a counterion density. As for the counterion interactions there is a conservative, electrostatic potential Φ_c, the equilibrium distribution should be a Boltzmann law

$$\rho_c(x) = \rho_c^0 e^{-\Phi_c/k_BT} \quad . \tag{A.4.8}$$

Similarly one would expect the DPD density to follow a Boltzmann law in equilibrium, if there is a conservative potential Φ_{DPD} describing the force term originating from the electrostatic coupling

$$\rho_{\text{DPD}}(x) = \rho_{\text{DPD}}^0 e^{-\Phi_{\text{DPD}}/k_BT} \quad . \tag{A.4.9}$$

Thus we can write

$$\rho_{\text{DPD}}^0 e^{-\Phi_{\text{DPD}}/k_BT} = \rho_s + \rho_c^0 e^{-\Phi_c/k_BT} \tag{A.4.10}$$

and take the logarithm to end up with

$$\frac{\Phi_{\text{DPD}}}{k_BT} = -\log(\rho_{\text{DPD}}^0) + \log\left(\rho_s + \rho_c^0 e^{-\Phi_c/k_BT}\right) \quad . \tag{A.4.11}$$

Hence there is a way to write the potential for the DPD particles. Taking the derivative to obtain the corresponding field we get

$$\begin{aligned} \nabla\Phi_{\text{DPD}} &= \frac{\rho_c}{\rho_s + \rho_c}\nabla\Phi_c \\ &= \frac{\rho_c}{\rho_{\text{DPD}}}\nabla\Phi_c \quad . \end{aligned} \tag{A.4.12}$$

This equation says that the force acting on the pseudo-ions has to be normalized with the densities before applying it to the DPD particles. The same follows if one asks for momentum conservation

$$\begin{aligned} & F_{\text{DPD}}^{\text{total}} &&= F_c^{\text{total}} && \\ \Rightarrow \quad & -\int dV \rho_{\text{DPD}}\nabla\Phi_{\text{DPD}} &&= -\int dV \rho_c \nabla\Phi_c && |\text{V arbitrary} \\ \Rightarrow \quad & \rho_{\text{DPD}}\nabla\Phi_{\text{DPD}} &&= \rho_c\nabla\Phi_c \quad . && \end{aligned} \tag{A.4.13}$$

Hence the density ratio acts as a prefactor to the force. If now the ratio is disturbed somewhere, e.g. there are more counterions, the force on the DPD particles is stronger. This is exactly the way the coupling is implemented in the algorithm, as explained in chapter 2.7.2. However, the discretization of the coupling seems to be the cause for the mismatches.

Up to now the strongest deviations occurred close to a boundary. Thus it is not strictly the algorithm itself, but the combination with repulsive boundaries that leads to anomalies. Time step effects as described in chapter A.1 also play a role for the specific shape of the pseudo-ion profiles close to the boundaries. The general discrepancy is then further controlled by the grid parameters, i.e. the assignment order and the grid spacing. The parameter N_q did not lead to any change in both profiles, neither for low counterion densities, nor for the high ones with the DPD overshoot. In summary, the standard parameters [cao 3, grid spacing $a = 10\sigma/12$] have proven to work well in most situations. However, one has to take care in situations where the boundary effects could be dominant, especially when high charge gradients are expected. In this case a more refined mesh, e.g. by a factor of 3-4 larger, could be advantageous.

A.4.8 An Alternative Coupling Approach

The large increase of DPD density close to the boundaries in situations of high charge gradients is not desirable. While it is a rather unphysical effect by itself, it also complicates the analysis, as a homogeneous density is easier to handle analytically. This approximation, however, would not hold in most of the situations presented throughout this chapter. A possibility to decrease the DPD overshoot is to use a different force coupling between pseudo-ions and DPD particles. In the usual procedure only the electrostatic forces are transferred to the DPD particles, whereas the boundary repulsion felt by the pseudo-ions is just considered a tool to keep them confined to the DPD fluid. Apparently the repulsion felt by the DPD particles is not sufficient to balance the electrostatic attractions properly. So one could in principle try to transfer the pseudo-ion repulsions together with the electrostatics, to decrease the attraction felt by the DPD particles. With this approach the WCA repulsion for the pseudo-ions is no longer considered simply a tool, but obtains a more physical meaning. Simulations with this coupling scheme lead to the profiles presented in Figure A.22. For low charge densities as in (a) this approach leads to much flatter DPD profiles. For high charge concentrations as in (b) the strong overshoot disappears completely, however, leaving a small range close to the boundaries with a reduced density.

Hence this coupling method is applicable in situations where one needs a more homogeneous DPD profile, and does not care about the exact representation of the total density, as the DPD density is closer to the pure solvent density in this situation. Also, the transport of momentum in driven situations, such as with an external electric field, is still working. Only the interpretation of forces orthogonal to the boundaries becomes questionable.

A.5 Additional Plots for the Polyelectrolyte Solutions

In this section we present some further figures that have been left out in the discussion of the polyelectrolyte solutions in chapter 4.

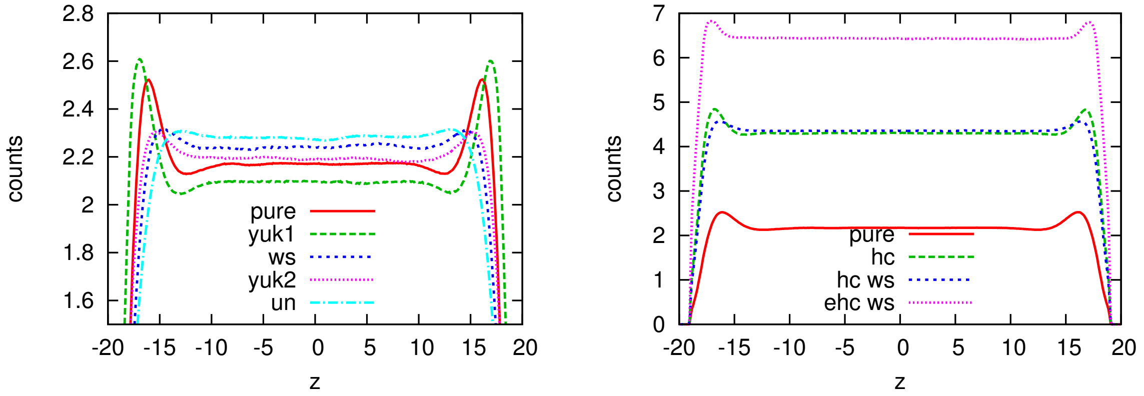

(a) (b)

Figure A.23: Monomer profiles in the channel. (a) comparison of both Yukawa cases, (b) the concentration dependence.

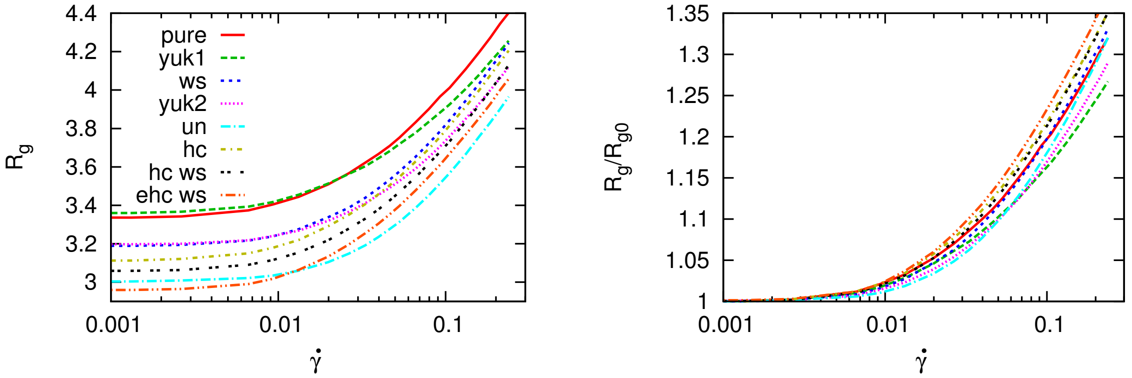

(a) (b)

Figure A.24: Radius of gyration for all studied systems in Couette flow. (a) shows the absolute values, (b) shows the relative change of R_g versus shear rate.

References

[1] V. Pokrovskii, *The Mesoscopic Theory of Polymer Dynamics*. Springer, 2000.

[2] J. Smiatek and F. Schmid, "Mesoscopic simulation methods for studying flow and transport in electric fields in micro- and nanochannels," *InTech, Advances in Microfluidics*, 2012.

[3] O. A. Hickey, C. Holm, J. L. Harden, and G. W. Slater, "Implicit method for simulating electrohydrodynamics of polyelectrolytes," *Physical Review Letters*, vol. 105, no. 14, p. 148301, 2010.

[4] O. A. Hickey, T. N. Shendruk, J. L. Harden, and G. W. Slater, "Simulations of free-solution electrophoresis of polyelectrolytes with a finite debye length using the debye-hückel approximation," *Physical Review Letters*, vol. 109, no. 9, p. 098302, 2012.

[5] D. Duong-Hong, J. Han, J.-S. Wang, N. G. Hadjiconstantinou, Y. Z. Chen, and G.-R. Liu, "Realistic simulations of combined DNA electrophoretic flow and EOF in nano-fluidic devices," *Electrophoresis*, vol. 29, no. 24, pp. 4880–4886, 2008.

[6] K. Kim, Y. Nakayama, and R. Yamamoto, "Direct numerical simulations of electrophoresis of charged colloids," *Physical Review Letters*, vol. 96, no. 20, p. 208302, 2006.

[7] S. Fischer, A. Naji, and R. R. Netz, "Salt-induced counterion-mobility anomaly in polyelectrolyte electrophoresis," *Physical Review Letters*, vol. 101, no. 17, p. 176103, 2008.

[8] J. P. Hernández-Ortiz, J. J. de Pablo, and M. D. Graham, "Fast computation of many-particle hydrodynamic and electrostatic interactions in a confined geometry," *Physical Review Letters*, vol. 98, no. 14, p. 140602, 2007.

[9] R. Groot, "Electrostatic interactions in dissipative particle dynamics–simulation of polyelectrolytes and anionic surfactants," *The Journal of Chemical Physics*, vol. 118, p. 11265, 2003.

[10] M. González-Melchor, E. Mayoral, M. E. Velázquez, and J. Alejandre, "Electrostatic interactions in dissipative particle dynamics using the ewald sums," *The Journal of Chemical Physics*, vol. 125, p. 224107, 2006.

[11] J. Horbach and D. Frenkel, “Lattice-boltzmann method for the simulation of transport phenomena in charged colloids,” *Physical Review E*, vol. 64, no. 6, p. 061507, 2001.

[12] F. Capuani, I. Pagonabarraga, and D. Frenkel, “Discrete solution of the electrokinetic equations,” *The Journal of Chemical Physics*, vol. 121, no. 2, pp. 973–986, 2004.

[13] J. El-Ali, P. K. Sorger, and K. F. Jensen, “Cells on chips,” *Nature*, vol. 442, no. 7101, pp. 403–411, 2006.

[14] P. S. Dittrich and A. Manz, “Single-molecule fluorescence detection in microfluidic channels – the holy grail in μtas?,” *Analytical and Bioanalytical Chemistry*, vol. 382, no. 8, pp. 1771–1782, 2005.

[15] C.-W. Kan, C. P. Fredlake, E. A. Doherty, and A. E. Barron, “Dna sequencing and genotyping in miniaturized electrophoresis systems,” *Electrophoresis*, vol. 25, no. 21-22, pp. 3564–3588, 2004.

[16] G. Batchelor, *An Introduction to Fluid Dynamics:*. Cambridge Mathematical Library, Cambridge University Press, 2000.

[17] H. Park, J. Lee, and T. Kim, “Comparison of the nernst–planck model and the poisson–boltzmann model for electroosmotic flows in microchannels,” *Journal of colloid and interface science*, vol. 315, no. 2, pp. 731–739, 2007.

[18] D. P. Chen, V. Barcilon, and R. S. Eisenberg, “Constant fields and constant gradients in open ionic channels,” *Biophysical Journal*, vol. 61, no. 5, pp. 1372–1393, 1992.

[19] B. Eisenberg, “Multiple scales in the simulation of ion channels and proteins,” *The Journal of Physical Chemistry C*, vol. 114, no. 48, pp. 20719–20733, 2010.

[20] P. Debye and E. Hückel, “Lowering of freezing point and related phenomena,” *Z. Phys*, vol. 24, p. 185, 1923.

[21] J. Smiatek and F. Schmid, “Polyelectrolyte electrophoresis in nanochannels: A dissipative particle dynamics simulation,” *The Journal of Physical Chemistry B*, vol. 114, no. 19, pp. 6266–6272, 2010.

[22] R. Probstein, *Physicochemical Hydrodynamics: An Introduction.* Wiley, 2005.

[23] M. Deserno, C. Holm, and S. May, “Fraction of condensed counterions around a charged rod: comparison of poisson-boltzmann theory and computer simulations,” *Macromolecules*, vol. 33, no. 1, pp. 199–206, 2000.

[24] C. Holm, P. Kékicheff, and R. Podgornik, *Electrostatic effects in soft matter and biophysics*, vol. 46. Springer, 2001.

[25] B. Alder and T. Wainwright, “Studies in molecular dynamics. i. general method,” *The Journal of Chemical Physics*, vol. 31, p. 459, 1959.

[26] D. Frenkel and B. Smit, *Understanding molecular simulation: from algorithms to applications*, vol. 1. Academic press, 2001.

[27] M. Allen and D. Tildesley, *Computer simulation of liquids.* Oxford University Press, USA, 1987.

[28] D. P. Landau and K. Binder, *A guide to Monte Carlo simulations in statistical physics.* Cambridge university press, 2005.

[29] D. C. Rapaport, *The art of molecular dynamics simulation.* Cambridge university press, 2004.

[30] H.-J. Limbach, A. Arnold, B. A. Mann, and C. Holm, “Espresso - an extensible simulation package for research on soft matter systems,” *Computer Physics Communications*, vol. 174, no. 9, pp. 704–727, 2006.

[31] J. Le Guillou and J. Zinn-Justin, “Critical exponents for the n-vector model in three dimensions from field theory,” *Physical Review Letters*, vol. 39, no. 2, pp. 95–98, 1977.

[32] P. J. Flory, *Principles of polymer chemistry.* Baker lectures 1948, CORNELL University Press, 1953.

[33] H. J. Limbach and C. Holm, “Conformational properties of poor solvent polyelectrolytes,” *Computer Physics Communications*, vol. 147, no. 1, pp. 321–324, 2002.

[34] J. Jeon and A. V. Dobrynin, “Necklace globule and counterion condensation,” *Macromolecules*, vol. 40, no. 21, pp. 7695–7706, 2007.

[35] J.-L. Barrat and J.-F. Joanny, “Theory of polyelectrolyte solutions,” *Advances in Chemical Physics, Polymeric Systems*, p. 1, 1997.

[36] G. S. Manning, “Limiting laws and counterion condensation in polyelectrolyte solutions i. colligative properties,” *The Journal of Chemical Physics*, vol. 51, p. 924, 1969.

[37] F. Oosawa, *Polyelectrolytes.* Marcel Dekker, 1971.

[38] G. S. Manning and J. Ray, “Counterion condensation revisited,” *Journal of Biomolecular Structure and Dynamics*, vol. 16, no. 2, pp. 461–476, 1998.

[39] D. Stigter, “Evaluation of the counterion condensation theory of polyelectrolytes,” *Biophysical Journal*, vol. 69, no. 2, pp. 380–388, 1995.

[40] L. Belloni, M. Drifford, and P. Turq, “Counterion diffusion in polyelectrolyte solutions,” *Chemical Physics*, vol. 83, no. 1, pp. 147–154, 1984.

[41] L. Belloni, “Ionic condensation and charge renormalization in colloidal suspensions,” *Colloids and Surfaces A: Physicochemical and Engineering Aspects*, vol. 140, no. 1, pp. 227–243, 1998.

[42] S. Frank and R. Winkler, “Polyelectrolyte electrophoresis: Field effects and hydrodynamic interactions,” *EPL (Europhysics Letters)*, vol. 83, no. 3, p. 38004, 2008.

[43] R. Netz, “Nonequilibrium unfolding of polyelectrolyte condensates in electric fields,” *Physical Review Letters*, vol. 90, no. 12, p. 128104, 2003.

[44] Q. Liao, J.-M. Y. Carrillo, A. V. Dobrynin, and M. Rubinstein, “Rouse dynamics of polyelectrolyte solutions: Molecular dynamics study,” *Macromolecules*, vol. 40, no. 21, pp. 7671–7679, 2007.

[45] M. Moeller and K. Matyjaszewski, “Polymer science: A comprehensive reference,” 2012.

[46] M. Doi and S. F. Edwards, *The theory of polymer dynamics*, vol. 73. Oxford University Press, USA, 1988.

[47] A. V. Dobrynin, “Theory and simulations of charged polymers: From solution properties to polymeric nanomaterials,” *Current Opinion in Colloid & Interface Science*, vol. 13, no. 6, pp. 376–388, 2008.

[48] D. C. Boris and R. H. Colby, “Rheology of sulfonated polystyrene solutions,” *Macromolecules*, vol. 31, no. 17, pp. 5746–5755, 1998.

[49] A. V. Dobrynin and M. Rubinstein, “Theory of polyelectrolytes in solutions and at surfaces,” *Progress in Polymer Science*, vol. 30, no. 11, pp. 1049–1118, 2005.

[50] M. Rubinstein and R. Colby, *Polymer Physics (Chemistry).* Oxford University Press, USA, 2003.

[51] J. D. Weeks, D. Chandler, and H. C. Andersen, “Role of repulsive forces in determining the equilibrium structure of simple liquids,” *The Journal of Chemical Physics*, vol. 54, p. 5237, 1971.

[52] H. Barnes, “Shear-thickening (dilatancy) in suspensions of nonaggregating solid particles dispersed in newtonian liquids,” *Journal of Rheology*, vol. 33, p. 329, 1989.

[53] C. Stoltz, J. J. de Pablo, and M. D. Graham, “Simulation of nonlinear shear rheology of dilute salt-free polyelectrolyte solutions,” *The Journal of Chemical Physics*, vol. 126, p. 124906, 2007.

[54] P. C. Hiemenz and R. Rajagopalan, *Principles of Colloid and Surface Chemistry, revised and expanded*, vol. 14. CRC, 1997.

[55] R. B. Bird, R. C. Armstrong, and O. Hassager, *Dynamics of polymeric liquids. Vol. 1: Fluid mechanics.* John Wiley and Sons Inc., New York, NY, 1987.

[56] J. S. Hansen, J. C. Dyre, P. J. Daivis, B. D. Todd, and H. Bruus, "Nanoflow hydrodynamics," *Physical Review E*, vol. 84, p. 036311, Sep 2011.

[57] L. Bocquet and E. Charlaix, "Nanofluidics, from bulk to interfaces," *Chemical Society Reviews*, vol. 39, no. 3, pp. 1073–1095, 2010.

[58] J. Rotne and S. Prager, "Variational treatment of hydrodynamic interaction in polymers," *The Journal of Chemical Physics*, vol. 50, p. 4831, 1969.

[59] J. F. Brady and G. Bossis, "Stokesian dynamics," *Annual Review of Fluid Mechanics*, vol. 20, pp. 111–157, 1988.

[60] A. Malevanets and R. Kapral, "Mesoscopic model for solvent dynamics," *The Journal of Chemical Physics*, vol. 110, p. 8605, 1999.

[61] A. Malevanets and R. Kapral, "Solute molecular dynamics in a mesoscale solvent," *The Journal of Chemical Physics*, vol. 112, p. 7260, 2000.

[62] G. Gompper, T. Ihle, D. Kroll, and R. Winkler, "Multi-particle collision dynamics: A particle-based mesoscale simulation approach to the hydrodynamics of complex fluids," in *Advanced Computer Simulation Approaches for Soft Matter Sciences III* (C. Holm and K. Kremer, eds.), vol. 221 of *Advances in Polymer Science*, pp. 1–87, Springer Berlin Heidelberg, 2009.

[63] R. Benzi, S. Succi, and M. Vergassola, "The lattice boltzmann equation: theory and applications," *Physics Reports*, vol. 222, no. 3, pp. 145–197, 1992.

[64] S. Chen and G. D. Doolen, "Lattice boltzmann method for fluid flows," *Annual Review of Fluid Mechanics*, vol. 30, no. 1, pp. 329–364, 1998.

[65] A. Ladd, "Numerical simulations of particulate suspensions via a discretized boltzmann equation. part 1. theoretical foundation," *Journal of Fluid Mechanics*, vol. 271, no. 1, pp. 285–309, 1994.

[66] A. Ladd, "Numerical simulations of particulate suspensions via a discretized boltzmann equation. part 2. numerical results," *Journal of Fluid Mechanics*, vol. 271, no. 1, pp. 311–339, 1994.

[67] P. Ahlrichs and B. Dünweg, "Lattice-boltzmann simulation of polymer-solvent systems," *International Journal of Modern Physics C*, vol. 9, no. 08, pp. 1429–1438, 1998.

[68] P. Ahlrichs and B. Dünweg, "Simulation of a single polymer chain in solution by combining lattice boltzmann and molecular dynamics," *The Journal of Chemical Physics*, vol. 111, p. 8225, 1999.

[69] R. A. Gingold and J. J. Monaghan, “Smoothed particle hydrodynamics-theory and application to non-spherical stars,” *Monthly notices of the royal astronomical society*, vol. 181, pp. 375–389, 1977.

[70] J. J. Monaghan, “Smoothed particle hydrodynamics,” *Reports on progress in Physics*, vol. 68, no. 8, p. 1703, 2005.

[71] P. Espanol and M. Revenga, “Smoothed dissipative particle dynamics.,” *Physical Review. E, Statistical, nonlinear, and soft matter physics*, vol. 67, no. 2 Pt 2, p. 026705, 2003.

[72] P. Hoogerbrugge and V. Koelman, “Simulating microscopic hydrodynamic phenomena with dissipative particle dynamics.,” *EPL (Europhysics Letters)*, vol. 19, no. 3, pp. 155–160, 1992.

[73] J. Koelman and P. Hoogerbrugge, “Dynamic simulations of hard-sphere suspensions under steady shear,” *EPL (Europhysics Letters)*, vol. 21, no. 3, p. 363, 1993.

[74] P. Español and P. Warren, “Statistical mechanics of dissipative particle dynamics,” *EPL (Europhysics Letters)*, vol. 30, pp. 191–196, 1995.

[75] J. Smiatek, M. P. Allen, and F. Schmid, “Tunable-slip boundaries for coarse-grained simulations of fluid flow,” *The European Physical Journal E: Soft Matter and Biological Physics*, vol. 26, no. 1, pp. 115–122, 2008.

[76] C. Lowe, “An alternative approach to dissipative particle dynamics,” *EPL (Europhysics Letters)*, vol. 47, no. 2, p. 145, 1999.

[77] J. Smiatek, M. Sega, C. Holm, U. D. Schiller, and F. Schmid, “Mesoscopic simulations of the counterion-induced electro-osmotic flow: A comparative study,” *The Journal of Chemical Physics*, vol. 130, no. 24, pp. 244702–244702, 2009.

[78] T. Soddemann, B. Dünweg, and K. Kremer, “Dissipative particle dynamics: A useful thermostat for equilibrium and nonequilibrium molecular dynamics simulations,” *Physical Review E*, vol. 68, no. 4, p. 046702, 2003.

[79] E. G. Flekkøy and P. V. Coveney, “From molecular dynamics to dissipative particle dynamics,” *Physical Review Letters*, vol. 83, no. 9, pp. 1775–1778, 1999.

[80] M. Serrano, G. De Fabritiis, P. Espanol, E. G. Flekkøy, and P. V. Coveney, “Mesoscopic dynamics of voronoi fluid particles,” *Journal of Physics A: Mathematical and General*, vol. 35, no. 7, p. 1605, 2002.

[81] C. Marsh, G. Backx, and M. Ernst, “Fokker-planck-boltzmann equation for dissipative particle dynamics,” *EPL (Europhysics Letters)*, vol. 38, no. 6, pp. 411–415, 1997.

[82] R. D. Groot and P. B. Warren, “Dissipative particle dynamics: Bridging the gap between atomistic and mesoscopic simulation,” *The Journal of Chemical Physics*, vol. 107, p. 4423, 1997.

[83] E. Peters, “Elimination of time step effects in DPD,” *EPL (Europhysics Letters)*, vol. 66, no. 3, p. 311, 2004.

[84] W. Jiang, J. Huang, Y. Wang, and M. Laradji, “Hydrodynamic interaction in polymer solutions simulated with dissipative particle dynamics,” *The Journal of Chemical Physics*, vol. 126, p. 044901, 2007.

[85] C. Junghans, M. Praprotnik, and K. Kremer, “Transport properties controlled by a thermostat: An extended dissipative particle dynamics thermostat,” *Soft Matter*, vol. 4, no. 1, pp. 156–161, 2008.

[86] I. Pagonabarraga, M. Hagen, and D. Frenkel, “Self-consistent dissipative particle dynamics algorithm,” *EPL (Europhysics Letters)*, vol. 42, no. 4, p. 377, 1998.

[87] M. P. Allen, “Configurational temperature in membrane simulations using dissipative particle dynamics,” *The Journal of Physical Chemistry B*, vol. 110, no. 8, pp. 3823–3830, 2006.

[88] M. Serrano, G. De Fabritiis, P. Espanol, and P. Coveney, “A stochastic trotter integration scheme for dissipative particle dynamics,” *Mathematics and Computers in Simulation*, vol. 72, no. 2, pp. 190–194, 2006.

[89] J. Backer, C. Lowe, H. Hoefsloot, and P. Iedema, “Poiseuille flow to measure the viscosity of particle model fluids,” *The Journal of Chemical Physics*, vol. 122, no. 15, pp. 154503–154503, 2005.

[90] J. Smiatek, *Mesoscopic simulations of electrohydrodynamic phenomena.* PhD thesis, Bielefeld University, 2009.

[91] E. Lauga, M. P. Brenner, and H. A. Stone, “Microfluidics: The no-slip boundary condition,” *arXiv preprint cond-mat/0501557*, 2005.

[92] S. V. Patankar, *Numerical heat transfer and fluid flow.* Taylor & Francis Group, 1980.

[93] P. Szymczak and A. Ladd, “Boundary conditions for stochastic solutions of the convection-diffusion equation,” *Physical Review E*, vol. 68, no. 3, p. 036704, 2003.

[94] J. Honerkamp, *Stochastic Dynamical Systems: Concepts, Numerical Methods, Data Analysis.* Wiley, 1993.

[95] H. Risken, “The fokker-planck equation: Methods of solution and applications,” 1984.

[96] H. Öttinger, *Stochastic processes in polymeric fluids: tools and examples for developing simulation algorithms.* Springer, 1996.

[97] P. E. Kloeden and E. Platen, *Numerical solution of stochastic differential equations*, vol. 23. Springer Verlag, 1992.

[98] R. W. Hockney and J. W. Eastwood, *Computer simulation using particles.* Taylor & Francis, 1988.

[99] M. Deserno and C. Holm, “How to mesh up ewald sums. i. a theoretical and numerical comparison of various particle mesh routines,” *The Journal of Chemical Physics*, vol. 109, pp. 7678–7693, 1998.

[100] G. Sutmann, P. Gibbon, and T. Lippert, *Fast Methods for Long-Range Interactions in Complex Systems.* Forschungszentrum Jülich, 2011.

[101] P. Ewald, “Die berechnung optischer und elektrostatischer gitterpotentiale,” *Annalen der Physik*, vol. 369, pp. 253–287, 1921.

[102] W. H. Press, S. A. Teukolsky, W. T. Vetterling, and B. P. Flannery, *Numerical recipes 3rd edition: The art of scientific computing.* Cambridge University Press, 2007.

[103] A. Arnold and C. Holm, “Mmm2d: A fast and accurate summation method for electrostatic interactions in 2d slab geometries,” *Computer Physics Communications*, vol. 148, no. 3, pp. 327–348, 2002.

[104] A. Arnold, J. de Joannis, and C. Holm, “Electrostatics in periodic slab geometries. i,” *The Journal of Chemical Physics*, vol. 117, no. 6, pp. 2496–2502, 2002.

[105] I.-C. Yeh and M. L. Berkowitz, “Ewald summation for systems with slab geometry,” *The Journal of Chemical Physics*, vol. 111, p. 3155, 1999.

[106] S. Tyagi, A. Arnold, and C. Holm, “Electrostatic layer correction with image charges: A linear scaling method to treat slab 2d+ h systems with dielectric interfaces,” *The Journal of Chemical Physics*, vol. 129, no. 20, pp. 204102–204102, 2008.

[107] S. Kesselheim, M. Sega, and C. Holm, “The icc* algorithm: A fast way to include dielectric boundary effects into molecular dynamics simulations,” *arXiv preprint arXiv:1003.1271*, 2010.

[108] R. J. Hunter, L. R. White, and D. Y. Chan, *Foundations of colloid science*, vol. 1. Clarendon Press Oxford, 1987.

[109] J. Beckers, C. Lowe, and S. De Leeuw, “An iterative pppm method for simulating coulombic systems on distributed memory parallel computers,” *Molecular Simulation*, vol. 20, no. 6, pp. 369–383, 1998.

[110] C. Marsh, G. Backx, and M. Ernst, “Static and dynamic properties of dissipative particle dynamics,” *Physical Review E*, vol. 56, no. 2, p. 1676, 1997.

[111] I. Nakamura, A.-C. Shi, and Z.-G. Wang, “Ion solvation in liquid mixtures: Effects of solvent reorganization,” *Physical Review Letters*, vol. 109, no. 25, p. 257802, 2012.

[112] Z.-G. Wang, “Fluctuation in electrolyte solutions: the self energy,” *Physical Review E*, vol. 81, no. 2, p. 021501, 2010.

[113] R. Wang and Z.-G. Wang, “Effects of ion solvation on phase equilibrium and interfacial tension of liquid mixtures,” *The Journal of Chemical Physics*, vol. 135, p. 014707, 2011.

[114] Y. Saito, N. Sasaki, and T. Komatsu, “Molecular dynamics simulation for lubricant shear properties during heating,” *Magnetics, IEEE Transactions on*, vol. 48, no. 6, pp. 2009–2015, 2012.

[115] K. K. Müller-Nedebock and T. A. Vilgis, “Dynamics of dense polyelectrolyte solutions,” *Macromolecules*, vol. 31, no. 17, pp. 5898–5903, 1998.

[116] M. Rubinstein, R. H. Colby, and A. V. Dobrynin, “Dynamics of semidilute polyelectrolyte solutions,” *Physical Review Letters*, vol. 73, no. 20, p. 2776, 1994.

[117] A. V. Dobrynin, R. H. Colby, and M. Rubinstein, “Scaling theory of polyelectrolyte solutions,” *Macromolecules*, vol. 28, no. 6, pp. 1859–1871, 1995.

[118] J. Wang, L. Benyahia, C. Chassenieux, J.-F. Tassin, and T. Nicolai, “Shear-induced gelation of associative polyelectrolytes,” *Polymer*, vol. 51, no. 9, pp. 1964–1971, 2010.

[119] A. Lees and S. Edwards, “The computer study of transport processes under extreme conditions,” *Journal of Physics C: Solid State Physics*, vol. 5, no. 15, p. 1921, 1972.

[120] U. Raviv, S. Giasson, N. Kampf, J.-F. Gohy, R. Jérôme, and J. Klein, “Lubrication by charged polymers,” *Nature*, vol. 425, no. 6954, pp. 163–165, 2003.

[121] J.-M. Y. Carrillo, D. Russano, and A. V. Dobrynin, “Friction between brush layers of charged and neutral bottle-brush macromolecules. molecular dynamics simulations,” *Langmuir*, vol. 27, no. 23, pp. 14599–14608, 2011.

[122] A. Galuschko, L. Spirin, T. Kreer, A. Johner, C. Pastorino, J. Wittmer, and J. Baschnagel, “Frictional forces between strongly compressed, nonentangled polymer brushes: molecular dynamics simulations and scaling theory,” *Langmuir*, vol. 26, no. 9, pp. 6418–6429, 2010.

[123] L. Chen, H. Merlitz, S.-z. He, C.-x. Wu, and J.-U. Sommer, "Approaching charged polymer brushes," in *Remote Sensing, Environment and Transportation Engineering (RSETE), 2011 International Conference on*, pp. 5749–5751, IEEE, 2011.

[124] J.-M. Y. Carrillo and A. V. Dobrynin, "Polyelectrolytes in salt solutions: Molecular dynamics simulations," *Macromolecules*, vol. 44, no. 14, pp. 5798–5816, 2011.

[125] C. Huang, R. Winkler, G. Sutmann, and G. Gompper, "Semidilute polymer solutions at equilibrium and under shear flow," *Macromolecules*, vol. 43, no. 23, pp. 10107–10116, 2010.

[126] R. Pamies, J. Cifre, D. La Torre, and J. García, "Brownian dynamics simulation of polyelectrolyte dilute solutions under shear flow," *Journal of Polymer Science Part B: Polymer Physics*, vol. 45, no. 1, pp. 1–9, 2007.

[127] W. E. Krause, E. G. Bellomo, and R. H. Colby, "Rheology of sodium hyaluronate under physiological conditions," *Biomacromolecules*, vol. 2, no. 1, pp. 65–69, 2001.

[128] S. Carrington, J. Odell, L. Fisher, J. Mitchell, and L. Hartley, "Polyelectrolyte behaviour of dilute xanthan solutions: Salt effects on extensional rheology," *Polymer*, vol. 37, no. 13, pp. 2871–2875, 1996.

[129] M. G. McKee, M. T. Hunley, J. M. Layman, and T. E. Long, "Solution rheological behavior and electrospinning of cationic polyelectrolytes," *Macromolecules*, vol. 39, no. 2, pp. 575–583, 2006.

[130] S. Campana, C. Andrade, M. Milas, and M. Rinaudo, "Polyelectrolyte and rheological studies on the polysaccharide welan," *International Journal of Biological Macromolecules*, vol. 12, no. 6, pp. 379–384, 1990.

[131] G. Gravanis, M. Milas, M. Rinaudo, and A. J. Clarke-Sturman, "Rheological behaviour of a succinoglycan polysaccharide in dilute and semi-dilute solutions," *International Journal of Biological Macromolecules*, vol. 12, no. 3, pp. 201–206, 1990.

[132] W. E. Krause, J. S. Tan, and R. H. Colby, "Semidilute solution rheology of polyelectrolytes with no added salt," *Journal of Polymer Science Part B: Polymer Physics*, vol. 37, no. 24, pp. 3429–3437, 1999.

[133] J. Irving and J. G. Kirkwood, "The statistical mechanical theory of transport processes. iv. the equations of hydrodynamics," *The Journal of Chemical Physics*, vol. 18, p. 817, 1950.

[134] B. Todd, D. J. Evans, and P. J. Daivis, "Pressure tensor for inhomogeneous fluids," *Physical Review E*, vol. 52, no. 2, p. 1627, 1995.

[135] H. Heinz, W. Paul, and K. Binder, "Calculation of local pressure tensors in systems with many-body interactions," *Physical Review E*, vol. 72, no. 6, p. 066704, 2005.

[136] D. A. Fedosov, G. E. Karniadakis, and B. Caswell, "Steady shear rheometry of dissipative particle dynamics models of polymer fluids in reverse poiseuille flow," *The Journal of Chemical Physics*, vol. 132, p. 144103, 2010.

[137] M. Ruths and J. N. Israelachvili, "Surface forces and nanorheology of molecularly thin films," in *Nanotribology and Nanomechanics*, pp. 417–515, Springer, 2008.

[138] R. R. Netz and D. Andelman, "Neutral and charged polymers at interfaces," *Physics Reports*, vol. 380, no. 1, pp. 1–95, 2003.

[139] R. Tadmor, E. Hernandez-Zapata, N. Chen, P. Pincus, and J. N. Israelachvili, "Debye length and double-layer forces in polyelectrolyte solutions," *Macromolecules*, vol. 35, no. 6, pp. 2380–2388, 2002.

[140] S. Lee, M. Müller, R. Heeb, S. Zürcher, S. Tosatti, M. Heinrich, F. Amstad, S. Pechmann, and N. Spencer, "Self-healing behavior of a polyelectrolyte-based lubricant additive for aqueous lubrication of oxide materials," *Tribology Letters*, vol. 24, no. 3, pp. 217–223, 2006.

[141] R. Heeb, S. Lee, N. V. Venkataraman, and N. D. Spencer, "Influence of salt on the aqueous lubrication properties of end-grafted, ethylene glycol-based self-assembled monolayers," *ACS Applied Materials & Interfaces*, vol. 1, no. 5, pp. 1105–1112, 2009.

[142] R. Tadmor, N. Chen, and J. N. Israelachvili, "Thin film rheology and lubricity of hyaluronic acid solutions at a normal physiological concentration," *Journal of Biomedical Materials Research*, vol. 61, no. 4, pp. 514–523, 2002.

[143] O. M. Stuetzer, "Ion drag pumps," *Journal of Applied Physics*, vol. 31, no. 1, pp. 136–146, 1960.

[144] A. Richter, A. Plettner, K. Hofmann, and H. Sandmaier, "A micromachined electrohydrodynamic (ehd) pump," *Sensors and Actuators A: Physical*, vol. 29, no. 2, pp. 159–168, 1991.

[145] J. Yang, F. Lu, L. W. Kostiuk, and D. Y. Kwok, "Electrokinetic microchannel battery by means of electrokinetic and microfluidic phenomena," *Journal of Micromechanics and Microengineering*, vol. 13, no. 6, p. 963, 2003.

[146] O. I. Vinogradova, K. Koynov, A. Best, and F. Feuillebois, "Direct measurements of hydrophobic slippage using double-focus fluorescence cross-correlation," *Physical Review Letters*, vol. 102, no. 11, p. 118302, 2009.

[147] C. Cottin-Bizonne, B. Cross, A. Steinberger, and E. Charlaix, "Boundary slip on smooth hydrophobic surfaces: Intrinsic effects and possible artifacts," *Physical Review Letters*, vol. 94, no. 5, p. 056102, 2005.

[148] L. Joly, C. Ybert, and L. Bocquet, "Probing the nanohydrodynamics at liquid-solid interfaces using thermal motion," *Physical Review Letters*, vol. 96, no. 4, p. 046101, 2006.

[149] J. Ou and J. P. Rothstein, "Direct velocity measurements of the flow past drag-reducing ultrahydrophobic surfaces," *Physics of Fluids*, vol. 17, no. 10, pp. 103606–103606, 2005.

[150] P. Joseph, C. Cottin-Bizonne, J.-M. Benoit, C. Ybert, C. Journet, P. Tabeling, and L. Bocquet, "Slippage of water past superhydrophobic carbon nanotube forests in microchannels," *Physical Review Letters*, vol. 97, no. 15, p. 156104, 2006.

[151] P. Tsai, A. M. Peters, C. Pirat, M. Wessling, R. G. Lammertink, and D. Lohse, "Quantifying effective slip length over micropatterned hydrophobic surfaces," *Physics of Fluids*, vol. 21, no. 11, pp. 112002–112002, 2009.

[152] A. V. Belyaev and O. I. Vinogradova, "Electro-osmosis on anisotropic superhydrophobic surfaces," *Physical Review Letters*, vol. 107, no. 9, p. 98301, 2011.

[153] J. Zhou, A. V. Belyaev, F. Schmid, and O. I. Vinogradova, "Anisotropic flow in striped superhydrophobic channels," *The Journal of Chemical Physics*, vol. 136, no. 19, p. 4706, 2012.

[154] V. Tandon, S. K. Bhagavatula, W. C. Nelson, and B. J. Kirby, "Zeta potential and electroosmotic mobility in microfluidic devices fabricated from hydrophobic polymers: 1. the origins of charge," *Electrophoresis*, vol. 29, no. 5, pp. 1092–1101, 2008.

[155] K. C. Grass, *Towards realistic modelling of free-solution electrophoresis : a case study on charged macromolecules.* PhD thesis, Goethe-Universität Frankfurt am Main, 2009.

[156] H. G. Petersen, "Accuracy and efficiency of the particle mesh ewald method," *The Journal of Chemical Physics*, vol. 103, p. 3668, 1995.

[157] M. Deserno and C. Holm, "How to mesh up ewald sums. ii. an accurate error estimate for the particle–particle–particle-mesh algorithm," *The Journal of Chemical Physics*, vol. 109, no. 18, 1998.

[158] J. Kolafa and J. W. Perram, "Cutoff errors in the ewald summation formulae for point charge systems," *Molecular Simulation*, vol. 9, no. 5, pp. 351–368, 1992.

[159] H. Behringer and R. Eichhorn, "Brownian dynamics simulations with hard-body interactions: Spherical particles," *The Journal of Chemical Physics*, vol. 137, p. 164108, 2012.

ACKNOWLEDGEMENTS

CURRICULUM VITAE